Mixing and NOx Emission Calculations of Confined Reacting Jet Flows in a Cylindrical Duct

Victor L. Oechsle
Allison Engine Company, Indianapolis, Indiana

Since its founding, NASA has been dedicated to the advancement of aeronautics and space science. The NASA Scientific and Technical Information (STI) Program Office plays a key part in helping NASA maintain this important role.

The NASA STI Program Office is operated by Langley Research Center, the Lead Center for NASA's scientific and technical information. The NASA STI Program Office provides access to the NASA STI Database, the largest collection of aeronautical and space science STI in the world. The Program Office is also NASA's institutional mechanism for disseminating the results of its research and development activities. These results are published by NASA in the NASA STI Report Series, which includes the following report types:

- TECHNICAL PUBLICATION. Reports of completed research or a major significant phase of research that present the results of NASA programs and include extensive data or theoretical analysis. Includes compilations of significant scientific and technical data and information deemed to be of continuing reference value. NASA's counterpart of peer-reviewed formal professional papers but has less stringent limitations on manuscript length and extent of graphic presentations.

- TECHNICAL MEMORANDUM. Scientific and technical findings that are preliminary or of specialized interest, e.g., quick release reports, working papers, and bibliographies that contain minimal annotation. Does not contain extensive analysis.

- CONTRACTOR REPORT. Scientific and technical findings by NASA-sponsored contractors and grantees.

- CONFERENCE PUBLICATION. Collected papers from scientific and technical conferences, symposia, seminars, or other meetings sponsored or cosponsored by NASA.

- SPECIAL PUBLICATION. Scientific, technical, or historical information from NASA programs, projects, and missions, often concerned with subjects having substantial public interest.

- TECHNICAL TRANSLATION. English-language translations of foreign scientific and technical material pertinent to NASA's mission.

Specialized services that complement the STI Program Office's diverse offerings include creating custom thesauri, building customized databases, organizing and publishing research results . . . even providing videos.

For more information about the NASA STI Program Office, see the following:

- Access the NASA STI Program Home Page at *http://www.sti.nasa.gov*

- E-mail your question via the Internet to help@sti.nasa.gov

- Fax your question to the NASA Access Help Desk at 301–621–0134

- Telephone the NASA Access Help Desk at 301–621–0390

- Write to:
  NASA Access Help Desk
  NASA Center for AeroSpace Information
  7121 Standard Drive
  Hanover, MD 21076

Mixing and NOx Emission Calculations of Confined Reacting Jet Flows in a Cylindrical Duct

Victor L. Oechsle
Allison Engine Company, Indianapolis, Indiana

National Aeronautics and
Space Administration

Glenn Research Center

Document Notice

This reseach was originally published internally as HSR005 in August 1995.

Available from

NASA Center for Aerospace Information
7121 Standard Drive
Hanover, MD 21076

National Technical Information Service
5285 Port Royal Road
Springfield, VA 22100

Available electronically at http://gltrs.grc.nasa.gov

Table of Contents

Nomenclature

A   area

A_m duct cross-sectional area, also A_{tot}, m^2

ACd   also A_j, effective orifice area, m^2

Ar   area ratio (jet/mainstream) = A_j/A_m = ACd/A_m

AMIX   area weighted overall T or ϕ deviation from equilibrium, Eq 6

B   area determined half width of the distribution function

C   constant of proportionality between $\sqrt{J}$ and S/R, Eq-9

d   diameter of the orifice

DR   density ratio (jet/mainstream)

DP/P   total pressure loss across the mixing wall, %

f   non-dimensional equivalence ratio, Eq 4

f/a   fuel to air ratio

j   radial vector direction

J   momentum-flux ratio (jet/mainstream) = M^2/DR, also $(MR)^2/[(DR)(A_j/A_m)^2]$

k   tangential vector direction

m_{tot} overall mixer mass flowrate, kg/sec = $m_{jet} + m_{main}$

M   mass flux ratio (jet/mainstream) = $DR\ V_{jet}\ /U_{main}$

MMIX   mass flow weighted overall T or ϕ deviation from equilibrium, Eq 6

MR   mass flowrate ratio (jet/mainstream)

n   optimum number of orifices / row, Eq-9

P   total pressure, atm.

R   radius of the mixing section, m

r   radial distance from the centerline of the mixer, m

S   orifice spacing in the circumferential direction

T   temperature, K

u   local axial velocity, m/sec

U_{main} approach mainstream axial velocity, m/sec

VR   velocity ratio (jet/mainstream) = V_{jet} / U_{main}

V_{jet} radial velocity of the jet, m/sec

x   axial distance from the leading edge of the orifice

δ value of the cumulative volume fraction at the f_{equil} , Fig-3

ρ fluid density, kg/m^3

ϕ equivalence ratio $(f/a)_{local}$ / $(f/a)_{stoi}$

Subscripts

equil   equilibrium

j   jet

m   mainstream, also (main)

RZ   rich-zone

stoi   stoichiometric

Introduction

In recent years, the design and development of gas turbine engines for the aeropropulsion and ground based power generation systems has been channeled towards decreasing the gaseous emissions without adversely affecting the system performance. The environmental effects of both carbon monoxide (CO) and oxides of nitrogen (NOx) have been investigated extensively for many years and their potential hazards are increasingly becoming a more world wide sensitive issue. The trend in the gas turbine engine design advancement has been channeled towards increasing both engine pressure ratio and rotor inlet temperature levels in order to increase the overall thermodynamic cycle efficiency. However, this evolution has been adversely affecting both engine durability and gaseous emissions, especially that of NOx. The production of NOx is generally a function of the combustion system design, hot section temperature distribution, residence time, and localized fuel/air mixture.

The development of an efficient and low-emission high speed civil transport combustion system demands increased insight in combustion chemical kinetics, efficient air/fuel mixture, and advanced materials and cooling techniques. The combustion liner cooling air flowrate significantly affects the combustion process by quenching the flame at localized regions near the wall thereby producing CO and also producing localized hot spots which increase the production of NOx. Current gas turbine combustion liner technology employs a single-stage combustion process in which both fuel and air are admitted into a controlled mixing chamber and are allowed to react. With the advent of higher temperature operating conditions, the reduction of NOx becomes a very difficult task to accomplish using single axial staged combustion. Therefore, alternative combustion methods are being explored by the main gas turbine engine manufacturers and other research organizations. Two of the main low NOx designs being developed are axially multistage combustion rich burn/quick mix/lean burn (RQL), and lean premixed prevaporized (LPP). Both have advantages and disadvantages regarding operation range and hardware complexity.

In this report, the advantages and limitations of the RQL design are being explored by focusing on the performance of the quick-mix region. The successful performance of the RQL combustor depends on a quick and efficient mixing of the rich zone combustion products with compressor discharge air to effectively reduce the overall and localized equivalence ratio from about 1.8 to about 0.5. This process must be accomplished with a minimum transient time (at or near equivalence ratio of 1) where most of the NOx is produced due to the high resulting temperature levels and Oxygen availability.

An experimental and analytical effort under the sponsorship of NASA Lewis Research Center (e.g. Howe,. et al., 1991; Smith, Talpallikar, and Holdeman, 1991; Talpallikar et al., 1991; Vranos et al., 1991; Bain, Smith, and Holdeman, 1992, 1993; Bain, Smith, and Holdeman, 1994; Liscinsky et al., 1992; Zhu and Lai, 1992; Doerr and Hennecke, 1993; Liscinsky, True, and Holdeman, 1993; Liscinsky, True, and Holdeman, 1994; Hatch, Sowa, Samuelsen, and Holdeman, 1992; Hatch, Sowa, and Samuelsen, 1994; Kroll, Sowa, Samuelsen, and Holdeman, 1993, Sowa, Kroll, Samuelsen, and Holdeman, 1994) is underway to study and identify the critical design and flow parameters affecting the mixing effectiveness.

In this study, a 3-D numerical tool is used to predict the performance of an RQL mixing section. The 3-D flow structure of the mixer can be modeled in detail and predictions can be obtained with a host of scalar and vector quantities to accurately evaluate the mixing flowfield. In addition, a relatively large number of configurations can be easily analyzed to predict the trends of both mixing uniformity and NOx production in a generalized jet in a crossflow problem. In this study, however, the flowfield of several different mixer configurations are evaluated and compared with their corresponding NOx predictions. The objective is to address the question whether a good mixing configuration produces low NOx. For this purpose, 18 different mixer configurations were analyzed with the 3-D numerical tool and the localized NOx production and overall mixer NOx production flowrate were calculated from each case. The local NOx value normalizes the NOx production flowrate per volume (g of NOx per sec per m³) with respect to the local volume of the micro sector in order to eliminate the ambiguity of the different volume sectors used to partition the mixing zone in the NOx prediction. The mixer configurations include the following orifice shapes: a) round holes, and b) elongated slots with aspect ratios of L/W=4 and 8 and different slant angles from 0 degrees (aligned with the flow) to 90 degrees (transversely aligned to the mainstream approach flow). The jet to mainstream momentum-flux ratio was varied from 25 to 80. An analysis was further carried out to evaluate and quantify the mixing flowfields in order to rank the best from the worst mixing and NOx production configurations.

Mathematical Model

3-D Flow Model

A production 3-D combustor code, COM-3D (Bruce, Mongia, and Reynolds, 1979) is used that solves the turbulent reacting flow transport equations using the SIMPLE algorithm of Patankar and Spalding (Patankar, 1980). This program simulates turbulence by the two-equation k-ε model (Launder and Spalding, 1974), and combustion following vaporization is determined by a four-step chemical reaction model based on Arrhenius and modified eddy breakup concepts. The transport equations for all dependent variables are of the following form as shown in Eq-1:

$$\text{div}[\rho_r u \xi - (\mu_{eff}/P_r)\, \text{grad}(\xi)] = S_\xi \qquad (1)$$

where ρ_r is the mixture density, u is the velocity, μ_{eff} is the effective turbulent viscosity, P_r is the effective Prandtl/Schmidt number, and S_ξ is the source term for the variable ξ. The following variables are computed by COM-3D: 1) axial, radial, and swirl velocity components; 2) specific enthalpy and temperature; 3) turbulence kinetic energy and dissipation rate; 4) unburned fuel, CO, H_2, intermediate fuel, and composite fuel mass fractions; and 5) fuel spray trajectory and evaporation rate.

The computational effort is significantly reduced by modeling a sector of the mixing section comprising a single orifice. Therefore, the shape of the sector was dependent on the number of orifices equally spaced in the circumferential direction. It should be noted that 8 orifices/row yield a computational domain of a 45 degree sector. Periodic boundary conditions were applied in the circumferential direction. No-slip and adiabatic boundary conditions were applied at the outer wall defining the inside wall of the mixing section. Zero-gradient boundary conditions

were applied at the center axis. Axial gradients at the exit boundary condition were assumed zero.

NOx model

The NOx model described herein was developed by Rizk and Mongia (1993). Because the NOx formation in the combustion liner is significantly affected by the details of the front end of the RQL and the subsequent admittance of air into the various downstream zones, the combustion liner needs to be divided into a number of regions for modeling purposes. The hybrid modeling technique therefore consists of using the 3-D simulation results obtained with COM-3D such as gas flowrate, flow averaged temperature, fuel/air ratio, in addition to the turbulence characteristics to accurately describe the flow nuances affecting the NOx production.

The NOx model is subdivided into three main zones: rich zone, mixing zone and lean zone. Each of these zones exhibit significantly different characteristics as to their role in the NOx production in an RQL combustion liner. Lefevre (1984) shows that the exhaust concentration of NOx could be calculated in terms of mean time in the combustion zone, chemical reaction rates, and mixing rates. Mellor (1976) describes a model that combines a number of perfectly stirred reactors and uses finite-rate mechanisms to calculate NOx. Furthermore, Fletcher and Heywood (1971) modeled the combustor primary zone as a partially stirred reactor burning gaseous fuel over a distribution about the primary zone equivalence ratio, a lateral mixing reactor, and a plug flow reactor.   Based on these studies it became clear that NOx production characteristics in an RQL combustor required a detailed model of the mixing flow phenomena along with detailed description of the chemical kinetics in the flame reaction zone.   The model used in this study subdivides the RQL combustor into the following zones: 1) rich zone made up of two parallel reactors: a stoichiometric reactor to account for the combustion at near-stoichiometric conditions and a rich zone feed. 2) Mixer air is admitted consecutively into the quench zone to form plug flow reactor, and 3) dilution air admitted into the dilution zone to form a secondary plug flow reactor similar to that of the quench zone.   To provide an accurate estimate of the trends of formation and reduction of NOx, the detailed reaction model developed by Westbrook and Pitz (1984), was combined with extended Zeldovich mechanisms for NOx. The detailed description of the mixing zone model will follow since this is the scope of this report. Both rich and lean zone design is categoric at this stage and assumptions about the modeling of these two are made as follows:

> 1) The input flow field exiting the rich zone and entering the quench zone is assumed to be fully reacted and in equilibrium. The species mole fractions for (CO, CO_2, H_2O, and H_2) were determined based on the given rich-zone equivalence ratio at chemical equilibrium at the prescribed operating conditions using JP-5 for the typical fuel properties. This assumption may not be totally realistic in an actual operating RQL rich section since more CO and unburned hydrocarbon emissions are expected as compared to this simplified rich zone model. The additional emissions are also expected to affect the mixing zone reaction prompted by the mixture of the rich zone products with additional air. However, since the rich-zone performance is not within the scope of this study, the assumed simplified rich-zone model (achieving chemical equilibrium) is a reasonable initial condition towards analyzing the reaction in the mixing zone. The four specified species used in the inlet mainstream condition correspond to the four-step chemical reaction used in COM-3D.

2) No expansion is assumed in the lean zone. The RQL liner is usually designed with an area expansion downstream of the quench zone in order to increase the residence time to further oxidize the CO produced in the rich zone.   In addition, no air is added in the lean zone downstream of the quench zone.

Based on these assumptions, the hybrid model was applied to the quench zone only.

Mixing zone model.

The kinetic scheme results for the quench zone reactor showed that a substantial increase in NOx formation occurred as the residence time in the reactor is increased. The results obtained at a number of pressure levels and rich zone equivalence ratios have been correlated as follows:

$$NO_q(g/kg) = 1.57E7 \ \tau_q^{nq} e^{\left[\frac{-38,000}{T_q}\right]} P^{0.2} \qquad (2)$$

T_q is the reaction temperature in the quench reactor, in K, and τ_q residence time in the reactor in ms. The exponent nq is given in terms of the rich zone equivalence ratio ϕ_r as follows:

$$nq = 0.834 \ \phi_r^{-0.36} \qquad (3)$$

The hybrid model consist in grouping the results obtained from a typical COM-3D grid with about 50,000 to 80,000 nodes into about 2,000 larger sub-volumes comprising of several computational nodes representing the entire mixing section of an RQL combustion liner. By this means, the reacting flow model results can be accurately represented and modeled using significantly less computational effort. For the NOx predictions only, the model of the quench zone extends to x/R=5 since the domain beyond the quench zone was not considered to be a realistic lean zone model for the given correlations. This was implemented to prevent any unrealistic discontinuities in the predictions near the real interface between the quench and lean zones (x/R=1) where x is the downstream axial distance from the leading edge of the orifice and R is the mixer radius evaluated at the outer wall.

Geometric Configuration

One potential design consideration for the hot section component of the high speed civil transport engine has been the "can" design RQL combustion liner. In a typical RQL combustion liner, the rich zone, quench zone, and lean zones are axially inter-connected with an area contraction in the mixing section to speed up mixing by increasing the mainstream momentum flux. However, in this study, the mixing section was modeled as a constant diameter cylindrical duct with a single row of equally spaced orifices. The outer wall diameter is 3 inches (0.076 m) and the axial length of the mixing section extended from x/R=-1.4 to x/R=6. Sufficient axial distance was provided both upstream and downstream of the orifice to minimize the impact of

the inlet and exit boundary conditions on the calculated flow structure in the primary domain of interest which is ($0 \leq x/R \leq 1$). The downstream limit ($x/R=1$) of the quench zone is and has been defined arbitrarily by this and many other authors listed in the reference.

The computational grid domain was typically discretized into 50,000 to 80,000 finite control volumes generally arranged with about 70 nodes in the axial direction, and 30 nodes in both the radial and tangential directions. The grid was typically denser near the orifice and near the outer wall to resolve the high velocity and temperature gradients resulting from the inlet of the crossflow jet. An orthogonal view of a typical grid arrangement is shown in Figure-1. The grid is normally configured to allow smooth progressive volume change between adjacent control volumes to help speed up the convergence of the solution. In the 3-D numerical model, a secondary grid (staggered grid) is interpolated from that shown in Figure-1 to obtain the boundaries upon which the vector quantities are acting upon. In other words, the staggered grid becomes the control surfaces of the micro control volumes that constitute the inner volume of the mixing section.

The geometric configuration of the mixer showing a round orifice is also shown in Figure-1. A total of 18 circular and slanted slot orifice configurations were analyzed as shown in Tables-1 and 2 and are also shown graphically in Figure-2. The blockage is defined as the circumferential projection of the orifice divided by the spacing between the orifice centers, and the T.E. x/R is the non-dimensional axial location (x/R) of the trailing edge of the orifice with respect to its leading edge (x/R=0). Both these parameters are shown in Tables-1 and 2. The matrix of slanted slot orifices summarized in this report include shape variations with an aspect ratio long/short (L/W) of 4 and 8, and slant angles of 0, 22.5, 45, 67.5, and 90 degrees with respect to the mainstream flow direction. NOTE that the nomenclature that identifies the configurations range from 19 through 36. Configurations 1 through 18 have previously been reported by Oechsle, Mongia, and Holdeman (1993), and they are the non-reacting counterparts of the same geometric configurations.

In this study, the following main parameters were kept constant throughout this analysis. The control of these parameters is essential for a valid comparison of both mixing non-uniformity and NOx production between the appropriate configurations.

1) rich zone equivalence ratio $\phi_{rz} = 1.80$
2) lean zone equivalence ratio $\phi_{lz} = 0.416$
3) overall mixer pressure = 14.1 atm.
4) jet temperature = 950 K
5) mainstream temperature = 2164 K, from the chemical equilibrium code (CEC) developed by NASA
6) mixer diameter = 0.076 m
7) jet to mainstream mass flow rate MR = 2.96
8) jet to mainstream density ratio DR = 2.28
9) number of orifices = 8

The following were allowed to vary:

1) jet to mainstream momentum-flux ratio J from nominal values of 25 to 80

2) overall mixer total pressure drop between 1.3 to 5%
3) orifice ACd depending on the value of J in order to maintain the same MR
4) orifice blockage and T.E. x/R values depending on the orifice shape and orientation
5) jet velocity depending on the value of J

The system pressure, temperature, J range, MR, and DP/P for the 18 configurations simulate actual HSCT engine altitude cruise design conditions

Modeling specifications

The species mole fractions, temperature, and velocity profiles exiting the rich zone and entering the mixer were assumed to be uniform across the inlet cross-section of the mixing section. The air jet flow was characterized by a radial, uniform flow across the orifice effective area. COM-3D is not a body conforming code therefore accurate modeling of the orifice shape was obtained by defining the orifice with 80 to 150 control surfaces. In this way the stair-stepping approximation in the slanted and round contours could be maximized. The assumption of uniform mass injection/area for the orifice air entry is applied in the mathematical model in all the analyzed configurations. The turbulence kinetic energy of the mainstream and jet flows were 0.3% of the square of the mean velocities. The turbulence length scales of the mainstream flow were 2% of the mixer diameter, and the turbulence length scale of the jet was of the order of the orifice diameter. The results from COM-3D were post processed into about 2000 sub-volumes typically 20 in the axial direction, 10 in the radial, and 10 in the circumferential direction. This input was used to generate the NOx predictions based on the flow characteristics.

A typical numerical solution took about 500 iterations for full reacting flow convergence with overall mass flow residuals of 0.05% of the total mixing section mass flowrate. All solutions were obtained using the Cray C-90 and a typically converged solution took about 2 hrs of CPU time.

Result representation

Of the results obtained numerically, several are plotted in this report:

1) The plots shown in Appendix-A are the sector views of the computational grids for each of the 18 configurations summarized in this report. Each plot contains three views of the grid. a) view in the radial-tangential plane, b) view in the axial-tangential plane looking down from the outside of the mixer (also shows the shape of the modeled orifice), and c) axial-radial plane view (bottom line is r=0, the axis of symmetry). The axial-radial and axial-tangential views define the abscissa as the axial direction.

2) Normalized temperature contour distributions, normalized equivalence ratio contour distributions, and velocity vector plots are represented for each configuration. These plots are shown in Appendix-B of this report. The equivalence ratio results are presented as normalized values with respect to the overall differential between the mainstream flow and the jet flow inlet values. The normalized parameter (f) is defined in Eq-4 applied to the equivalence ratio scalar quantity (ϕ). The normalized temperature distribution plots shown in Appendix-B are defined in Eq-5.

$$f = \frac{\phi_{jk} - \phi_{jet}}{\phi_{main} - \phi_{jet}} \qquad (4)$$

$$\text{Non-dimensional Temperature} = \frac{T_{jk} - T_{jet}}{T_{stoic} - T_{jet}} \qquad (5)$$

Note that the equivalence ratio is a conserved scalar. The temperature is not a conserved scalar due to the added production term in the energy equation as a result of the reacting flow.

The value of (f) varies from 0 to 1, where 0 is the value of the unmixed jet equivalence ratio and 1 is the value of the mainstream flow equivalence ratio. Note that $f = 1-\theta$, where θ is as defined previously (Holdeman, 1993) and used elsewhere also. Also note that the definition of (f) does not apply to the temperature distribution in the reacting flow solutions since the temperature in some areas of the mixing region rise above that of the incoming mainstream flow due to the chemical reaction of the rich-zone exit composition. The equilibrium (f) value was calculated in a purely adiabatic system at any location downstream of the jet injection. The temperature, equivalence ratio, and velocity plot views in Appendix-B are the following:

a) axial-radial plane through the center of the orifice where the axial direction is in the same direction as the mainstream flow direction (flow towards the turbine). Both axial and radial directions are non-dimensionalized with respect to the mixer radius. The x/R=0 location denotes the leading edge of the orifice and a r/R location of 1 is the outer wall location. The view is such that the left side of the plot is the upstream side of the mixer

b) radial-tangential plane at x/R=1. The plot has also been non-dimensionalized so that the r/R equals the mixer radius at the outer wall. The view is looking downstream from the inlet of the mixer.

c) axial-tangential plane at the plane closest to the outer wall of the mixer. This view shows the location of the orifice with respect to the outer wall of the mixer. The axial direction has been non-dimensionalized with respect to the mixer radius R and the tangential direction has been non-dimensionalized with respect to the orifice-to-orifice center spacing (S) in the tangential direction. z/S=0 is at the top boundary of the plot looking from the outside of the mixer towards the centerline. NOTE that the modeled sector has the orifice in the center as shown in Figure-1.

3) 3-D orthogonal views of the NOx production, fuel/air ratio, and temperature are shown in Appendix-C. The 3-D orthogonal view plots show four different planes that essentially lengthwise split the mixer domain in half. The planes shown are: a) the radial-tangential planes at slightly upstream of x/R=0, b) slightly downstream of x/R=1, c) axial-radial plane through the center of the orifice, and d) axial-tangential plane at the outer wall of the mixing section. In order to eliminate any 3-dimensional ambiguity in the interpretation of these 3-D

plots, it is necessary to understand that the view is looking up at the inside surface of the outer wall of the mixing section and half of the orifice can be seen since the axial-radial plane slices the orifice. It is also worth noting that the viewer is located downstream looking upstream at the mixing section. In these color contour plots, the flow moves from left to right and the color spectrum is devised so that the largest parameters are plotted in red while the smallest in blue (purple). The output results from COM-3D for each configuration were plotted in one page as follows:

a) The top plot is the localized NOx production per volume in grams of NOx per sec per m^3. The contour values are expressed in logarithmic scale due to the large range of variation throughout the mixing section. These results were obtained with Allison's hybrid modeling technique.

b) The middle plot is the fuel/air distribution in the mixer. Note that the incoming f/a from the rich zone is equivalent to a rich zone equivalence ratio of 1.8 as shown in Table-1. In a similar manner, the output f/a from the mixing zone is equivalent of a lean zone equivalence ratio of 0.416.

c) The bottom color contour plot depicts the temperature distribution in K for the entire mixing section. Note that the temperature rises above that of the incoming rich zone temperature due to the reaction produced by the additional air entering the mixer.

4) The localized NOx production in (gr of NOx per sec per cubic meter) shown in Appendix-D in a different perspective as compared to the previous plots. These plots show the interpolated iso-surfaces of constant NOx production in the mixing section. These 3-D orthogonal plots show the mixing section looking downstream from the upstream end of the mixer. The Cartesian coordinates are represented by 3 intersecting planes such that the mixing section is contained inside the box. This open box is shown along with each plot to eliminate the ambiguity of the 3-D perspective. NOTE: that the outer contour (showing the pie section of the mixer) is slightly smaller than the actual mixer (the outer wall is located at r/R=1) since it is described by the center points of each of the boundary sub-volumes in the NOx analysis. Figure-D37 in Appendix-D shows the post processed mixer domain and sub-volume breakup used in the NOx calculations. The intersecting points correspond to the center of the sub-volumes. The true 3-D location of the orifice is also shown in the white contour in each plot. The flow is moving from left to right, and the coordinates have been normalized in the x, y, and z directions. Three different NOx production surfaces are shown ranging from 10^2 to 10^4 gr of NOx / sec m^3 where the red surface is the highest and green is the lowest range. Note that in most plots, the red contour is not shown since no surface was found at this level.

Two types of plots are shown for each configuration: a) the entire computational domain -1 < x/R < 5, and b) the mixer domain 0 < x/R < 1. The shape of the orifice in the plots showing the entire computational domain are disfigured due to the normalization scales. A truer shape of the orifice can be seen in the plots showing only the mixer domain ($0 \leq x/R \leq 1$).

5) The temperature, local NOx, and normalized equivalence ratio plots are also shown in the figures in Appendix-E for all 16 configurations described in this report. The 3-D perspective of these plots places the observer downstream looking upstream at the orthogonal view of a 90 degree section of the mixer containing 2 orifices. Five different radial-tangential planes have

been chosen at x/R = 0.08, 0.25, 0.5, 0.75, and 1.0 showing the flow development and NOx production throughout the mixing section. The axial direction is plotted vertically and the flow moves from bottom towards the top. Note that the corresponding non-reacting distributions appear in Oechsle, Mongia, and Holdeman (1992) and corresponding experimental equivalence ratio plots and NOx inference distributions appear in Hatch, Sowa, and Samuelsen (1994)

The representation of the analyzed results and statistical results will be described in detail in the next section.

Results and Discussion

The mixing performance for all configurations analyzed in this study were ultimately evaluated at x/R =1. It is however recognized that the performance throughout the mixing section volume of interest (0 ≤ x/R ≤ 1) should also be considered since complex structures are present in the flow field especially near the entry of the jet.

Two different methods were used to analyze the numerical results: qualitative analysis and quantitative analysis. Both of these are described in detail below.

Qualitative analysis

The results were analyzed qualitatively by visual observation of the temperature, equivalence ratio, and velocity field solutions shown in Appendices-A, B, C, D, and E. The streamline traces in the velocity plots indicate the penetration of the jet and also indicate the degree of swirl imparted by the jets entering the mixer through the slanted slot orifices. The evaluation of the mixing non-uniformity is clearly identified by looking at the color contour plots and noting the variation in the color distribution in both temperature and equivalence ratio distribution contours. The mixing evaluation should only be made in reference to the color band or the equilibrium value of (f). The normalized temperature plots indicate locations, especially behind the orifice, where the reaction between the mainstream and jet flow produce the expected temperature rise.

The plots shown in Appendices-C, D, and E can also be used to evaluate the critical NOx production locations. The NOx production results shown in these plots denote the NOx production per sub-volume. The mixing section is sub-divided into 2000 sub-volumes and the result of each is plotted in the 3-D orthogonal view. These plots have been constructed to help the viewer interpret the 3-D NOx production with the given planes allowing the viewer interpolate the planes which are not shown.

Quantitative analysis

The quantitative analysis method involves the detailed characterization of the mixing flowfield using several different statistical techniques. This technique is especially useful for the numerical results since a copious amount of data is obtained from the numerical model with a host of different scalar and vector quantities at several thousand locations in the flowfield. The

statistical techniques reported herein therefore characterize the mixing non-uniformity only. Three different statistical methods are reported in this report:

a) The performance of the mixing section at the radial-tangential planes at x/R=1 was quantified by using area weighted planar deviation parameters. The smallest deviation with respect to the equilibrium value indicates the best mixing configuration. This parameter (AMIX) is described in Eq-6. It is also important to note that AMIX does not correct the mixing non-uniformity for the bias introduced in the region of the mixer where the air is being injected through the orifice. However, AMIX is only evaluated at the exit of the mixer x/R=1 and is therefore applicable since this plane is downstream of the air injection in all 18 configurations summarized in this report. The area-weighted non-uniformity results are shown in Table-3.

$$\text{AMIX} = \left[\frac{1}{A_{tot}} \sum_{jk} A_{jk} \left[\frac{\phi_{jk} - \phi_{eq}}{\phi_{main} - \phi_{jet}} \right]^2 \right]^{1/2} \tag{6}$$

b) The mass flow weighted planar deviation parameter (also evaluated at x/R=1) as defined in Eq-7 is also used to evaluate the mixing region. Note that this parameter is similar to the area weighted parameter in Eq-6, with the added density and velocity weighting terms. The mass flow weighted mixing non-uniformity results for all configurations are shown in Table-3. The smallest MMIX value with respect to the f_{equil} corresponds to the best mixing uniformity.

$$\text{MMIX} = \left[\frac{1}{\dot{m}_{tot}} \sum_{jk} A_{jk} \rho_{jk} u_{jk} \left[\frac{\phi_{jk} - \phi_{eq}}{\phi_{main} - \phi_{jet}} \right]^2 \right]^{1/2} \tag{7}$$

c) The flow field was also evaluated by performing a numerical volume integration throughout the mixing section of interest ($0 \le x/R \le 1$) as shown in Eq-8.

$$\text{Volume Fraction/bin} = \frac{\sum\limits_{f_{l_i}}^{fh_i} \text{Volume}_{ijk}}{\sum\limits_{f_{jet}}^{f_{main}} \text{Volume}_{ijk}} \tag{8}$$

The volume integration parameters allow the analysis of the entire flow field mixture which is more descriptive of the overall flow phenomena in the mixing section as compared to a planar deviation analysis shown in Eqs-6 and 7. This volume integration was only performed on the equivalence ratio distributions. The entire range of the normalized parameter f (from 0 to 1) was sub-divided into 200 equal size bins and the

volume of the computational control volumes corresponding to the value of (f) at a certain bin size (f_i to $f_{i+\Delta f}$) was integrated as shown in Figure-3. The integrated volume in each bin was normalized based on the entire analyzed mixer volume, thus obtaining the normalized volume fraction. The volume fraction for each bin was plotted in the ordinate with the corresponding value of f in the abscissa forming a histogram plot. In addition, the incremental partial volume per bin was integrated from f = 0 to 1 and the cumulative volume fraction was obtained for all the 18 analyzed configurations as shown in Figures 4 and 5. If the histogram is integrated from f=0 to f=1, the value of the cumulative volume fraction will be 1 since the overall volume itself is also normalized to 1.

The shape of the volume fraction histogram was also characterized by the definition of B(+) and B(-) similar to that used by Oechsle, Mongia, and Holdeman, 1992. The value of B(+) is the "area determined" distribution half width above f_{equil} such that the integrated area under the histogram above f_{equil} is 1/2 that of the overall histogram area above f_{equil}. The same applies to B(-) for the area below f_{equil}. The definitions of B(+) and B(-) are shown pictorially in Figure-3. The best mixing results yields lowest B(+) and B(-), meaning that the histogram distribution width effectively collapses towards the equilibrium value of (f). The histogram shape value SUM-B is defined as the sum of B(+) and B(-).

The summary of both mixing uniformity and NOx production flowrate trends for the 18 configurations are shown in Figure-6. In this report, the following comparisons are made:

1) effect of orifice shape on mixing and NOx
2) effect of J on mixing and NOx production,
3) effect of slot slant angle on mixing and NOx,
4) configuration optimization at different J, and
5) correlation between NOx production and the mixing flowfield

Effect of orifice shape on NOx production and mixing non-uniformity

The mixing non-uniformity and NOx production were compared for the round orifices, 45° slots with L/W=4, and 45° slot with L/W=8 for J=25 (configuration numbers 19, 20, and 24 respectively), at J=52 (configuration numbers 23, 29, and 25), and J=80 (configuration numbers 22, 30, and 26). The results for this comparison are shown in Figures-6a through 6c, Figure-7, and Figure-8. Additional results are also shown in Appendix-B plots (Figure-B1-1 through Figure-B3-9), Appendix-C, Appendix-D, and Appendix-E plots for the configurations listed above.

J=25

The results at J=25 shown in Figures-6a Figure-7a, 7b, and 8a through 8c indicate that the round orifice produces less NOx. Figure-6 shows the cumulative NOx production flowrate up to a plane x/R=1, and Figure-7 shows the NOx production trends per axial plane plotted for x/R from -1 to 2, and the cumulative NOx production flowrate from x/R of -1 to 2. The results

indicate that even though the round orifice has stronger jet penetration, thus producing a large orifice wake, the cumulative NOx production is lower as compared to the slanted slots which generally underpenetrate. The plots in Appendix-D for configurations 19, 20 and 24 indicate that the round orifice produced very low NOx elsewhere as compared to the wake region behind the orifice. The slot configurations # 20 and 24 indicate additional NOx was produced below the orifice near the center of the mixer due to shallow penetration and induced swirl. Also note that the results generally indicate an increase in NOx production near the x/R=1 region (see Figure-7a) which is caused by the mixture between the hot gases entering the mixer and the cool gases from the jets along with the high residence time which mainly occurs in and downstream of the wake of the jet.

The mixing results indicate marginal improvement in the mixing nonuniformity with increased orifice aspect ratio (best mixer is the L/W=8 slot conf # 24) as shown consistently by all the three statistical parameters (AMIX, MMIX, and volume histograms). Both mixing results and NOx predictions show no general correlating trends. Note that the histograms shown in Figure-8a through 8c indicate that the round orifice has a significantly large portion of the overall volume at the nondimensionalized equivalence ratio (f) near zero (see Figure-8a) as compared to the slanted slot cases in Figures-8b and 8c. This indicates that the NOx production will be low since the jet flow quenches the mainstream flow. It is also recognized (although not analyzed in this study) that the production of CO and unburned hydrocarbons may be high since the jet flow appears to be overly quenching the rich zone products to a value much below the equilibrium value.

J=52

The results at J=52 are shown in Figures-6b, 7c, 7d, and 8d through 8f. At J=52 the increase in penetration for the round jet appears to increase the NOx production since the wake behind the jet is large. In likely manner, the slanted orifices however appear to have better NOx performance as compared to the round orifice due to improved jet penetration. The figures in Appendix-D for configurations 23, 29, and 25 indicate that the round hole (conf #23) produces NOx near both sides and slightly upstream of the orifice while the L/W=8 slot produced a significant amount of NOx near the center of the mixer due to its shallow jet penetration. The lowest NOx configuration was the 45 degree slot L/W=4 (conf #29). The jet penetration appears to be an essential parameter in the control of NOx production. The production of NOx upstream of the orifice is also shown in Figures-7c and 7d and will later be shown to be an important factor for orifice selection in an RQL design.

The area weighted parameters (AMIX, MMIX, and volume integrals) indicate improvement in mixing uniformity as the slot aspect ratio increases (assume the round hole as a slot with an aspect ratio L/W=1). It is however interesting that the histogram shapes shown in Figures-8d through 8f show some similarities for varying orifice shapes. It appears that both NOx and mixing trends are opposing in this comparison since the best mixing configuration is the highest NOx producer and these results seem to agree with the comparison at J=25 summarized previously.

J=80

The results at J=80 are shown in Figures-6c, 7e, 7f, and 8g through 8i. As J is increased to 80, the results indicate that the highest NOx production is attributed to the round holes and lowest NOx production is attributed to the 45 degree slot, L/W=8 and the ratio of the highest to the lowest NOx production is about 1.8 (see Figure-6c). The round orifice jet appears to penetrate to the core of the mixer as shown in Figure-B3-6 in Appendix-B. The 45° slot with L/W=4 seems to be somewhat over penetrating but the L/W=8 slot appears to have optimum penetration (see Appendix-B Figure-B3-6). The difference in the local NOx production for these three configurations is clearly shown in the Appendix-D plots for configurations (22, 30 and 26). In all three configurations, majority of the NOx production occurs in the orifice wake but the round orifice shows more prominent NOx production upstream of the orifice due to the over-penetrating jets.

The histogram shapes shown in Figures-8g through 8i indicate somewhat low sensitivity of the orifice shape to the mixing non-uniformity at J=80. The round orifice shows a slight increase in NOx production over the other configurations probably due to the somewhat bi-modal histogram shape starting to be apparent in Figure-8g with a secondary peak appearing near f=0.33. Note that the histograms shown in most plots in Figure-8 show a slight increase near f=1 due to the unmixed mainstream flow usually located near the core of the mixer near x/R=0 (leading edge of the orifice). In most cases this will be present for all configurations with jets not immediately penetrating to the center core of the mixer. The NOx production reduction trends appear to agree with the improvement in the mixing at J=80. This probably is due to the general decrease in jet penetration as the slot aspect ratio is increased from 1 (round) to 8 only superseded by the fact that optimum jet penetration is being approached from the over-penetrating side. Conversely, the previous comparison at J=25, optimum jet penetration appears to be approached from the under-penetrating side, and therefore NOx production and mixing trends appear to contradict. It is therefore perceived that if a parameter, directly affecting jet penetration, is varied, then NOx production optimization could be observed only to the extent of optimizing jet penetration. Consequently deviations from this condition may produce increased NOx emission.

It is also important to note that the lowest overall NOx production configuration of the 9 cases cited in this section is the 45 degree slot L/W=8 at J=80.

Effect of J on NOx production and mixing non-uniformity

Three different orifice shapes were compared for increasing J: round orifices (configuration numbers 19, 23, and 22), 45 degree slanted slots with aspect ratio L/W=4 (configuration numbers 20, 29, and 30), and 45 degree slanted slots with aspect ratio L/W=8 (configuration numbers 24, 25, and 26). The NOx production and mixing non-uniformity results are shown in Figures-6d, 6e, and 6f, 9, and 10. In addition plots are shown in Appedices- B (Figures-B4-1 through Figure-B6-9) and Appendix-C, Apendix-D, and Appendix-E figures for the configurations listed above.

Round orifices

The effect of the increase in J on the NOx production of the round orifices indicates that over-penetration tends to increase the NOx formation by increasing the orifice wake volume as shown in Figures-6d, 9a, and 9b. In addition, increase in penetration produces an upstream recirculation near the center core of the mixer (see Figure-B4-6 in Appendix-B) and this added mixing structure produces NOx formation upstream of the orifice. It is also worthy to note that the J=80 case produces more NOx upstream of the orifice leading edge as compared to the J=52 and 25 cases as shown in Figure-9b but the cumulative production rate in the axial direction is similar for all three cases. Therefore, the NOx production upstream of the orifice appears to be an important and undesirable effect in a mixing configuration with round orifices at high J conditions.

The area weighted parameters AMIX and MMIX indicate a slight improvement in the mixing at the J=25 as compared to J=52 and 80. The best mixing configuration is the lowest NOx producer in this case (Round hole conf # 19 at J=25). In addition, this configuration appears to be the best overall for all configurations modeled at J=25. As J is increased, the volume integral results shown in Figures-10a through 10c indicate a more definite bimodal histogram shape with a secondary peak above $f_{equil.}$. This may indicate a cause for higher NOx production with increasing J.

45° Slots, with aspect ratio L/W=4

The effect of the increase in J on the NOx production of the 45° slots with aspect ratio L/W=4 is shown in Figures-6e, 9c, 9d, and 10d through 10f. The results indicate that the NOx production with this slanted slot decreases with increasing J from 25 to 80 probably mostly due to the optimization of the jet penetration as approached from the under-penetrating side. The results for conf # 20, 29 and 30 in Appendix-D show that for the lowest J condition, significant NOx was produced near the center of the mixer making it an undesirable configuration. The planar mixing non-uniformity deviations (AMIX and MMIX) indicate deteriorating mixing performance at x/R=1 with increasing J from 25 to 80 which generally opposes the NOx production trends. This is shown in Figure-B5-8 in Appendix-B where the hot mainstream flow tends to be stratified near the outer wall region of the mixer. This phenomena was discussed previously by Oechsle, Mongia, and Holdeman (1993). The volume histogram results in Figures-10d through 10f, show similar trends to the planar deviations and these results also disagree with the NOx production results. The best mixing configuration (45 degree slot, L/W=4 at J=25) appears to be the highest NOx producer. Similarly, the worst mixing configuration (45 degree slot, L/W=4 at J=80) produces the lowest NOx producer.

45° Slots, with aspect ratio L/W=8

The effect of the increase of J on the NOx production of the 45° slots with aspect ratio L/W=8 is shown in Figures-6f, 9e, 9f, and 10g through 10i. The results are not surprising since this configuration approaches optimal jet penetration from the under-penetrating side with the increase in J from 25 to 80. Minimum NOx production is obtained with the highest J condition and highest NOx production obtained at J=25. The figures for configurations 24, 25, and 26 in Appendix-D show the effect of under-penetration on NOx formation near the center of the mixer for both configuration # 24 and 25 (L/W=8 slot, J=25 and 52 respectively). As J is subse-

quently increased to J=80, the jet penetration sufficiently prevents any NOx production in the center core of the mixer.

The planar deviations (AMIX and MMIX) indicate small changes in mixing non-uniformity for increasing J probably due to the weak effect of jet penetration with changes in J for this particular orifice shape as shown in Table-3. Note that the histogram shapes in Figures-10g through 10i show that the peak of the histogram approaches f_{eq} with increase in J and this generally describes a better mixer however, the relative differences between these histograms appears to be small which is reflected in Figure-6f. The area weighted mixing non-uniformity results at x/R=1 also show little change with J and this can also be visually shown in the normalized equivalence ratio plots in (Figure-B6-8 in Appendix-B). It is therefore evident from these results that flow similarities at x/R=1 do not indicate flow similarities throughout the entire mixing section x/R=0 to x/R=1, especially since NOx production is a localized phenomena and therefore dependent on the local parameters such as f/a ratio, residence time, and temperature. It is therefore believed that the overall mixing non-uniformity parameter such as the volume integral concept would tend to correlate the mixing and NOx results for a specific orifice configuration. Note that in spite of this, the volume histogram appears to predict somewhat different trends as compared to the NOx production for most of the orifice configurations described above. One reason for this discrepancy may be that the volume integral does not weigh the histogram distribution with respect to the velocity of the gas. This term is the next logical step in the correlation between the mixing non-uniformity and NOx production since the residence time of a specific gas in a specific volume parcel greatly dictates the amount of NOx that will be produced in that partial volume.

Effect of slot slant angle on NOx production and mixing non-uniformity

In this section, the parametric study was performed by varying the slot slant angle from 0° (in line with the flow) to 90° (transverse direction) for the aspect ratio L/W=4 slot only. The results are presented for constant J conditions. The cases compared are: at J=25, configuration numbers are 34, 27, and 20 at slant angles 0, 22.5, and 45 degrees respectively; at J=52, configuration numbers are 21, 28, 29, and 31 at slant angles of 0, 22.5, 45, and 67.5 degrees; and at J=80, configuration numbers are 32, 35, 30, 33, and 36 for slant angles of 0, 22.5, 45, 67.5, and 90 degrees. Note that some of the slant angles have been omitted from the study such as the transverse slots at J=25 and 52 since they cannot fit without interfering with the adjacent orifices. The results are shown in Figures-6g through 6i, Figure-11 and 12. Additional plots are shown in Appendix-B Figures-B7-1 through B9-9, and in Appenix-C, Appendix-D, and Appendix-E for the configurations with the same numbers as the ones listed immediately above.

J=25

At the lowest J condition (J=25), the change in NOx production for slant angles (varying from 0 to 45°) are shown in Figures-6g, 11a, 11b, and 12a through 12c. It is apparent that slot slant angle at low J has a visible effect on NOx production at x/R=1 with a 45% change in NOx production from the best to worst. In addition, the jet penetration also changes significantly in these three cases (see Figure-B7-6 in Appendix-B and Table-3). The NOx production flow structure shown in the plots in Appendix-C indicate that even though jet penetration varies significantly for varying slant angle, most of the NOx production occurs in either the orifice wake and/or the center core of the mixer. The 45 degree slot appears to produce slightly higher

NOx due to the large wake produced by the orifice (see Appendix-D plots for conf # 20). The aligned slot appears to produce a smaller wake due to its low blockage value of 0.25 and also due to a large T.E. x/R value of 0.79 (see Table-2). The orifice actually extends almost the entire length of the mixer. Note that this is the longest slot of all the 18 configurations. Therefore, if x/R=1 is considered to be the end of the mixer, the orifice wake will start producing NOx beyond the mixer length (and therefore not included in this analysis). Therefore, slot orientation is beneficial to NOx production in the mixing section if the NOx production in the orifice wake is considered to be substantial as it is shown in the results in Appendix-C and D.

The area and mass flow weighted statistical results at x/R=1 appear to contradict the NOx predictions and better mixing is shown with the 45 degree slot as compared to the aligned slot (Figure-6g). The volume integral histogram results however indicate significant differences in the histogram shapes as shown in Figures 12a through 12c. As the slot slant angle ranges from 0 to 22.5 degrees, a significant amount of flow is grouped near f=0 (Figures-12a, 12b). As the slant angle increases to 45 degrees, the histogram shape changes and grouping near the f_{eq} seems to be more prominent thereby indicating it to be a better mixing configuration as compared to the previous two. It is again apparent that the mixing non-uniformity results do not correlate with NOx production and the best mixing configuration is the highest NOx production case (45 degree slot, L/W=4).

J=52

The results for the comparison at J=52 are shown in Figures-6h, 11c, 11d, and 12d through 12g. At J=52, the NOx production appears to change significantly with slant angle and the lowest NOx producer was obtained with the largest slant angle slot (67.5°) slant angle slot as seen in Figure-6h. Conversely, the highest NOx (only 25% above the lowest NOx producer) was obtained with the 0° slant (in-line slot). Note that the NOx production appears to be directly proportional to the increase in slant angle, which itself is inversely proportional to the jet penetration. The cumulative NOx production up to x/R=1 is affected by the upstream recirculation created by over penetrating jets (see Figure-11d) and this phenomena has been described previously in this report. The mixture of gases which recirculate upstream (see the aligned slot Configuration # 21 in Appendix-C) of the orifice tend to produce NOx which would not be produced in a more optimum jet penetration case as shown for the 67.5 degree slanted slot results (configuration # 31) in Appendix-C. However, the amount of NOx produced upstream of the orifice (upstream of x/R=0) is generally low compared to that produced in the mixing section itself between x/R=0 to 1 (see Figure-11c), moreover the highest NOx production usually occurred near the exit of the mixer and in the orifice wake at x/R=1. Perhaps the size (volume) of the jet wake is a possible key parameter to correlate mixing with the NOx production and results from this correlation are shown later in this report. Both jet penetration and orifice blockage affect the volume of this wake area. The determination of the wake volume is however not simple since it also depends on the axial location where the re-attachment of the flow to the outer wall is present downstream of the orifice which is also dependent on the jet penetration depth, orifice blockage, and orifice contour shape.

The area and mass flow weighted mixing non-uniformity results shown in Figure-6h indicate that slot slant angle variation from 0 to 45 degrees does not appear to significantly affect the mixing performance. The volume integral results also show this trend (see Figures-12d, 12e,

and 12f. There however seems to be a noticeable improvement in the mixing when the slant angle is increased from 45 to 67.5 degrees. All statistical parameters indicate the same trend. Apparently, the blockage value and jet penetration are optimal such that only a small amount of the mainstream flow is entrained in the wake area behind the orifice. Perhaps the combination of the jet penetration and blockage forms the right size and shape wake region to optimize mixing as shown in Figure-B8-8 in Appendix-B, and in the configuration # 31 results in Appendix-C and D. In likely manner, the histogram shape for the 67.5 degree slanted slot also looks significantly different from the 0, 22.5, and 45 degree slot configurations (see Figure-12d through 12g). In this comparison, the best mixing configuration is the lowest NOx producer.

J=80

The results for the comparison at J=80 are shown in Figures-6i, 11e, 11f, and 12h through 12l. the NOx production changes significantly with slant angle and the best performance was obtained with the 67.5° slant angle slot at x/R=1 as seen in Figures-6i. It is also important to note that the 67.5° slot produced the lowest NOx compared to all the 18 configurations reported in this report and this correlates since it is one of the best mixing configurations as reported by Oechsle, Mongia, and Holdeman (1993). This trend appears to be somewhat similar to the comparison made at J=52 for varying slot slant angle. As the slot slant angle increases, mixing improves and NOx production decreases. The highest NOx production configuration at J=80 for varying slant angles is the aligned slot. The plots shown in Appendix-D for configurations 32, 35, 30, 33, and 36 indicate that NOx formation around the orifice becomes more prominent for the low slant angle high jet penetration configurations. As the slant angle increases, the NOx production becomes localized only in the region behind the orifice. The NOx production for the transverse slot shows a slight NOx increase as compared to the 67.5 degree slot since it shows a more dominant wake NOx production (see Appendix-D plot for conf # 36). It is therefore believed that optimum jet penetration is obtained with the 67.5 degree slanted slot and decreasing or increasing this slant angle deviates from this optimum setting thereby increasing the NOx emission (see Figure-6i).

All the mixing non-uniformity results generally agree with each other in selecting the best mixing configuration which is the transverse slot configuration # 36. This configuration also is the best overall mixing configuration of all 18 compared in this report. It is also worthy to note that the histogram shape of conf # 36 shown in figure-12l is approaching to what is considered to be a good mixing configuration with a single peak located at f_{eq}. The trends of both the mixing results and NOx results do not appear to correlate in this comparison. Worst mixing was obtained with the 45 degree slot at J=80. Therefore it is apparent from this comparison as well as the previous ones described above that NOx production does not correlate with the statistical parameters used to describe the mixing criteria and this may also signify that mixing non-uniformity may not be a good correlating parameter for NOx production. The results of the: NOx and mixing criteria correlations are described in the next section.

Configuration optimization at different J conditions

The best and worst NOx production cases as a function of J are shown in Figures-13, and 14. All configurations at a particular J condition are compared, noting that both MR and DR are constant in the comparison. It is also worth considering that the 18 configurations analyzed herein, in many cases, do not display the particularly optimum condition for best mixing (best jet

penetration) and NOx production for a particular J. The plots shown in these two figures are the same type as described for the Appendix-D plots (duplicates for these are also found in Appendix-D). It is apparent in Figures-13 and 14 that the bulk of the NOx production is formed in the wake of the orifice and this is clearly shown in Figure-14 (throughout the domain of the mixer ($0 \leq x/R \leq 1$). The correlation between the localized NOx production and position in the mixer from ($0 \leq x/R \leq 1$) is shown in Figure-15. In this figure, the localized NOx production for all configurations are displayed together. Figure-15a indicates that the NOx production increases with distance from the orifice leading edge, Figure-15b indicates that it is also more concentrated towards the outer wall of the mixer, and finally, Figure-15c indicates that NOx production is concentrated in the middle of the sector in the circumferential direction behind the orifice. These results appear to be similar for all the 18 configurations analyzed in this report.

Repeating the results summarized above and shown in Figures 13a and 14a, the round hole appeared to be lowest NOx production configuration at the lowest J condition due to its optimum penetration. Optimum penetration is calculated by Holdeman (1991) using Eq-9 where n is the optimum number of orifices and C=2.5. Based on Eq-9. Also the optimum number of holes is 9 which is similar to the 8 round hole case modeled in conf # 19.

$$n = \frac{\pi \sqrt{2J}}{C} \qquad (9)$$

Increasing the operating condition (J) appears to shift the optimum low NOx configuration from the round holes to the slanted slots and lowest NOx was produced with the large slant angle slots (67.5 degrees) with aspect ratio of 4 as shown in Figures 13c, 13e, 14c, and 14e. It is believed that the optimum L/W=8 slot was not within the J range analyzed in this parametric study since these exhibited the lowest jet penetration. Therefore, if RQL applications require a high mixing region pressure drop (J above 80), it is possible that the optimum low NOx configuration could be shifted to this type of orifice. This extrapolation is based on the fact that the second lowest NOx production configuration was the L/W=8 slot at 45 degree slant angle at J=80. Note that this study only investigates configurations with the same number of orifices (8) per mixer

In likely manner, configurations as shown in Figures-13b, 13d, 13f, 14b, 14d, and 14f indicate that the high NOx production was either due to shallow jet penetration (as the case for the L/W=8 slot at J=25) or jet over penetration (as the case for the aligned slots at J=52 and 80).

Correlation between NOx production and mixing results

After reviewing these results, it becomes apparent that jet wake volume is a possible correlating parameter between mixing and NOx production. For this purpose, a non-dimensional wake volume parameter was constructed using the Eq-1. This non dimensional volume approximates the volume of the wake behind the orifice up to x/R=1. Note that it is only an approximation because this parameter does not consider the jet penetration angle change as the jet flow is assimilated into the mainstream flow. Therefore its purpose is only to establish general trends between mixing flow characteristics and the cumulative NOx production rate up to x/R=1.

$$\text{Wake Vol} = \left[1 - (1 - \text{pen})^2\right] \times \text{(blockage)} \times (1 - (\text{T.E. } x/R)) \qquad (10)$$

Where,

pen = non-dimensional jet penetration (r/R) from the outer wall of the mixer (see Table-3)
blockage = orifice blockage (see Tables-1, 2, and 3)
T.E. x/R = the orifice trailing edge x/R (see Tables-1, and2)

The results showing the correlation between NOx production and the non-dimensional wake volume are shown in Figures-16a through 16c. The results shown in Figure-16a indicate that as the non-dimensional shape orientation ratio (blockage / T.E. x/R) increases, for the symmetrical orifice configurations, the NOx production decreases regardless of J. The non-dimensional orifice shape orientation ratio is the smallest for the aligned slot and the largest for the transverse slot (conf # 36). The results shown in Figure-16b indicate that as slot slant angle increases, NOx increases only for the low J condition since a somewhat under penetrated case (22.5 degree slot conf # 27) becomes even more under penetrated with the increase of slant angle to 45 degree (conf # 20). This trend however reverses for the higher J conditions which have sufficient jet momentum to allow for slot slant angle variation to a more optimized geometric configuration. All the data points plotted in Figure-16b are only for the L/W=4 slots. The results shown in Figure-16c indicate the approach towards NOx reduction optimization of each orifice configuration as J is increased. For the orifices with lower orifice shape orientation ratio such as the aligned slot, 22.5 degree slot, and round hole, the NOx production increases for increasing J, generally as a result of over penetration. However, higher orifice shape orientation ratios such as the 67.5 degree slot and transverse slot reverse the trend due to their inherent low jet penetration and approach to optimum jet penetration from the under-penetrated side in the J range from 25 through 80. The correlation results thus indicate that the non-dimensional wake volume is a possible correlating parameter linking the mixing flow structure to the NOx production; however, improvements could be made if parameters such as J, orifice shape orientation, and velocity distribution are added in order to obtain a more generalized correlating parameter.

Conclusions

1) The mixing statistical parameters in most cases do not correlate with the NOx production rates at $x/R=1$. The planar variances at $x/R=1$ lack the mixing history throughout the entire mixing region and the volume integrals require the residence time factor for completeness.

2) NOx production is shown to be highly related to the jet penetration. Over penetrating configurations show increased NOx production as so do under-penetrating cases. At low J conditions, orifices with large orientation shape ratios tend to under penetrate and show

characteristics of a non-optimal NOx reduction configuration; and subsequently higher J, tends to decrease the NOx production. Similarly, in the range of J analyzed herein, orifices with low orientation shape ratios tend to over penetrate indicating non-optimal mixer configurations; and subsequent increase J, increases the amount of NOx produced.

3) NOx production correlation with position indicated that for all the 18 configurations summarized in this report, most of he NOx produced occurs near or in the orifice wake region. After correlating the NOx production with the non-dimensional wake volume, results indicate that trends do exist but additional terms such as orifice shape ratio, velocity, and J need to be incorporated to obtain a more general relation to correlate mixing with NOx.

4) At the lowest J condition, the circular orifice indicated the lowest NOx production, and at higher J conditions, the optimization shifted towards the large slant angle slots such as the 67.5 degree slot L/W=4. High NOx production was obtained with the aligned slots due to the over-penetrating jet structure. Over penetrating jets also cause additional NOx to be produced upstream of the orifice

References

Bain, D.B., Smith, C.E., and Holdeman, J.D., "CFD Mixing Analysis of Jets Injected from Straight and Slanted Slots into Confined Crossflow in Rectangular Ducts," AIAA paper No. 92-3087 (1992). (Also NASA TM 105699).

Bain, D.B., Smith, C.E., and Holdeman, J.D., "Parametric CFD Analysis of Jet Mixing into Confined Crossflow in Rectangular Ducts," AIAA paper No. 93-2044 (1993). (Also NASA TM 106179).

Bain, D.B., Smith, C.E., and Holdeman, J.D., "CFD Assessment of Orifice Aspect Ratio and Mass Flow Ratio on Jet Mixing in Rectangular Ducts," AIAA Paper No. 94-0218 (1994). (Also NASA TM 106434).

Bruce, T.W., Mongia, H.C., and Reynolds, R.S., "Combustion design criteria validation," (1979), (USARTL-TR-78-55A, B, and C).

Doerr, Th., and Hennecke, D.K., "The Mixing Process in the Quenching Zone of the Rich-Lean-Combustion Concept," AGARD-PEP 81st Symposium of Fuels and Combustion Technology for Advanced Aircraft Engines, (1993).

Glassman, I., "Combustion," Academic Press, New York (1977)

Fletcher, R.S., and Heywood, J.B., "A Model for Nitric Oxide Emissions from Aircraft Gas Turbine Engines," AIAA Paper No. 71-123 (1971).

Hatch, M.S., Sowa, W.A., Samuelsen, G.S., and Holdeman, J.D., "Jet Mixing Into a Heated Cross Flow in a Cylindrical Duct: Influence of Geometry and Flow Variations," AIAA Paper No. 92-0773 (1992). (Also NASA TM 105390).

Hatch, M.S., Sowa, W.A., Samuelsen, G.S., " Influence of Geometry and Flow Variation on Jet Mixing and NO Formation in a Model Staged Combustor Mixer with Eight Orifices," NASA CR No. 194473 (1994). (Also NASA TM 105639).

Holdeman, J.D., "Mixing of Multiple Jets with a Confined Subsonic Crossflow," Prog. Energy Combust. Sci., (1993), Vol 19, pp 31-70. (Also see AIAA Paper No. 91-2458 (1991), and NASA TM 104412).

Howe, G.W., Li, Z., Shih, T.I.-P., and Nguyen, H.L., "Simulation of mixing in the quick quench region of a rich burn - quick quench mix - lean burn combustor," AIAA Paper No. 91-0410 (1991).

Kroll, J.T., Sowa, W.A., Samuelsen, G.S., and Holdeman, J.D., "Optimization of Circular Orifice Jets Mixing into a Heated Crossflow in a Cylindrical Duct," AIAA Paper No. 93-0249 (1993).

Launder, B.E., and Spalding, D.B., "Lectures in Mathematical Models of Turbulence," Academic Press Inc. (London) LTD., (1972).

Lefebvre, A.H., "Fuel Effects on Gas Turbine Combustion-Liner Temperature, Pattern Factor, and Pollutant Emissions," *AIAA Journal of Aircraft*, Vol21, No. 11, pp 887-98 (1984).

Liscinsky, D.S., True, B., Vranos, A., and Holdeman, J.D., "Experimental Study of Cross-Stream Mixing in a Rectangular Ducts," AIAA Paper No. 92-3090 (1992). (Also NASA TM 106194).

Liscinsky, D.S., True, B., and Holdeman, J.D., "Experimental Investigation of Crossflow Jet Mixing in a Rectangular Duct." AIAA Paper No. 93-2037 (1993). (Also NASA TM 106152).

Liscinsky, D.S., True, B., and Holdeman, J.D., "Mixing Characteristics of Directly Opposed Rows of Jets Injected Normal to a Crossflow in a Rectangular Duct," AIAA Paper No. 94-0217 (1994). (Also NASA TM 106477).

Mellor, A.M., "Gas Turbine Engine Pollution," Prog. *Energy Combustion Science,* Pergamon Press, Vol 1, pp 111-33 (1976).

Oechsle, V.L., Mongia, H.C., and Holdeman, J.D. "A Parametric Numerical Study of Mixing in a Cylindrical Duct," AIAA Paper No. 92-3088 (1992). (Also NASA TM 105695).

Oechsle, V.L., Mongia, H.C., and Holdeman, J.D. "An Analytical Study of Jet Mixing in a Cylindrical Duct," AIAA Paper No. 93-2043 (1993). (Also NASA TM 106181).

Oechsle, V.L., Mongia, H.C., and Holdeman, J.D. "Comparison of the Mixing Calculations of Reacting and Nonreacting Flows in a Cylindrical Duct," AIAA Paper No. 94-0865 (1994). (Also NASA TM 106435).

Patankar,S.V., "Numerical Heat Transfer and Fluid Flows," Hemisphere, Washington D.C. (1980).

Rizk, N.K., Mongia, H.C., "Ultra-Low NO_x Rich Lean Combustion," ASME Paper No. 90-GT-87 (1990).

Rizk, N.K., Mongia, H.C., "Low NO_x Rich-Lean Combustion Concept Application," AIAA Paper No. 91-1962 (1991).

Rizk, N.K., Mongia, H.C., "Three-Dimensional NO_x Model for Rich/Lean Combustor," AIAA Paper No. 93-0251 (1993).

Shaw, R.J., "Engine Technology Challenges for a 21st Century High Civil Speed Transport," AIAA 10th International Symposium on Air Breathing Engines (1991). (Also NASA TM 104361).

Smith, C.E., Talpallikar, M.V., and Holdeman, J.D., "A CFD Study of Jet Mixing in Reduced Flow Areas for Lower Combustion Emissions," AIAA Paper No. 91-2460 (1991). (Also NASA TM 104411).

Sowa, W.A., Kroll, J.T., Samuelsen, G.S., "Optimization of Orifice Geometry for Cross-Flow Mixing in a Cylindrical Duct," AIAA Paper No. 94-0219 (1994). (Also NASA TM 103436).

Talpallikar, M.V., Smith, C.E., Lai, M.C., and Holdeman, J.D., "CFD Analysis of Jet Mixing in Low NO_x Flametube Combustors," J. Eng. *Gas Turbine* Pwr. **114**, 416 (1992). (Also ASME Paper No. 91-GT-217; NASA TM 104466).

Vranos, A., Liscinsky, D.S., True, B., and Holdeman, J.D., "Experimental Study of Cross-Stream Mixing in a Cylindrical Duct," AIAA Paper No. 91-2459 (1991). (Also NASA TM 105180).

Westbrook, C.K., and Pitz, W.J., "A Comprehensive Chemical Kinetic Reaction Mechanism for Oxidation and Pyrolysis of Propane and Propene," *Comb. Sci. Tech.*, Vol 37, pp 117-52 (1984)

Zhu, G., and Lai, M.-C., "A parametric study of penetration and mixing of radial jets in necked-down cylindrical crossflow," AIAA Paper No. 92-3091 (1992).
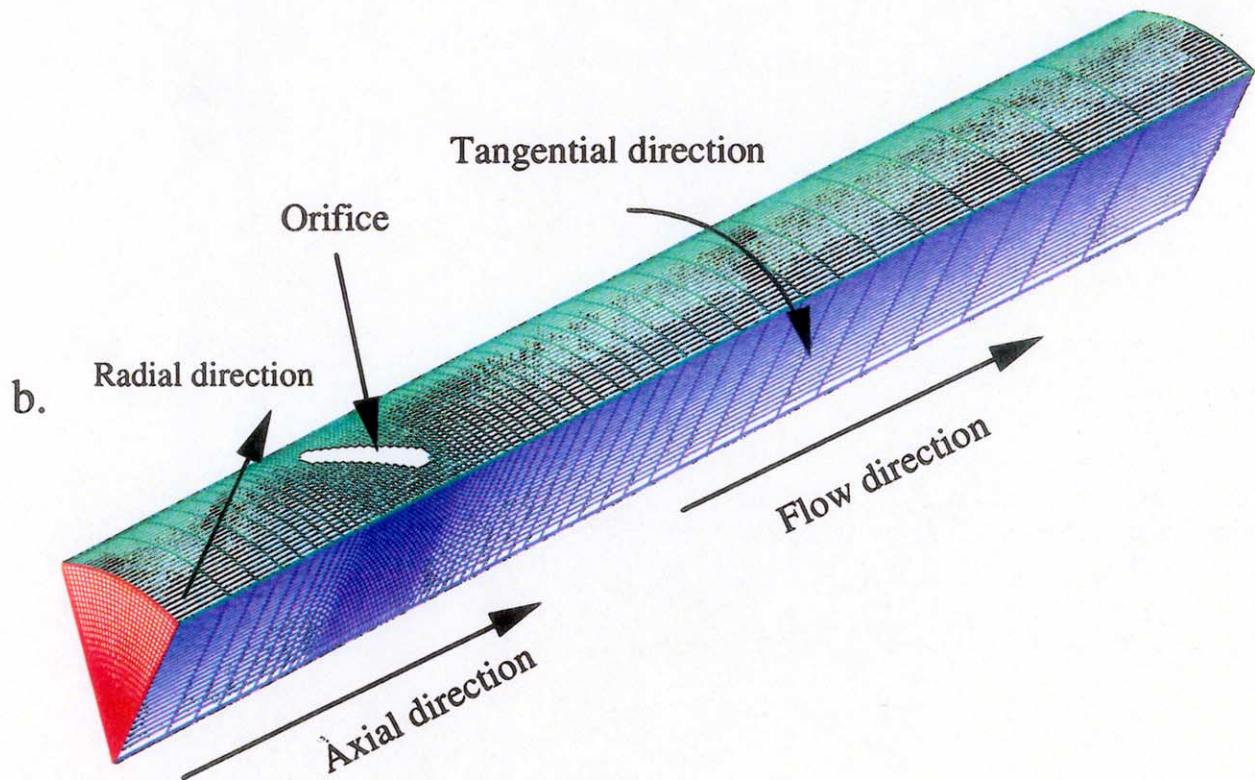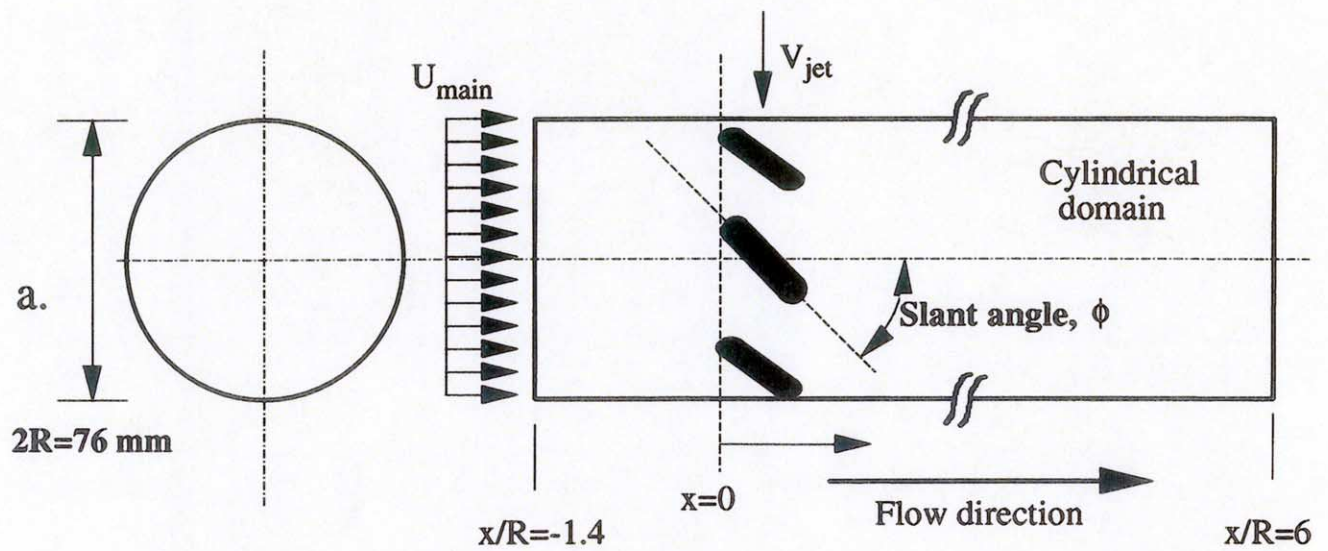
Figure-1. a) geometric configuration of the mixing section
b) computational grid
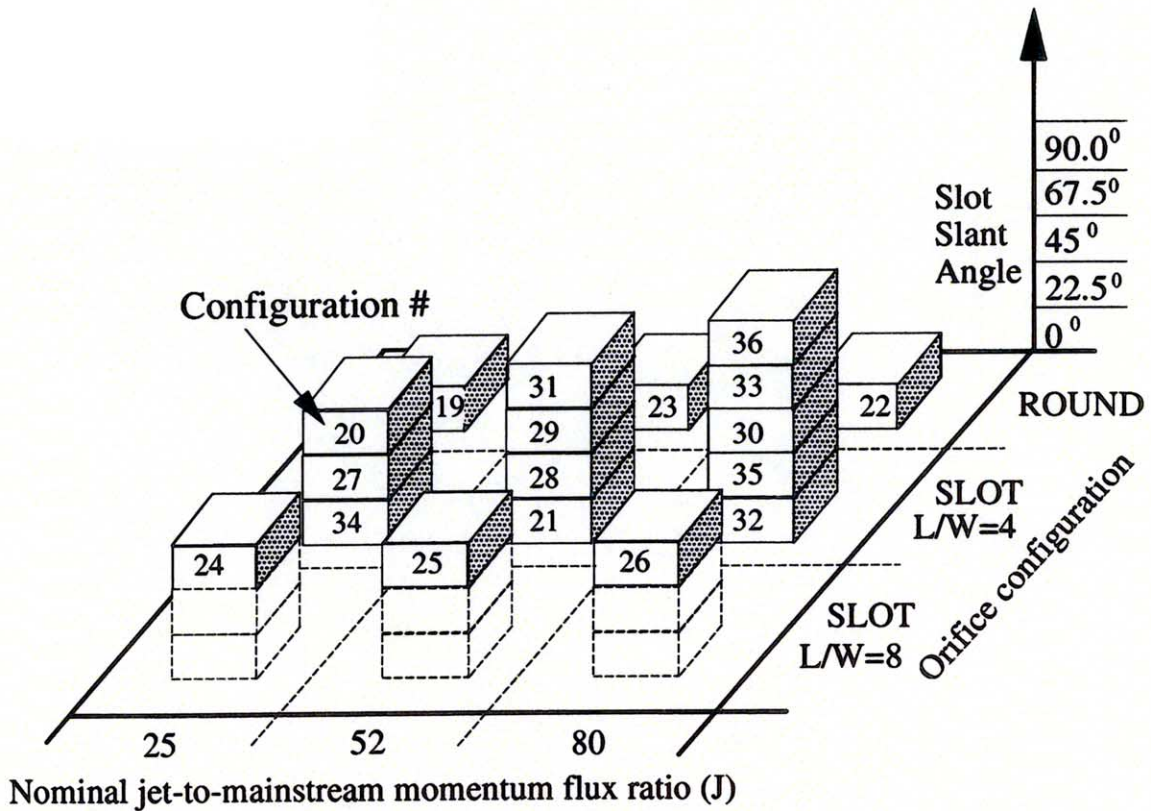
Figure-2. Matrix depiction of the analyzed configurations in a circular mixer
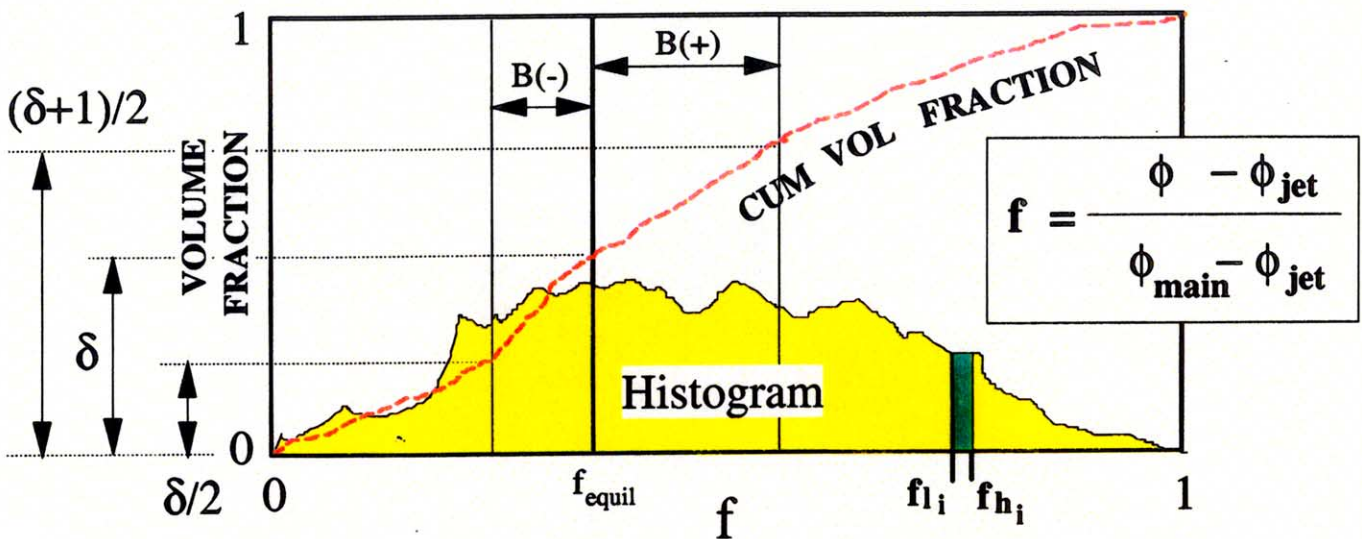
Figure-3. Description of the statistical analysis for the mixing non-uniformity evaluation
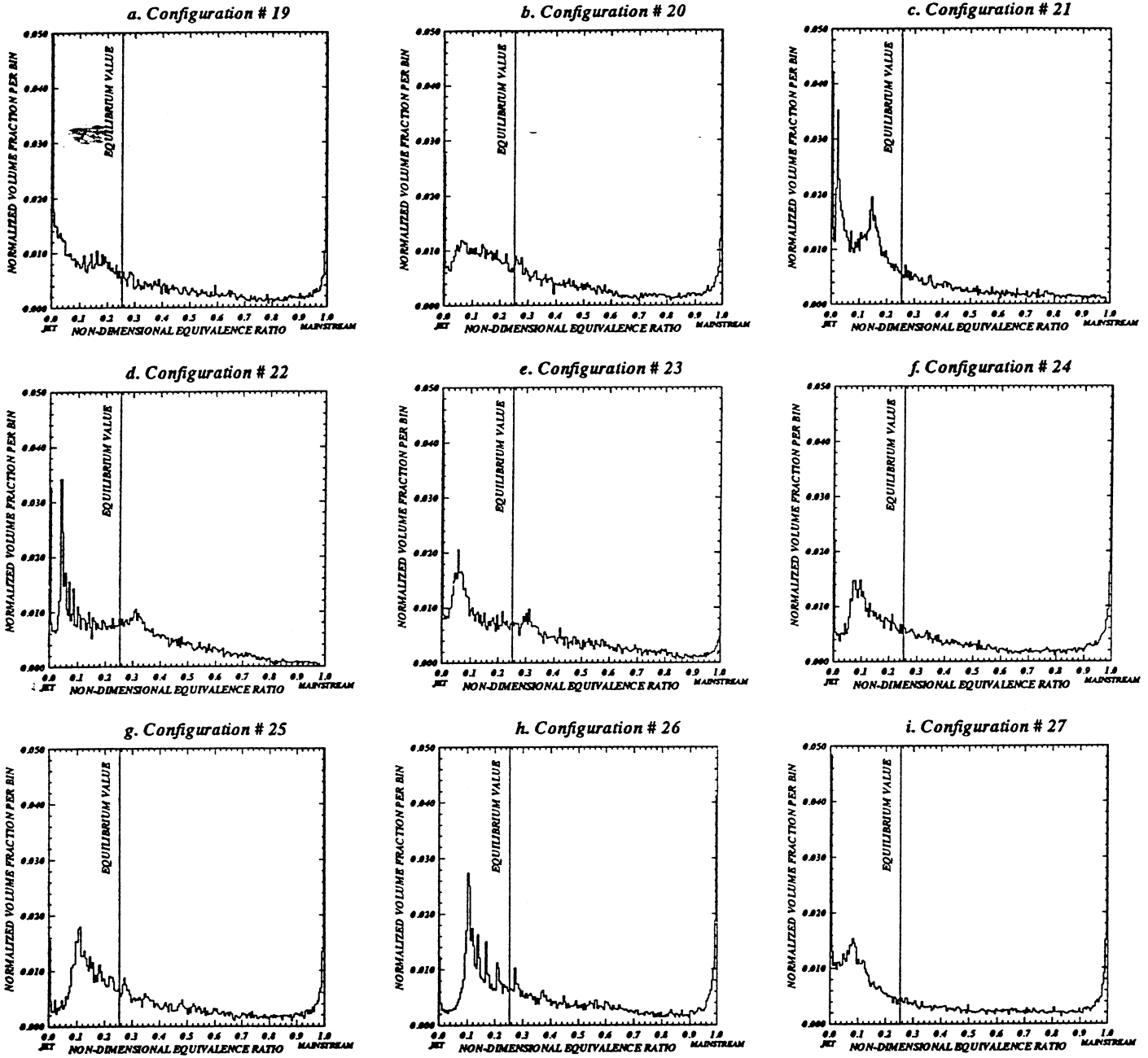
Figure-4. Volume histogram results for configurations # 19 through # 27
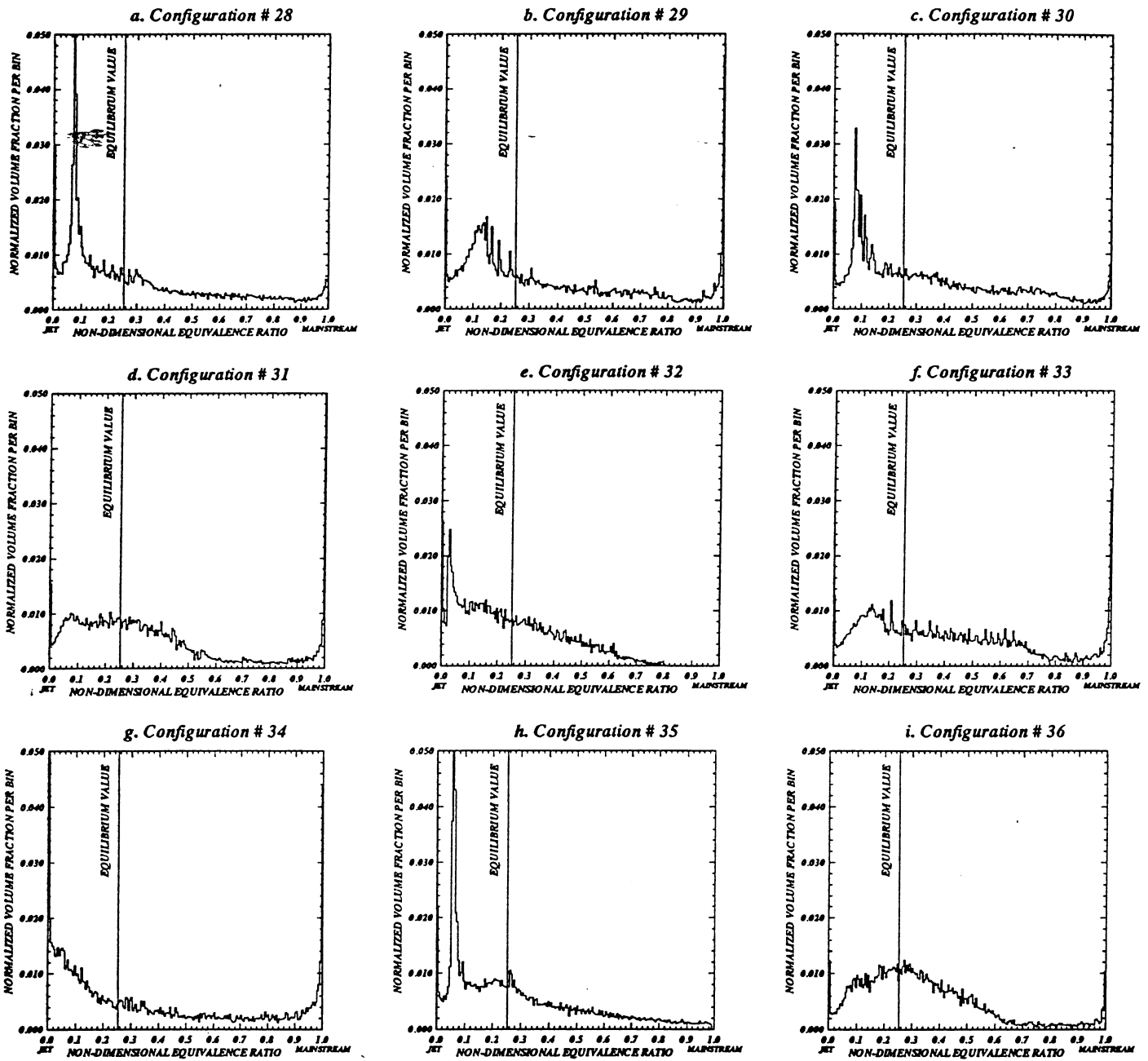
Figure-5. Volume histogram results for configurations # 28 through # 36
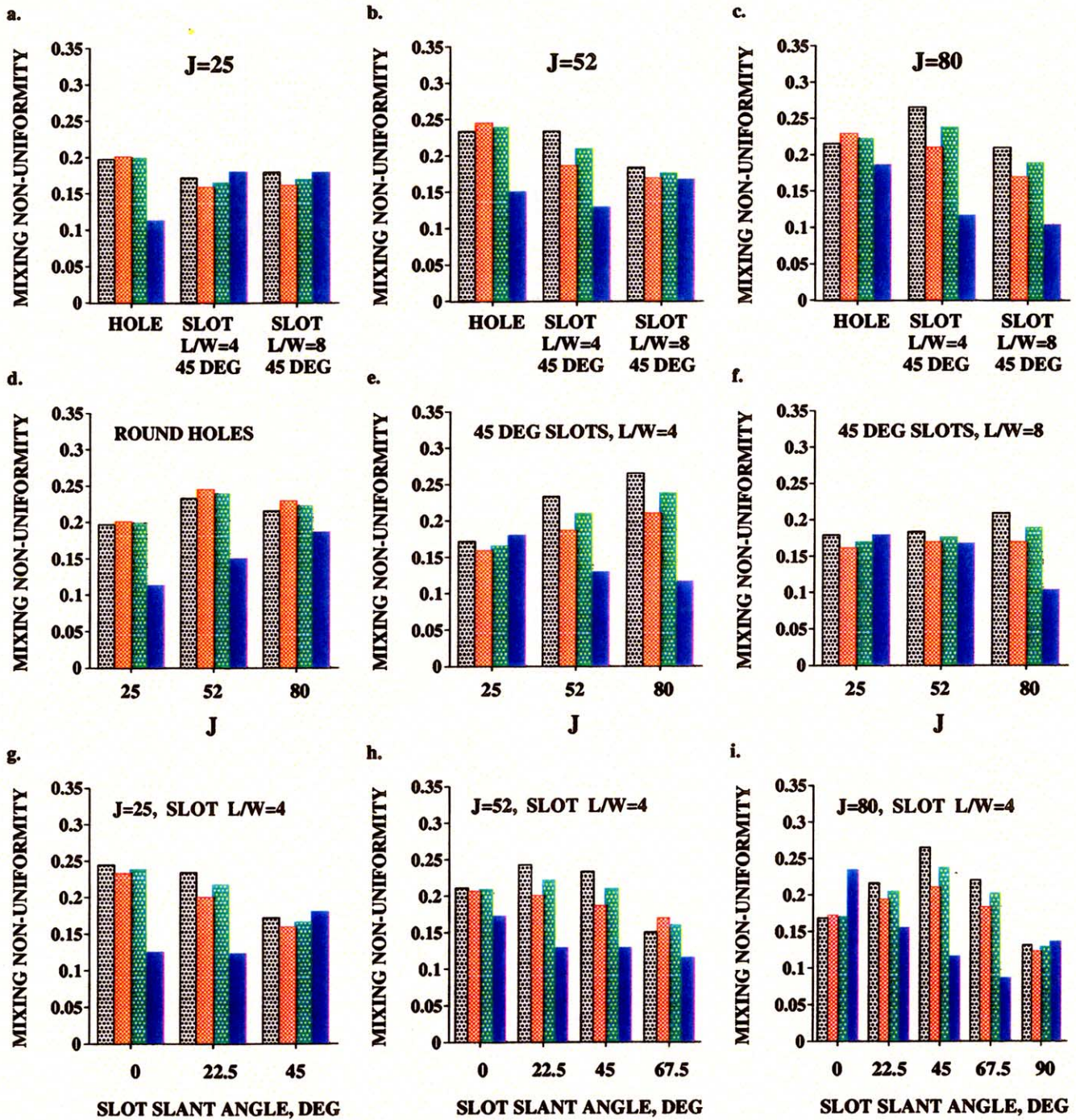
Figure-6. Mixing non-uniformity comparison with the cumulative NOx production rate up to x/R=1 for configurations # 19 through 36.
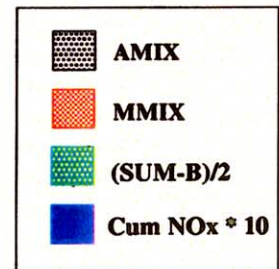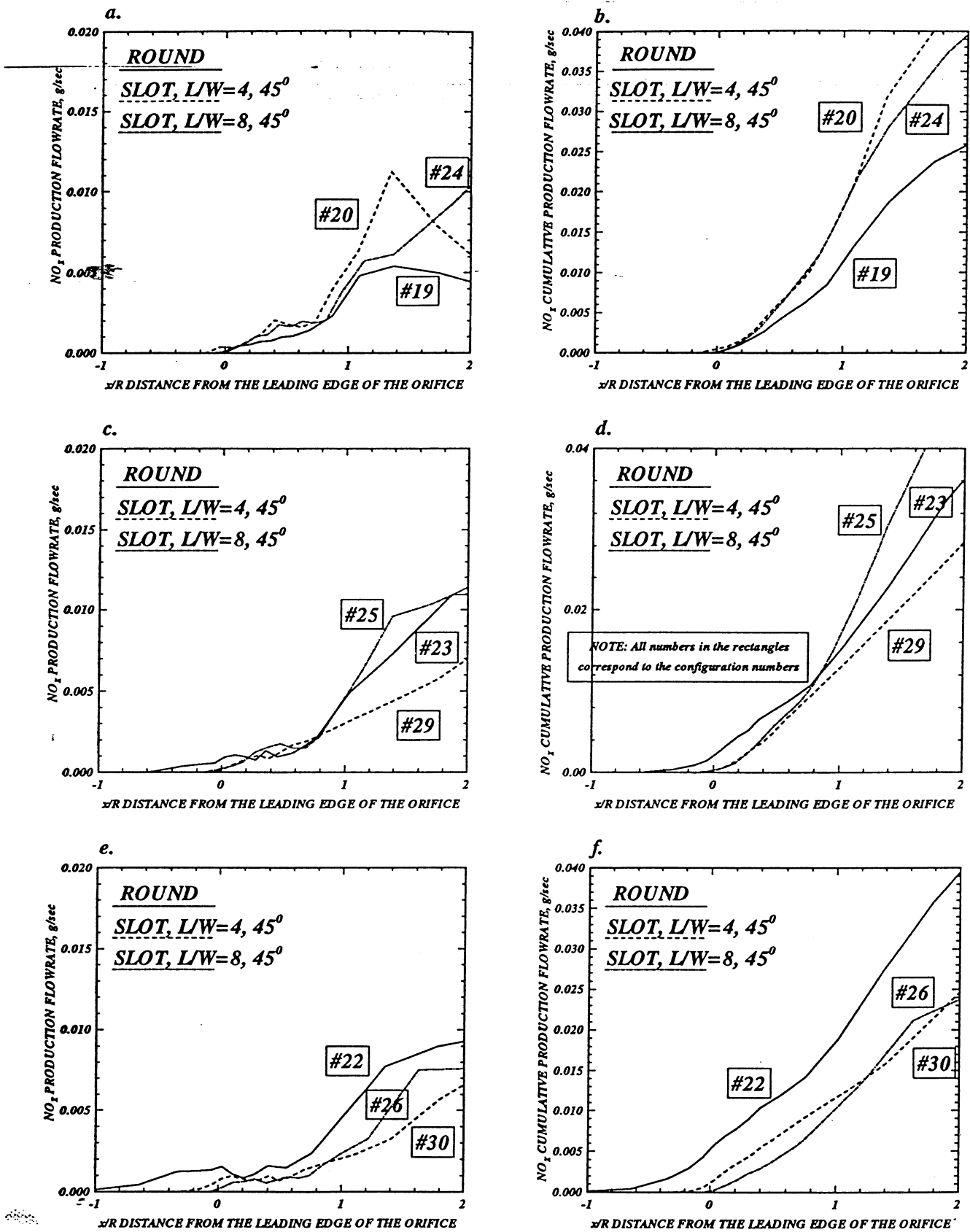
Figure-7. Effect of orifice geometry on NO$_x$ production at x/R=1
J=25 (a,b), J=52 (c,d), J=80 (e,f)
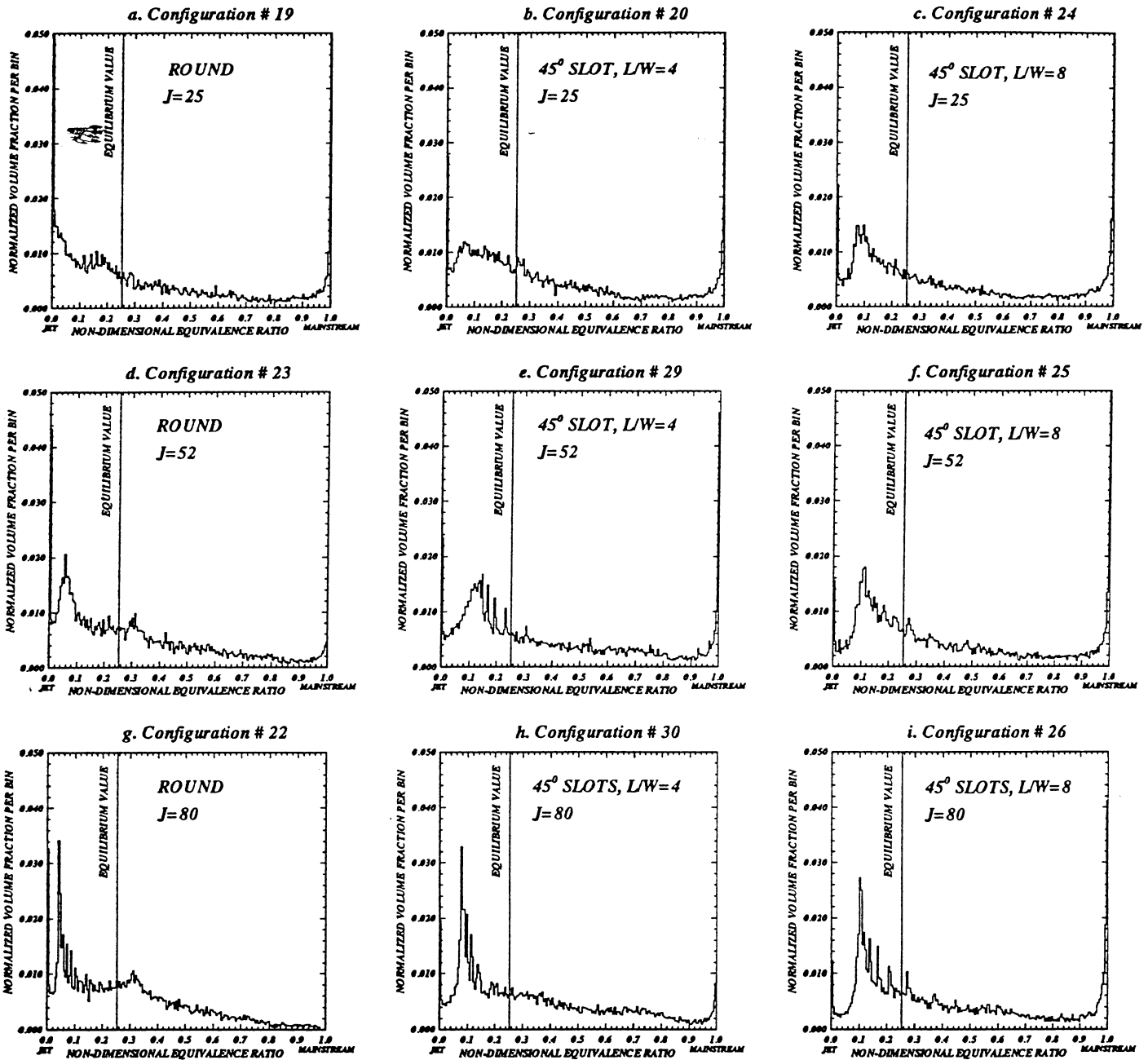
Figure-8. Efect of the change of orifice shape on the volume integral histogram for constant J: J=25 (a,b,c), J=52 (d,e,f), ans J=80 (g,h,i)
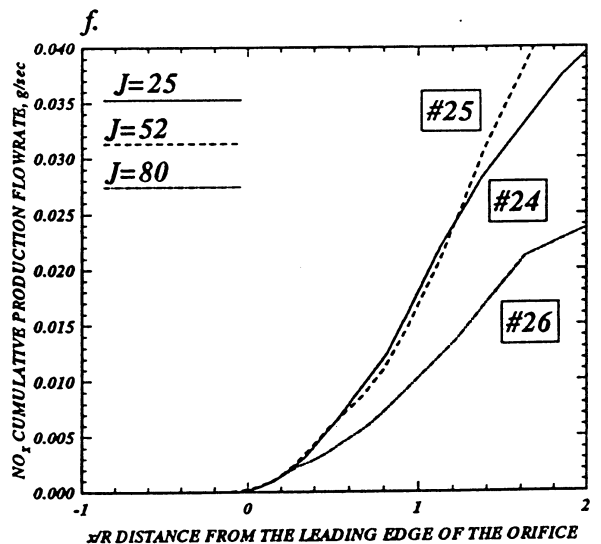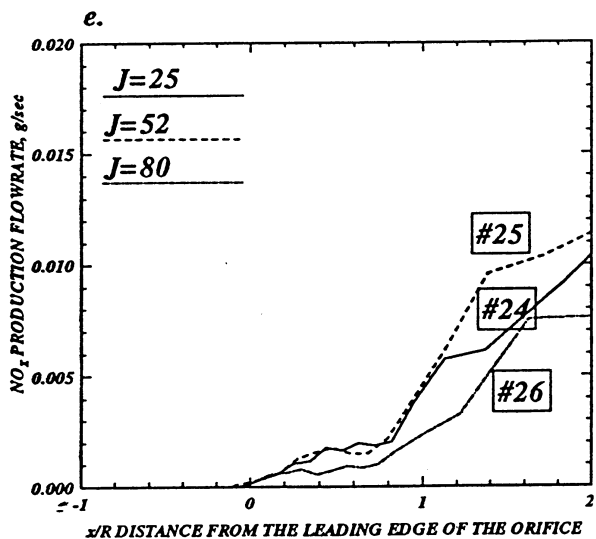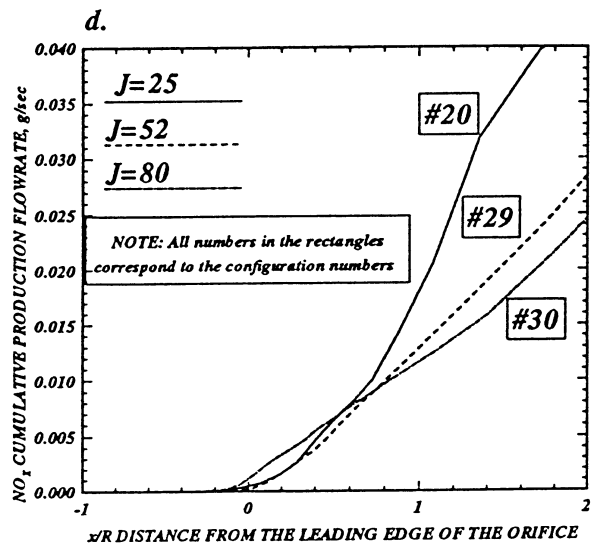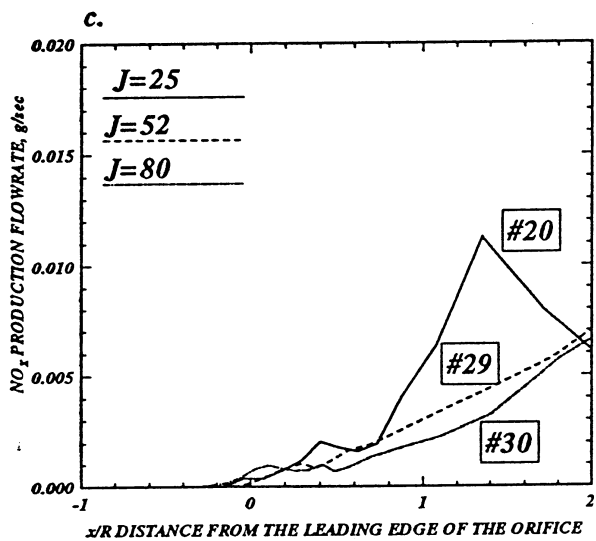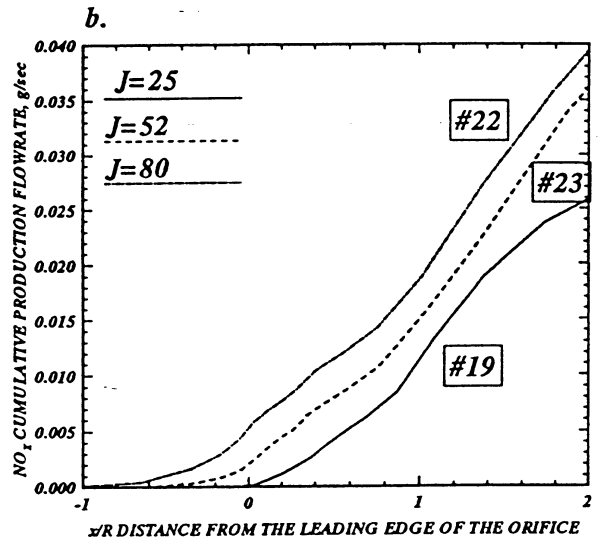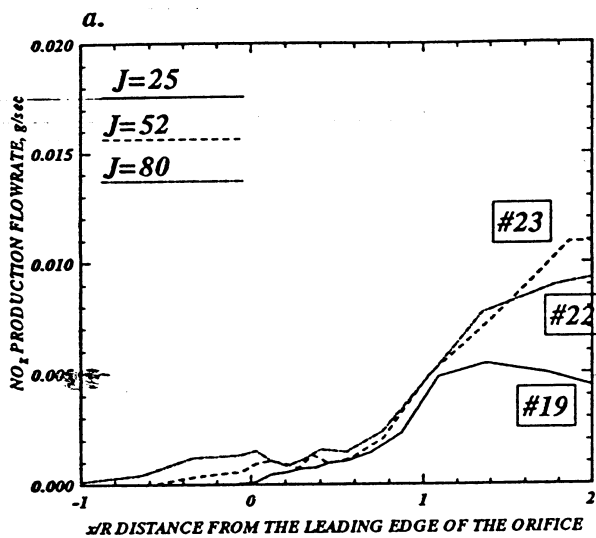
**Figure-9. Effect of the increase in J on NOₓ production at x/R=1
Round orifices (a,b), Slot L/W=4, 45⁰ (c,d), Slot L/W=8, 45⁰ (e,f)**
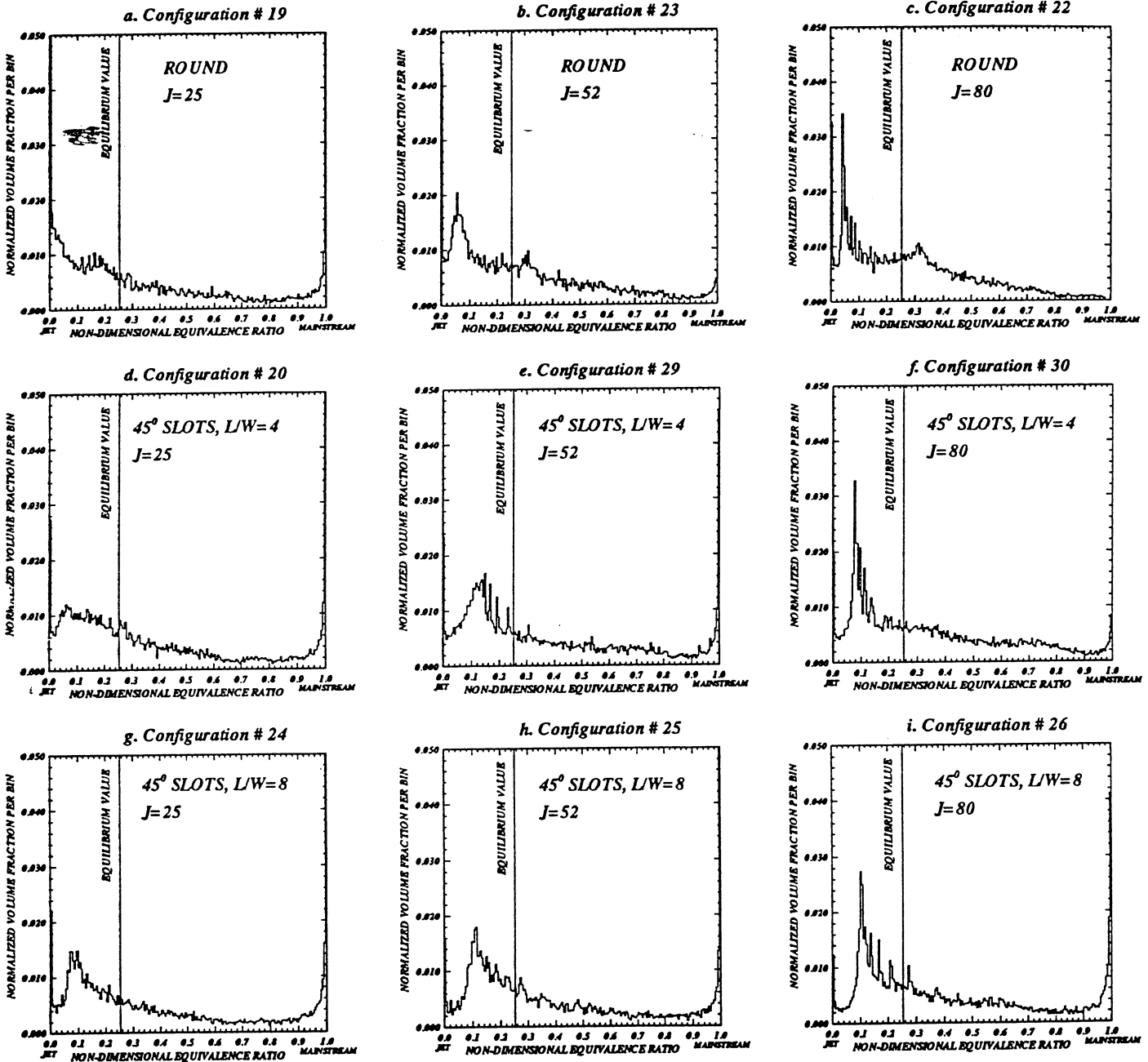
Figure-10. Effect of the change in J on the volume integral histogram
for constant orifice shape: round (a,b,c), 45⁰ slots L/W=4 (d,e,f)
and 45⁰ slots, L/W=8 (g,h,i)
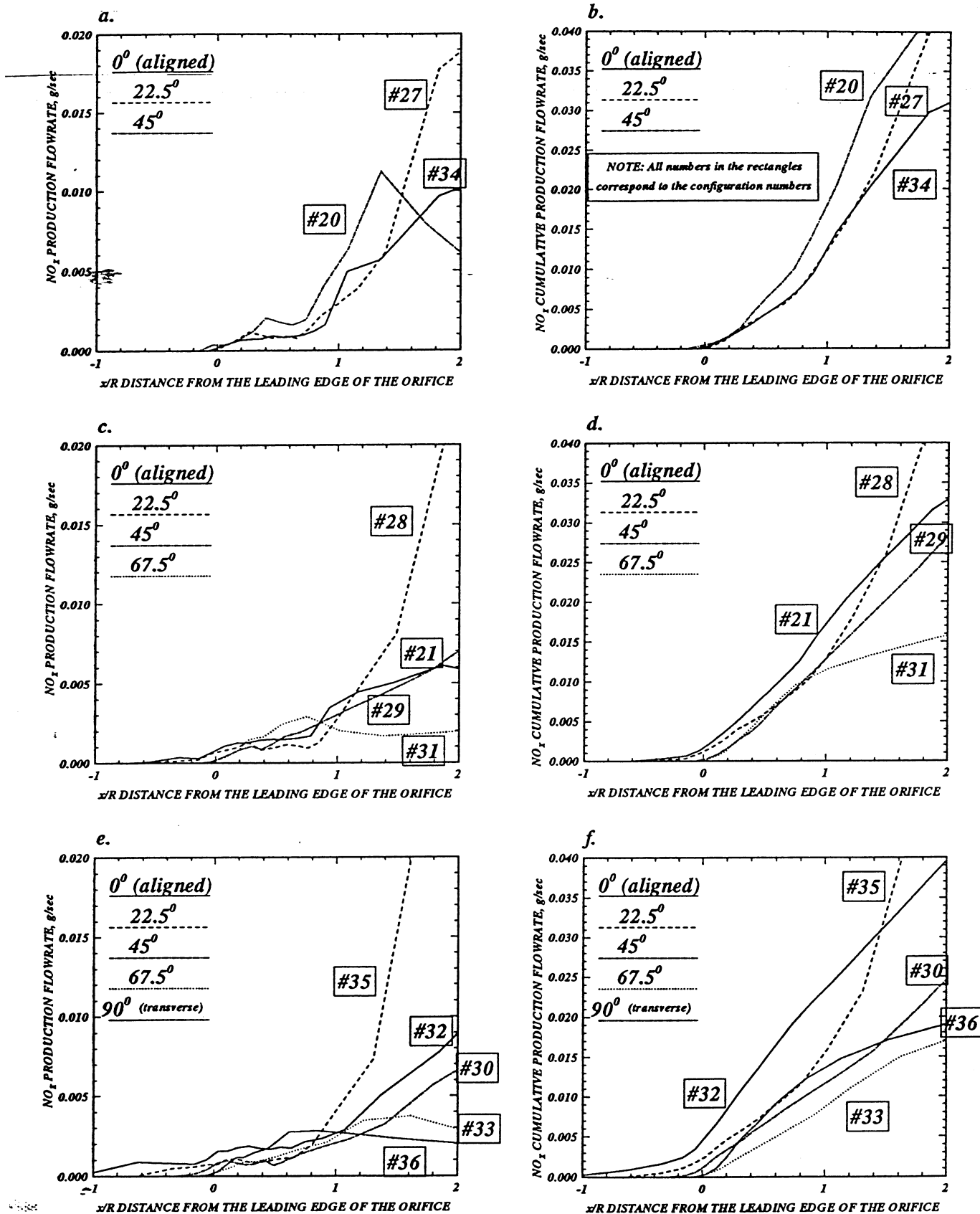
Figure-11. Effect of the increase slot slant angle on NO_x at x/R=1

$$J=25 \ (a,b), \quad J=52 \ (c,d), \quad J=80 \ (e,f)$$
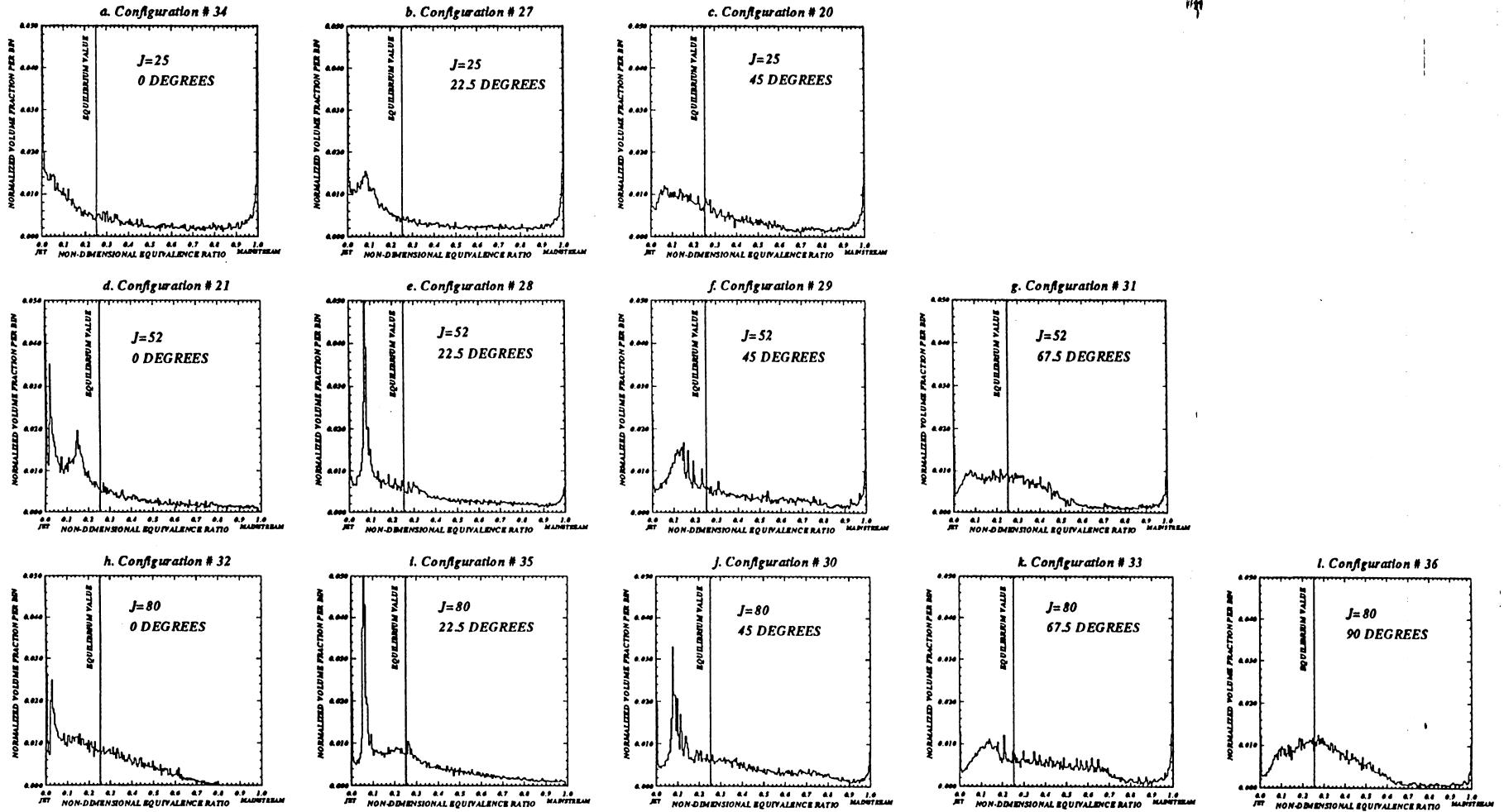
Figure-12. Effect of the change in slot slant angle on the volume integral histogram for constant slot aspect ratio L/W=4 and constant J: J=25 (a, b, c),   J=52 (d, e, f, g),   J=80 (h, i, j, k, l)
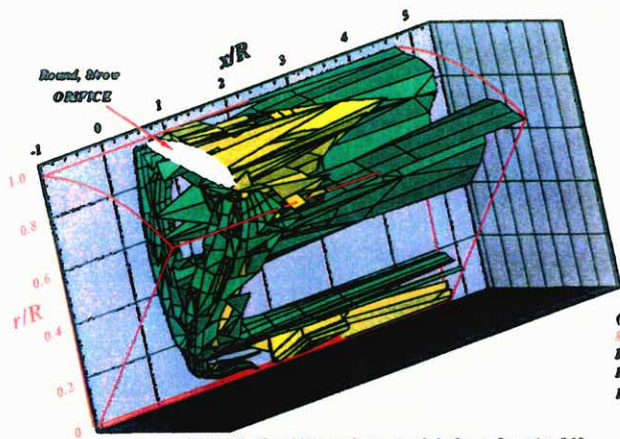
Figure-13a. Local NO$_x$ production isoplets for configuration # 19
J=26.7, MR=2.96, DR=2.28, Phi$_{EE}$ = 1.80, Phi$_{LL}$ = 0.416
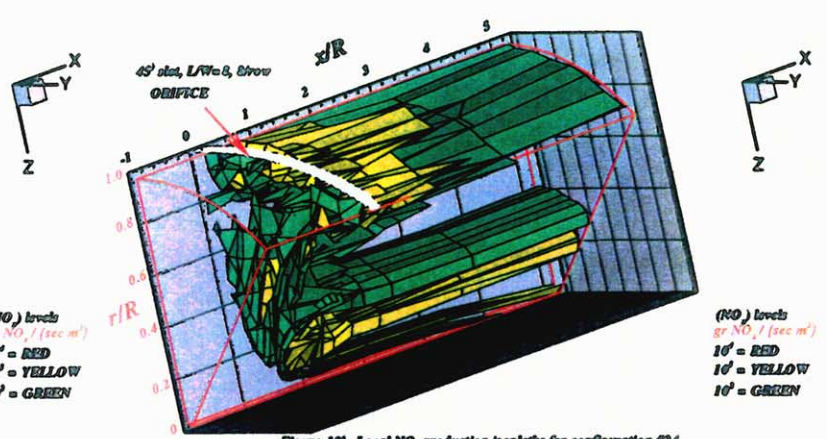
Figure-13b. Local NO$_x$ production isoplets for configuration #24
J=28.1, MR=2.96, DR=2.28, Phi$_{EE}$ = 1.80, Phi$_{LL}$ = 0.416
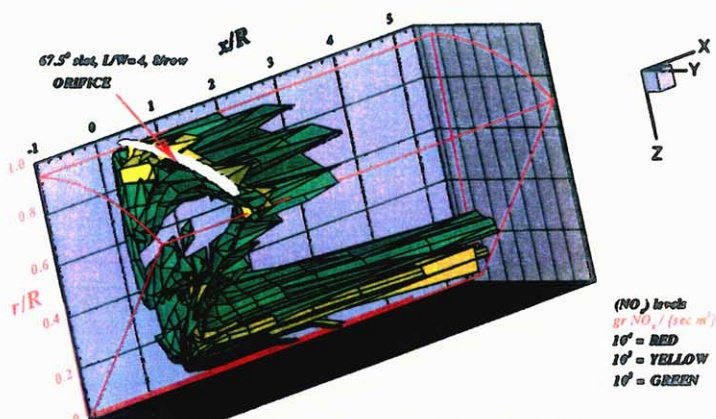
Figure-13c. Local NO$_x$ production isoplets for configuration # 31
J=59.9, MR=2.96, DR=2.28, Phi$_{EE}$ = 1.80, Phi$_{LL}$ = 0.416
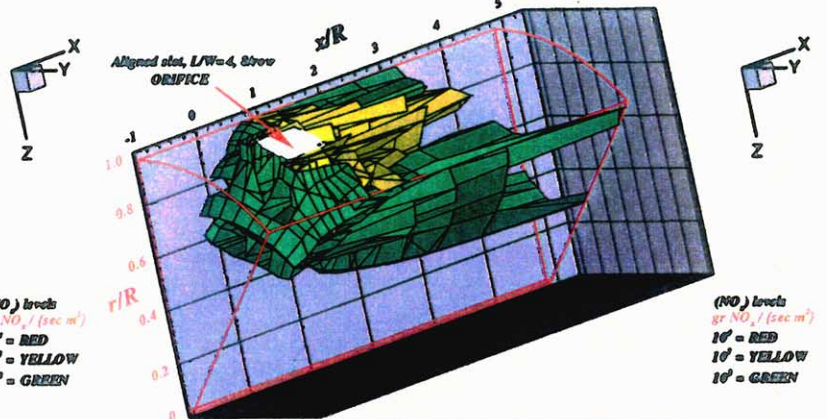
Figure-13d. Local NO$_x$ production isoplets for configuration # 21
J=51.1, MR=2.96, DR=2.28, Phi$_{EE}$ = 1.80, Phi$_{LL}$ = 0.416
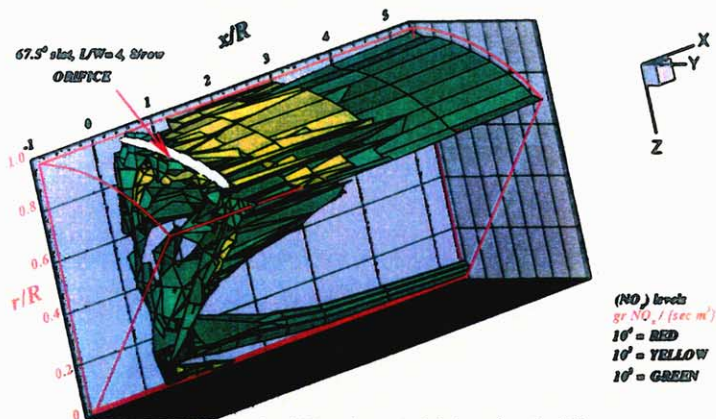
Figure-13e. Local NO$_x$ production isoplets for configuration # 33
J=99.3, MR=2.96, DR=2.28, Phi$_{EE}$ = 1.80, Phi$_{LL}$ = 0.416
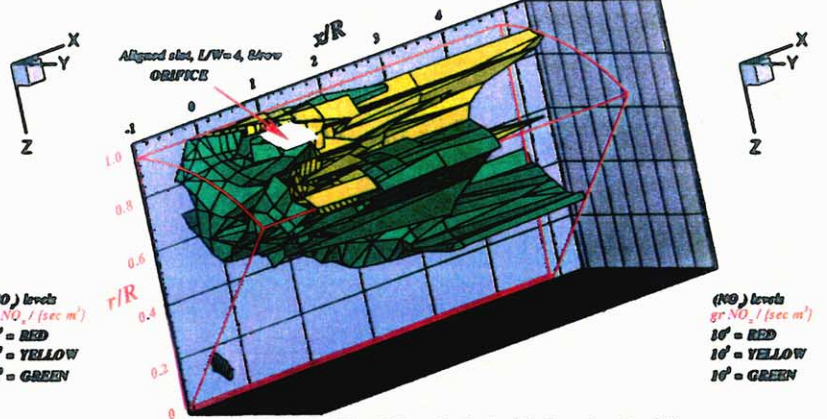
Figure-13f. Local NO$_x$ production isoplets for configuration # 32
J=93.0, MR=2.96, DR=2.28, Phi$_{EE}$ = 1.80, Phi$_{LL}$ = 0.416

Figure-13. Comparison of the best (left column) and worst (right) local NO$_x$ production configurations for nominal J=25 (a, b), 52 (c, d), and 80 (e, f). The interpolated surfaces correspond to NO$_x$ local production of 10^2 to 10^4 (g NO$_x$ /{sec m^3}). The view of the mixer is from 0 < x/R < 5.
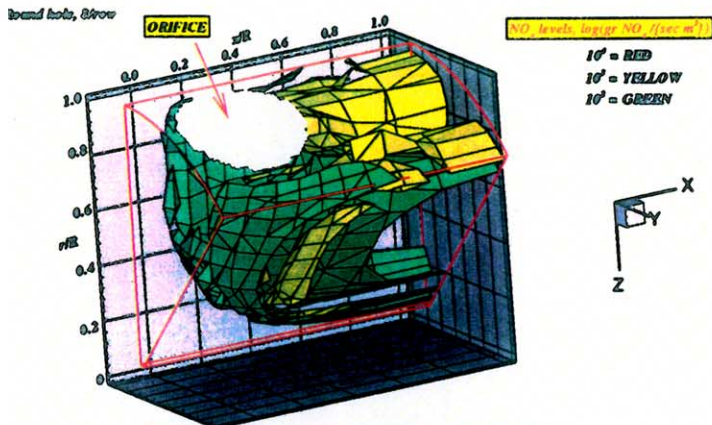
Figure-14a. Local NO$_x$ production isopleths for configuration #19
J=26.7, MR=2.96, DR=2.28, phi rz=1.80, phi lz=0.416
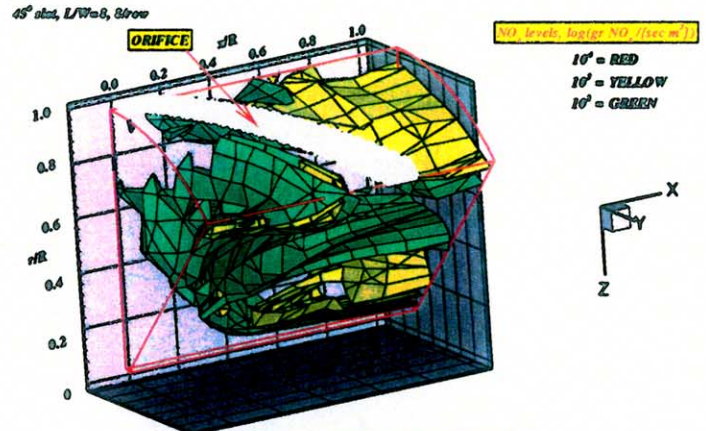
Figure-14b. Local NO$_x$ production isopleths for configuration #24
J=28.1, MR=2.96, DR=2.28, phi rz=1.80, phi lz=0.416
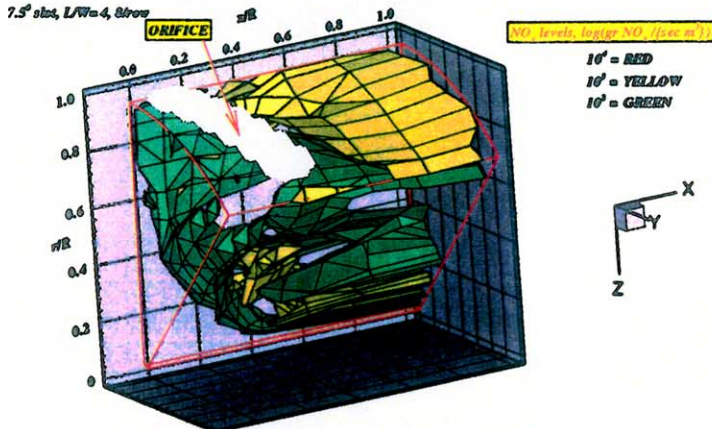
Figure-14c. Local NO$_x$ production isopleths for configuration #31
J=59.9, MR=2.96, DR=2.28, phi rz=1.80, phi lz=0.416
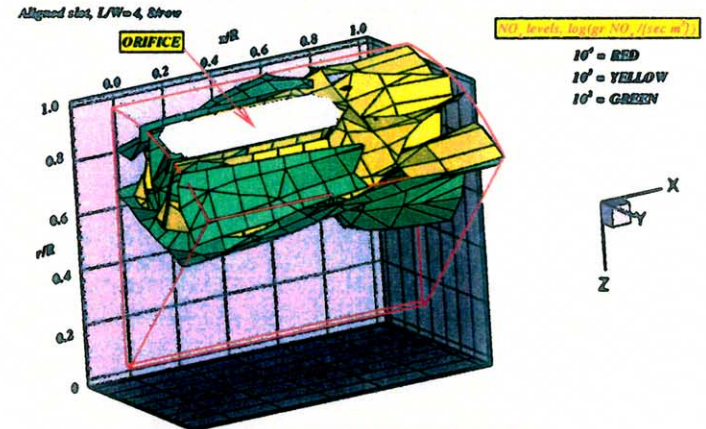
Figure-14d. Local NO$_x$ production isopleths for configuration #21
J=51.1, MR=2.96, DR=2.28, phi rz=1.80, phi lz=0.416
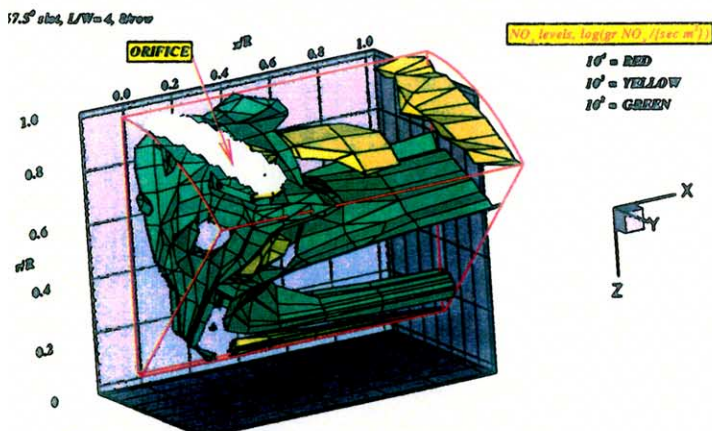
Figure-14e. Local NO$_x$ production isopleths for configuration # 33
J=99.3, MR=2.96, DR=2.28, phi rz=1.80, phi lz=0.416
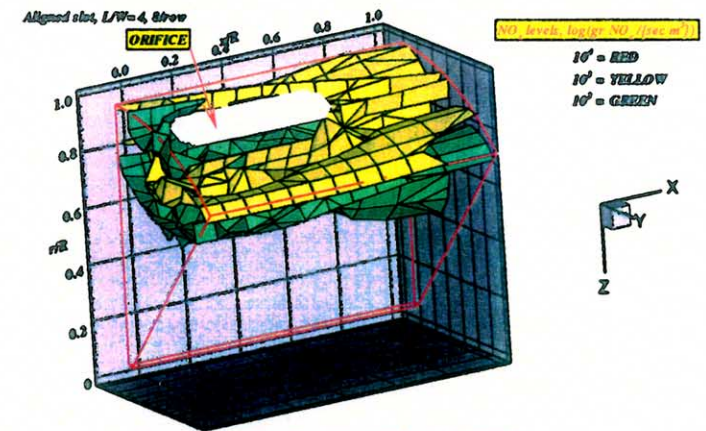
Figure-14f. Local NO$_x$ production isopleths for configuration #32
J=93.0, MR=2.96, DR=2.28, phi rz=1.80, phi lz=0.416

Figure-14. Comparison of the best (left column) and worst (right) local NO$_x$ production configurations for nominal J= 25 (a, b), 52 (c, d), and 80 (e, f). The interpolated surfaces shown correspond to NO$_x$ local production of 10^2 to 10^4 (g NO$_x$ /{sec m^3}). The view of the mixer is from 0 < x/R < 1.
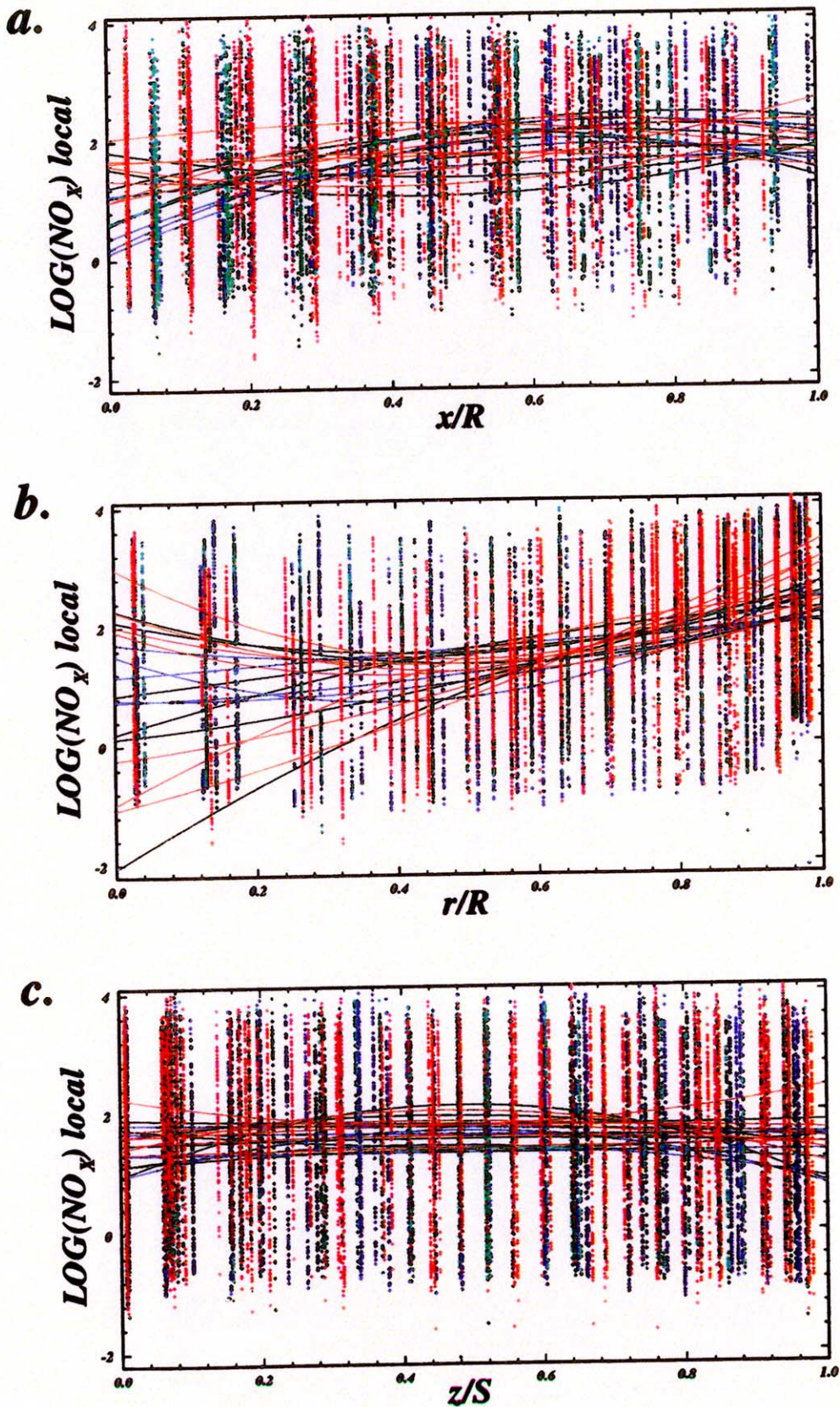
Figure-15. Correlation of localized NO_x production with position for all configurations # 19 through 36. Mixer domain is 0 < x/R < 1. blue is for J=25, green is for J=52, and red is for J=80

APPENDIX-A

Grid configuration for configuration number 19 through 36. Each plot contains three views:

a) Radial-tangential plane (view from upstream looking downstream)

b) axial-tangential plane (view from the outside of the mixer looking towards the centerline)

c) axial radial plane (mixer inlet is towards the left side)

CONF #	FIG #
19	A1
20	A2
21	A3
22	A4
23	A5
24	A6
25	A7
26	A8
27	A9
28	A10
29	A11
30	A12
31	A13
32	A14
33	A15
34	A16
35	A17
36	A18

RADIAL-TANGENTIAL PLANE

OUTER WALL
AXIAL-TANGENTIAL PLANE

AXIAL-RADIAL PLANE
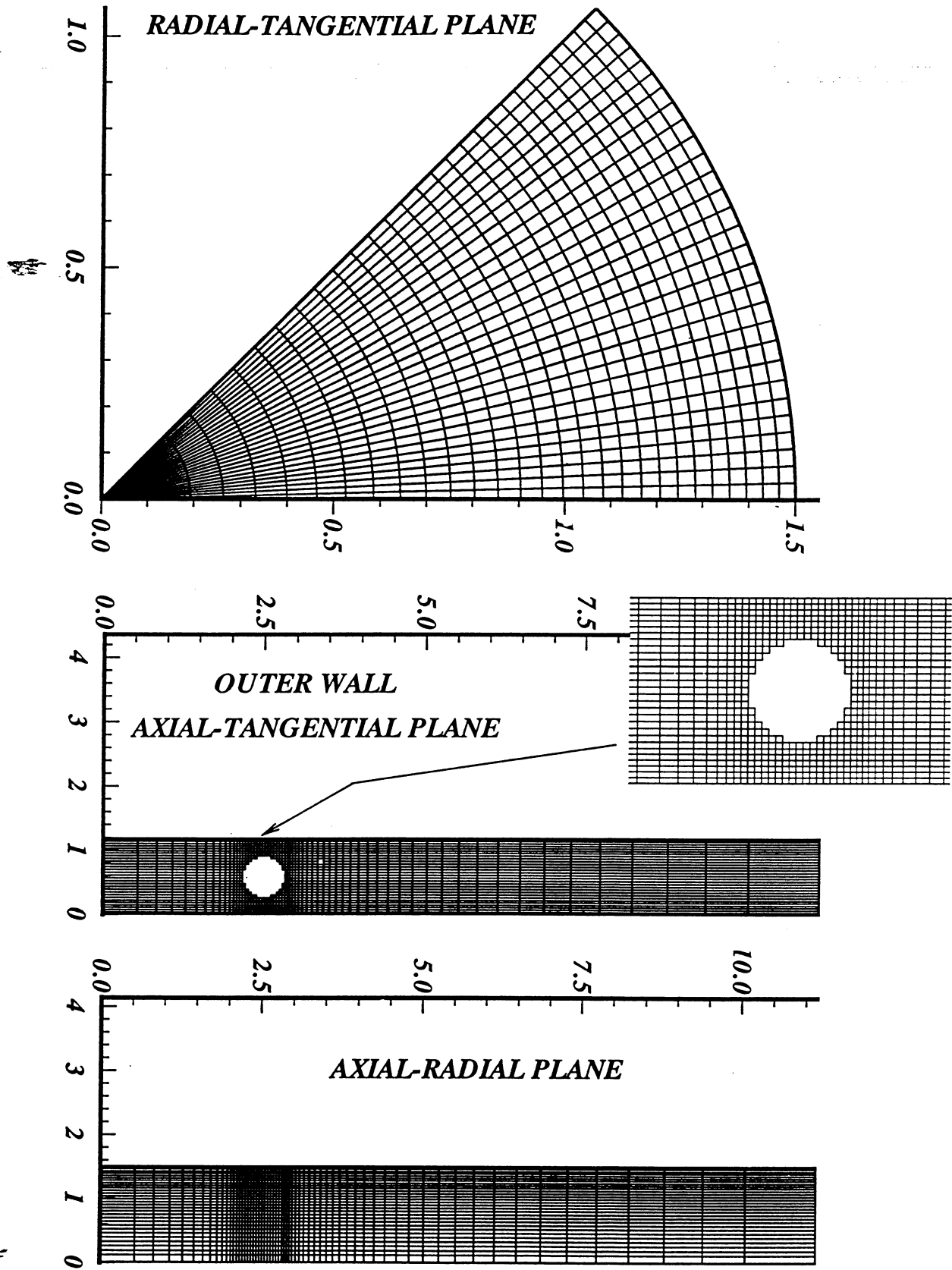
Figure-A1. Computational grid for configuration # 19

RADIAL-TANGENTIAL PLANE

OUTER WALL
AXIAL-TANGENTIAL PLANE

AXIAL-RADIAL PLANE
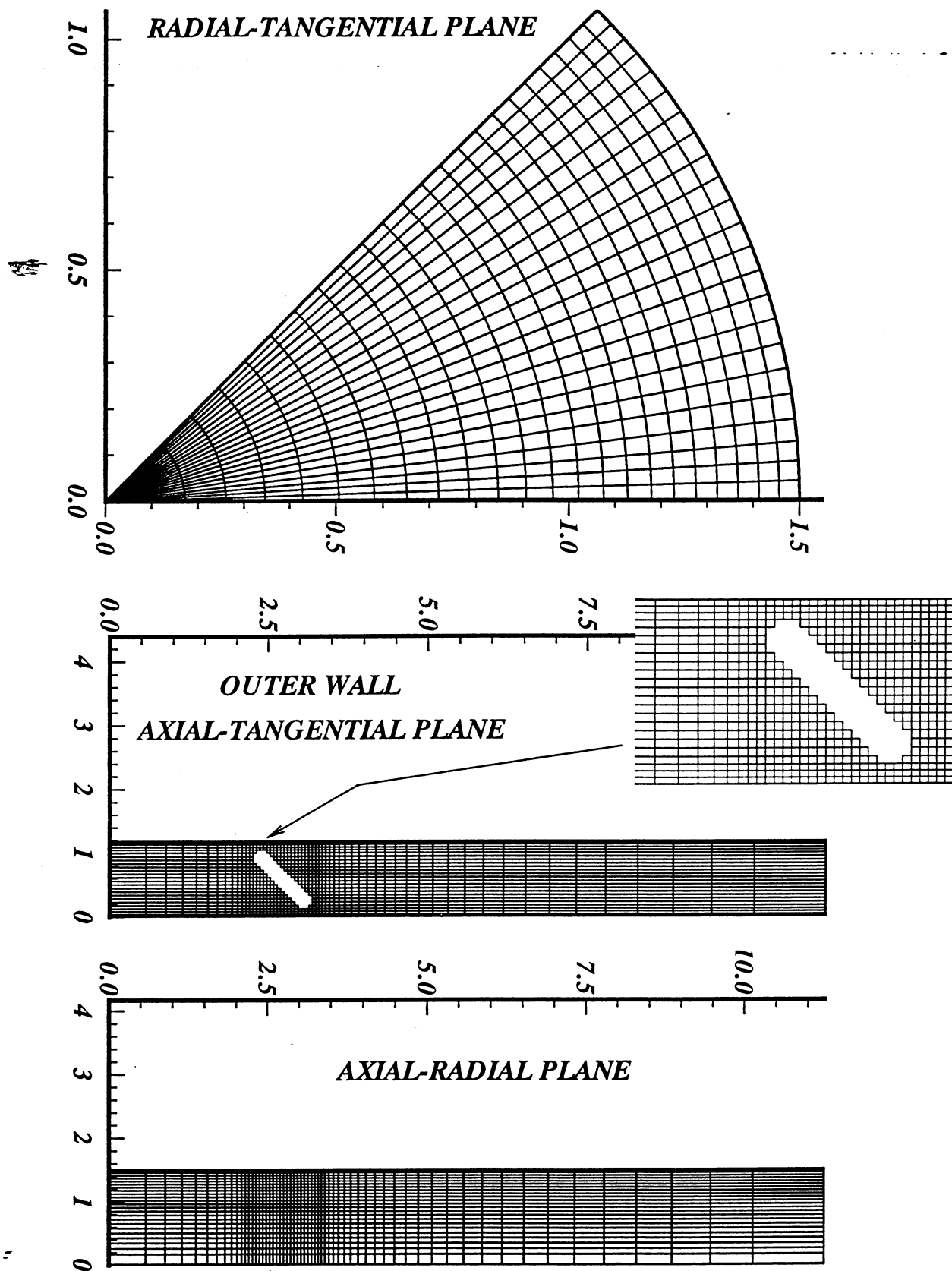
Figure-A2. Computational grid for configuration # 20

RADIAL-TANGENTIAL PLANE

OUTER WALL
AXIAL-TANGENTIAL PLANE

AXIAL-RADIAL PLANE
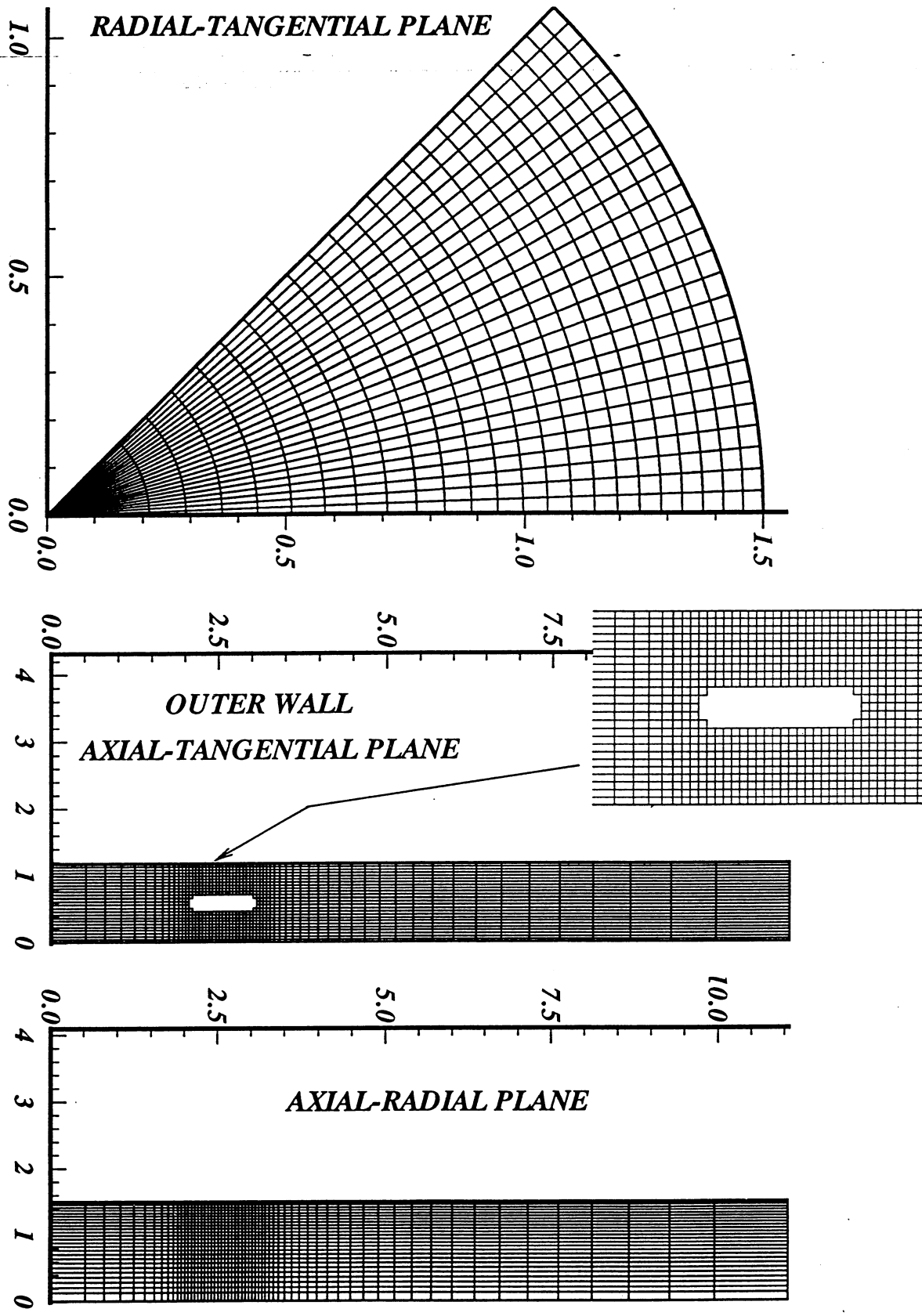
Figure-A3. Computational grid for configuration # 21

RADIAL-TANGENTIAL PLANE

OUTER WALL
AXIAL-TANGENTIAL PLANE

AXIAL-RADIAL PLANE
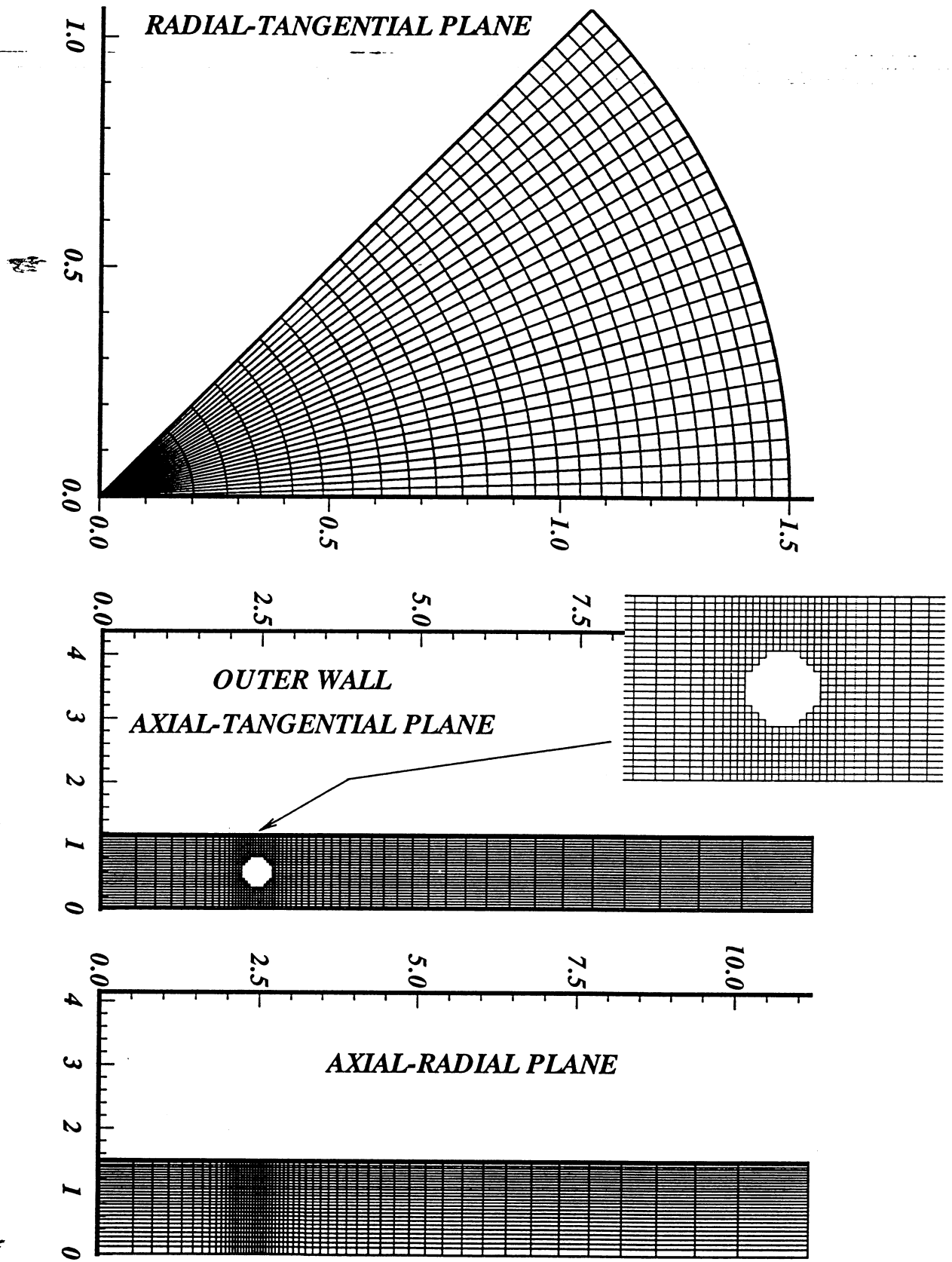
Figure-A4. Computational grid for configuration # 22

RADIAL-TANGENTIAL PLANE

OUTER WALL
AXIAL-TANGENTIAL PLANE

AXIAL-RADIAL PLANE
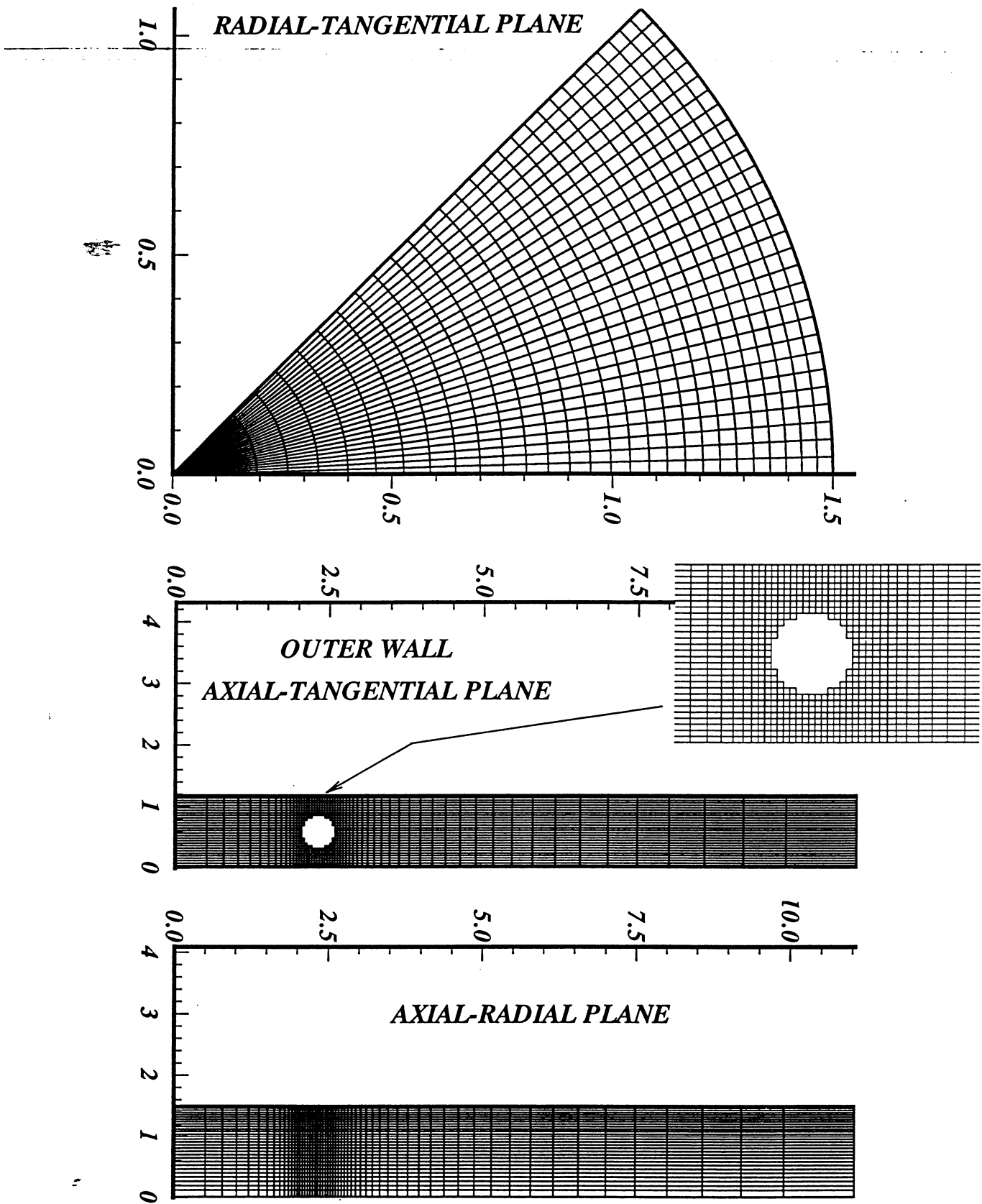
Figure-A5. Computational grid for configuration # 23

RADIAL-TANGENTIAL PLANE

**OUTER WALL
AXIAL-TANGENTIAL PLANE**

AXIAL-RADIAL PLANE
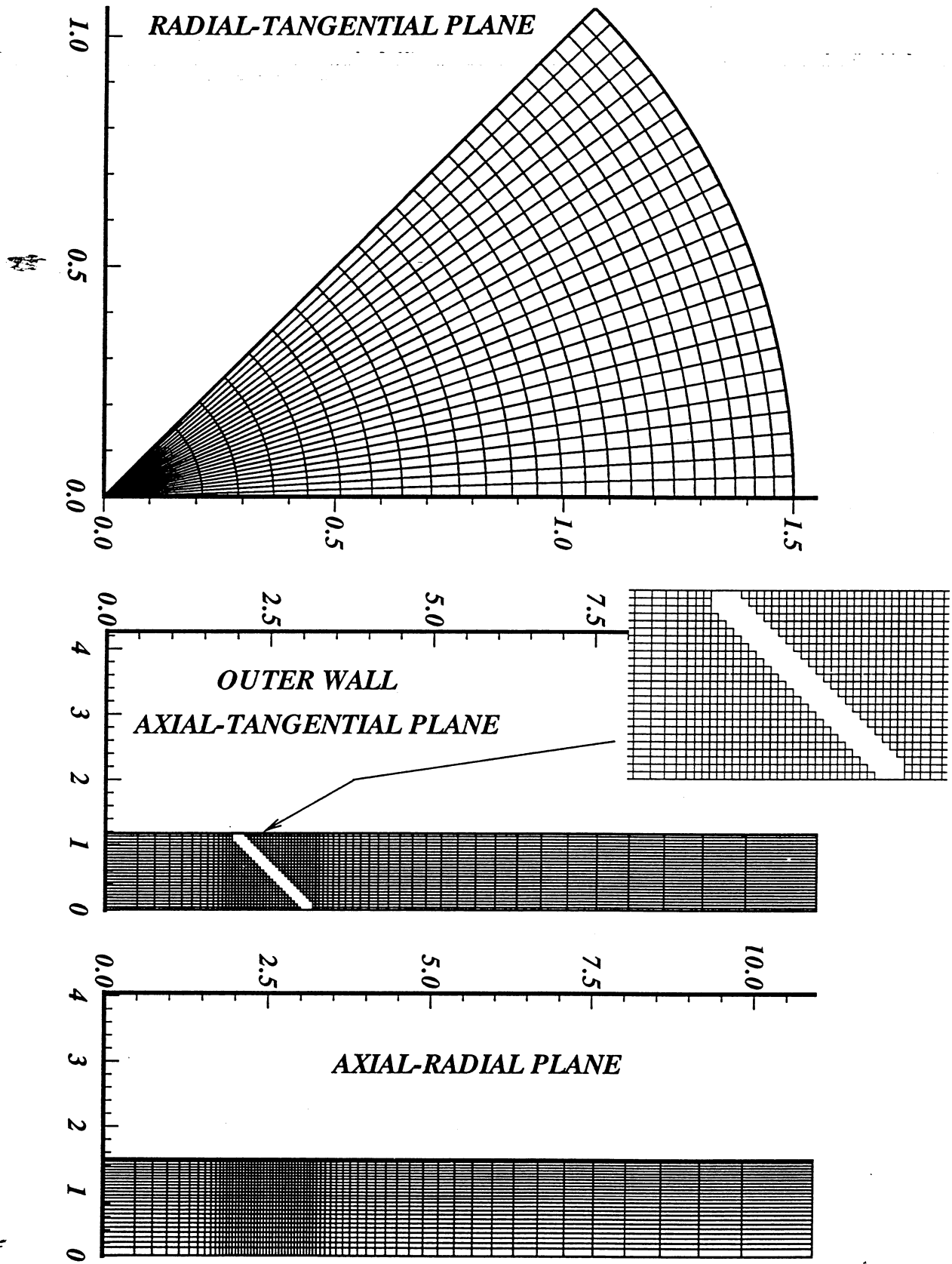
Figure-A6. Computational grid for configuration # 24

RADIAL-TANGENTIAL PLANE

OUTER WALL
AXIAL-TANGENTIAL PLANE

AXIAL-RADIAL PLANE
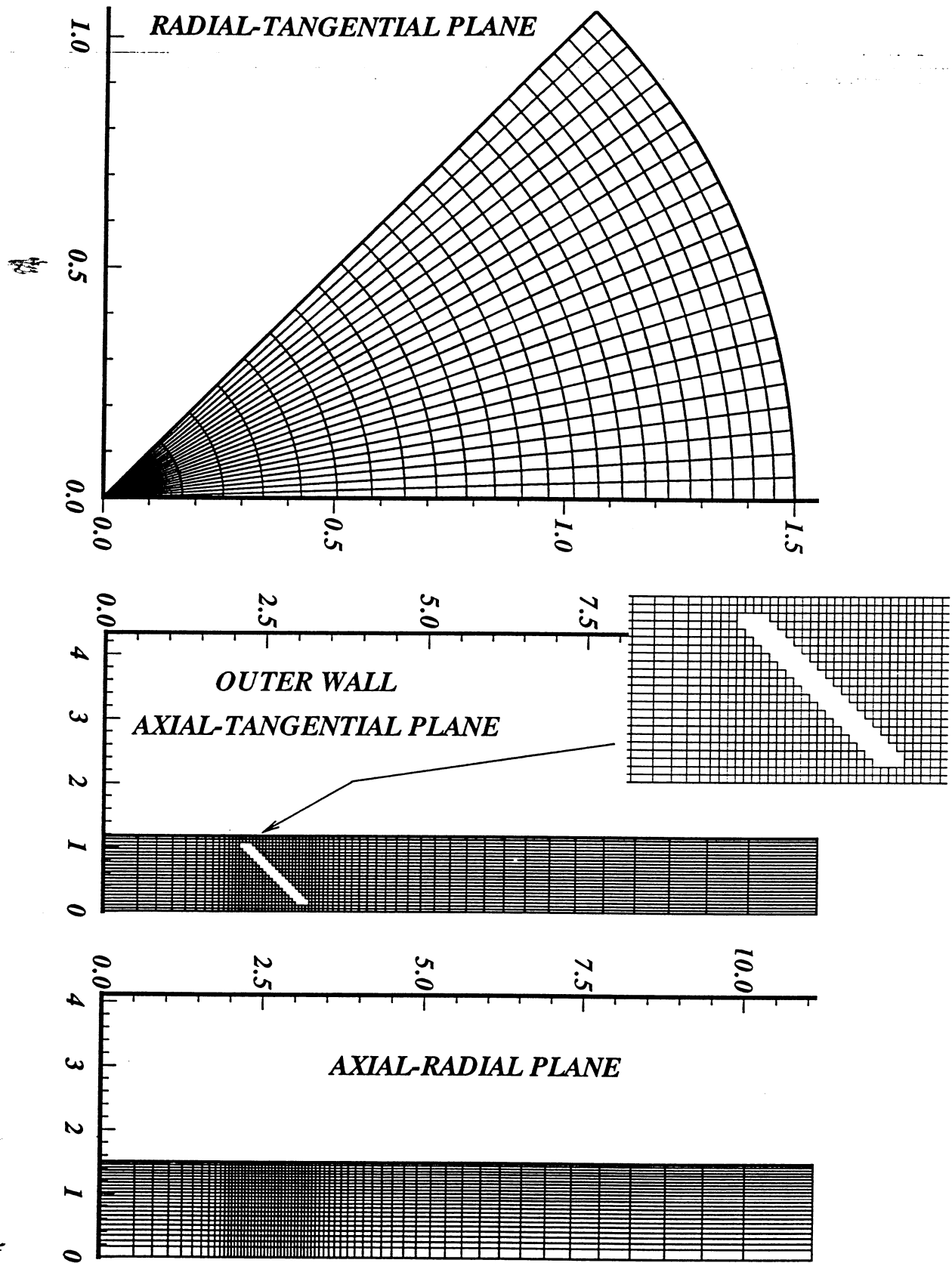
Figure-A7. Computational grid for configuration # 25
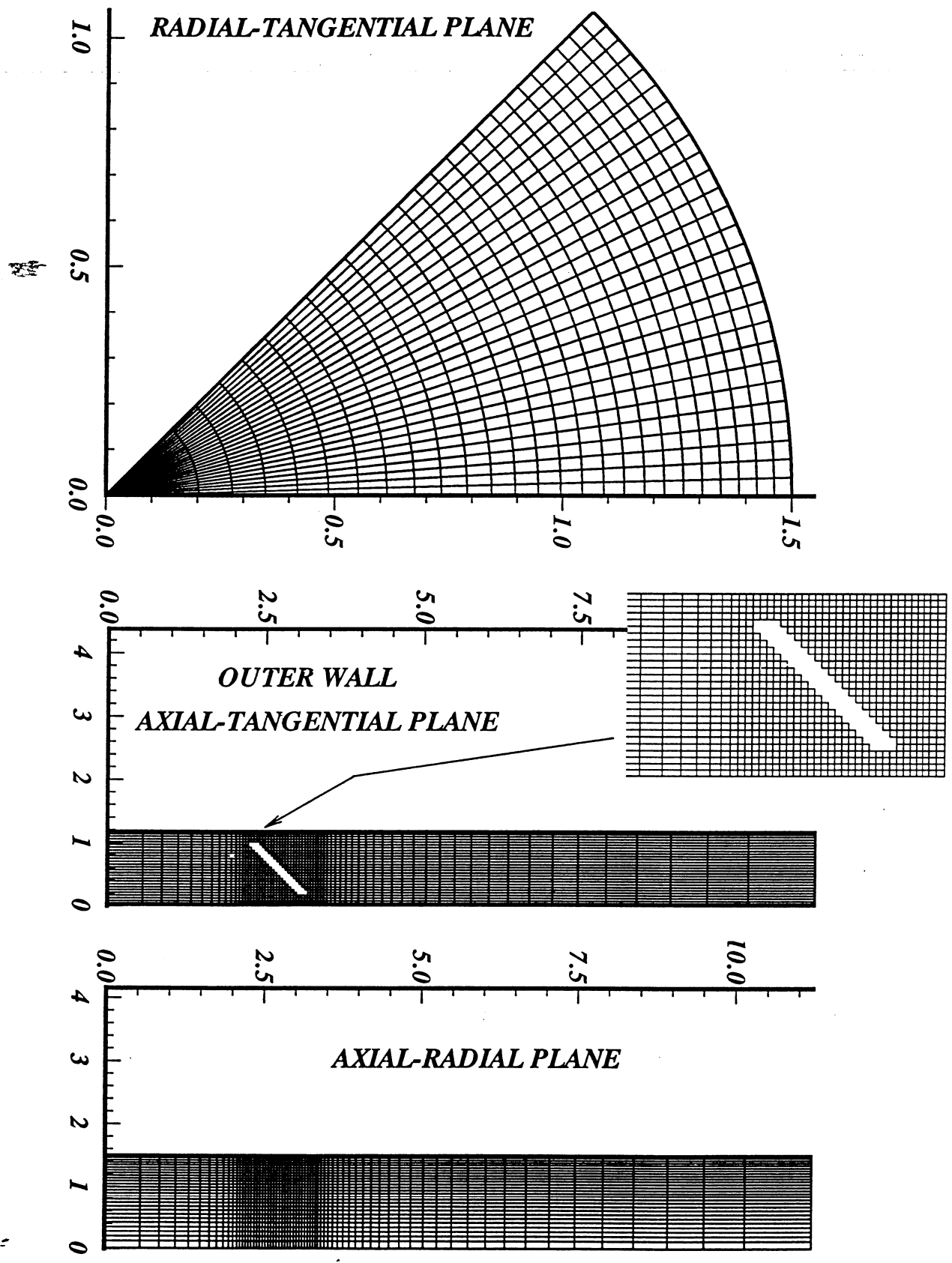
Figure-A8. Computational grid for configuration # 26

RADIAL-TANGENTIAL PLANE

**OUTER WALL
AXIAL-TANGENTIAL PLANE**

AXIAL-RADIAL PLANE
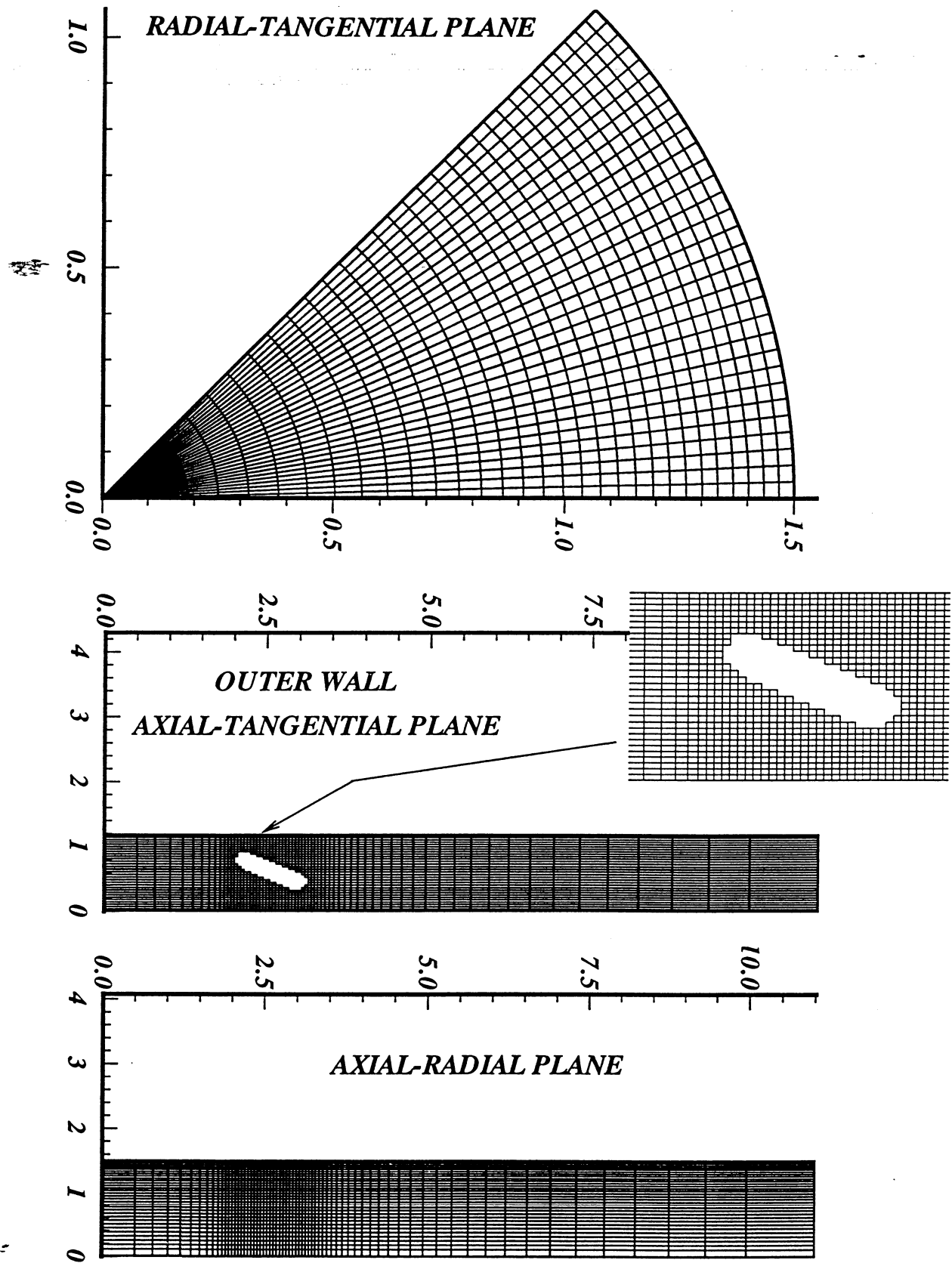
Figure-A9. Computational grid for configuration # 27

RADIAL-TANGENTIAL PLANE

OUTER WALL
AXIAL-TANGENTIAL PLANE

AXIAL-RADIAL PLANE
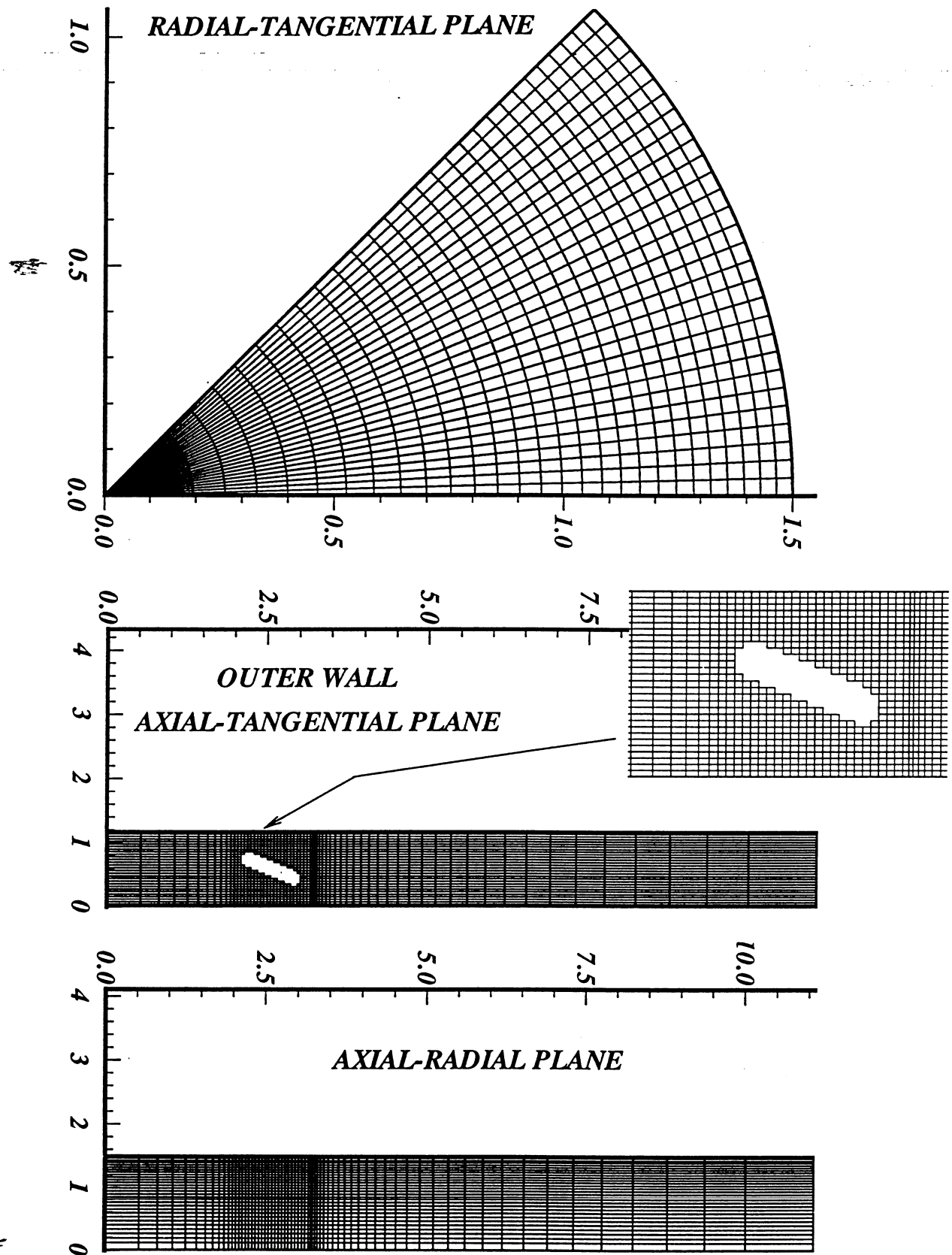
Figure-A10. Computational grid for configuration # 28

RADIAL-TANGENTIAL PLANE

OUTER WALL
AXIAL-TANGENTIAL PLANE

AXIAL-RADIAL PLANE
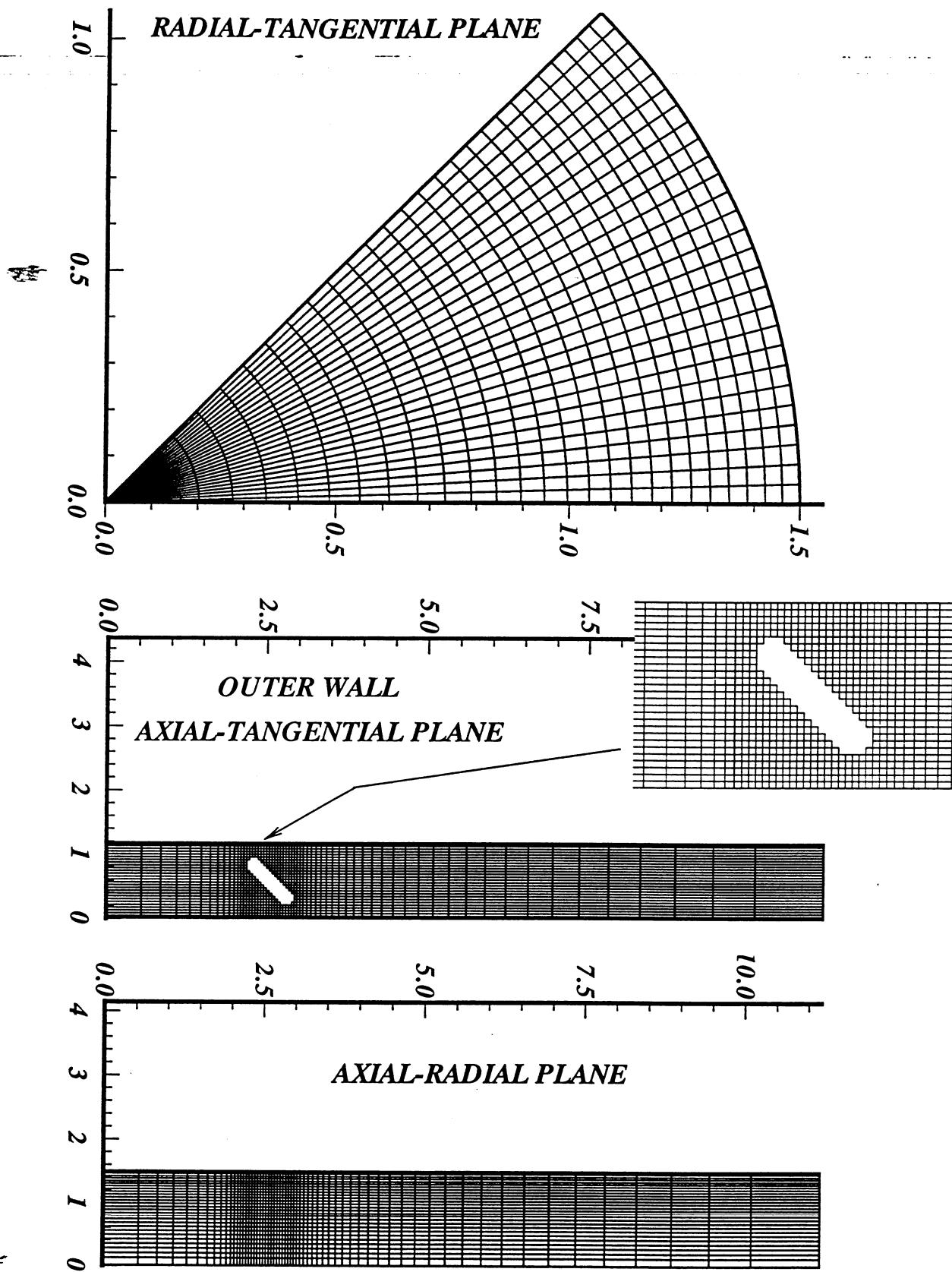
Figure-A11. Computational grid for configuration # 29

RADIAL-TANGENTIAL PLANE

OUTER WALL
AXIAL-TANGENTIAL PLANE

AXIAL-RADIAL PLANE
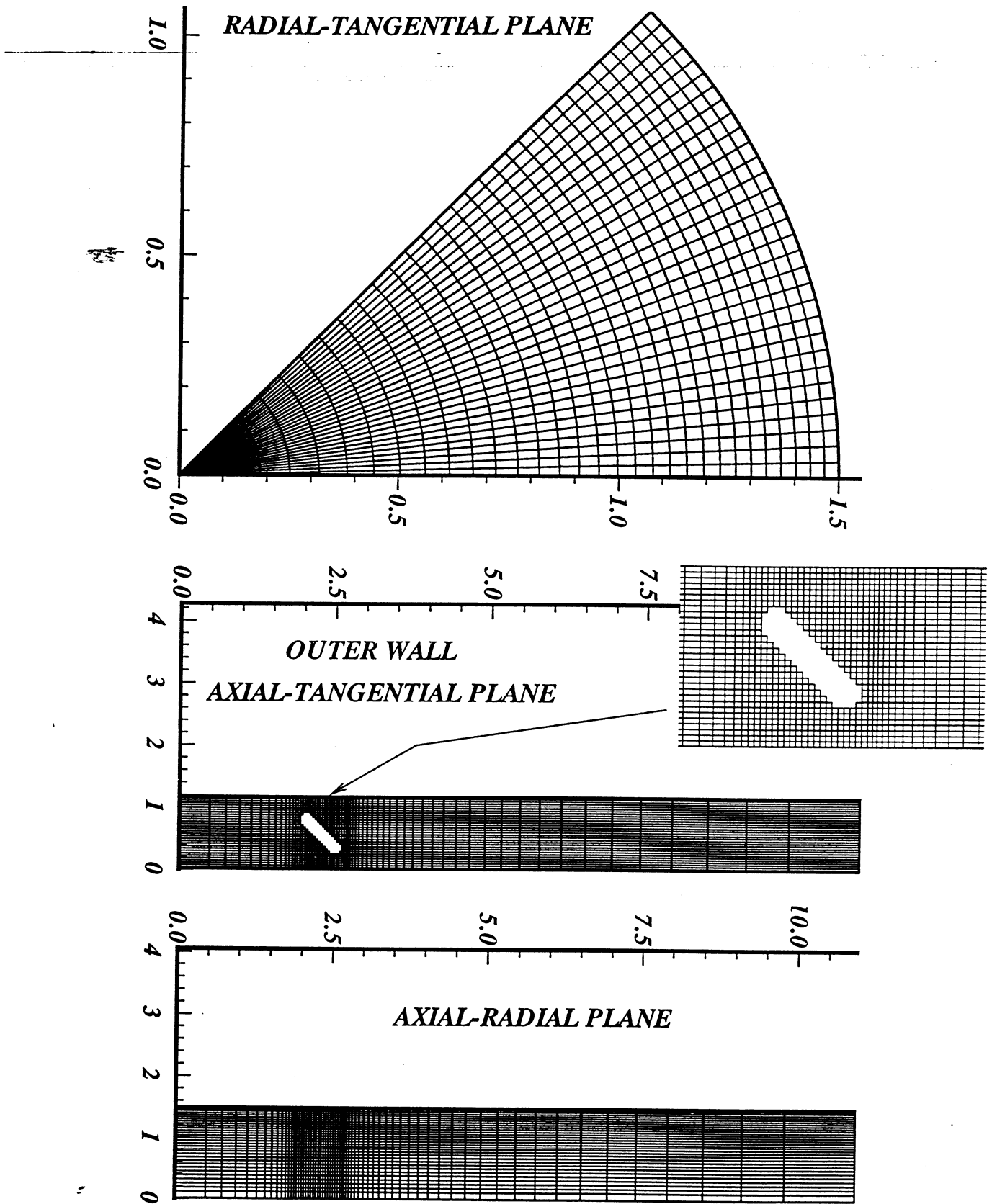
Figure-A12. Computational grid for configuration # 30

RADIAL-TANGENTIAL PLANE

OUTER WALL
AXIAL-TANGENTIAL PLANE

AXIAL-RADIAL PLANE
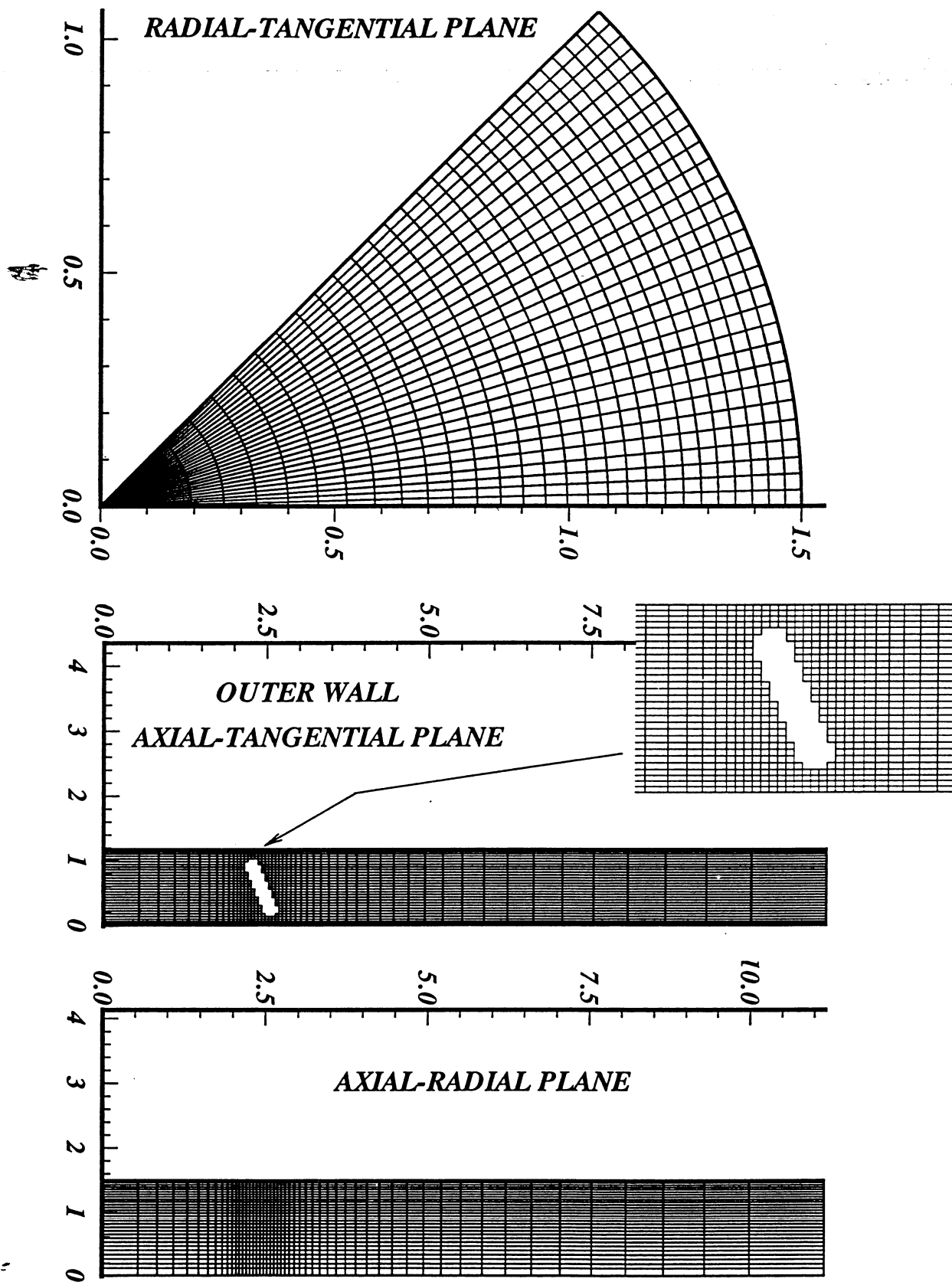
Figure-A13. Computational grid for configuration # 31

RADIAL-TANGENTIAL PLANE

OUTER WALL
AXIAL-TANGENTIAL PLANE

AXIAL-RADIAL PLANE
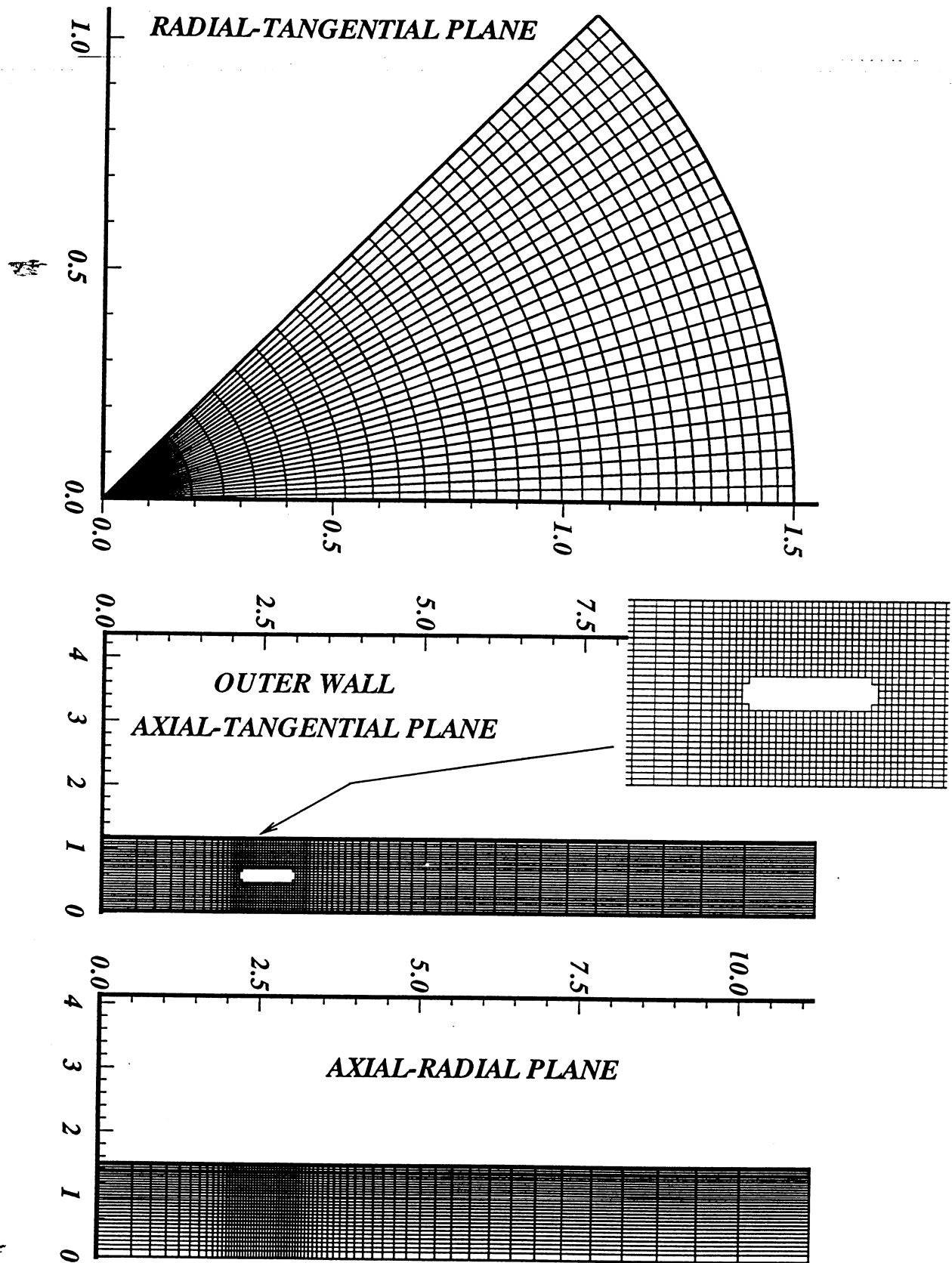
Figure-A14. Computational grid for configuration # 32

RADIAL-TANGENTIAL PLANE

OUTER WALL
AXIAL-TANGENTIAL PLANE

AXIAL-RADIAL PLANE
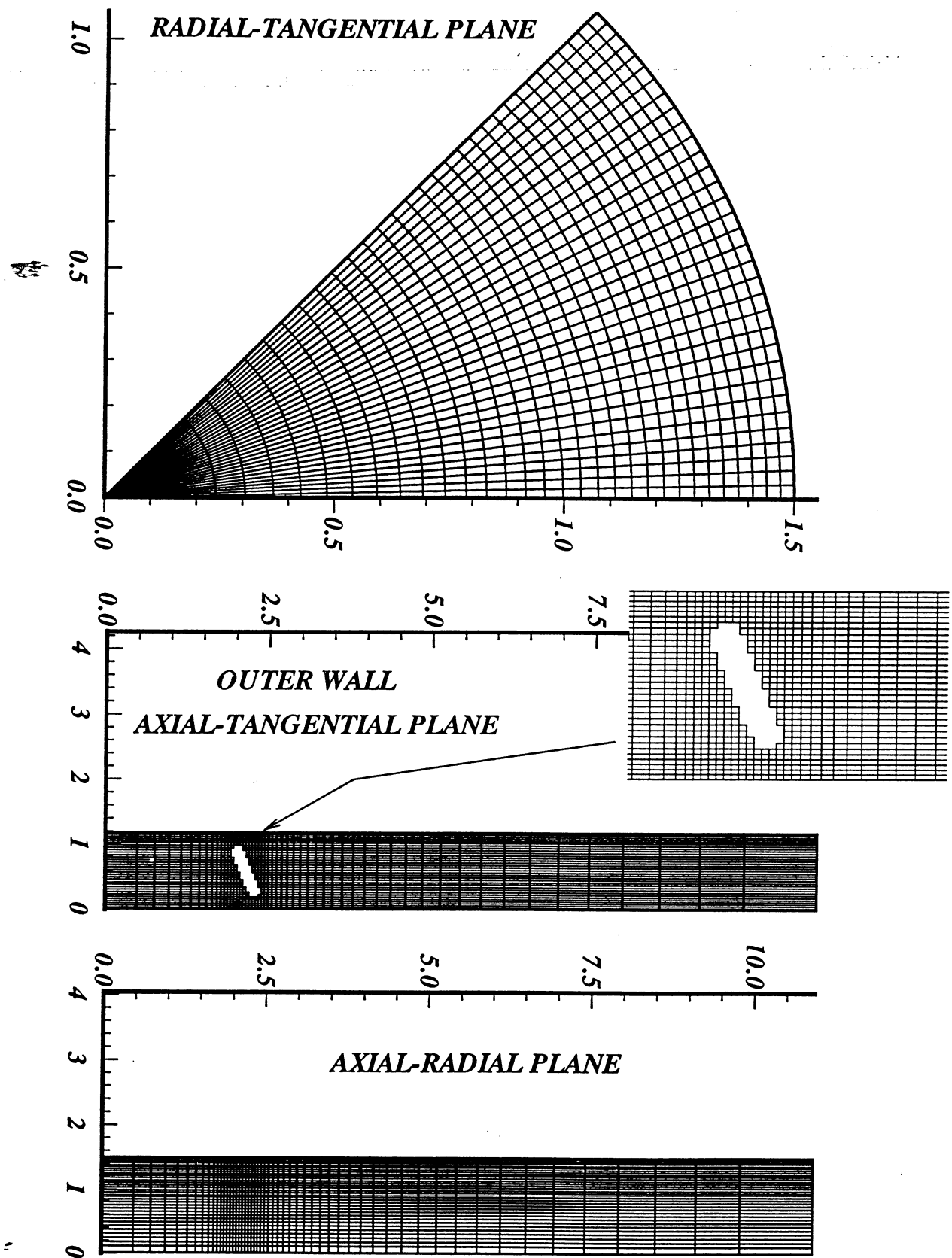
Figure-A15. Computational grid for configuration # 33

RADIAL-TANGENTIAL PLANE

OUTER WALL
AXIAL-TANGENTIAL PLANE

AXIAL-RADIAL PLANE
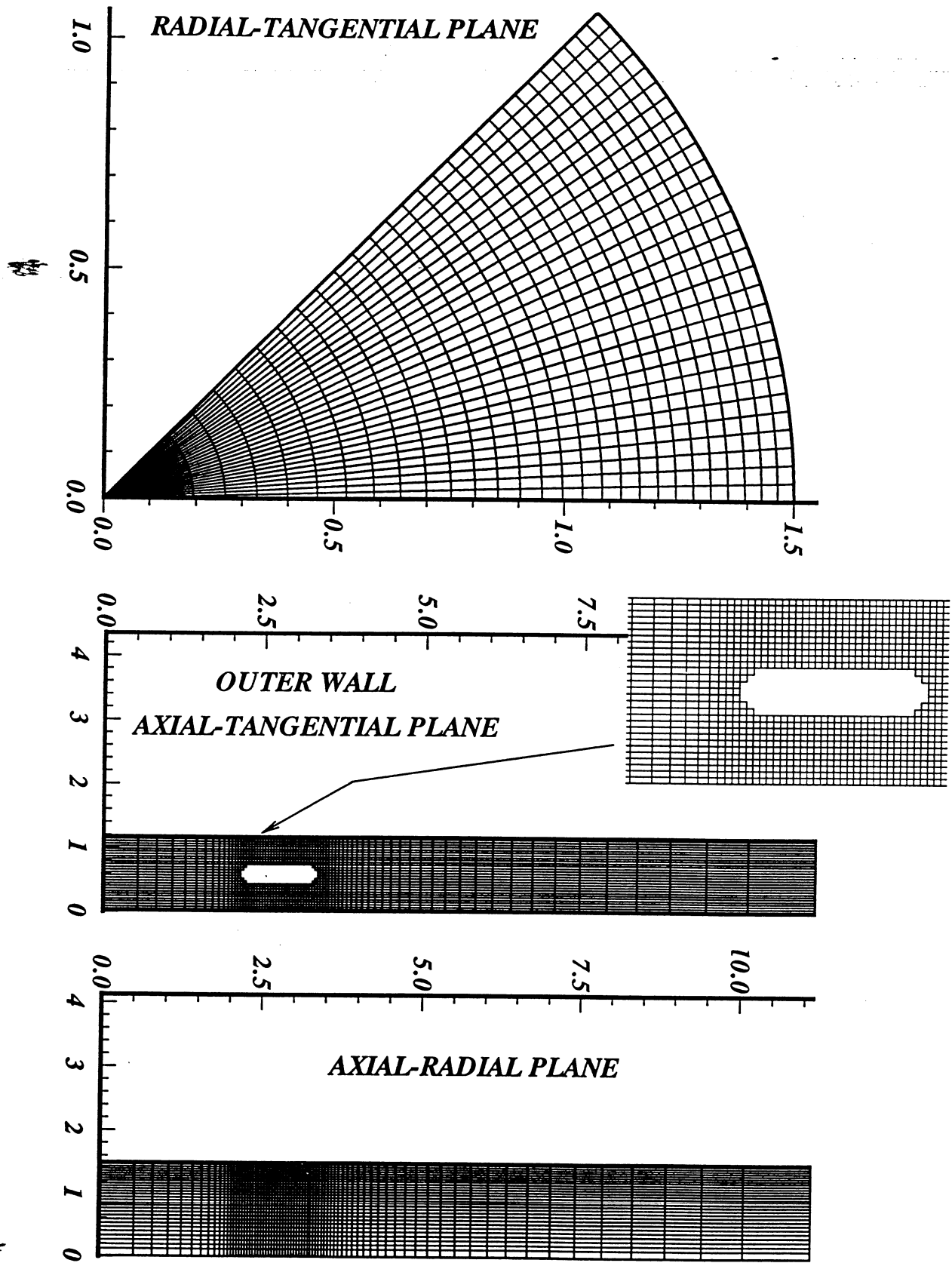
Figure-A16. Computational grid for configuration # 34

RADIAL-TANGENTIAL PLANE

OUTER WALL
AXIAL-TANGENTIAL PLANE

AXIAL-RADIAL PLANE
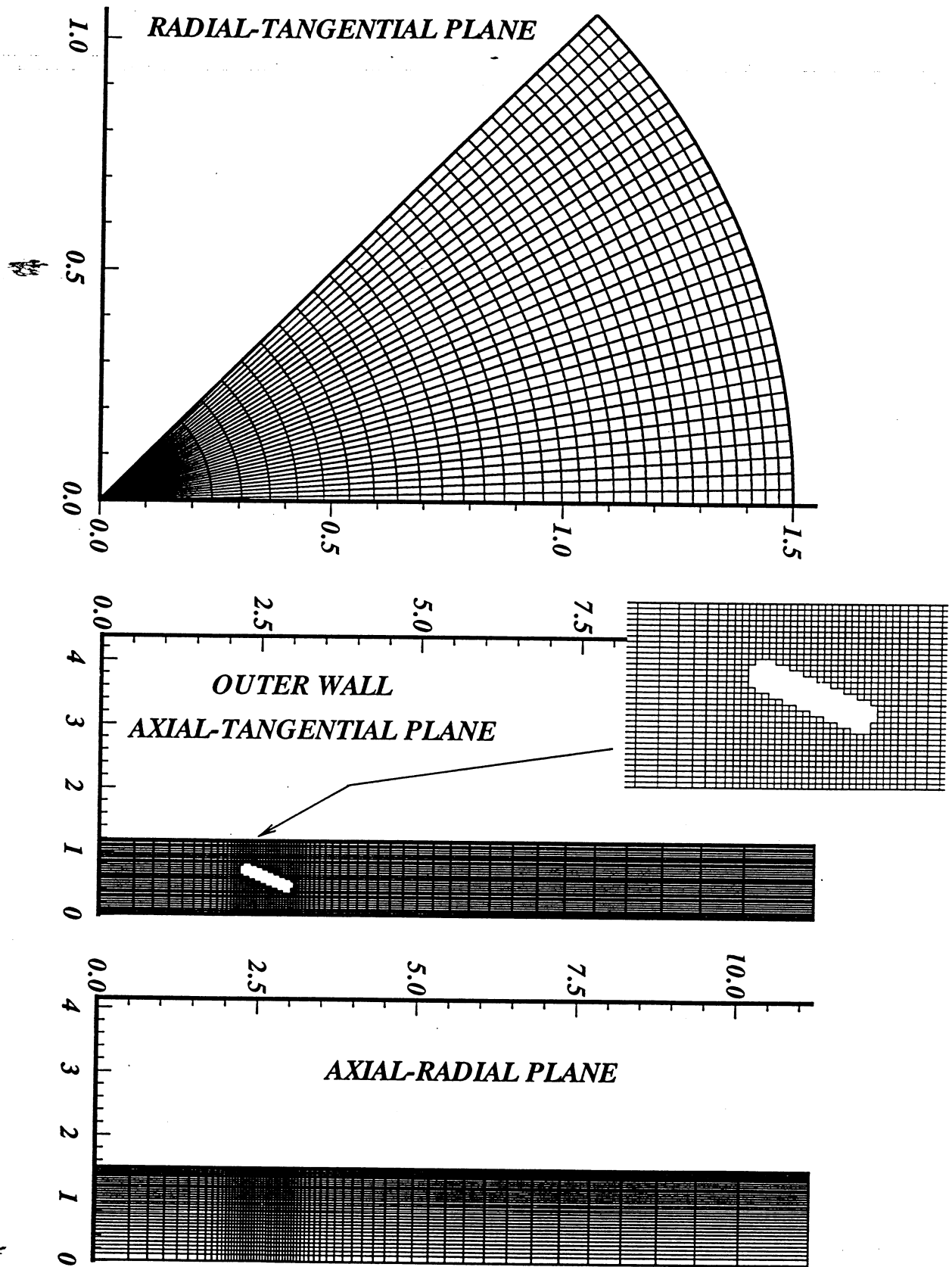
Figure-A17. Computational grid for configuration # 35

RADIAL-TANGENTIAL PLANE

**OUTER WALL
AXIAL-TANGENTIAL PLANE**

AXIAL-RADIAL PLANE
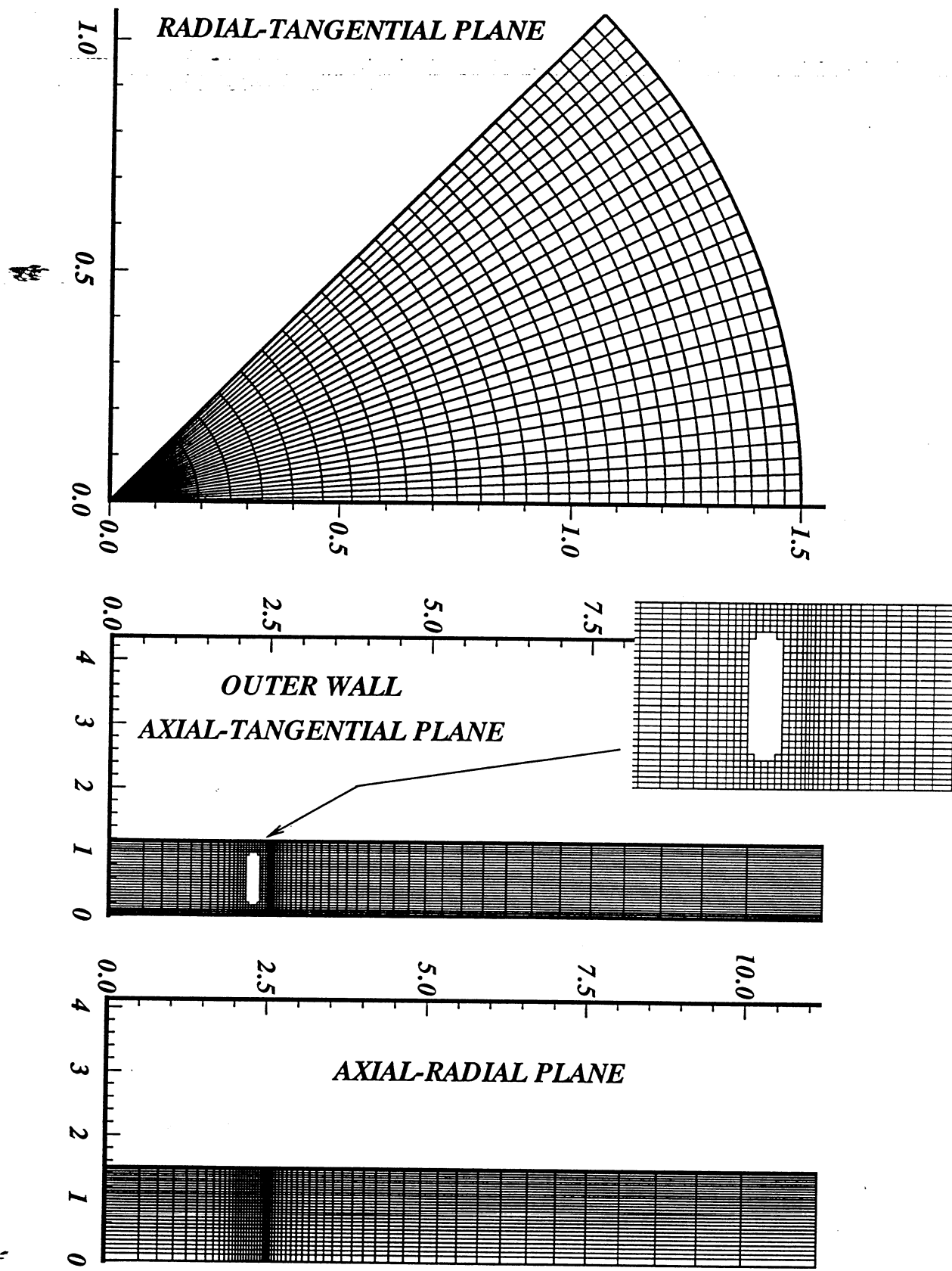
Figure-A18. Computational grid for configuration # 36

APPENDIX-B

Effect of orifice shape on mixing (J=25)			
Variable	AT	AR	RT
N.T.	B1-1	B1-4	B1-7
f	B1-2	B1-5	B1-8
VEL	B1-3	B1-6	B1-9

Effect of orifice shape on mixing (J=52)			
Variable	AT	AR	RT
N.T.	B2-1	B2-4	B2-7
f	B2-2	B2-5	B2-8
VEL	B2-3	B2-6	B2-9

Effect of orifice shape on mixing (J=80)			
Variable	AT	AR	RT
N.T.	B3-1	B3-4	B3-7
f	B3-2	B3-5	B3-8
VEL	B3-3	B3-6	B3-9

Effect of J on mixing (round holes)			
Variable	AT	AR	RT
N.T.	B4-1	B4-4	B4-7
f	B4-2	B4-5	B4-8
VEL	B4-3	B4-6	B4-9

Effect of J on mixing (45 deg slots, L/W=4)			
Variable	AT	AR	RT
N.T.	B5-1	B5-4	B5-7
f	B5-2	B5-5	B5-8
VEL	B5-3	B5-6	B5-9

Effect of J on mixing (45 deg slots, L/W=8)			
Variable	AT	AR	RT
N.T.	B6-1	B6-4	B6-7
f	B6-2	B6-5	B6-8
VEL	B6-3	B6-6	B6-9

Effect of slot slant angle on mixing (J=25)			
Variable	AT	AR	RT
N.T.	B7-1	B7-4	B7-7
f	B7-2	B7-5	B7-8
VEL	B7-3	B7-6	B7-9

Effect of slot slant angle on mixing (J=52)			
Variable	AT	AR	RT
N.T.	B8-1	B8-4	B8-7
f	B8-2	B8-5	B8-8
VEL	B8-3	B8-6	B8-9

Effect of slot slant angle on mixing (J=80)			
Variable	AT	AR	RT
N.T.	B9-1	B9-4	B9-7
f	B9-2	B9-5	B9-8
VEL	B9-3	B9-6	B9-9

where,

AR = axial-radial plane, RT= radial-tangential plane, and AT= axial-tangential plane
N.T. = normalized temperature distribution, f = normalized equivalence ratio distribution, VEL = velocity distribution

$$N.T. = \frac{T_{jk} - T_{jet}}{T_{stoic} - T_{jet}} \quad \text{and} \quad f = \frac{\alpha_{jk} - \alpha_{jet}}{\alpha_{stoic} - \alpha_{jet}} \quad \text{where } T = \text{temperature and}$$
$$\alpha = \text{equivalence ratio}$$

AXIAL-TANGENTIAL PLANE

NORMALIZED TEMPERATURE

ABCSISSA = x/R
ORDINATE = z/S

AXIAL-TANGENTIAL PLANE

NORMALIZED TEMPERATURE

ABCSISSA = x/R
ORDINATE = z/S

AXIAL-TANGENTIAL PLANE

NORMALIZED TEMPERATURE

ABCSISSA = x/R
ORDINATE = z/S
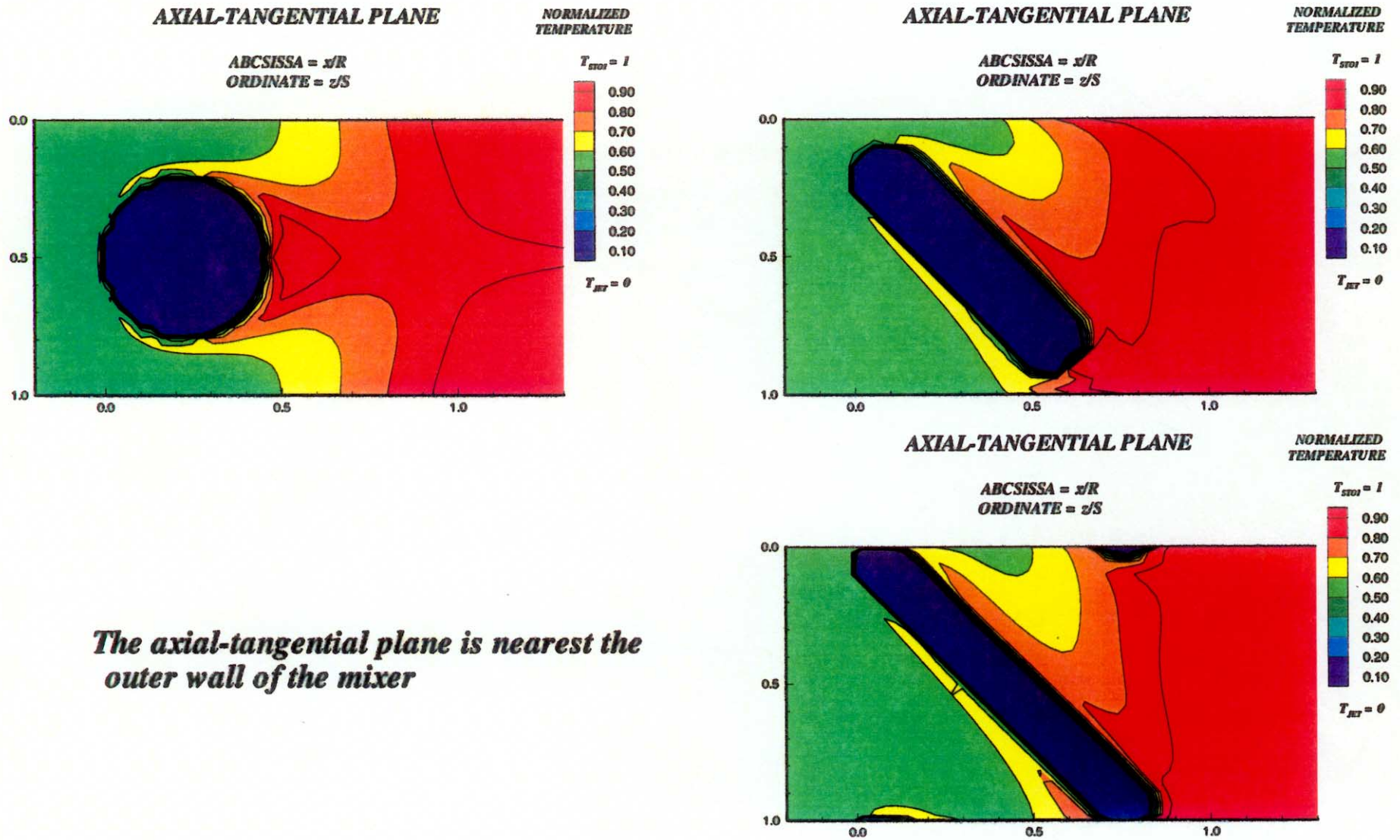
*The axial-tangential plane is nearest the outer wall of the mixer*

**Figure-B1-1. Effect of the change in orifice geometry on the temperature distribution
Clockwise from top left: round, 45° slot with L/W=4, and 45° slot with L/W=8
J=25, MR=2.96, DR=2.28, 8 orifices/row**
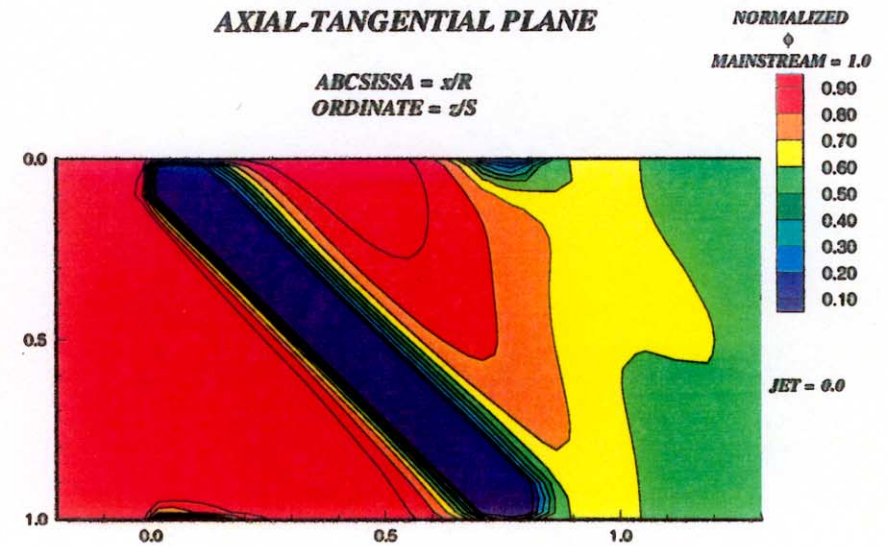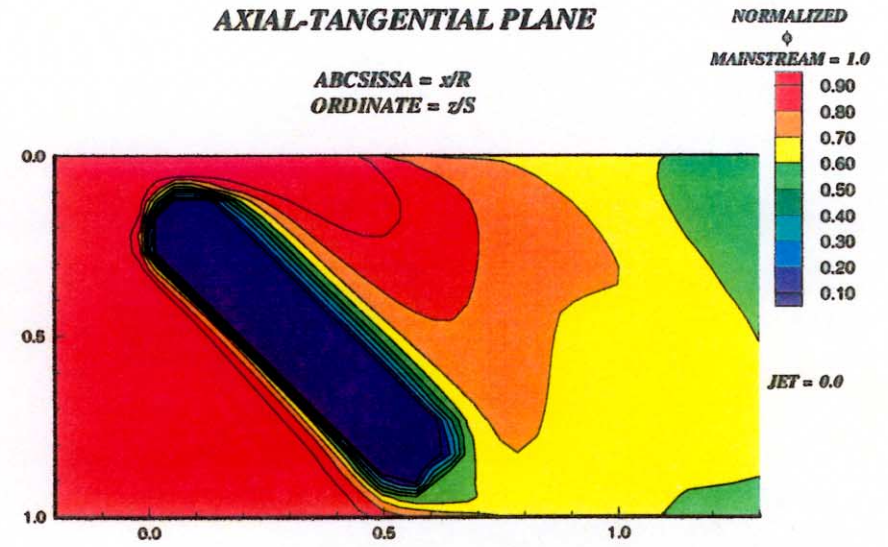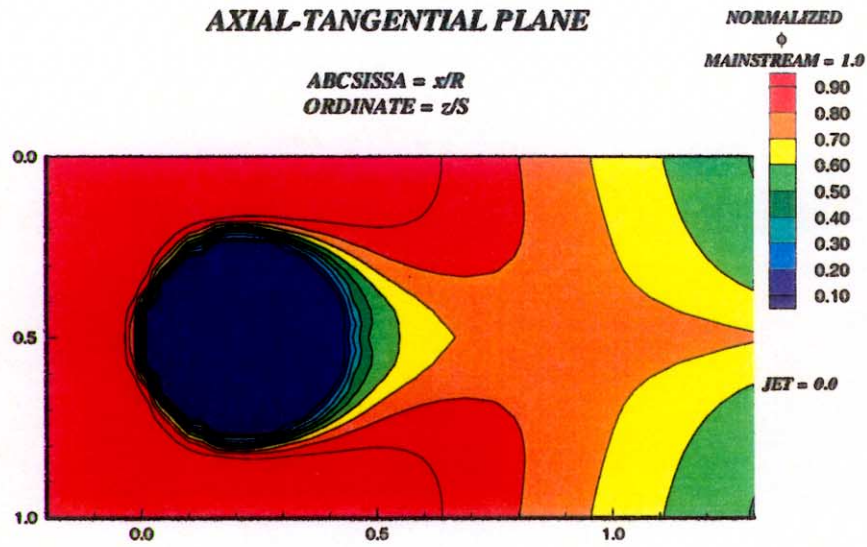
The axial-tangential plane is nearest the outer wall of the mixer

Figure-B1-2. Effect of the change in orifice geometry on the equivalence ratio distribution
Clockwise from top left: round, 45° slot with L/W=4, and 45° slot with L/W=8
J=25, MR=2.96, DR=2.28, 8 orifices/row

AXIAL-TANGENTIAL PLANE

ABCSISSA = x/R
ORDINATE = z/S

AXIAL-TANGENTIAL PLANE

ABCSISSA = x/R
ORDINATE = z/S

The axial-tangential plane is nearest the outer wall of the mixer

AXIAL-TANGENTIAL PLANE

ABCSISSA = x/R
ORDINATE = z/S
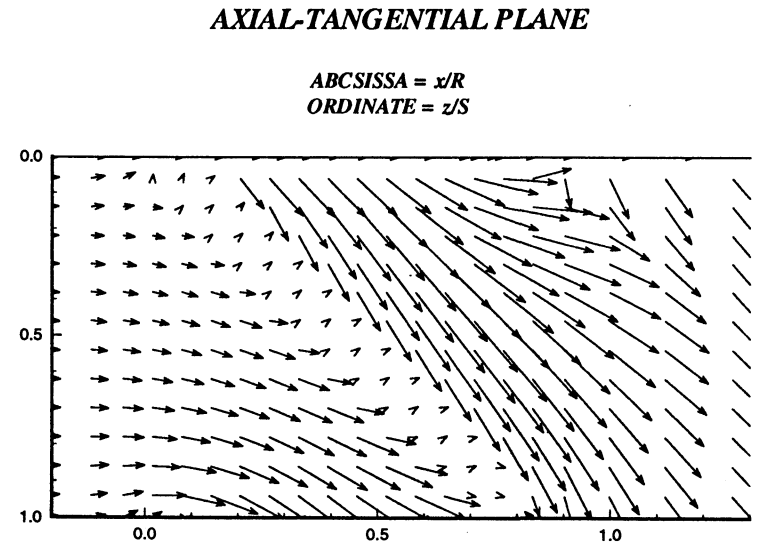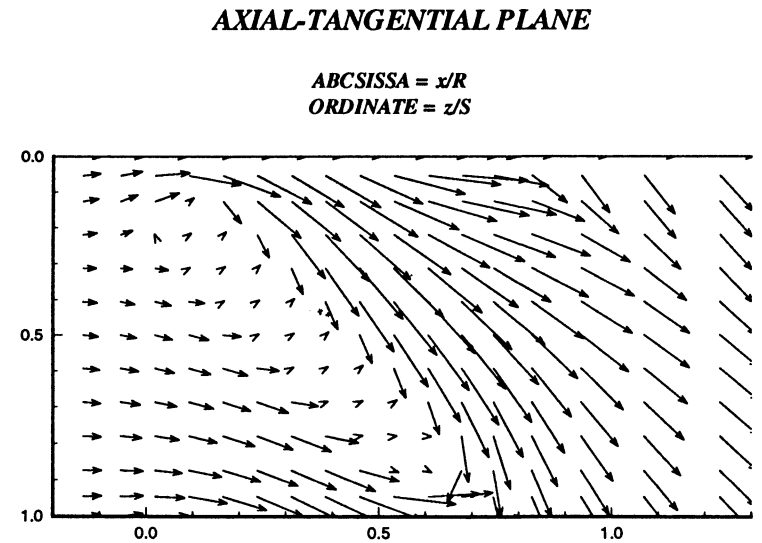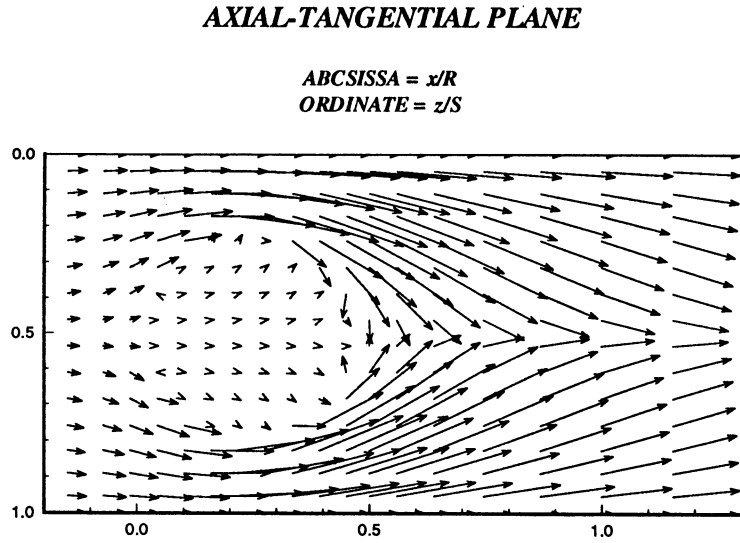
Figure-B1-3. Effect of the change in orifice geometry on the velocity distribution Clockwise from top left: round, 45° slot with L/W=4, and 45° slot with L/W=8 J=25, MR=2.96, DR=2.28, 8 orifices/row

AXIAL-RADIAL PLANE

ABSCISSA = x/R
ORDINATE = r

NORMALIZED
TEMPERATURE

$T_{STOI} = 1$

0.90
0.80
0.70
0.60
0.50
0.40
0.30
0.20
0.10

$T_{JET} = 0$

AXIAL-RADIAL PLANE

ABSCISSA = x/R
ORDINATE = r

NORMALIZED
TEMPERATURE

$T_{STOI} = 1$

0.90
0.80
0.70
0.60
0.50
0.40
0.30
0.20
0.10

$T_{JET} = 0$

The axial-radial plane is through the center of the jet

AXIAL-RADIAL PLANE

ABSCISSA = x/R
ORDINATE = r

NORMALIZED
TEMPERATURE

$T_{STOI} = 1$

0.90
0.80
0.70
0.60
0.50
0.40
0.30
0.20
0.10

$T_{JET} = 0$
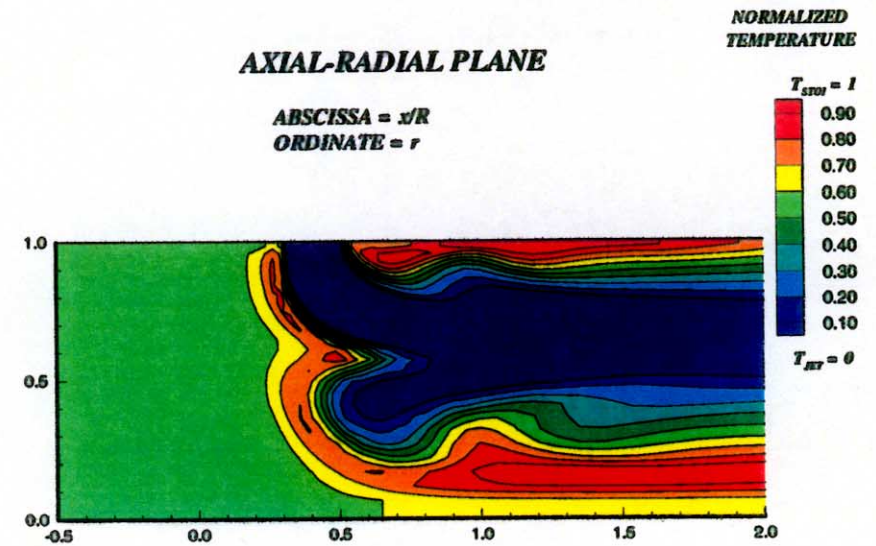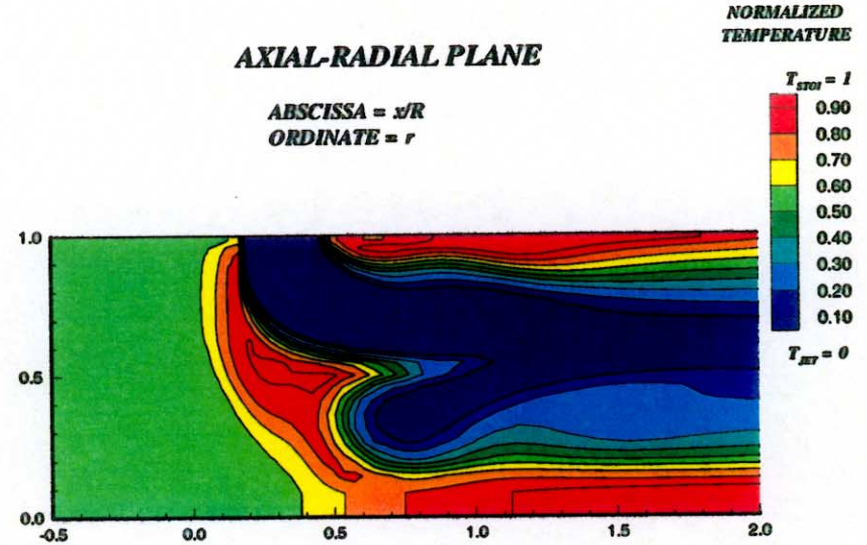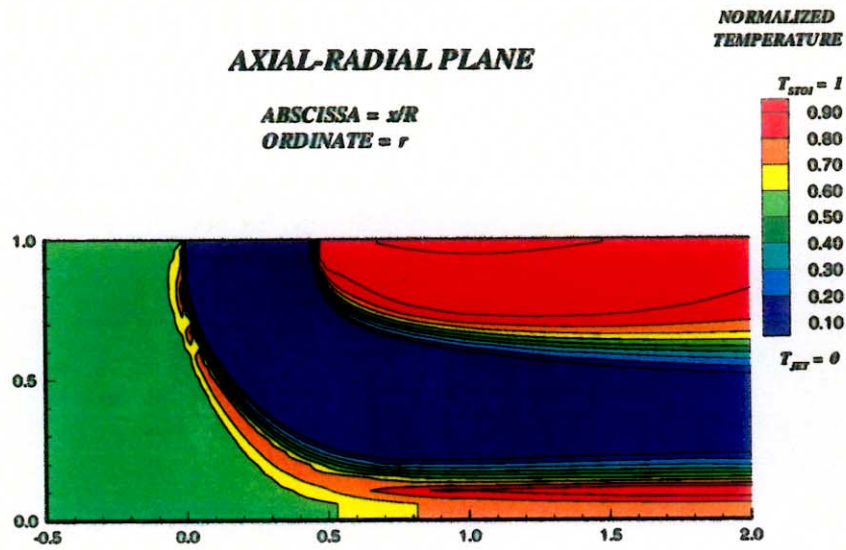
Figure-B1-4. Effect of the change in orifice geometry on the temperature distribution
Clockwise from top left: round, 45° slot with L/W=4, and 45° slot with L/W=8
J=25, MR=2.96, DR=2.28, 8 orifices/row

AXIAL-RADIAL PLANE

ABSCISSA = x/R
ORDINATE = r

NORMALIZED
◇
MAINSTREAM = 1.0

	0.90
	0.80
	0.70
	0.60
	0.50
	0.40
	0.30
	0.20
	0.10

JET = 0.0

AXIAL-RADIAL PLANE

ABSCISSA = x/R
ORDINATE = r

NORMALIZED
◇
MAINSTREAM = 1.0

	0.90
	0.80
	0.70
	0.60
	0.50
	0.40
	0.30
	0.20
	0.10

JET = 0.0

The axial-radial plane is through the center of the jet

AXIAL-RADIAL PLANE

ABSCISSA = x/R
ORDINATE = r

NORMALIZED
◇
MAINSTREAM = 1.0

| | 0.90 |
	0.80
	0.70
	0.60
	0.50
	0.40
	0.30
	0.20
	0.10

JET = 0.0
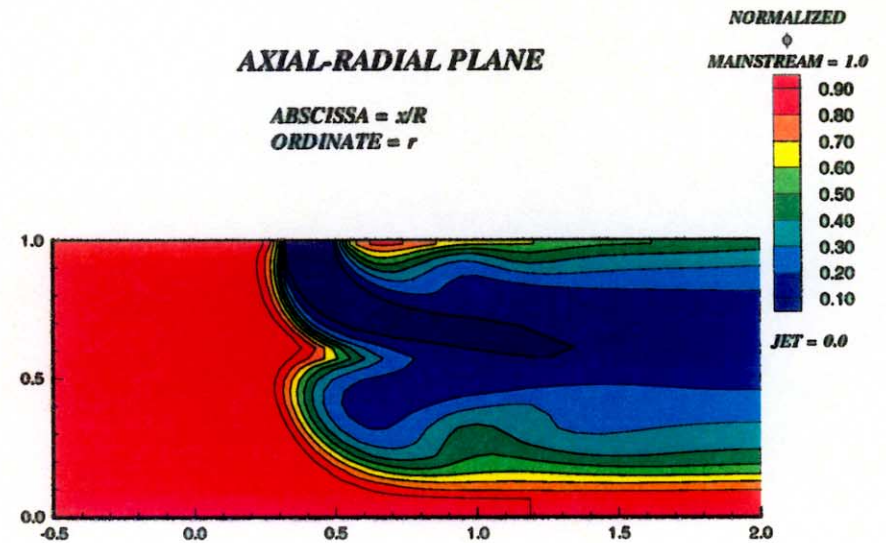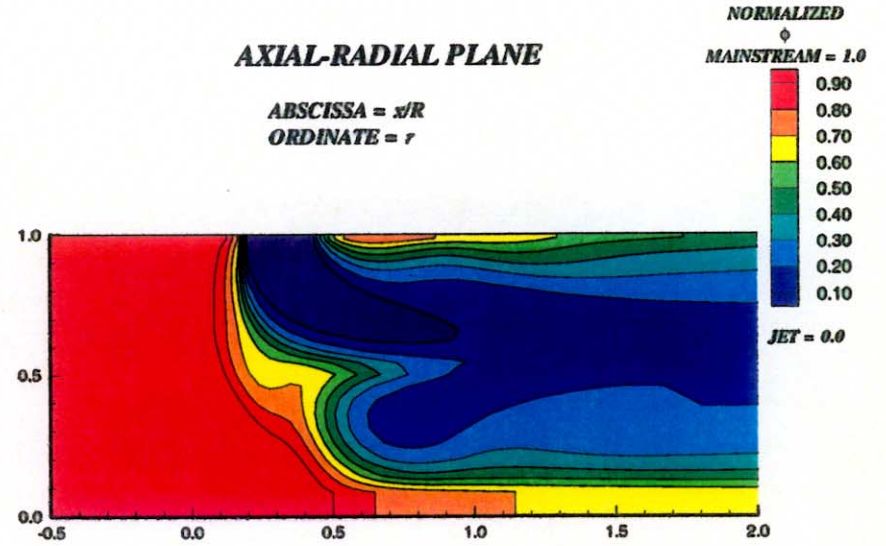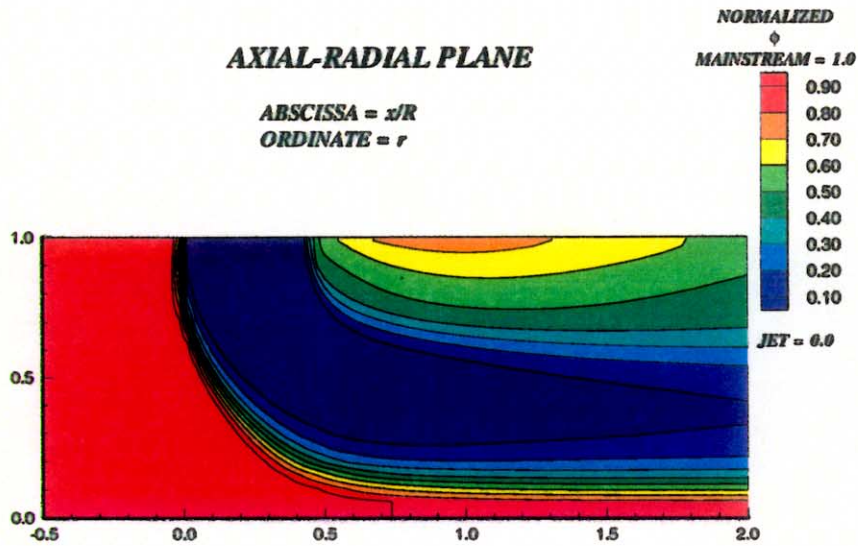
Figure-B1-5. Effect of the change in orifice geometry on the equivalence ratio distribution
Clockwise from top left: round, 45° slot with L/W=4, and 45° slot with L/W=8
J=25, MR=2.96, DR=2.28, 8 orifices/row

AXIAL-RADIAL PLANE

ABSCISSA = x/R
ORDINATE = r
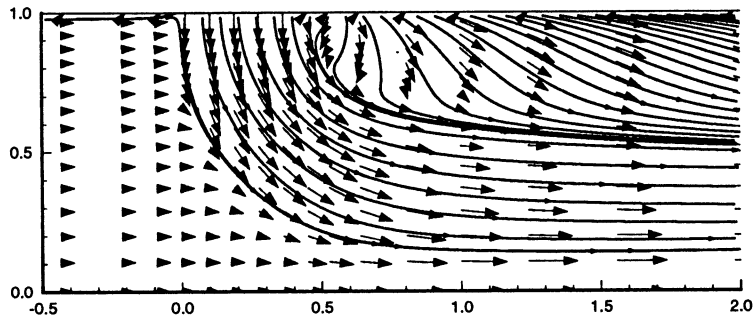
AXIAL-RADIAL PLANE

ABSCISSA = x/R
ORDINATE = r
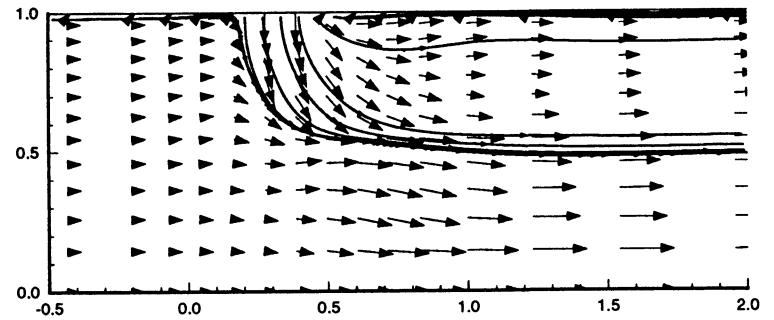
AXIAL-RADIAL PLANE

ABSCISSA = x/R
ORDINATE = r
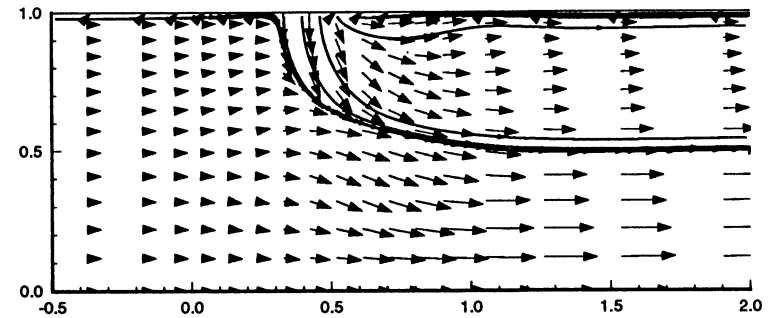
The axial-radial plane is through the center of the jet

Figure-B1-6. Effect of the change in orifice geometry on the velocity distribution Clockwise from top left: round, 45° slot with L/W=4, and 45° slot with L/W=8 J=25, MR=2.96, DR=2.28, 8 orifices/row
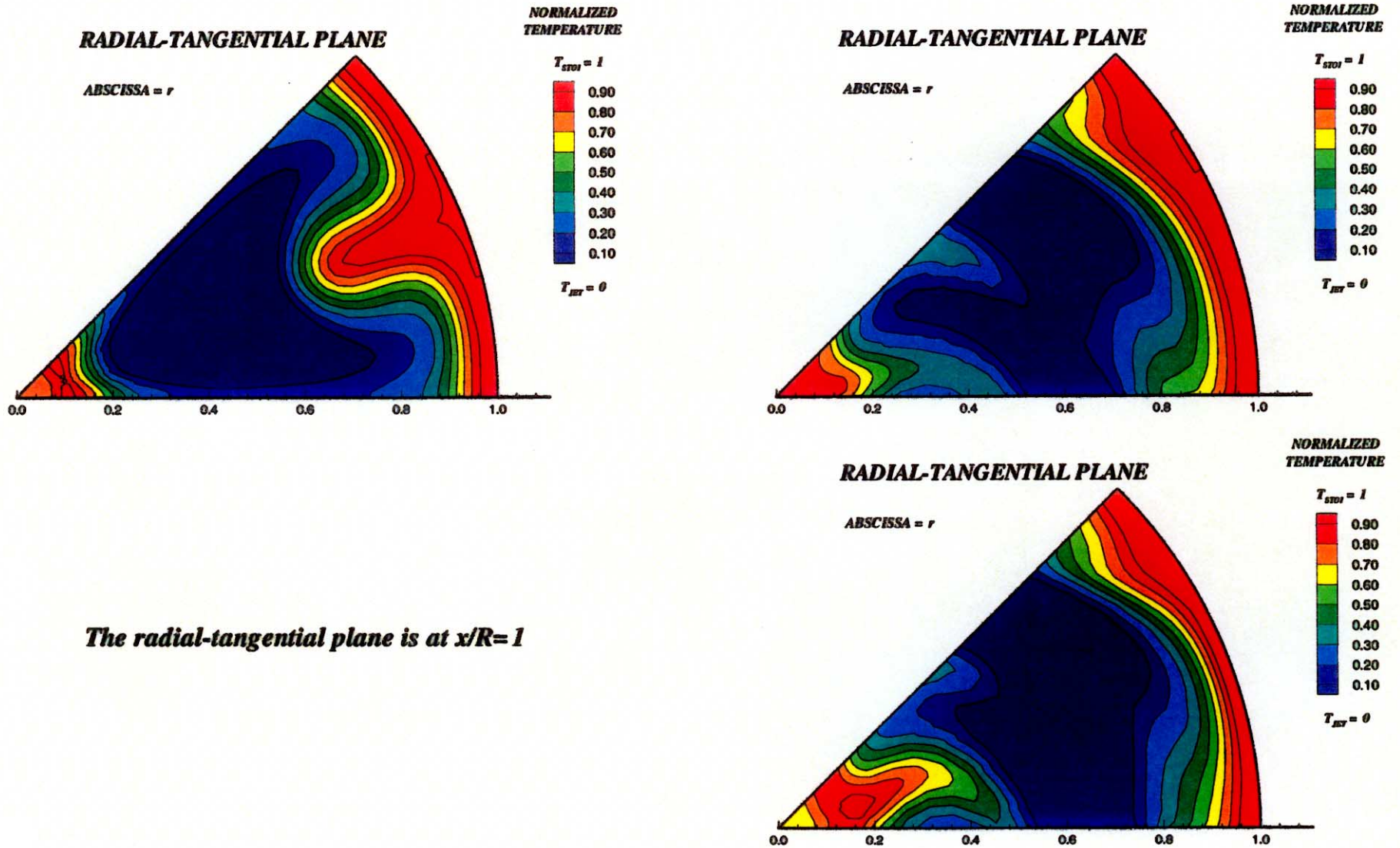
The radial-tangential plane is at x/R=1

Figure-B1-7. Effect of the change in orifice geometry on the temperature distribution
Clockwise from top left: round, 45° slot with L/W=4, and 45° slot with L/W=8
J=25, MR=2.96, DR=2.28, 8 orifices/row

RADIAL-TANGENTIAL PLANE

ABSCISSA = r

NORMALIZED
ϕ
MAINSTREAM = 1.0

0.90
0.80
0.70
0.60
0.50
0.40
0.30
0.20
0.10

JET = 0.0

RADIAL-TANGENTIAL PLANE

ABSCISSA = r

NORMALIZED
ϕ
MAINSTREAM = 1.0

0.90
0.80
0.70
0.60
0.50
0.40
0.30
0.20
0.10

JET = 0.0

The radial-tangential plane is at x/R= 1

RADIAL-TANGENTIAL PLANE

ABSCISSA = r

NORMALIZED
ϕ
MAINSTREAM = 1.0

0.90
0.80
0.70
0.60
0.50
0.40
0.30
0.20
0.10

JET = 0.0
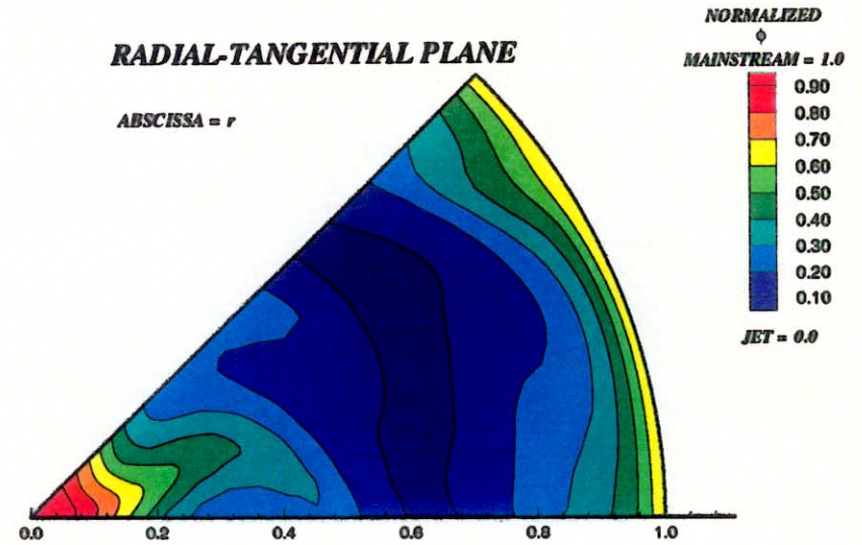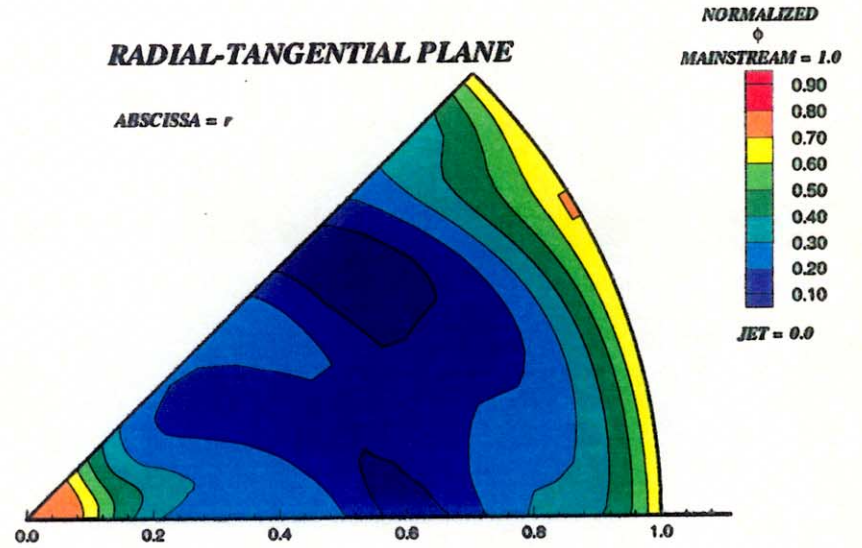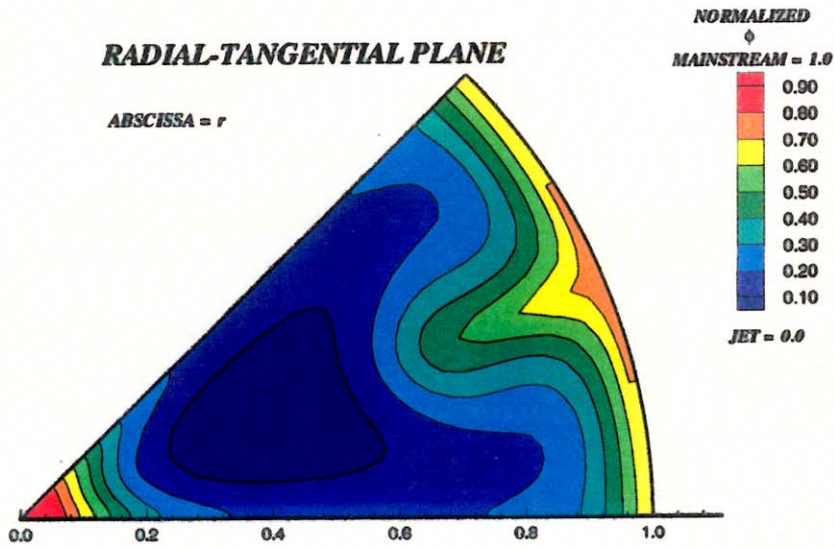
Figure-B1-8. Effect of the change in orifice geometry on the equivalence ratio distribution
Clockwise from top left: round, 45° slot with L/W=4, and 45° slot with L/W=8
J=25, MR=2.96, DR=2.28, 8 orifices/row

RADIAL-TANGENTIAL PLANE

ABSCISSA = r

RADIAL-TANGENTIAL PLANE

*ABSCISSA = r*

RADIAL-TANGENTIAL PLANE

ABSCISSA = r
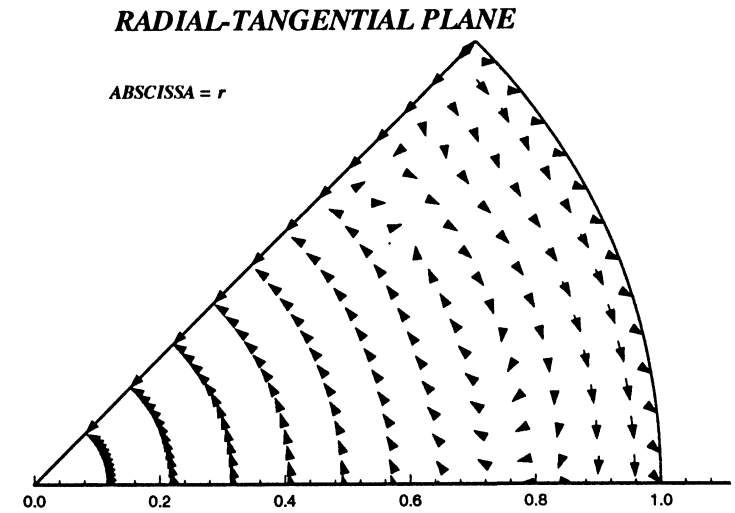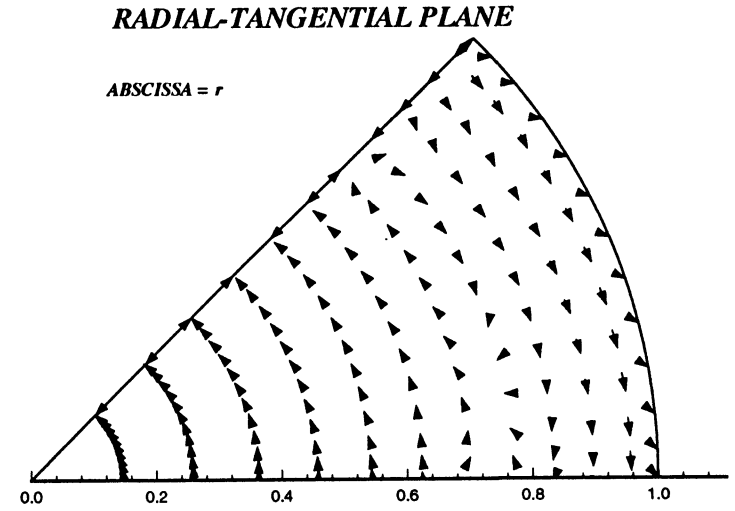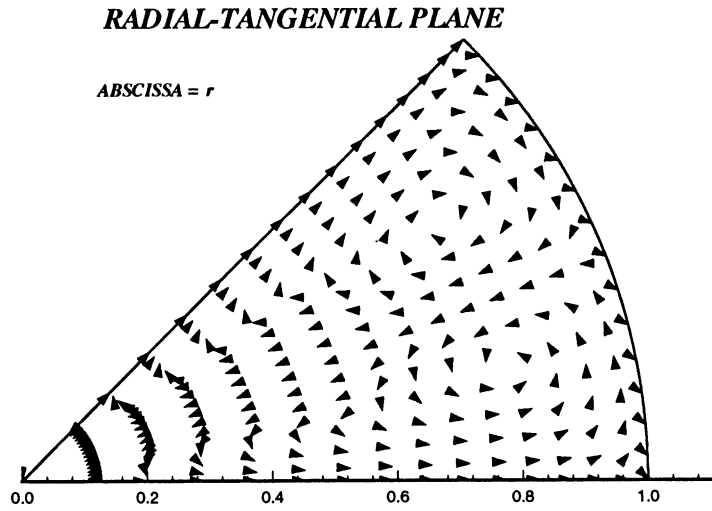
The radial-tangential plane is at x/R=1

Figure-B1-9. Effect of the change in orifice geometry on the velocity distribution
Clockwise from top left: round, 45° slot with L/W=4, and 45° slot with L/W=8
J=25, MR=2.96, DR=2.28, 8 orifices/row

AXIAL-TANGENTIAL PLANE

NORMALIZED TEMPERATURE

ABCSISSA = x/R
ORDINATE = z/S

$T_{STOI} = 1$

0.90
0.80
0.70
0.60
0.50
0.40
0.30
0.20
0.10

$T_{JET} = 0$

AXIAL-TANGENTIAL PLANE

NORMALIZED TEMPERATURE

ABCSISSA = x/R
ORDINATE = z/S

$T_{STOI} = 1$

0.90
0.80
0.70
0.60
0.50
0.40
0.30
0.20
0.10

$T_{JET} = 0$

The axial-tangential plane is nearest the outer wall of the mixer

AXIAL-TANGENTIAL PLANE

NORMALIZED TEMPERATURE

ABCSISSA = x/R
ORDINATE = z/S

$T_{STOI} = 1$

0.90
0.80
0.70
0.60
0.50
0.40
0.30
0.20
0.10

$T_{JET} = 0$
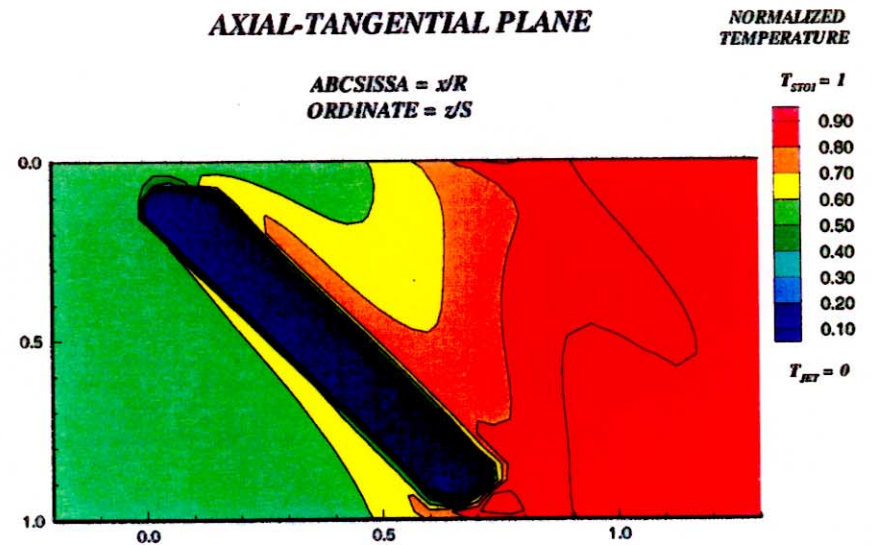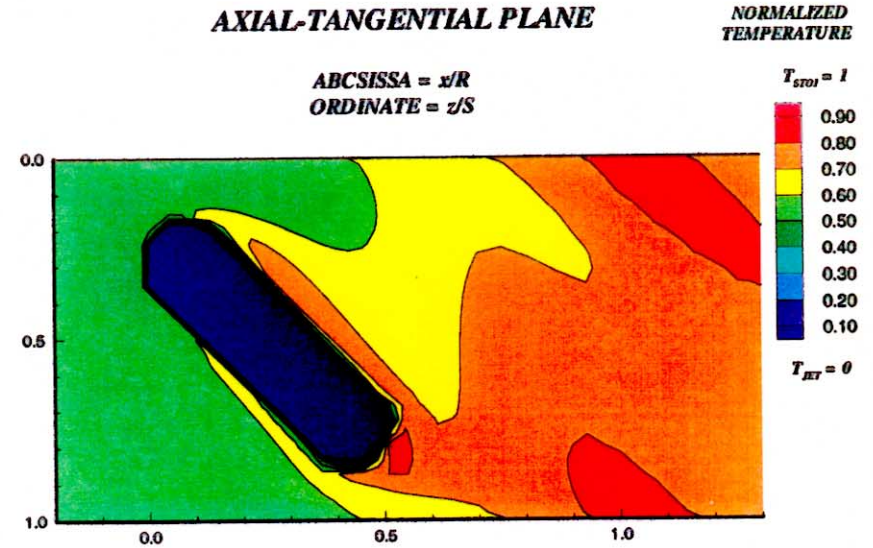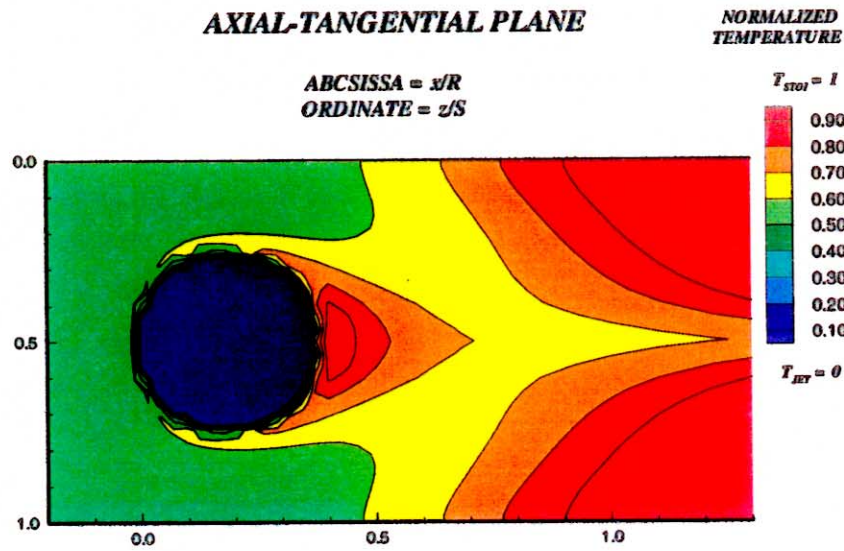
Figure-B2-1. Effect of the change in orifice geometry on the temperature distribution
Clockwise from top left: round, 45° slot with L/W=4, and 45° slot with L/W=8
J=52, MR=2.96, DR=2.28, 8 orifices/row

AXIAL-TANGENTIAL PLANE

ABCSISSA = x/R
ORDINATE = z/S

NORMALIZED
φ
MAINSTREAM = 1.0

JET = 0.0

AXIAL-TANGENTIAL PLANE

ABCSISSA = x/R
ORDINATE = z/S

NORMALIZED
φ
MAINSTREAM = 1.0

JET = 0.0

AXIAL-TANGENTIAL PLANE

ABCSISSA = x/R
ORDINATE = z/S

NORMALIZED
φ
MAINSTREAM = 1.0

JET = 0.0
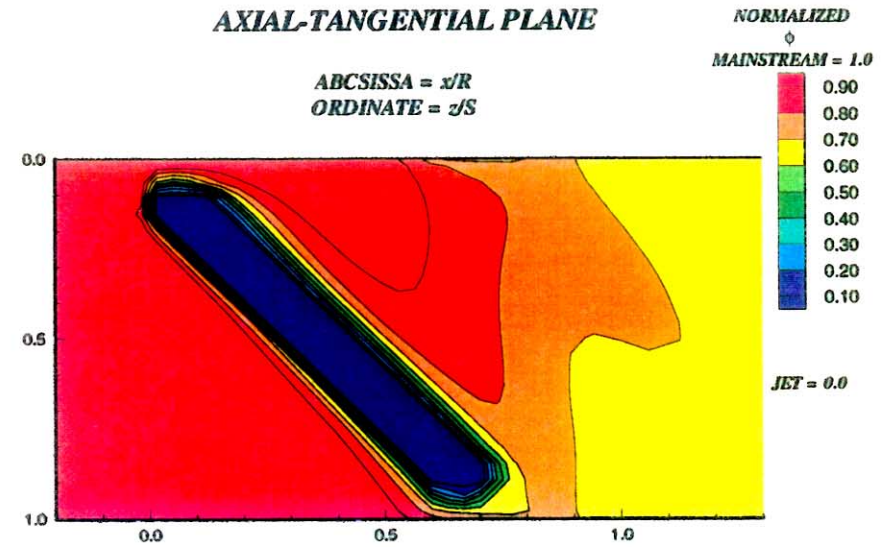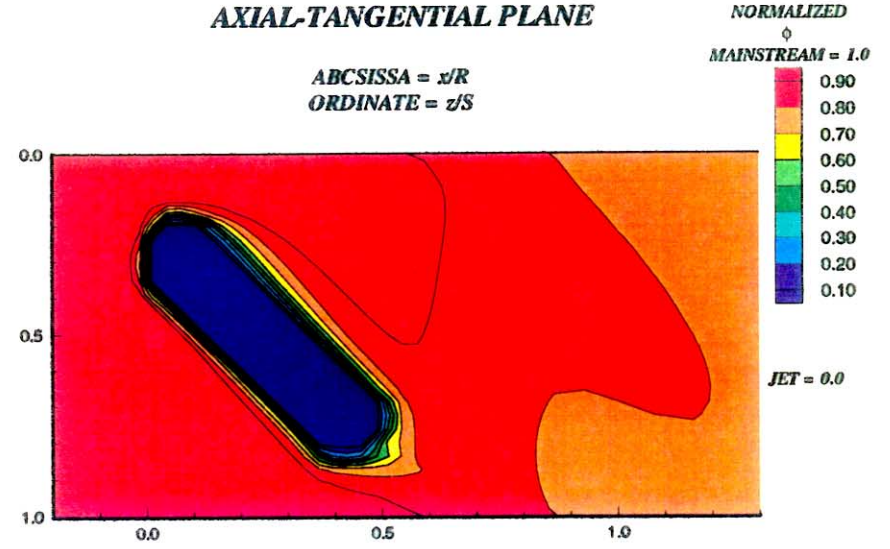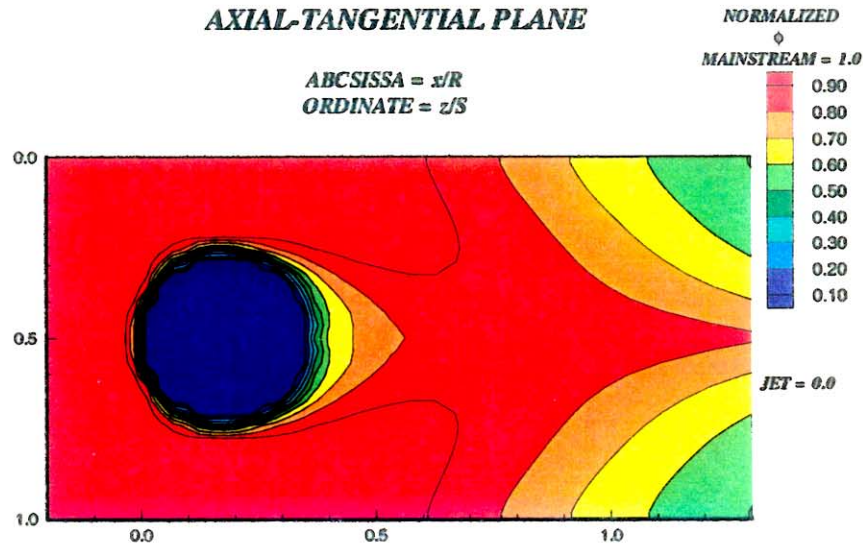
The axial-tangential plane is nearest the outer wall of the mixer

Figure-B2-2. Effect of the change in orifice geometry on the equivalence ratio distribution
Clockwise from top left: round, 45° slot with L/W=4, and 45° slot with L/W=8
J=52, MR=2.96, DR=2.28, 8 orifices/row

AXIAL-TANGENTIAL PLANE

ABCSISSA = x/R
ORDINATE = z/S

AXIAL-TANGENTIAL PLANE

ABCSISSA = x/R
ORDINATE = z/S

AXIAL-TANGENTIAL PLANE

ABCSISSA = x/R
ORDINATE = z/S
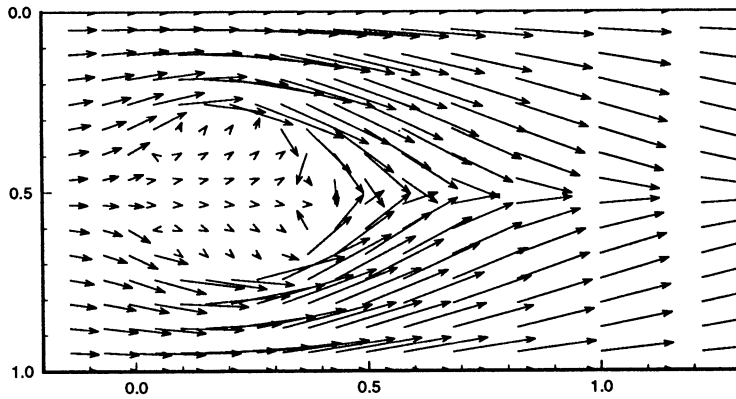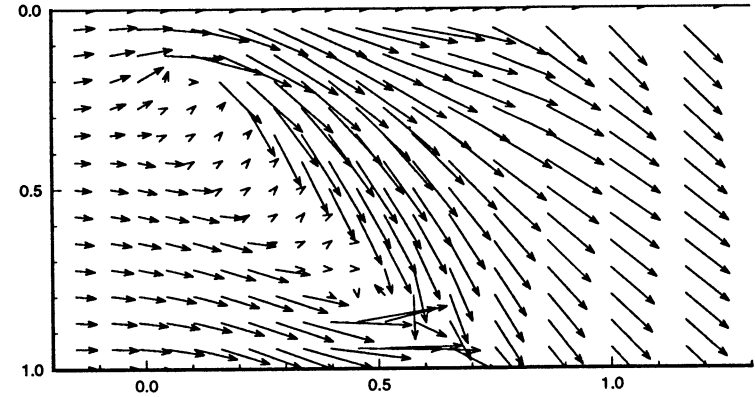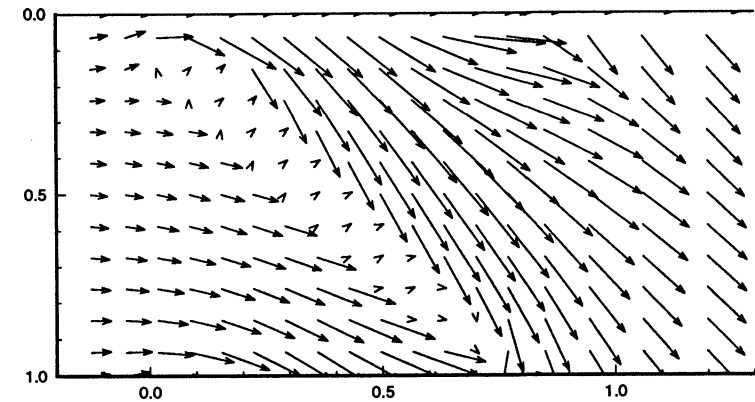
The axial-tangential plane is nearest the outer wall of the mixer

*Figure-B2-3. Effect of the change in orifice geometry on the velocity distribution*
*Clockwise from top left: round, 45° slot with L/W= 4, and 45° slot with L/W= 8*
J= 52, MR= 2.96, DR= 2.28, 8 orifices/row

AXIAL-RADIAL PLANE

ABSCISSA = x/R
ORDINATE = r

NORMALIZED
TEMPERATURE

$T_{STOI} = 1$
0.90
0.80
0.70
0.60
0.50
0.40
0.30
0.20
0.10

$T_{JET} = 0$

AXIAL-RADIAL PLANE

ABSCISSA = x/R
ORDINATE = r

NORMALIZED
TEMPERATURE

$T_{STOI} = 1$
0.90
0.80
0.70
0.60
0.50
0.40
0.30
0.20
0.10

$T_{JET} = 0$

The axial-radial plane is through the center of the jet

AXIAL-RADIAL PLANE

ABSCISSA = x/R
ORDINATE = r

NORMALIZED
TEMPERATURE

$T_{STOI} = 1$
0.90
0.80
0.70
0.60
0.50
0.40
0.30
0.20
0.10

$T_{JET} = 0$
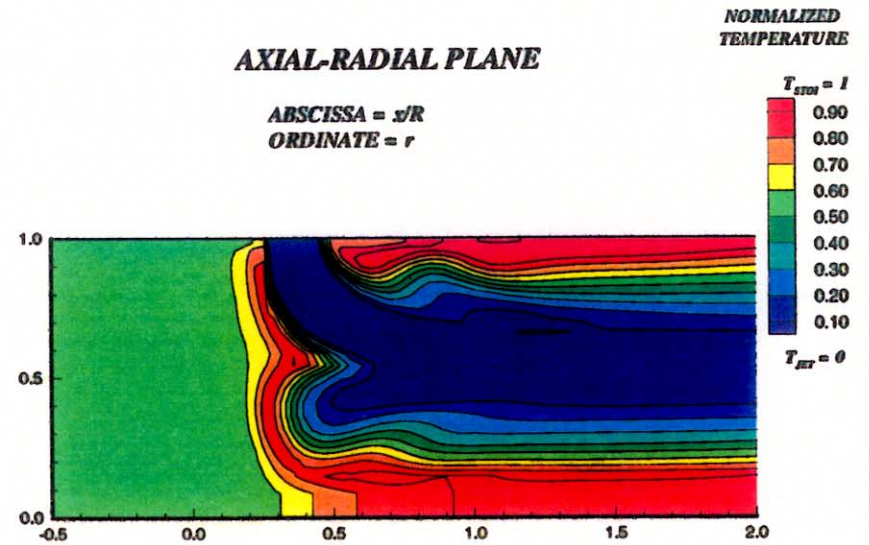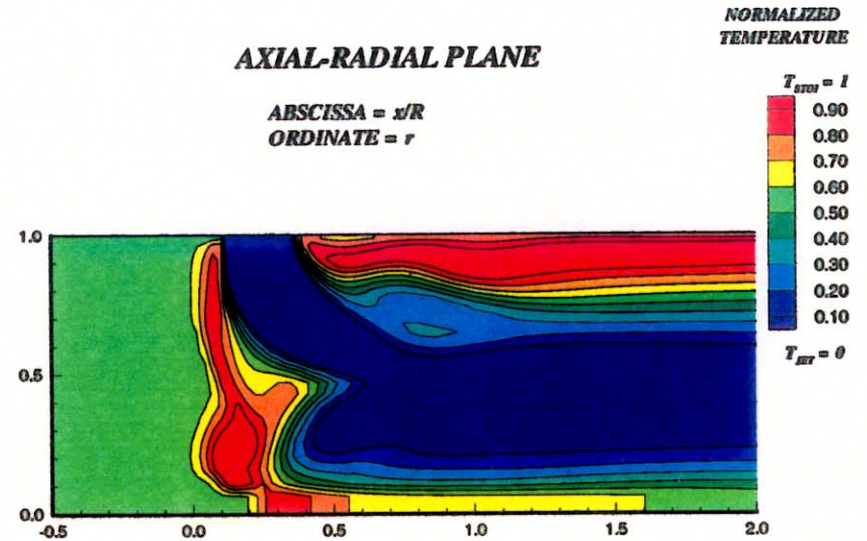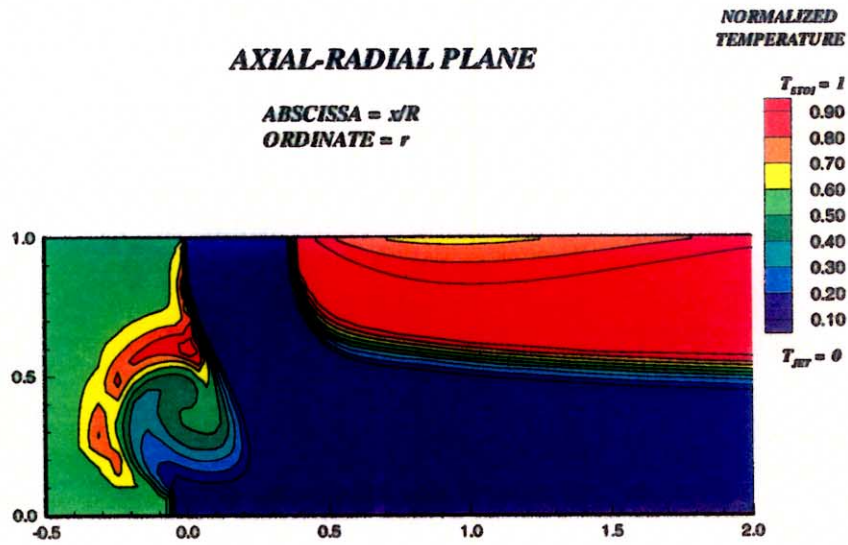
Figure-B2-4. Effect of the change in orifice geometry on the temperature distribution
Clockwise from top left: round, 45° slot with L/W=4, and 45° slot with L/W=8
*J=52, MR=2.96, DR=2.28, 8 orifices/row*
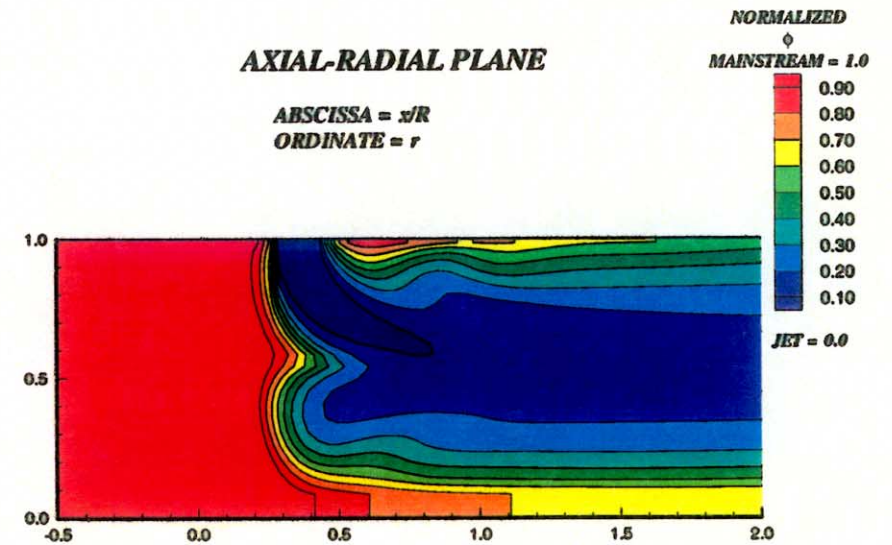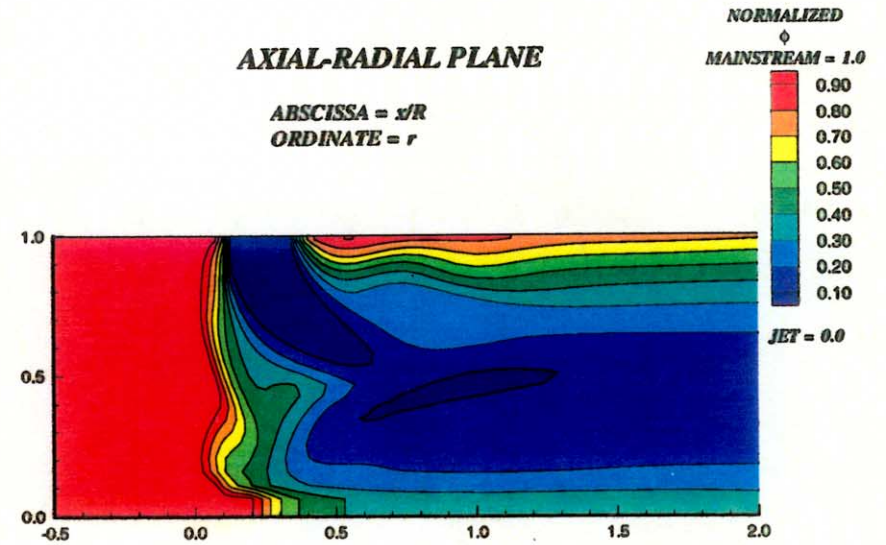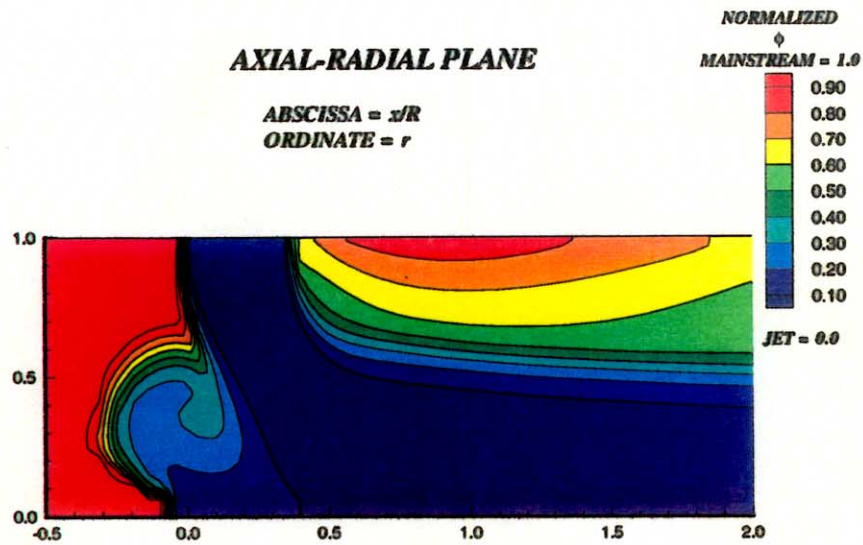
The axial-radial plane is through the center of the jet

Figure-B2-5. Effect of the change in orifice geometry on the equivalence ratio distribution Clockwise from top left: round, 45° slot with L/W=4, and 45° slot with L/W=8 J=52, MR=2.96, DR=2.28, 8 orifices/row

AXIAL-RADIAL PLANE

ABSCISSA = x/R
ORDINATE = r
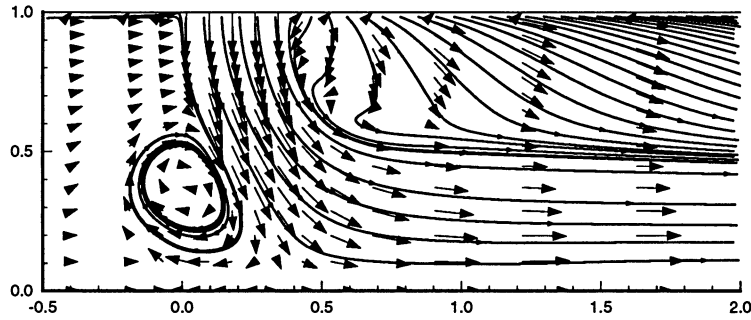
AXIAL-RADIAL PLANE

ABSCISSA = x/R
ORDINATE = r
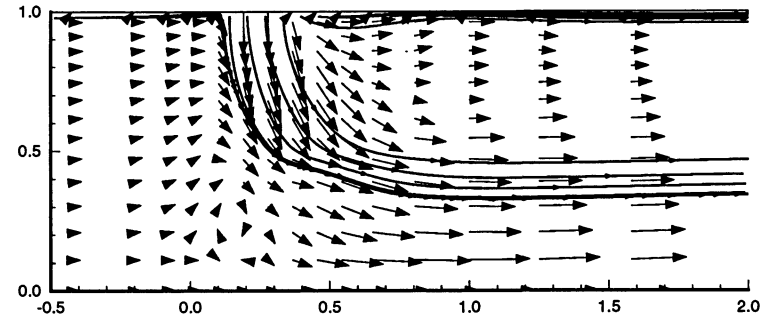
*AXIAL-RADIAL PLANE*

ABSCISSA = x/R
ORDINATE = r
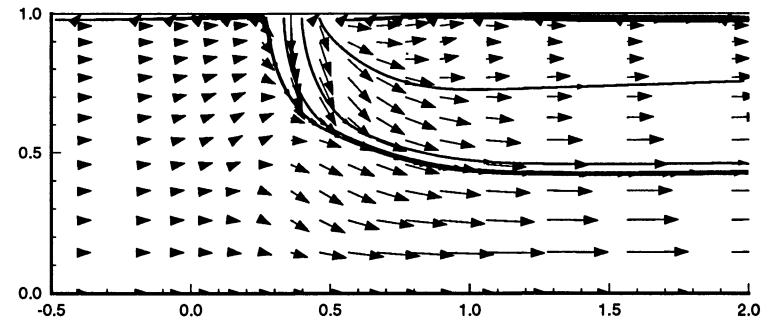
The axial-radial plane is through the center of the jet

Figure-B2-6. Effect of the change in orifice geometry on the velocity distribution
Clockwise from top left: round, 45° slot with L/W=4, and 45° slot with L/W=8
J=52, MR=2.96, DR=2.28, 8 orifices/row
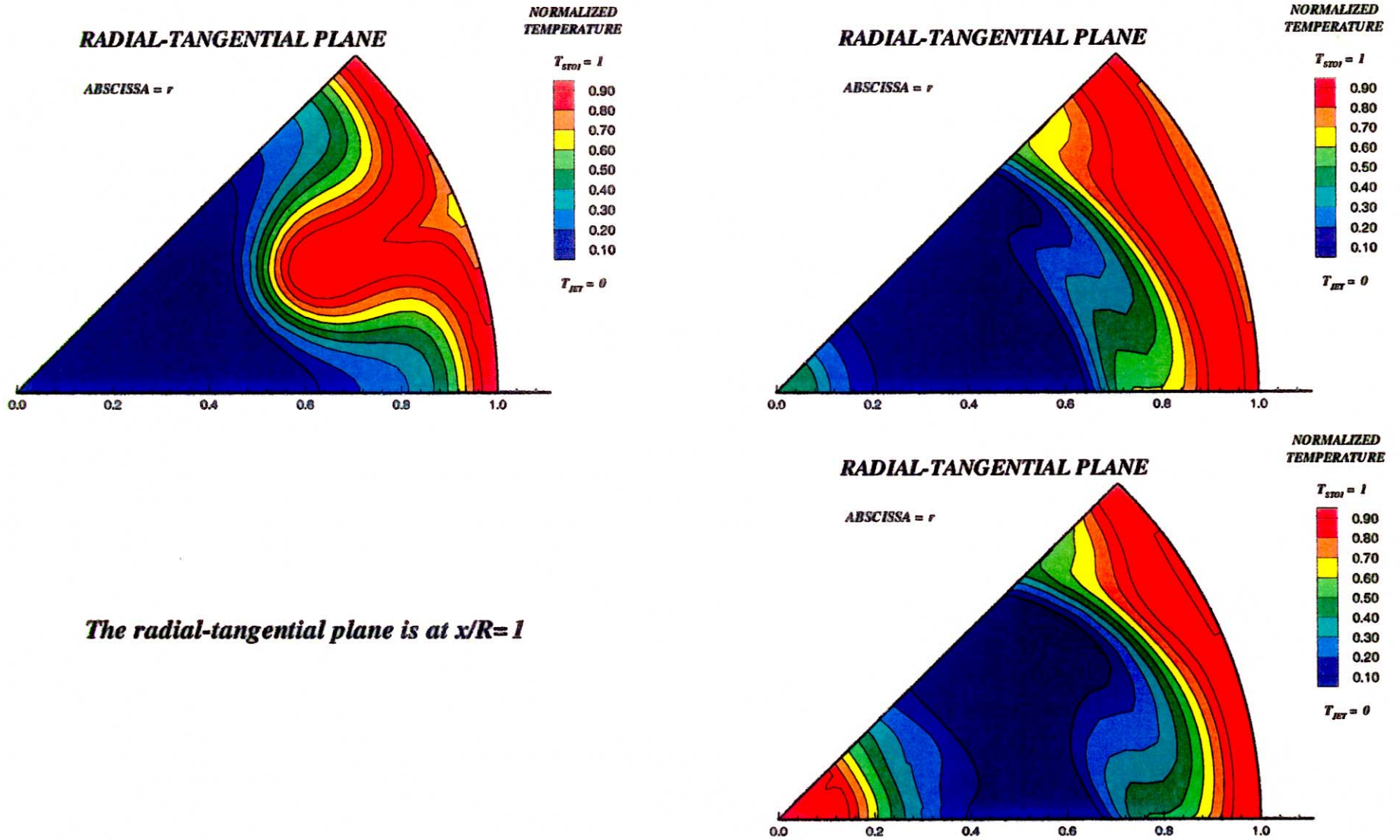
Figure-B2-7. Effect of the change in orifice geometry on the temperature distribution
Clockwise from top left: round, 45° slot with L/W=4, and 45° slot with L/W=8
J=52, MR=2.96, DR=2.28, 8 orifices/row
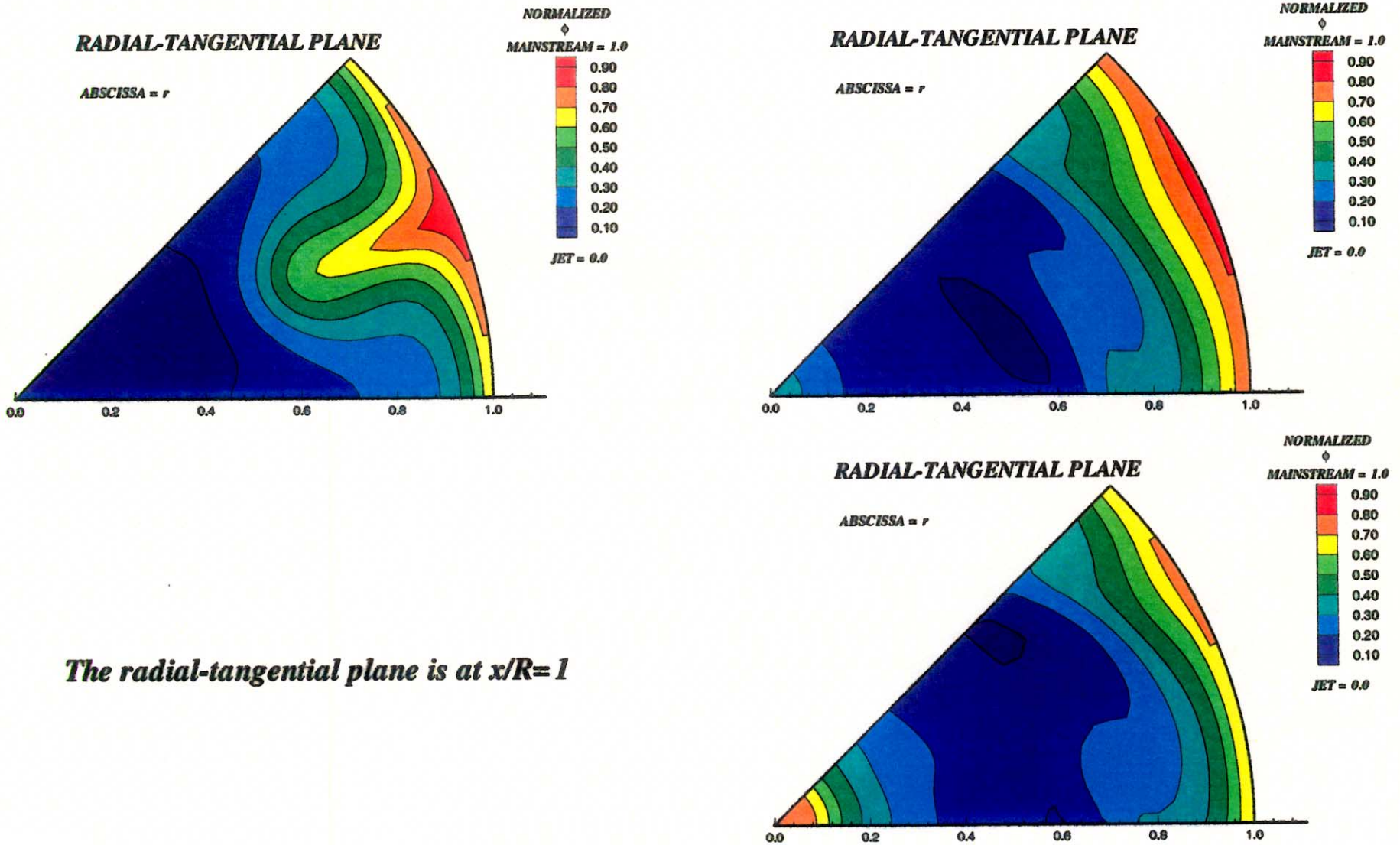
The radial-tangential plane is at x/R=1

Figure-B2-8. Effect of the change in orifice geometry on the equivalence ratio distribution
Clockwise from top left: round, 45° slot with L/W=4, and 45° slot with L/W=8
J=52, MR=2.96, DR=2.28, 8 orifices/row

RADIAL-TANGENTIAL PLANE

ABSCISSA = r

0.0   0.2   0.4   0.6   0.8   1.0

RADIAL-TANGENTIAL PLANE

ABSCISSA = r

0.0   0.2   0.4   0.6   0.8   1.0

RADIAL-TANGENTIAL PLANE

ABSCISSA = r

0.0   0.2   0.4   0.6   0.8   1.0
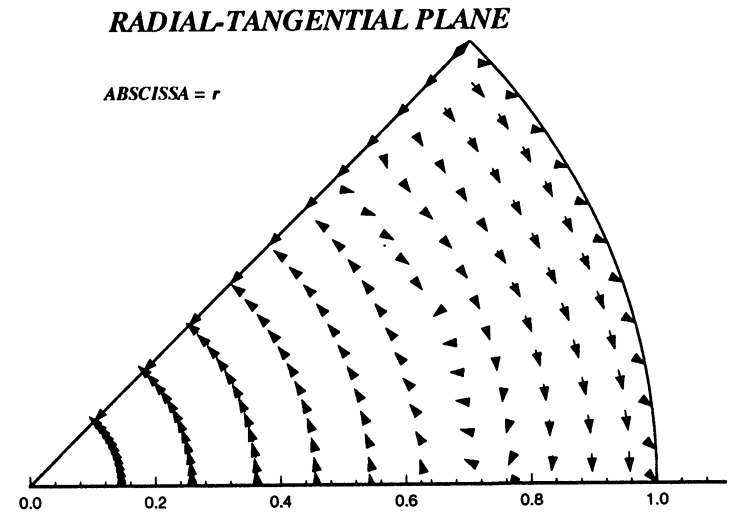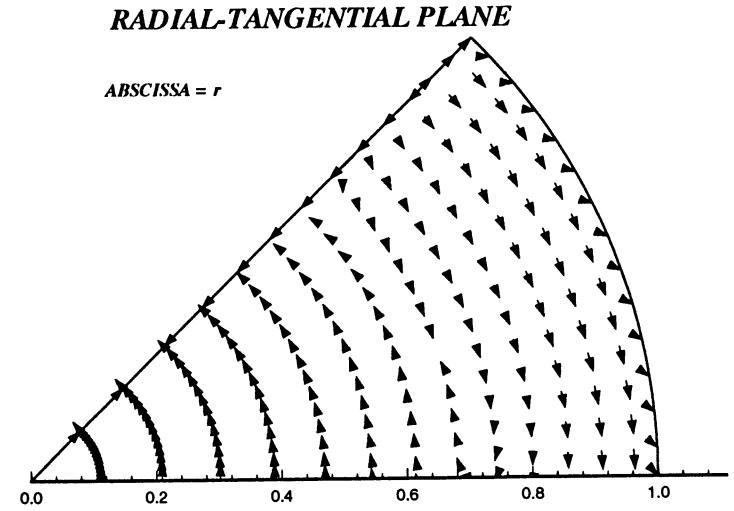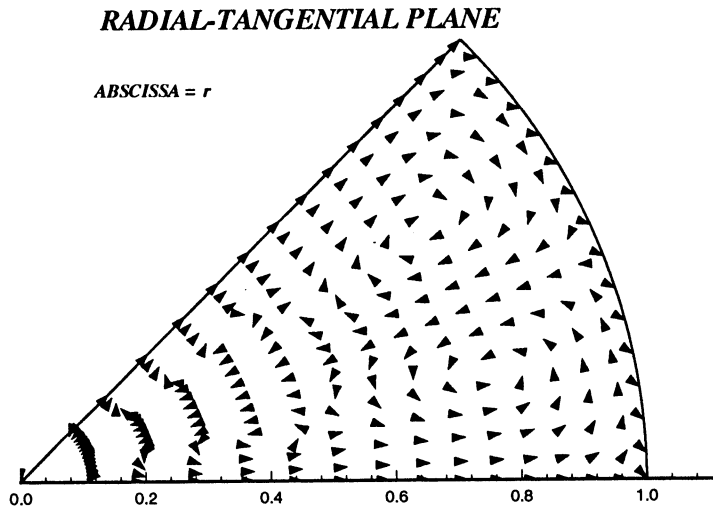
The radial-tangential plane is at x/R=1

Figure-B2-9. Effect of the change in orifice geometry on the velocity distribution
Clockwise from top left: round, 45° slot with L/W=4, and 45° slot with L/W=8
J=52, MR=2.96, DR=2.28, 8 orifices/row

AXIAL-TANGENTIAL PLANE

NORMALIZED TEMPERATURE

ABCSISSA = x/R
ORDINATE = z/S

$T_{STOI} = 1$

| 0.90 |
| 0.80 |
| 0.70 |
| 0.60 |
| 0.50 |
| 0.40 |
| 0.30 |
| 0.20 |
| 0.10 |

$T_{JET} = 0$

AXIAL-TANGENTIAL PLANE

NORMALIZED TEMPERATURE

ABCSISSA = x/R
ORDINATE = z/S

$T_{STOI} = 1$

| 0.90 |
| 0.80 |
| 0.70 |
| 0.60 |
| 0.50 |
| 0.40 |
| 0.30 |
| 0.20 |
| 0.10 |

$T_{JET} = 0$

The axial-tangential plane is nearest the outer wall of the mixer

AXIAL-TANGENTIAL PLANE

NORMALIZED TEMPERATURE

ABCSISSA = x/R
ORDINATE = z/S

$T_{STOI} = 1$

| 0.90 |
| 0.80 |
| 0.70 |
| 0.60 |
| 0.50 |
| 0.40 |
| 0.30 |
| 0.20 |
| 0.10 |

$T_{JET} = 0$
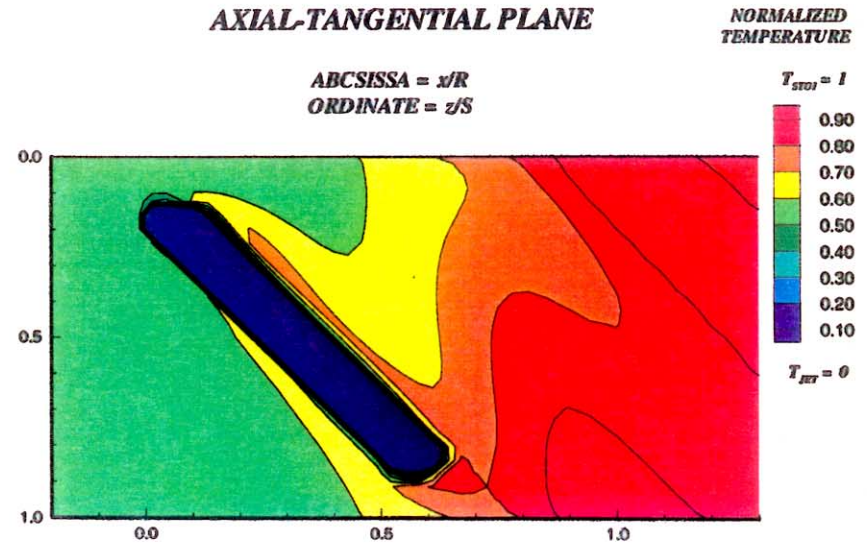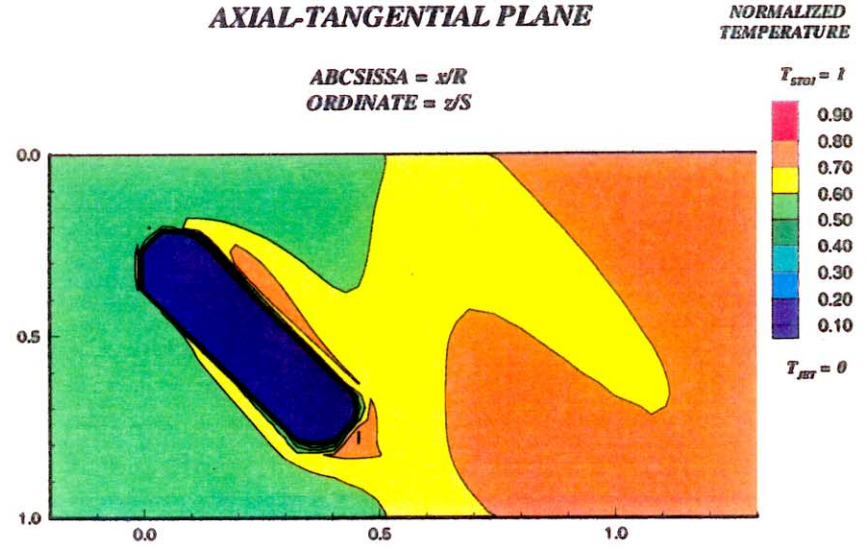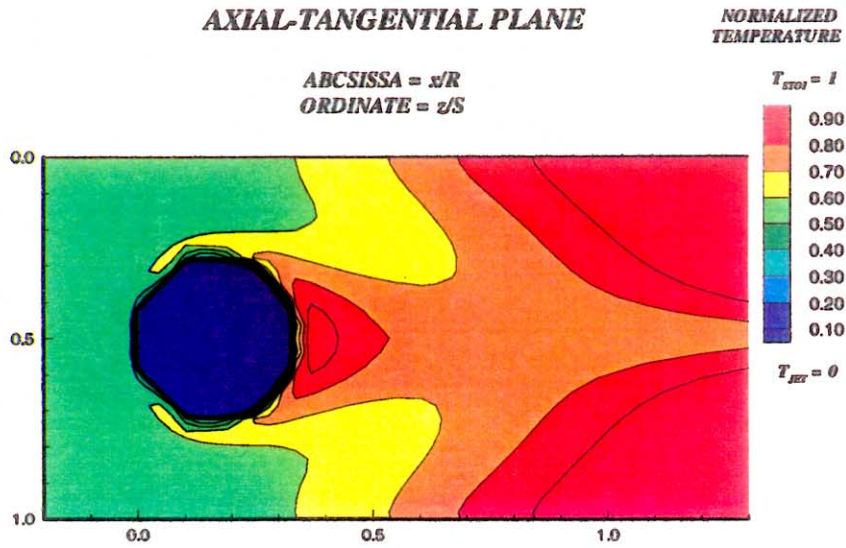
Figure-B3-1. Effect of the change in orifice geometry on the temperature distribution
Clockwise from top left: round, 45° slot with L/W=4, and 45° slot with L/W=8
J=80, MR=2.96, DR=2.28, 8 orifices/row
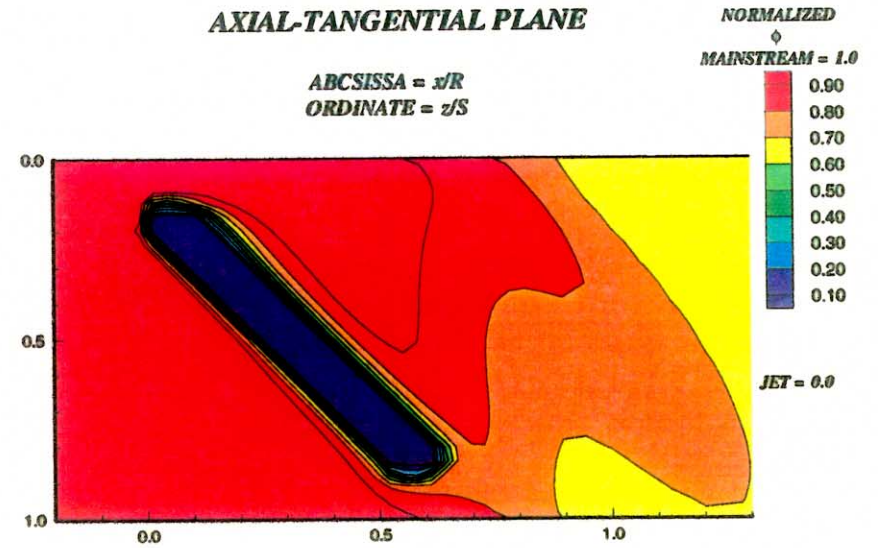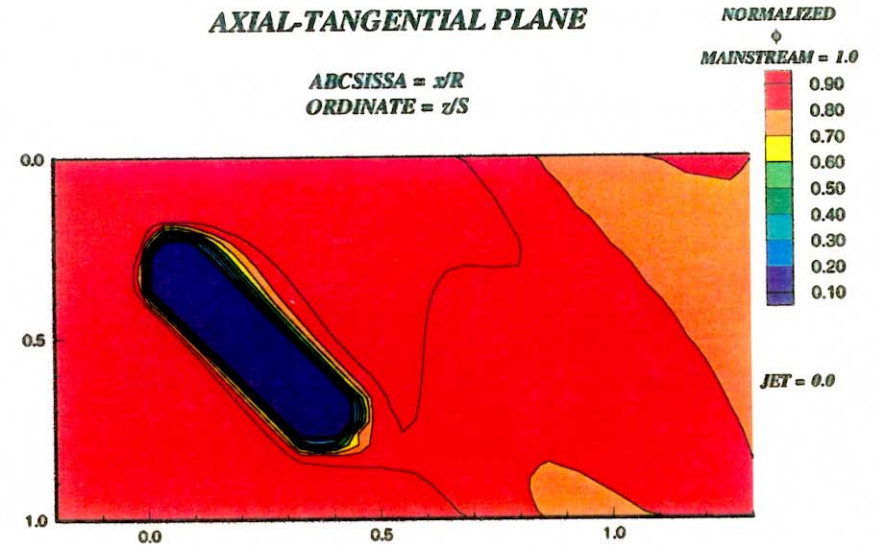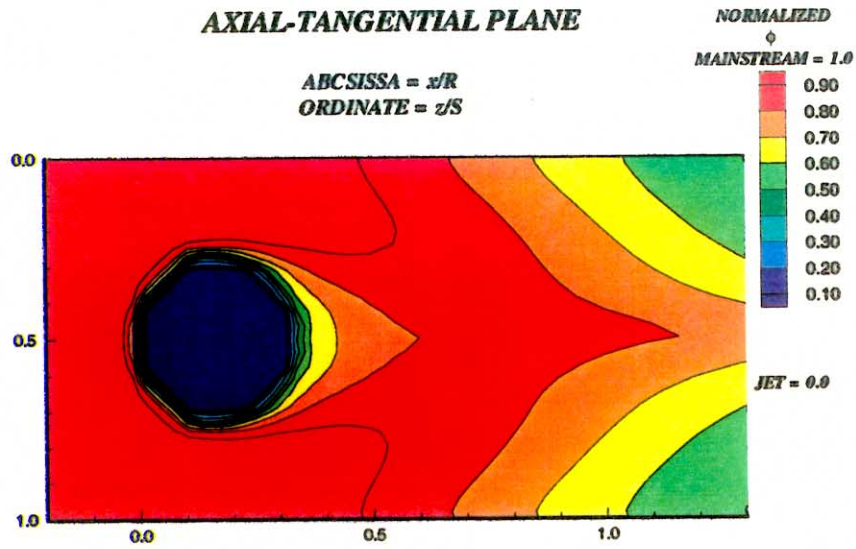
The axial-tangential plane is nearest the outer wall of the mixer

Figure-B3-2. Effect of the change in orifice geometry on the equivalence ratio distribution
Clockwise from top left: round, 45° slot with L/W=4, and 45° slot with L/W=8
J=80, MR=2.96, DR=2.28, 8 orifices/row

AXIAL-TANGENTIAL PLANE

ABCSISSA = x/R
ORDINATE = z/S

AXIAL-TANGENTIAL PLANE

ABCSISSA = x/R
ORDINATE = z/S

AXIAL-TANGENTIAL PLANE

ABCSISSA = x/R
ORDINATE = z/S
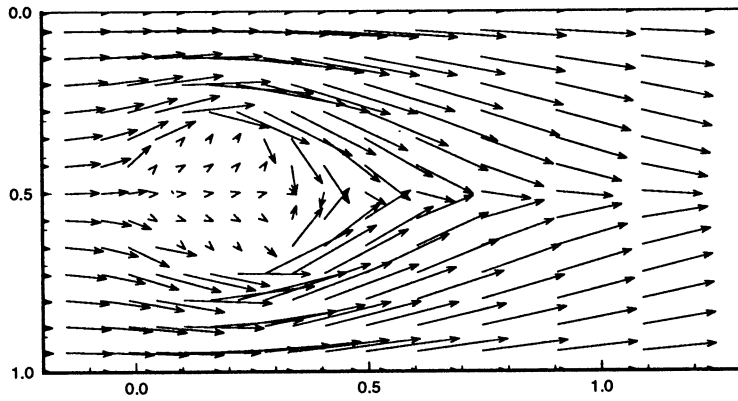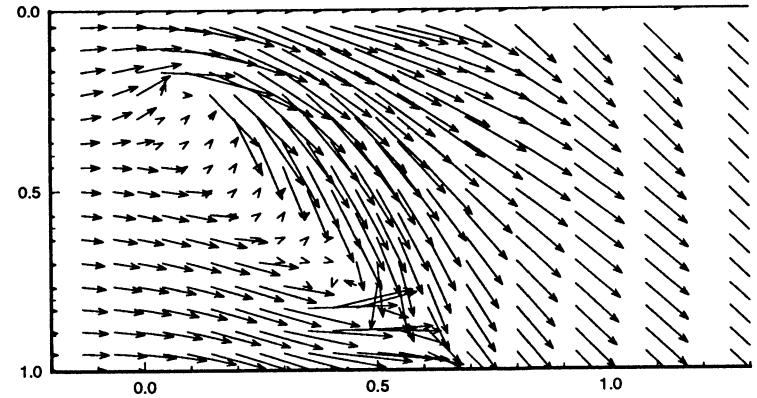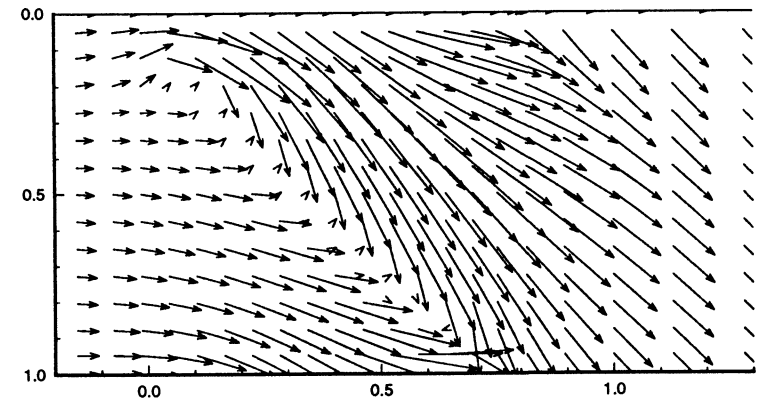
*The axial-tangential plane is nearest the outer wall of the mixer*

Figure-B3-3. Effect of the change in orifice geometry on the velocity distribution Clockwise from top left: round, 45° slot with L/W=4, and 45° slot with L/W=8 J=80, MR=2.96, DR=2.28, 8 orifices/row

AXIAL-RADIAL PLANE

ABSCISSA = x/R
ORDINATE = r

NORMALIZED
TEMPERATURE

$T_{STOI} = 1$

0.90
0.80
0.70
0.60
0.50
0.40
0.30
0.20
0.10

$T_{JET} = 0$

AXIAL-RADIAL PLANE

ABSCISSA = x/R
ORDINATE = r

NORMALIZED
TEMPERATURE

$T_{STOI} = 1$

0.90
0.80
0.70
0.60
0.50
0.40
0.30
0.20
0.10

$T_{JET} = 0$

*The axial-radial plane is through the
center of the jet*

AXIAL-RADIAL PLANE

ABSCISSA = x/R
ORDINATE = r

NORMALIZED
TEMPERATURE

$T_{STOI} = 1$

0.90
0.80
0.70
0.60
0.50
0.40
0.30
0.20
0.10

$T_{JET} = 0$
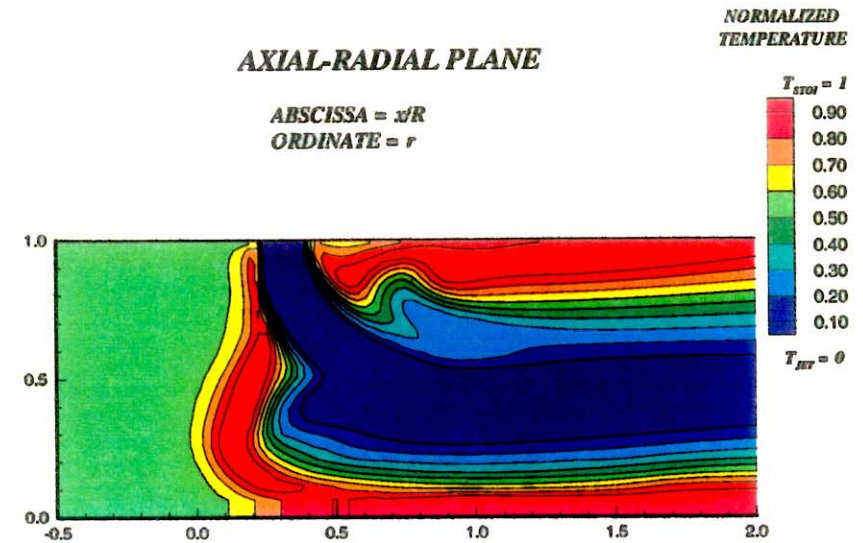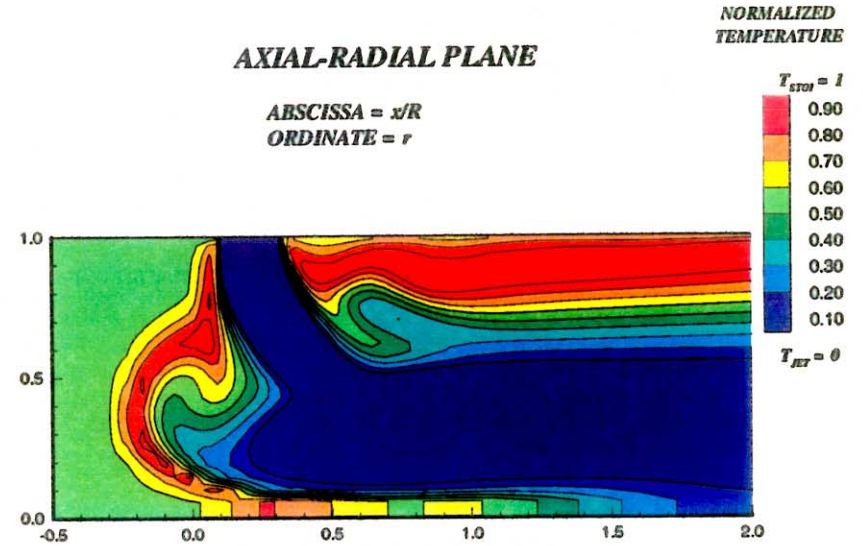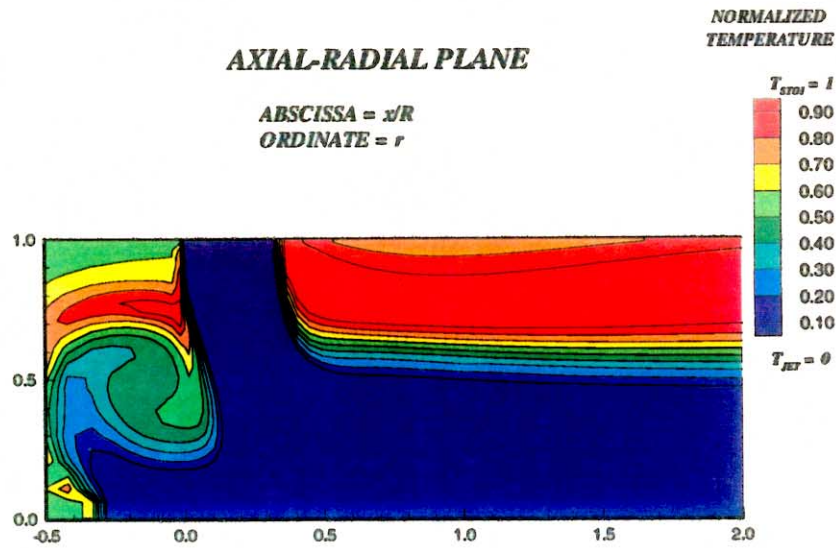
*Figure-B3-4. Effect of the change in orifice geometry on the temperature distribution
Clockwise from top left: round, 45° slot with L/W=4, and 45° slot with L/W=8
J=80, MR=2.96, DR=2.28, 8 orifices/row*

AXIAL-RADIAL PLANE

ABSCISSA = x/R
ORDINATE = r
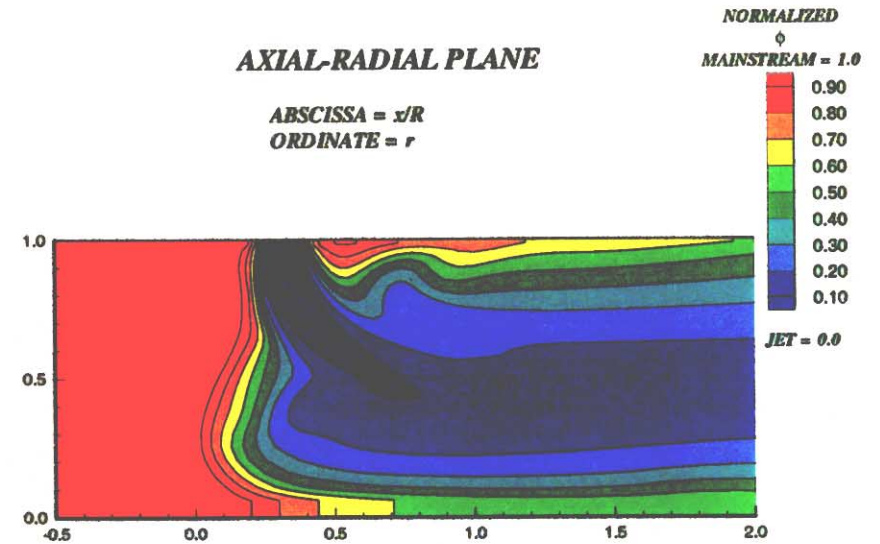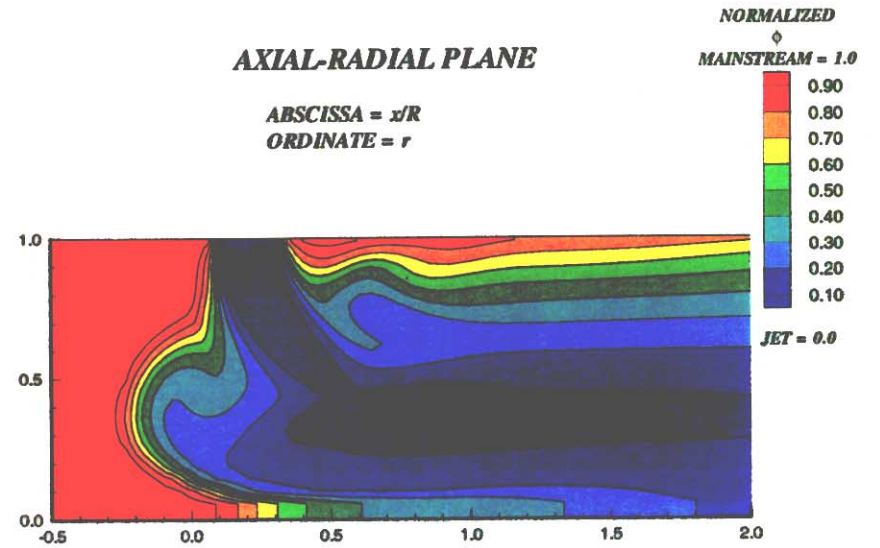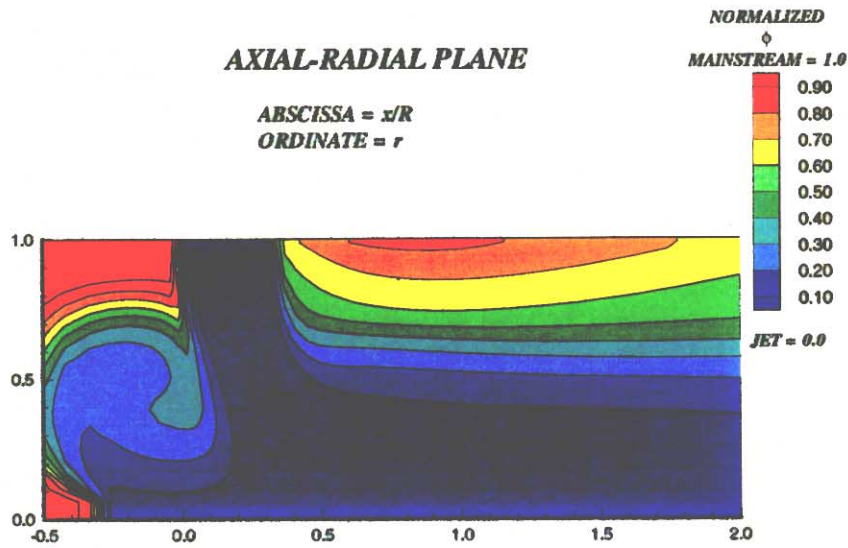
The axial-radial plane is through the center of the jet

Figure-B3-5. Effect of the change in orifice geometry on the equivalence ratio distribution
Clockwise from top left: round, 45° slot with L/W=4, and 45° slot with L/W=8
J=80, MR=2.96, DR=2.28, 8 orifices/row

AXIAL-RADIAL PLANE

ABSCISSA = x/R
ORDINATE = r
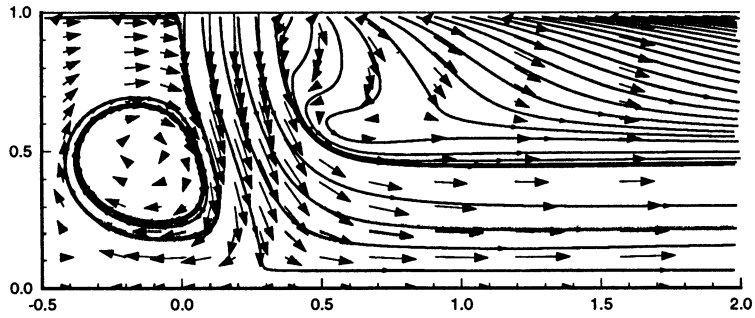
AXIAL-RADIAL PLANE

ABSCISSA = x/R
ORDINATE = r
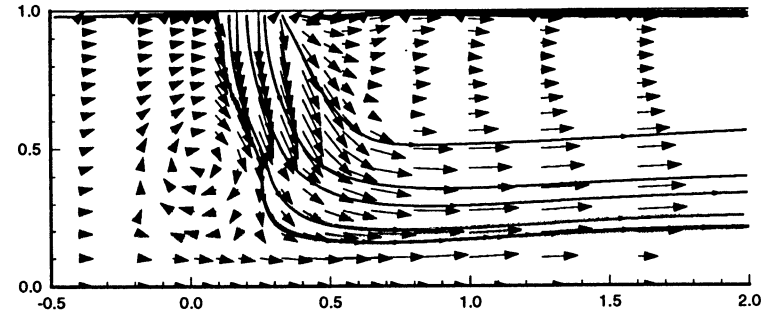
AXIAL-RADIAL PLANE

ABSCISSA = x/R
ORDINATE = r
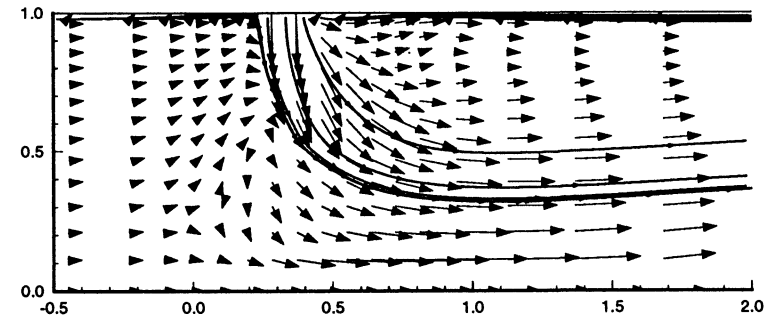
The axial-radial plane is through the center of the jet

Figure-B3-6. Effect of the change in orifice geometry on the velocity distribution Clockwise from top left: round, 45° slot with L/W=4, and 45° slot with L/W=8 J=80, MR=2.96, DR=2.28, 8 orifices/row

RADIAL-TANGENTIAL PLANE

ABSCISSA = r

NORMALIZED TEMPERATURE

$T_{SLOT} = 1$

0.90
0.80
0.70
0.60
0.50
0.40
0.30
0.20
0.10

$T_{JET} = 0$

RADIAL-TANGENTIAL PLANE

ABSCISSA = r

NORMALIZED TEMPERATURE

$T_{SLOT} = 1$

0.90
0.80
0.70
0.60
0.50
0.40
0.30
0.20
0.10

$T_{JET} = 0$

The radial-tangential plane is at x/R=1

RADIAL-TANGENTIAL PLANE

ABSCISSA = r

NORMALIZED TEMPERATURE

$T_{SLOT} = 1$

0.90
0.80
0.70
0.60
0.50
0.40
0.30
0.20
0.10

$T_{JET} = 0$
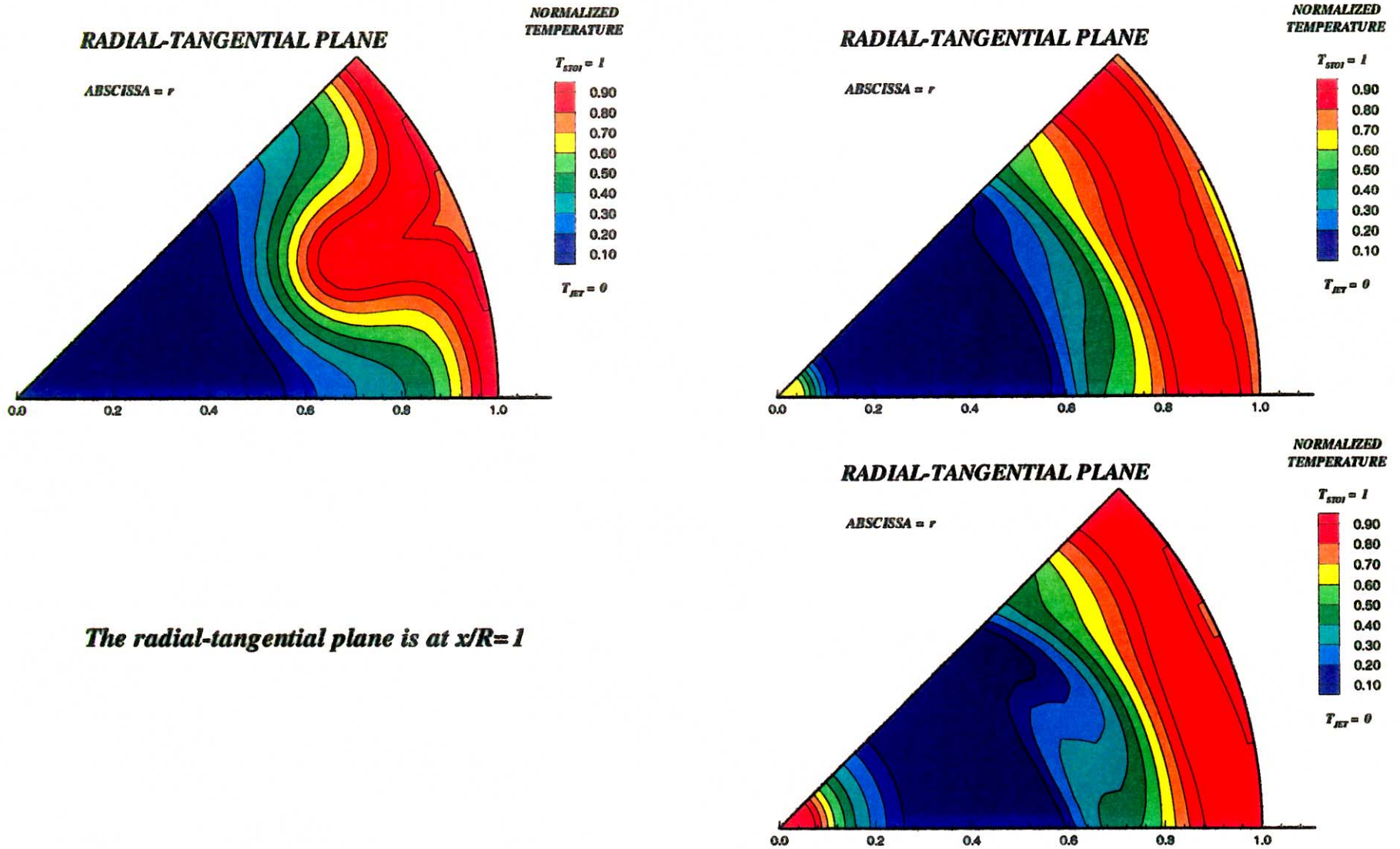
Figure-B3-7. Effect of the change in orifice geometry on the temperature distribution
Clockwise from top left: round, 45° slot with L/W=4, and 45° slot with L/W=8
J=80, MR=2.96, DR=2.28, 8 orifices/row

The radial-tangential plane is at x/R=1
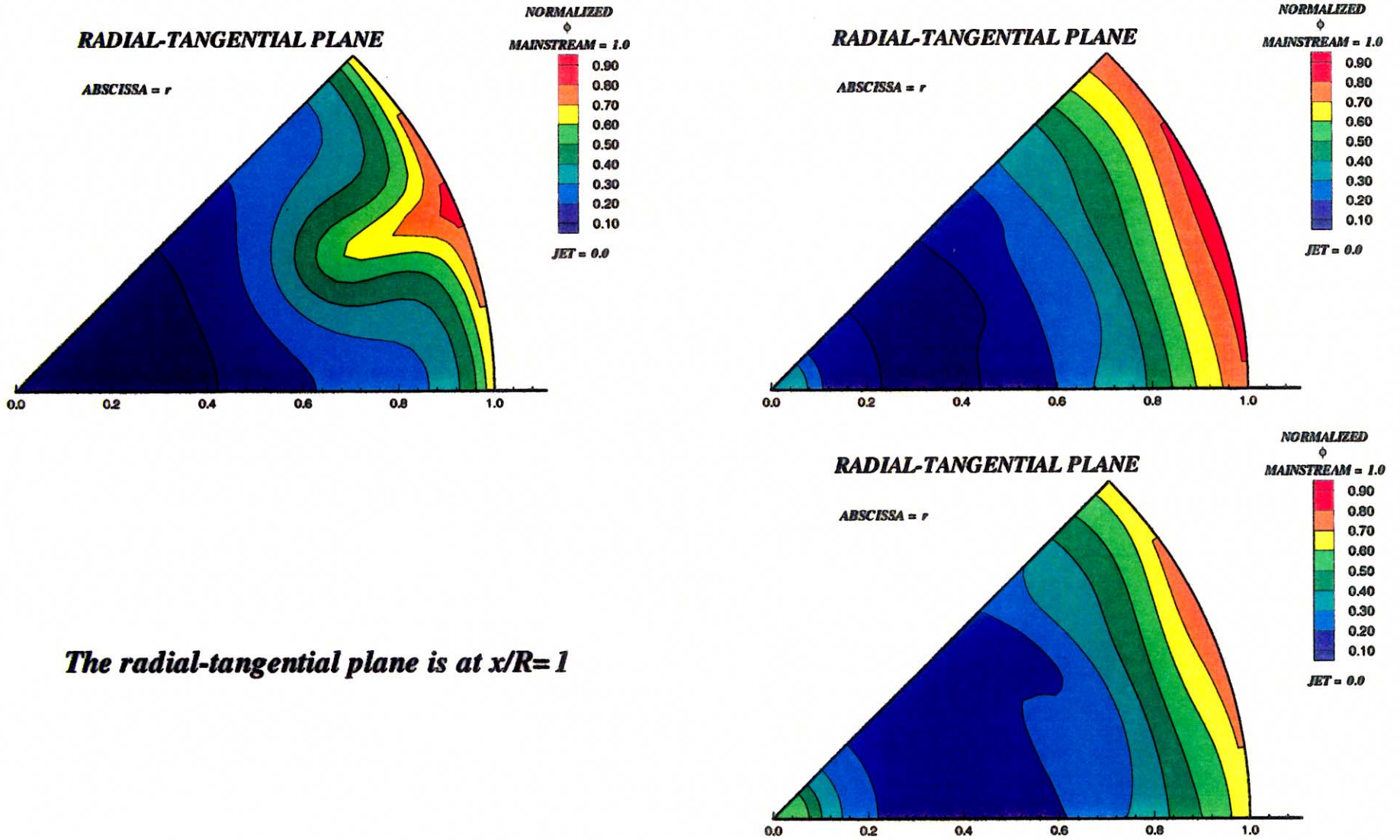
Figure-B3-8. Effect of the change in orifice geometry on the equivalence ratio distribution
Clockwise from top left: round, 45° slot with L/W=4, and 45° slot with L/W=8
J=80, MR=2.96, DR=2.28, 8 orifices/row

RADIAL-TANGENTIAL PLANE

ABSCISSA = r

RADIAL-TANGENTIAL PLANE

ABSCISSA = r

RADIAL-TANGENTIAL PLANE

ABSCISSA = r
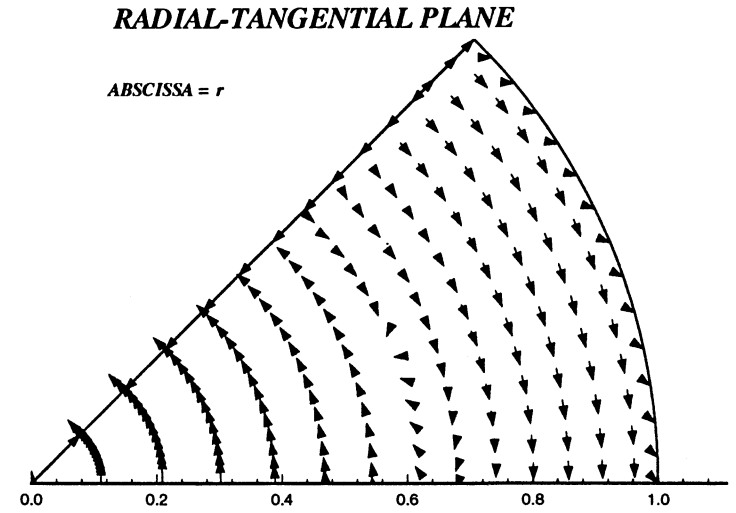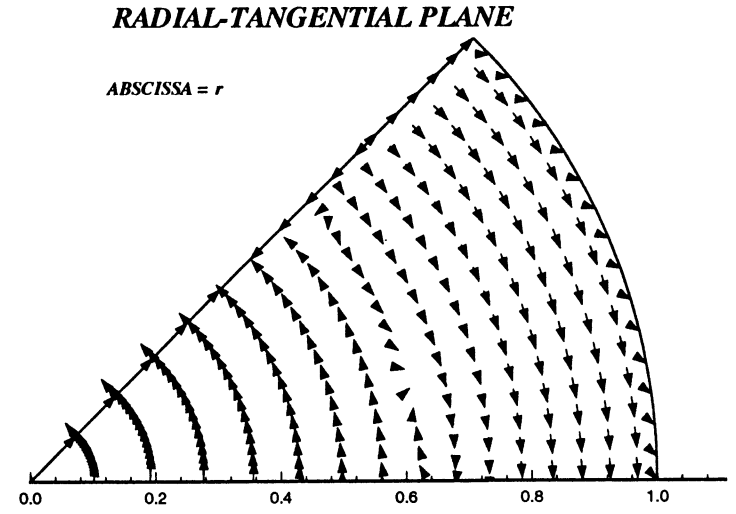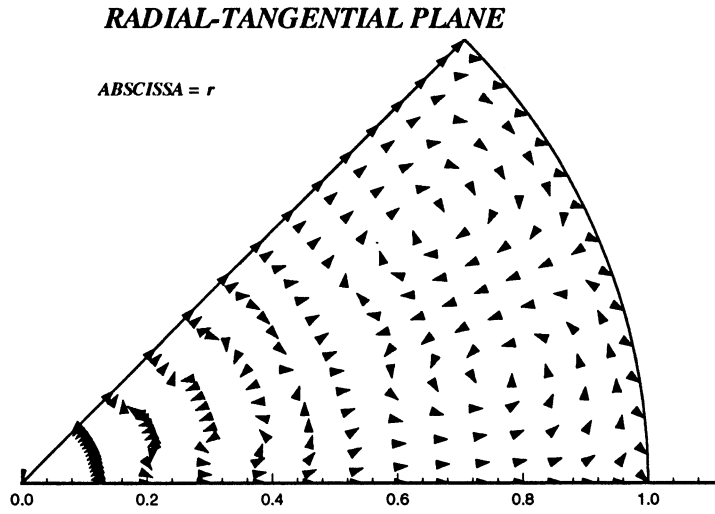
The radial-tangential plane is at x/R=1

Figure-B3-9. Effect of the change in orifice geometry on the velocity distribution
Clockwise from top left: round, 45° slot with L/W=4, and 45° slot with L/W=8
J=80, MR=2.96, DR=2.28, 8 orifices/row
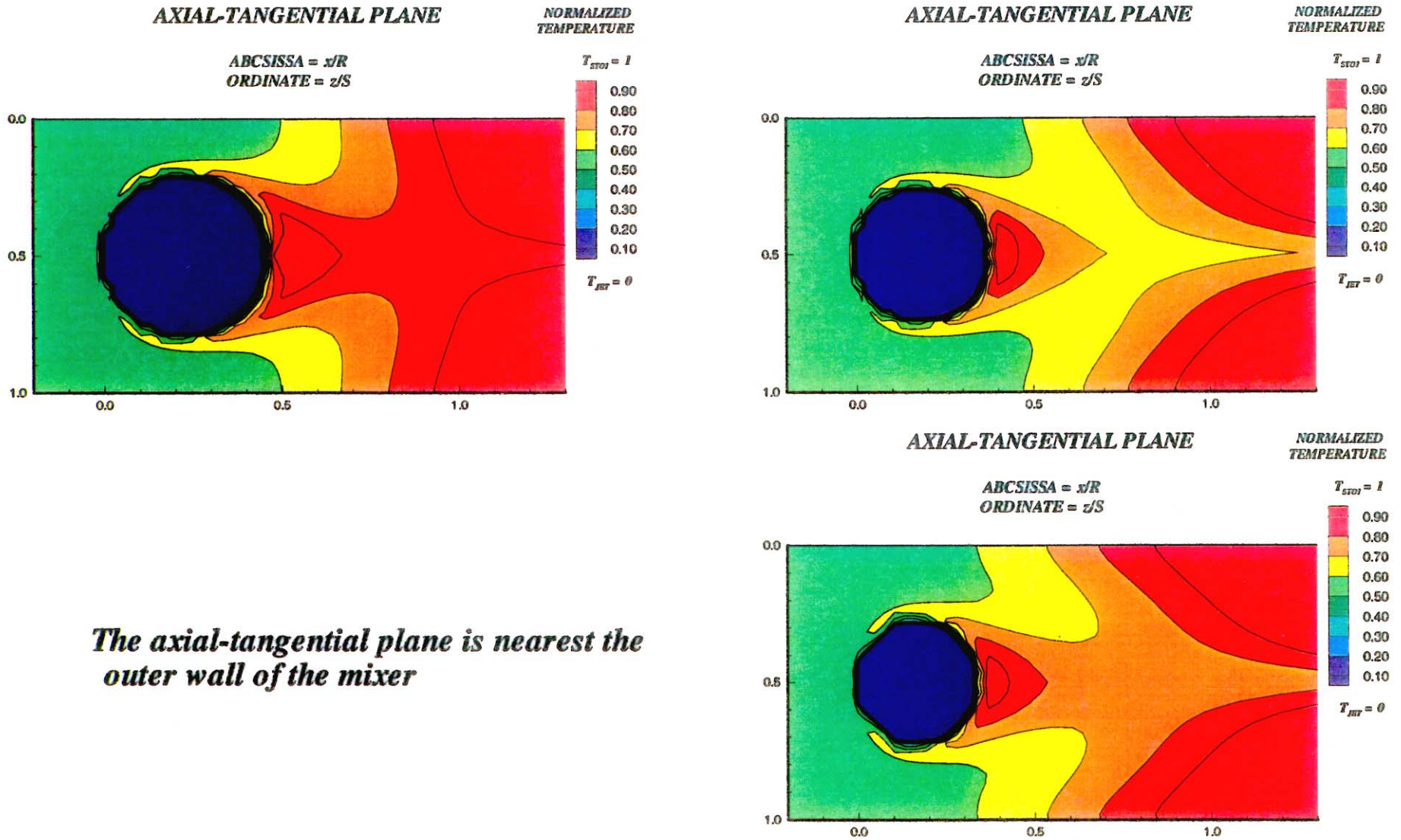
The axial-tangential plane is nearest the outer wall of the mixer

Figure-B4-1. Effect of the change in J on the temperature distribution
Clockwise from top left: J= 25, 52, and 80
*Round orifices, MR=2.96, DR=2.28, 8 orifices/row*
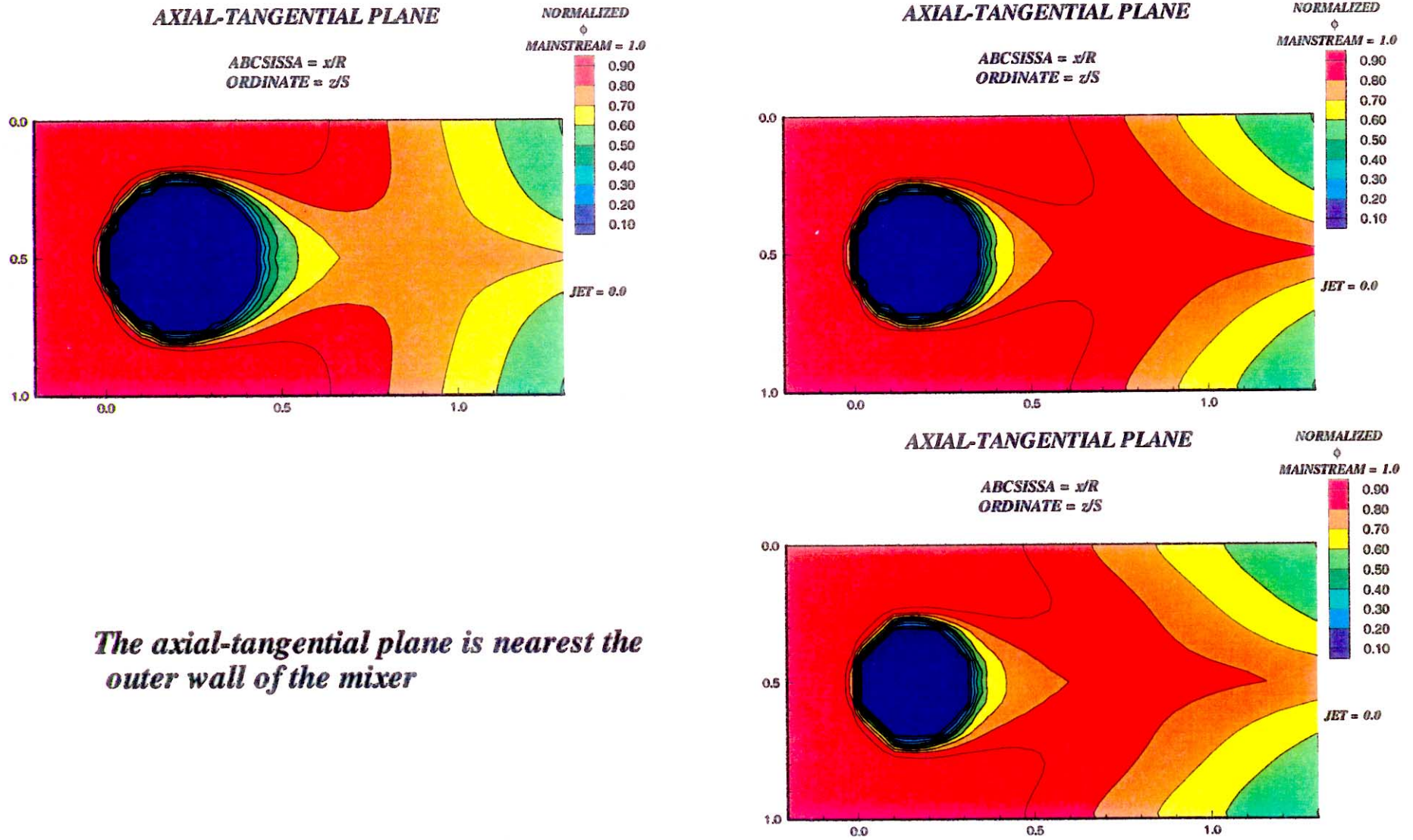
The axial-tangential plane is nearest the outer wall of the mixer

**Figure-B4-2. Effect of the change in J on the equivalence ratio distribution
Clockwise from top left: J= 25, 52, and 80
Round orifices, MR=2.96, DR=2.28, 8 orifices/row**

AXIAL-TANGENTIAL PLANE

ABCSISSA = x/R
ORDINATE = z/S

AXIAL-TANGENTIAL PLANE

ABCSISSA = x/R
ORDINATE = z/S

AXIAL-TANGENTIAL PLANE

ABCSISSA = x/R
ORDINATE = z/S
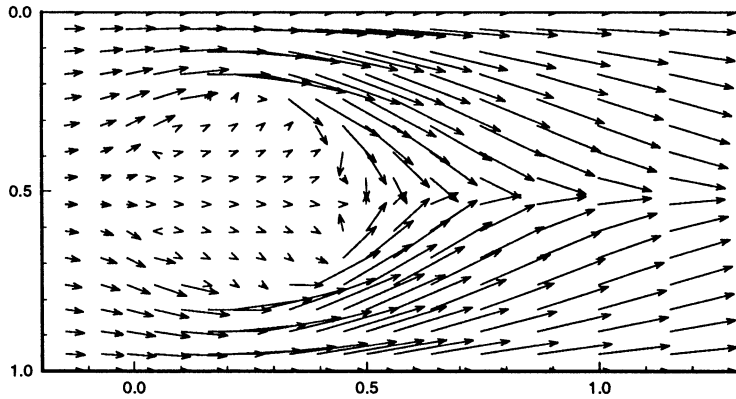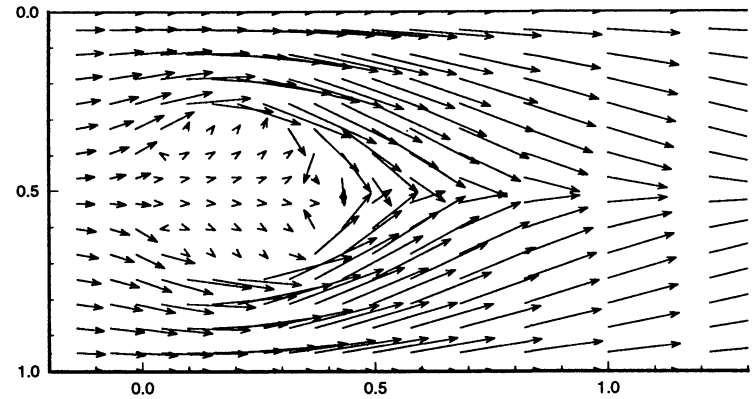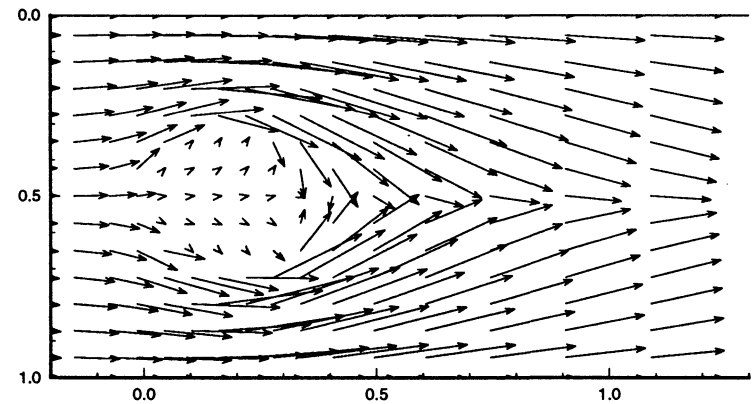
The axial-tangential plane is nearest the outer wall of the mixer

Figure-B4-3. Effect of the change in J on the velocity distribution
Clockwise from top left: J= 25, 52, and 80
Round orifices, MR=2.96, DR=2.28, 8 orifices/row
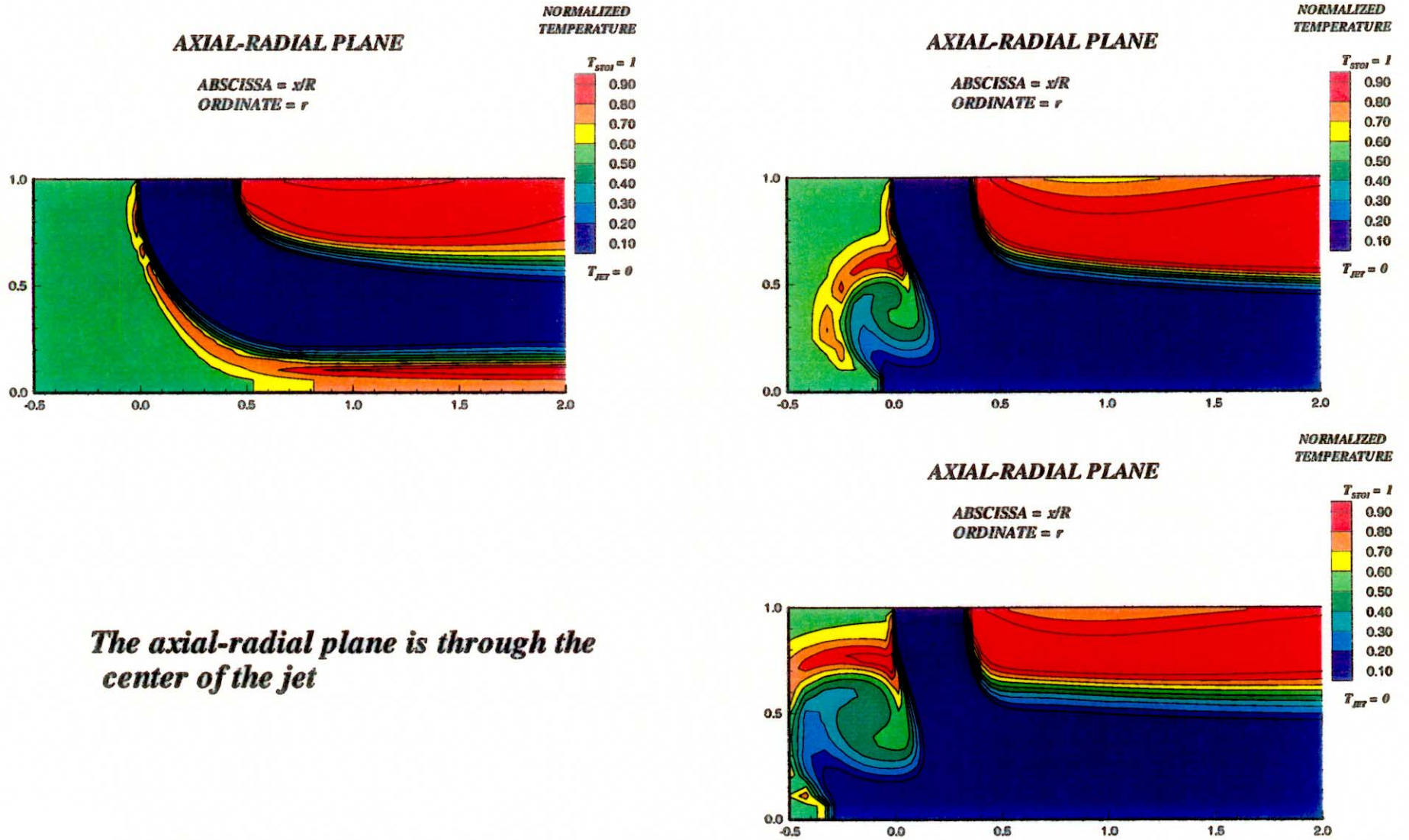
The axial-radial plane is through the center of the jet

Figure-B4-4. Effect of the change in J on the temperature distribution
Clockwise from top left: J= 25, 52, and 80
Round orifices, MR=2.96, DR=2.28, 8 orifices/row

AXIAL-RADIAL PLANE

ABSCISSA = x/R
ORDINATE = r

NORMALIZED
φ
MAINSTREAM = 1.0

0.90
0.80
0.70
0.60
0.50
0.40
0.30
0.20
0.10

JET = 0.0

AXIAL-RADIAL PLANE

ABSCISSA = x/R
ORDINATE = r

NORMALIZED
φ
MAINSTREAM = 1.0

0.90
0.80
0.70
0.60
0.50
0.40
0.30
0.20
0.10

JET = 0.0

The axial-radial plane is through the center of the jet

AXIAL-RADIAL PLANE

ABSCISSA = x/R
ORDINATE = r

NORMALIZED
φ
MAINSTREAM = 1.0

0.90
0.80
0.70
0.60
0.50
0.40
0.30
0.20
0.10

JET = 0.0
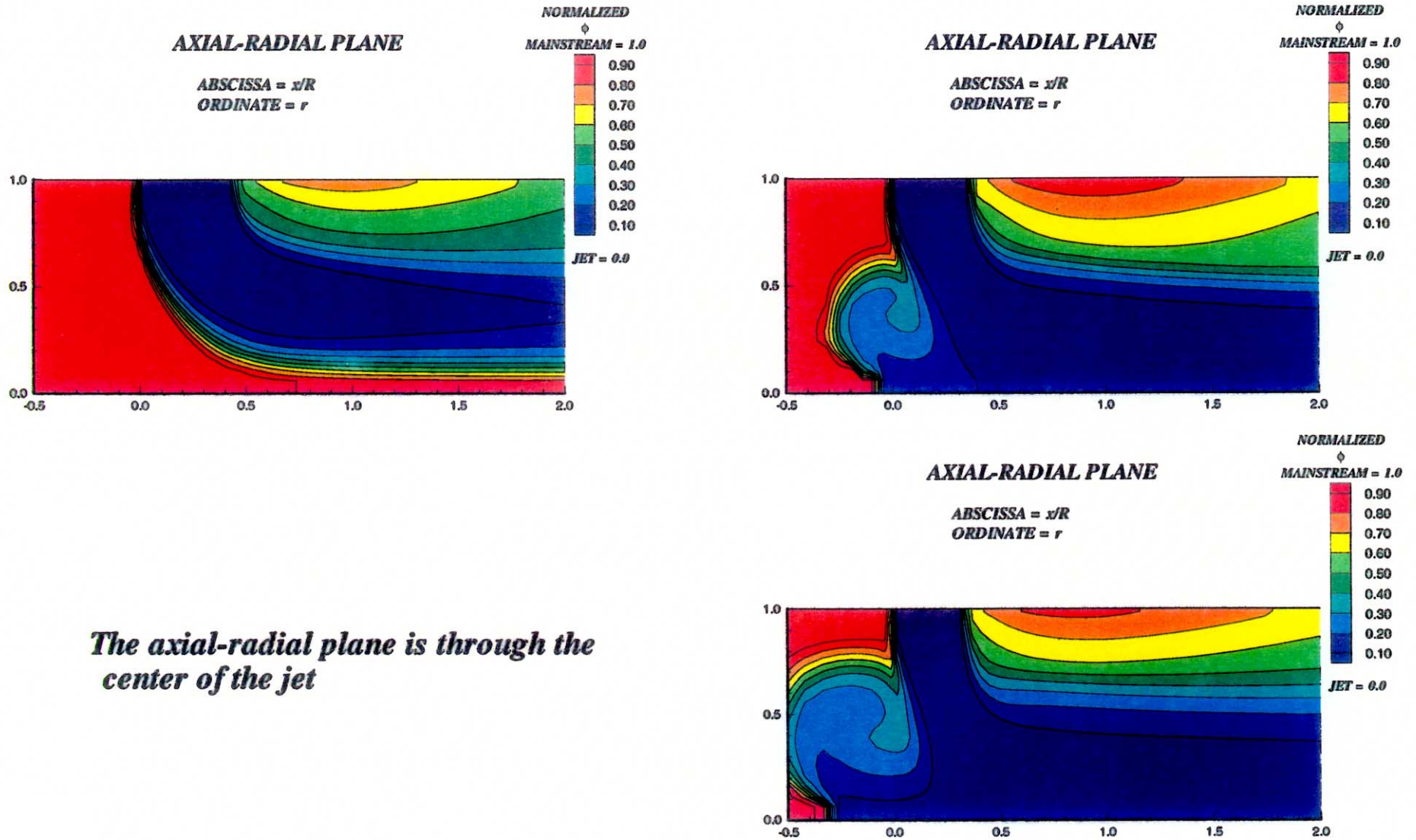
*Figure-B4-5. Effect of the change in J on the equivalence ratio distribution
Clockwise from top left: J= 25, 52, and 80
Round orifices, MR=2.96, DR=2.28, 8 orifices/row*

AXIAL-RADIAL PLANE

ABSCISSA = x/R
ORDINATE = r
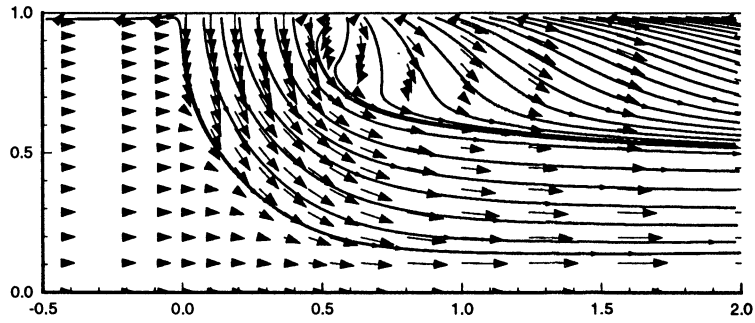
AXIAL-RADIAL PLANE

ABSCISSA = x/R
ORDINATE = r
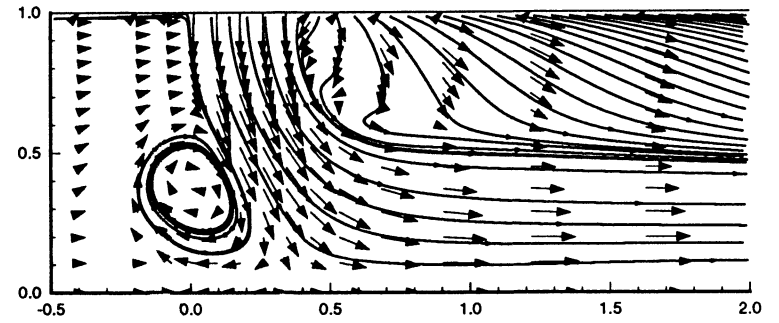
The axial-radial plane is through the center of the jet

AXIAL-RADIAL PLANE

ABSCISSA = x/R
ORDINATE = r
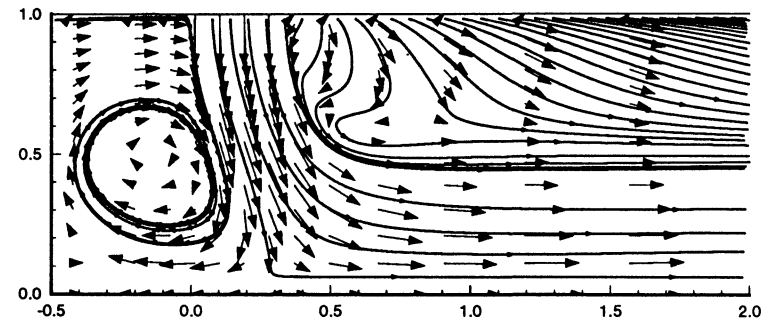
Figure-B4-6. Effect of the change in J on the velocity distribution
Clockwise from top left: J= 25, 52, and 80
Round orifices, MR=2.96, DR=2.28, 8 orifices/row

RADIAL-TANGENTIAL PLANE

NORMALIZED TEMPERATURE

$T_{STOI} = 1$

ABSCISSA = r

0.90
0.80
0.70
0.60
0.50
0.40
0.30
0.20
0.10

$T_{JET} = 0$

RADIAL-TANGENTIAL PLANE

NORMALIZED TEMPERATURE

$T_{STOI} = 1$

ABSCISSA = r

0.90
0.80
0.70
0.60
0.50
0.40
0.30
0.20
0.10

$T_{JET} = 0$

The radial-tangential plane is at x/R=1

RADIAL-TANGENTIAL PLANE

NORMALIZED TEMPERATURE

$T_{STOI} = 1$

ABSCISSA = r

0.90
0.80
0.70
0.60
0.50
0.40
0.30
0.20
0.10

$T_{JET} = 0$
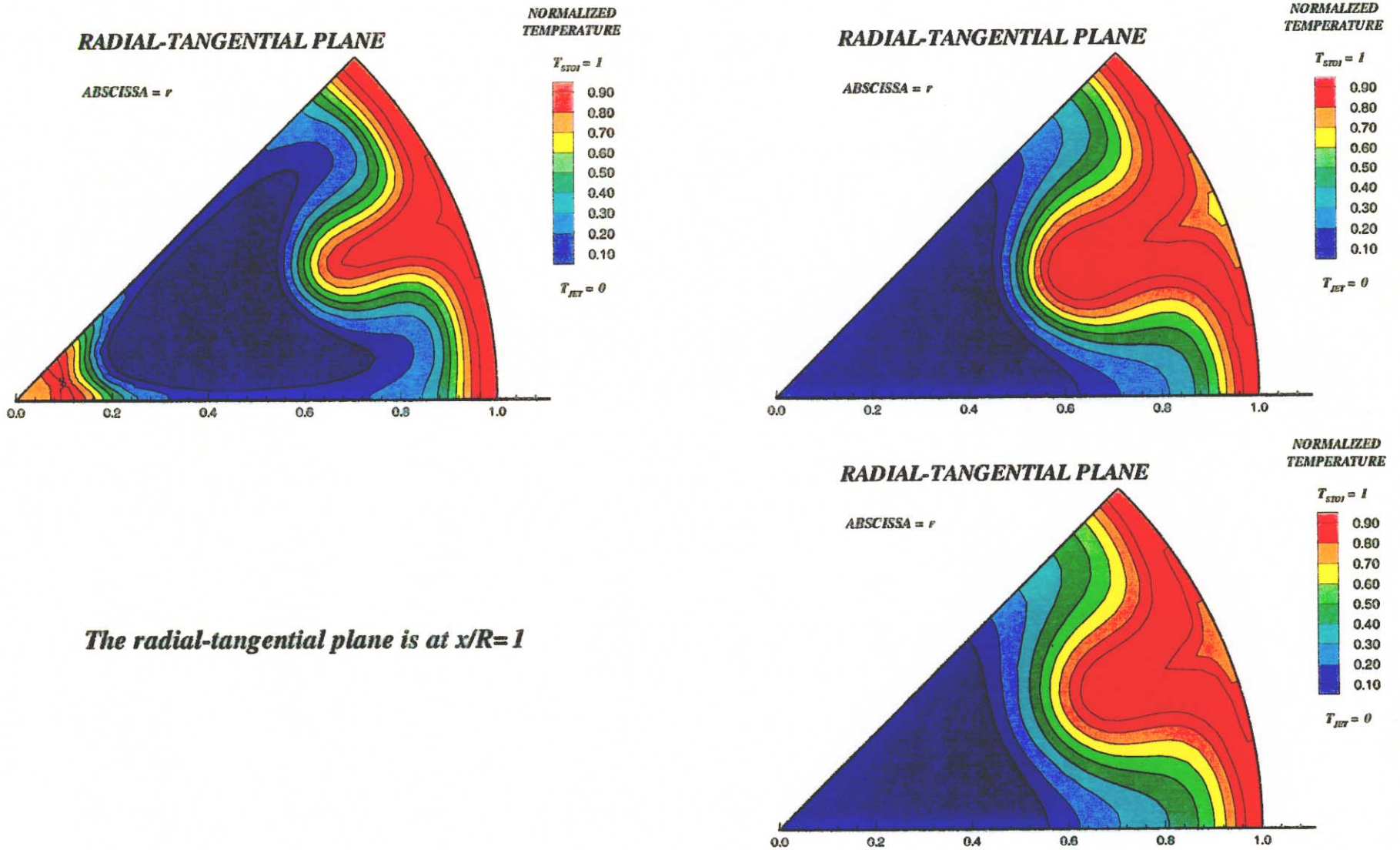
Figure-B4-7. Effect of the change in J on the temperature distribution
Clockwise from top left: J= 25, 52, and 80
Round orifices, MR=2.96, DR=2.28, 8 orifices/row

RADIAL-TANGENTIAL PLANE

ABSCISSA = r

NORMALIZED
φ
MAINSTREAM = 1.0

0.90
0.80
0.70
0.60
0.50
0.40
0.30
0.20
0.10

JET = 0.0
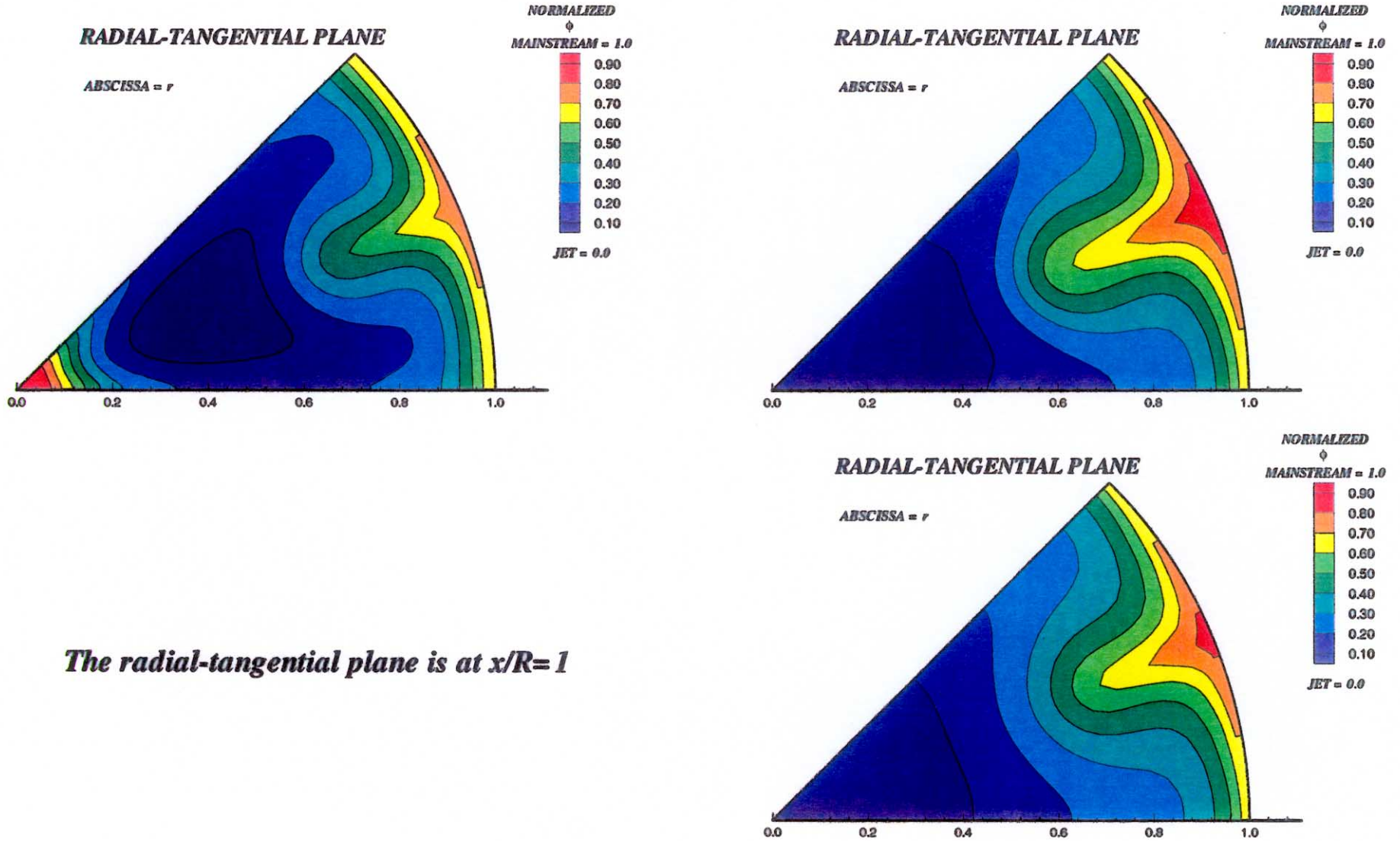
The radial-tangential plane is at x/R=1

Figure-B4-8. Effect of the change in J on the equivalence ratio distribution
Clockwise from top left: J= 25, 52, and 80
Round orifices, MR=2.96, DR=2.28, 8 orifices/row

RADIAL-TANGENTIAL PLANE

ABSCISSA = r

RADIAL-TANGENTIAL PLANE

ABSCISSA = r

RADIAL-TANGENTIAL PLANE

ABSCISSA = r
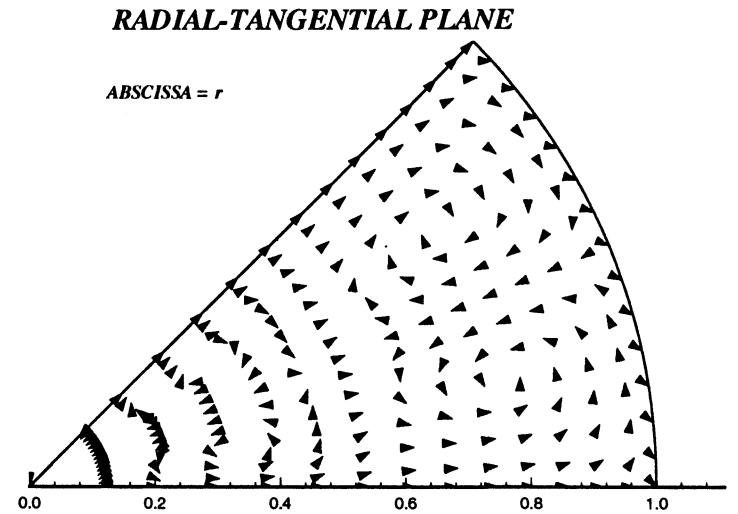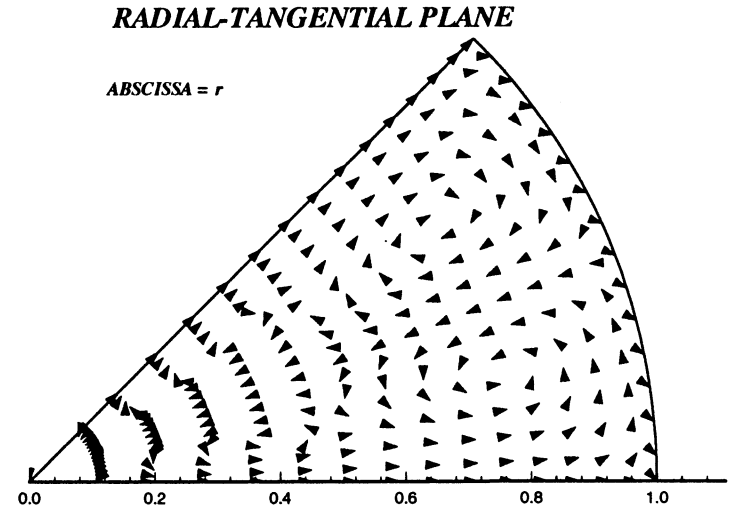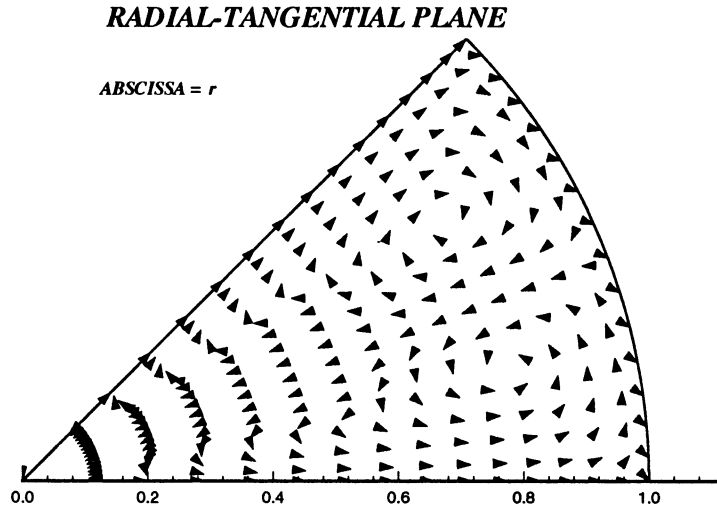
The radial-tangential plane is at x/R=1

Figure-B4-9. Effect of the change in J on the velocity distribution
Clockwise from top left: J= 25, 52, and 80
Round orifices, MR=2.96, DR=2.28, 8 orifices/row

AXIAL-TANGENTIAL PLANE

ABCSISSA = x/R
ORDINATE = z/S

NORMALIZED TEMPERATURE

$T_{STOI} = 1$

0.90
0.80
0.70
0.60
0.50
0.40
0.30
0.20
0.10

$T_{JET} = 0$

AXIAL-TANGENTIAL PLANE

ABCSISSA = x/R
ORDINATE = z/S

NORMALIZED TEMPERATURE

$T_{STOI} = 1$

0.90
0.80
0.70
0.60
0.50
0.40
0.30
0.20
0.10

$T_{JET} = 0$

AXIAL-TANGENTIAL PLANE

ABCSISSA = x/R
ORDINATE = z/S

NORMALIZED TEMPERATURE

$T_{STOI} = 1$

0.90
0.80
0.70
0.60
0.50
0.40
0.30
0.20
0.10

$T_{JET} = 0$
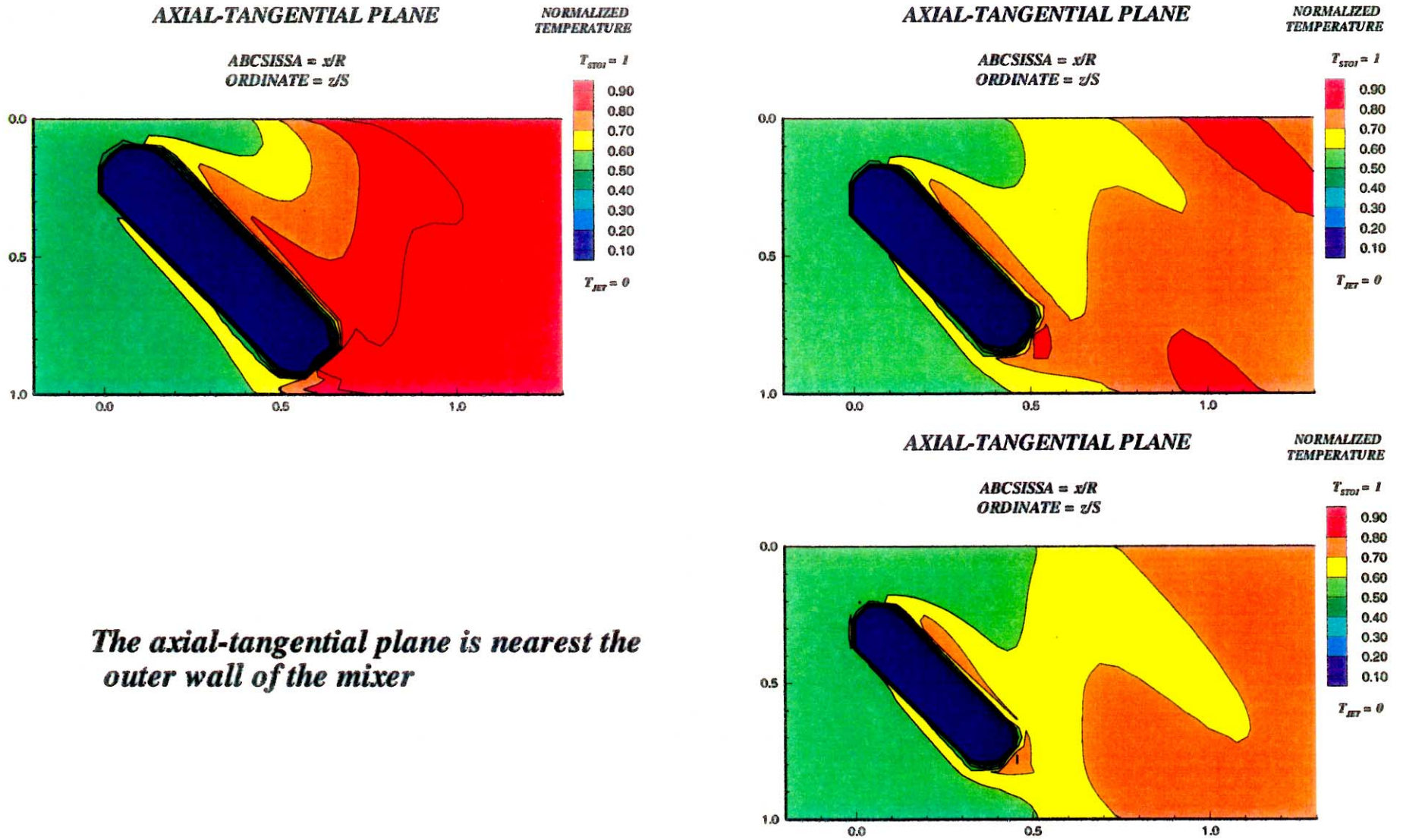
The axial-tangential plane is nearest the outer wall of the mixer

Figure-B5-1. Effect of the change in J on the temperature distribution
Clockwise from top left: J= 25, 52, and 80
45^0 slots, L/W= 4, MR= 2.96, DR= 2.28, 8 orifices/row

**AXIAL-TANGENTIAL PLANE**

ABCSISSA = x/R
ORDINATE = z/S

NORMALIZED
φ
MAINSTREAM = 1.0

0.90
0.80
0.70
0.60
0.50
0.40
0.30
0.20
0.10

JET = 0.0

AXIAL-TANGENTIAL PLANE

ABCSISSA = x/R
ORDINATE = z/S

NORMALIZED
φ
MAINSTREAM = 1.0

0.90
0.80
0.70
0.60
0.50
0.40
0.30
0.20
0.10

JET = 0.0

The axial-tangential plane is nearest the outer wall of the mixer

AXIAL-TANGENTIAL PLANE

ABCSISSA = x/R
ORDINATE = z/S

NORMALIZED
φ
MAINSTREAM = 1.0

0.90
0.80
0.70
0.60
0.50
0.40
0.30
0.20
0.10

JET = 0.0
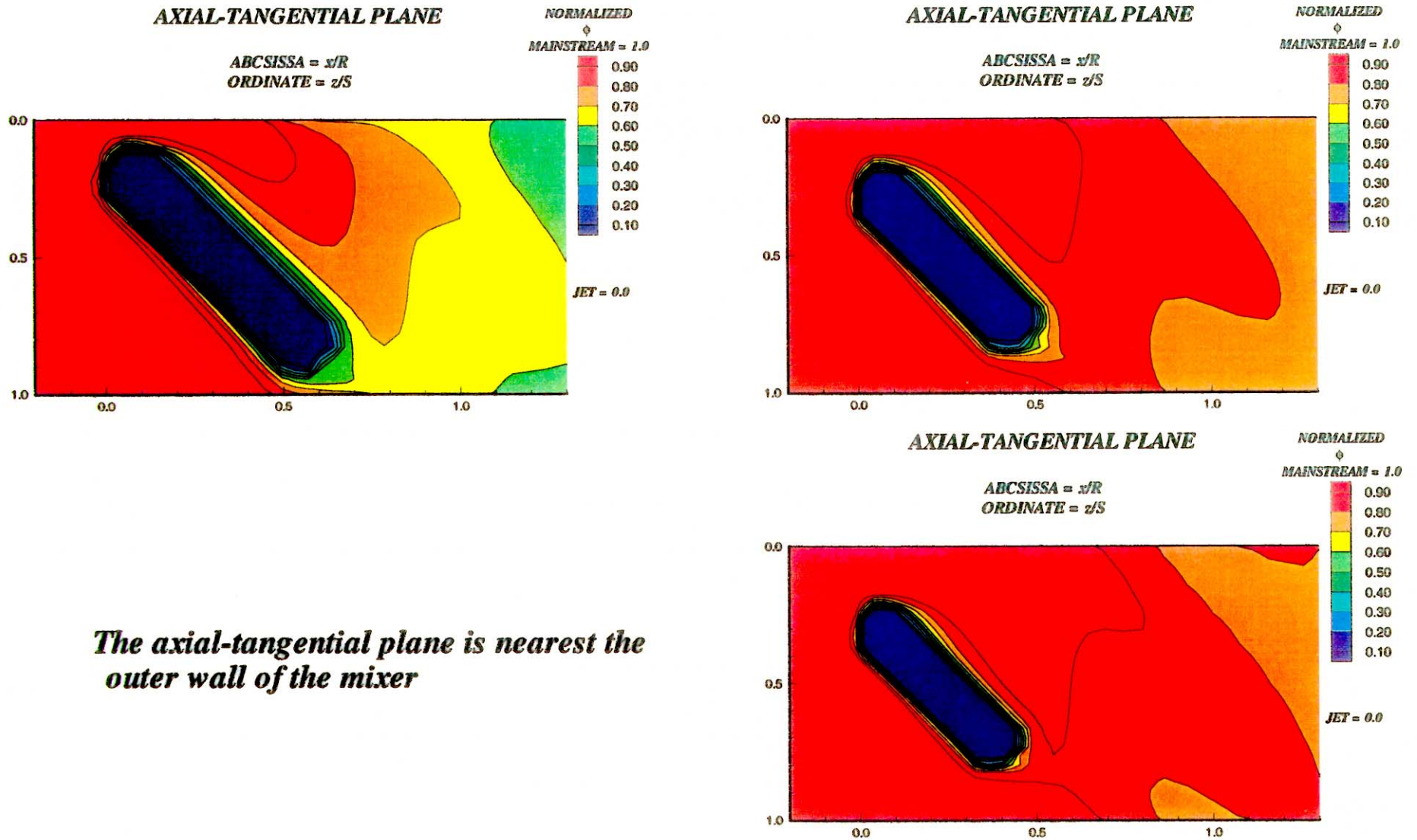
Figure-B5-2. Effect of the change in J on the equivalence ratio distribution
Clockwise from top left: J= 25, 52, and 80
45⁰ slots, L/W=4, MR=2.96, DR=2.28, 8 orifices/row

AXIAL-TANGENTIAL PLANE

ABCSISSA = x/R
ORDINATE = z/S

AXIAL-TANGENTIAL PLANE

ABCSISSA = x/R
ORDINATE = z/S

AXIAL-TANGENTIAL PLANE

ABCSISSA = x/R
ORDINATE = z/S
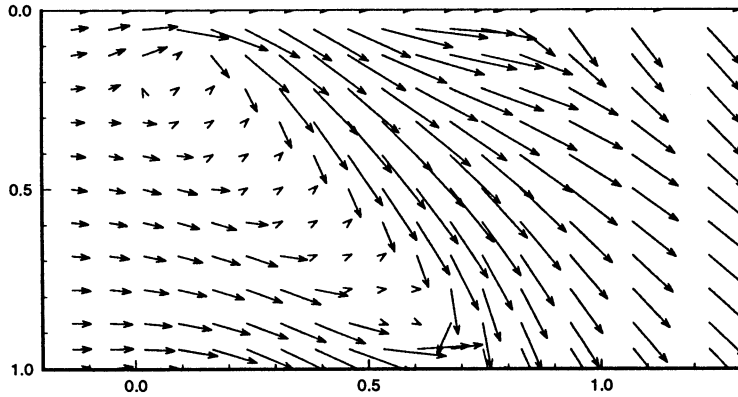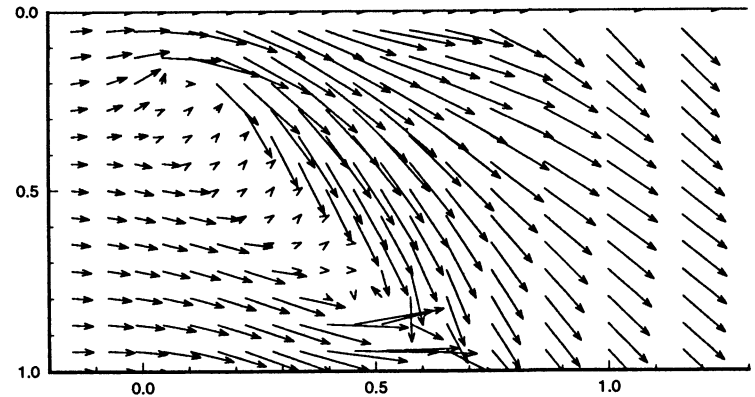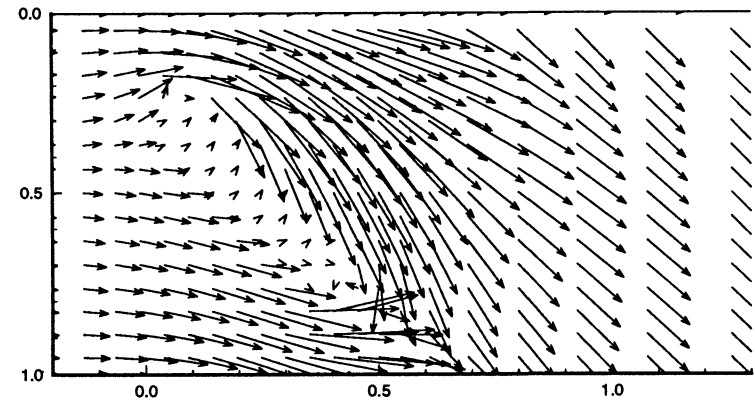
*The axial-tangential plane is nearest the
outer wall of the mixer*

*Figure-B5-3. Effect of the change in J on the velocity distribution
Clockwise from top left: J= 25, 52, and 80
45⁰ slots, L/W=4, MR=2.96, DR=2.28, 8 orifices/row*
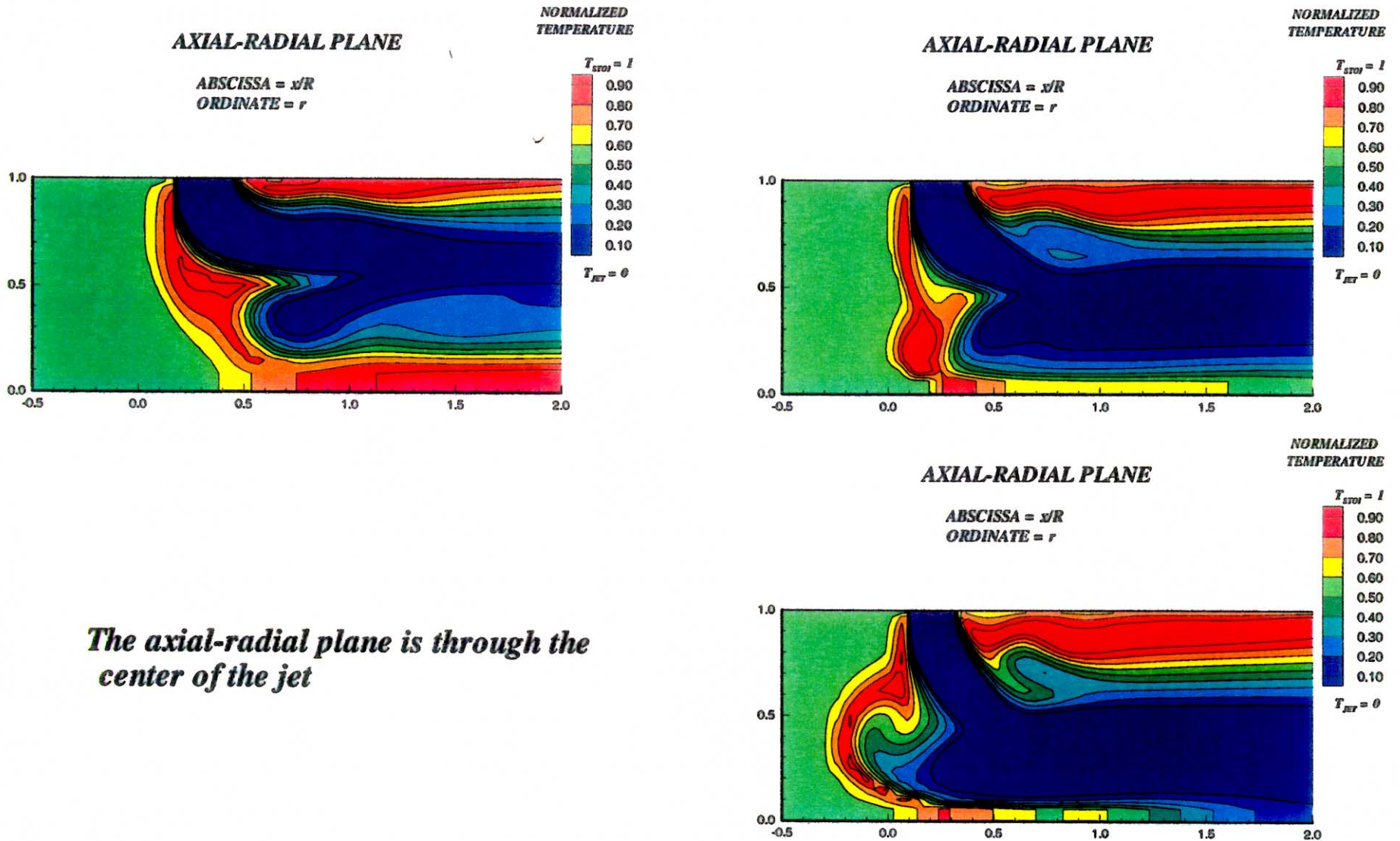
The axial-radial plane is through the center of the jet

Figure-B5-4. Effect of the change in J on the temperature distribution
Clockwise from top left: J= 25, 52, and 80
**45^0 slots, L/W= 4, MR= 2.96, DR= 2.28, 8 orifices/row**
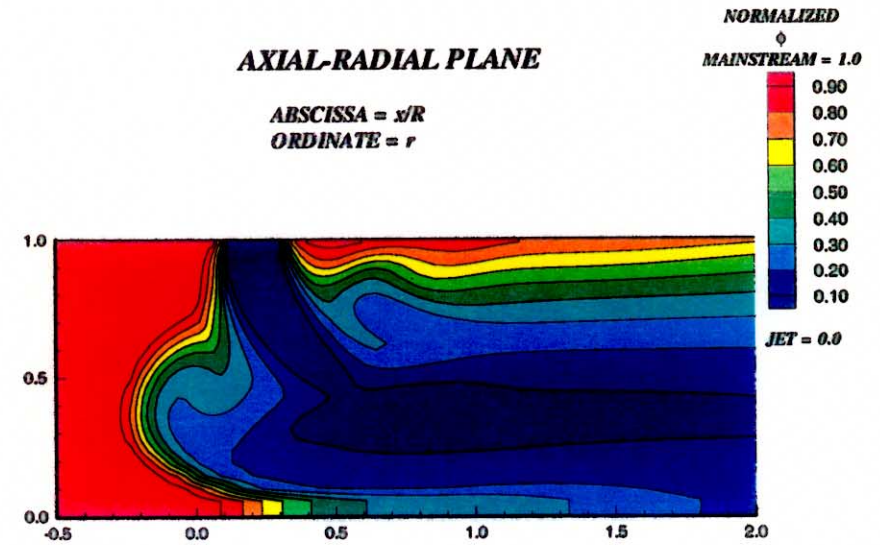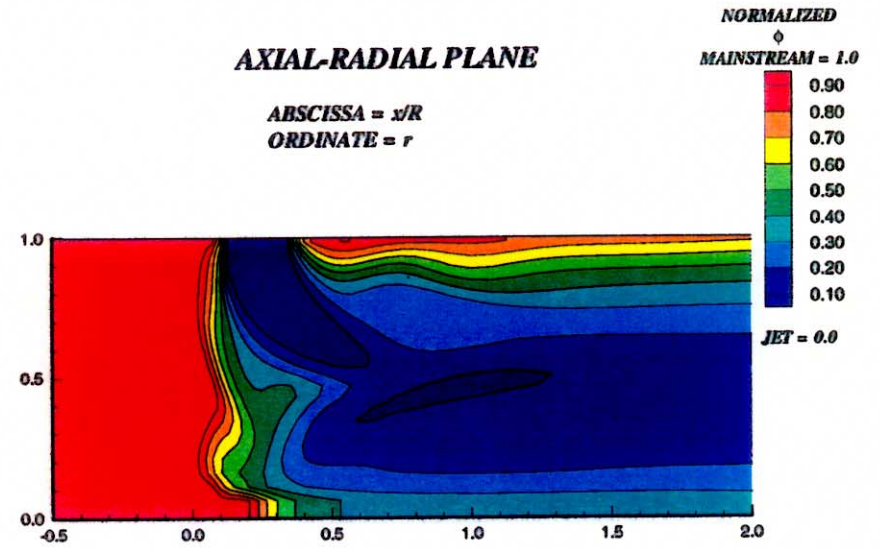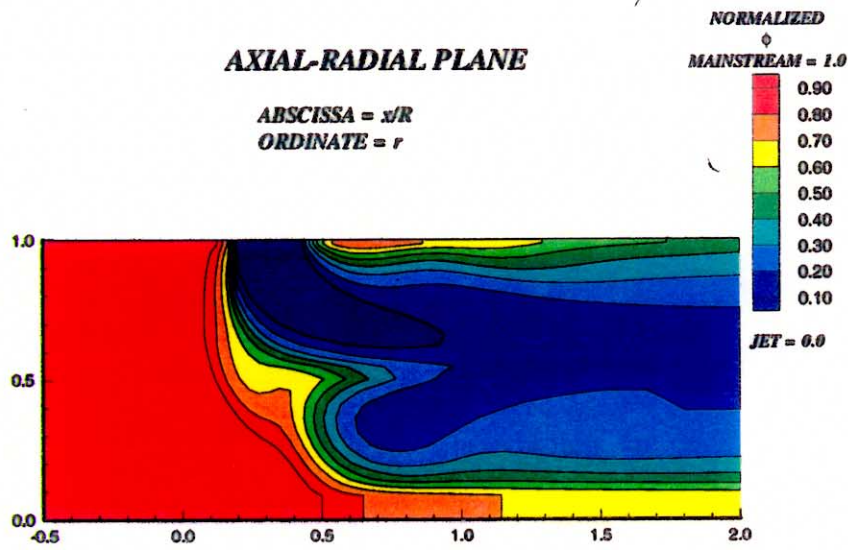
The axial-radial plane is through the center of the jet

Figure-B5-5. Effect of the change in J on the equivalence ratio distribution
Clockwise from top left: J= 25, 52, and 80
45° slots, L/W=4, MR=2.96, DR=2.28, 8 orifices/row

**AXIAL-RADIAL PLANE**

ABSCISSA = x/R
ORDINATE = r
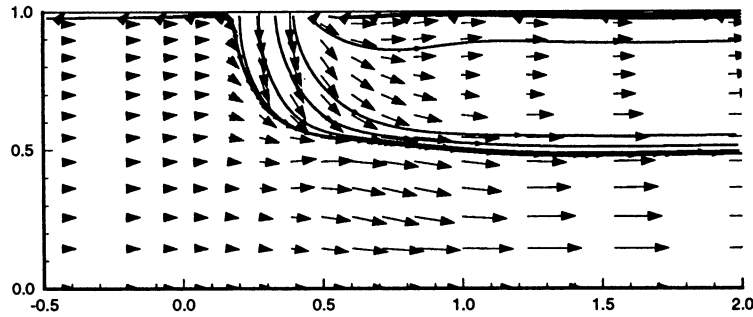
AXIAL-RADIAL PLANE

ABSCISSA = x/R
ORDINATE = r
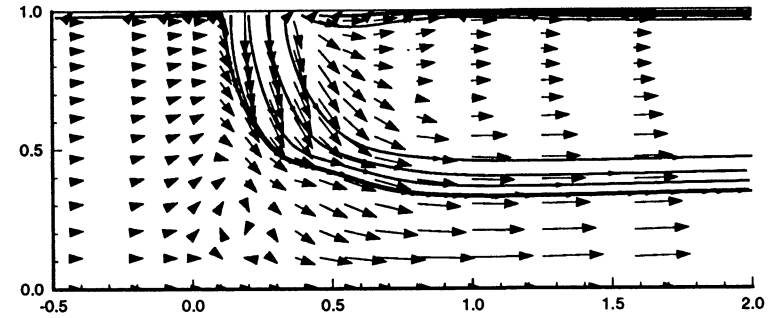
AXIAL-RADIAL PLANE

ABSCISSA = x/R
ORDINATE = r
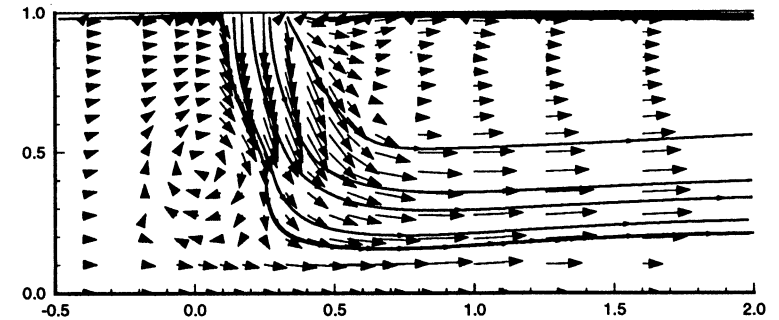
The axial-radial plane is through the center of the jet

Figure-B5-6. Effect of the change in J on the velocity distribution
Clockwise from top left: J= 25, 52, and 80
45° slots, L/W=4, MR=2.96, DR=2.28, 8 orifices/row

RADIAL-TANGENTIAL PLANE

ABSCISSA = r

NORMALIZED TEMPERATURE

$T_{STOI} = 1$

0.90
0.80
0.70
0.60
0.50
0.40
0.30
0.20
0.10

$T_{JET} = 0$

RADIAL-TANGENTIAL PLANE

ABSCISSA = r

NORMALIZED TEMPERATURE

$T_{STOI} = 1$

0.90
0.80
0.70
0.60
0.50
0.40
0.30
0.20
0.10

$T_{JET} = 0$

The radial-tangential plane is at x/R= 1

RADIAL-TANGENTIAL PLANE

ABSCISSA = r

NORMALIZED TEMPERATURE

$T_{STOI} = 1$

0.90
0.80
0.70
0.60
0.50
0.40
0.30
0.20
0.10

$T_{JET} = 0$
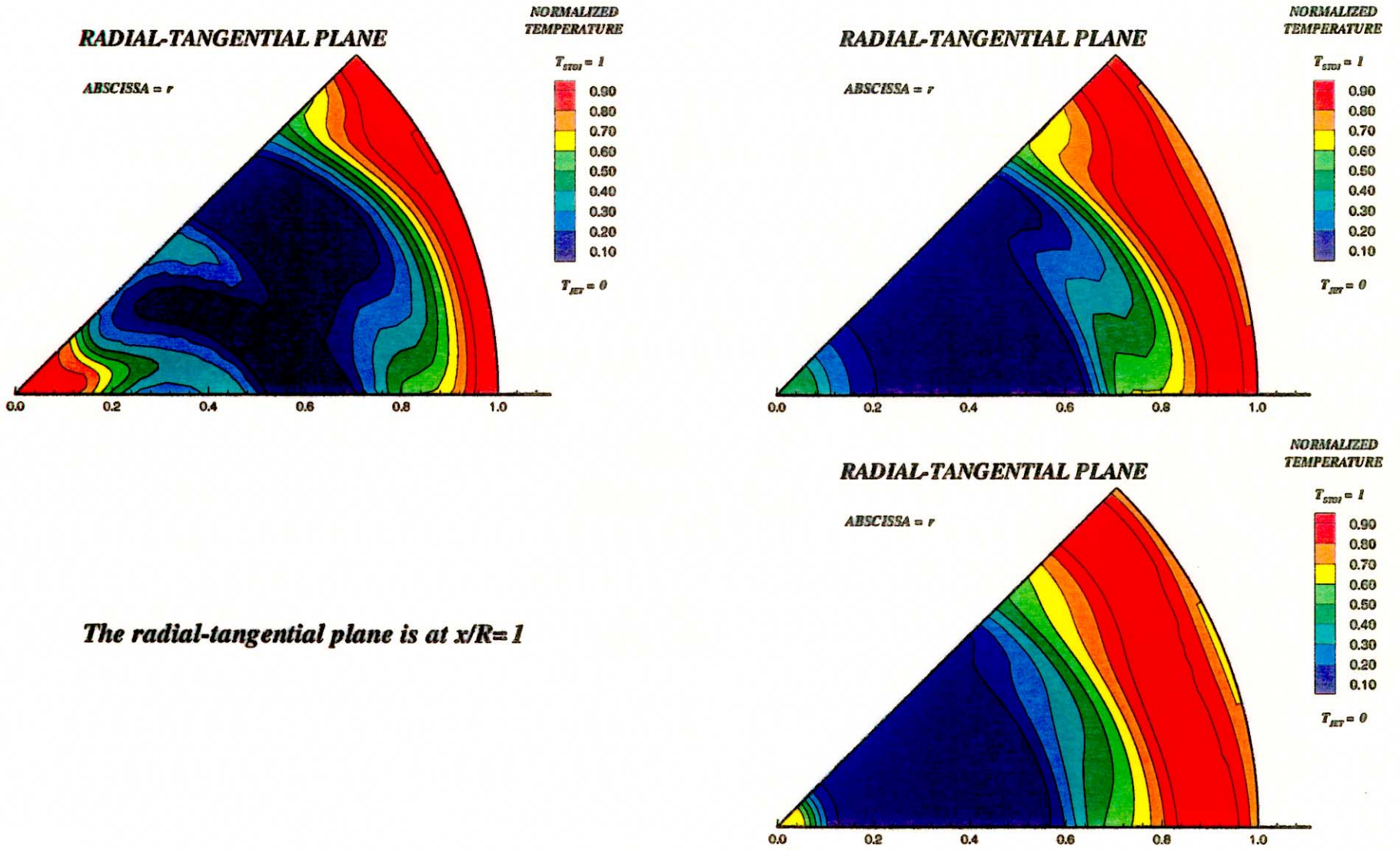
Figure-B5-7. Effect of the change in J on the temperature distribution
Clockwise from top left: J= 25, 52, and 80
45° slots, L/W= 4, MR= 2.96, DR= 2.28, 8 orifices/row
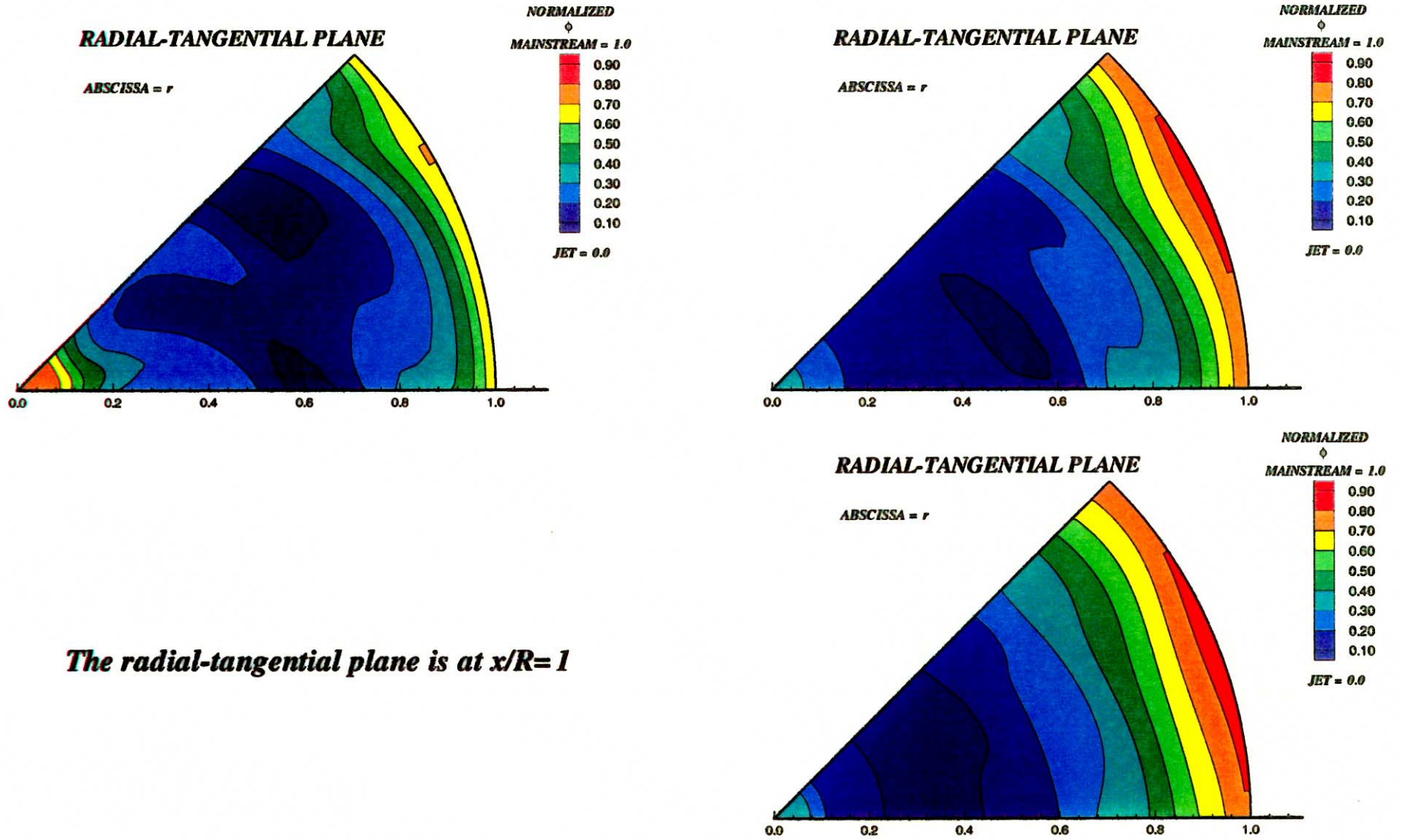
The radial-tangential plane is at x/R=1

Figure-B5-8. Effect of the change in J on the equivalence ratio distribution
Clockwise from top left: J= 25, 52, and 80
45° slots, L/W=4, MR=2.96, DR=2.28, 8 orifices/row

RADIAL-TANGENTIAL PLANE

ABSCISSA = r

RADIAL-TANGENTIAL PLANE

ABSCISSA = r

The radial-tangential plane is at x/R=1

RADIAL-TANGENTIAL PLANE

ABSCISSA = r
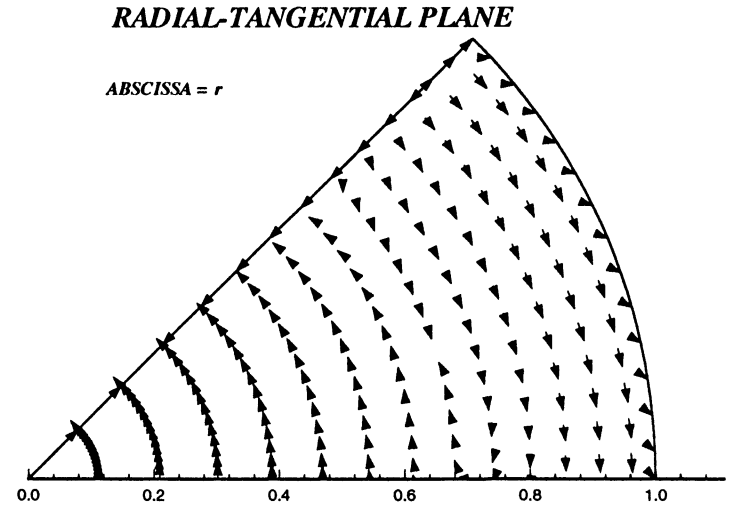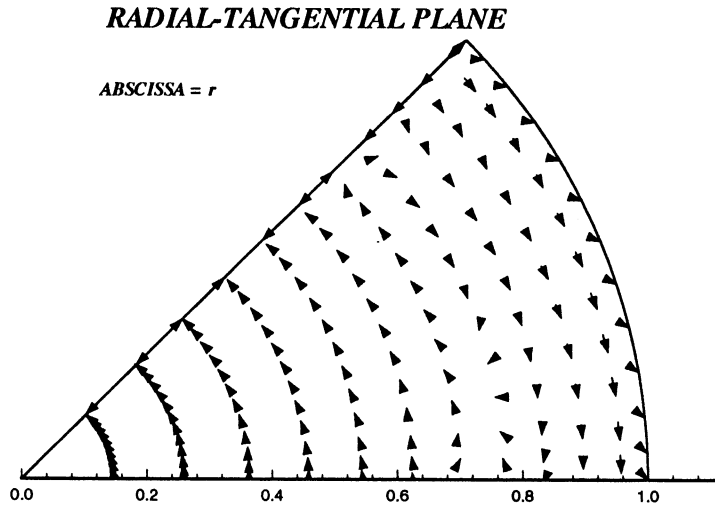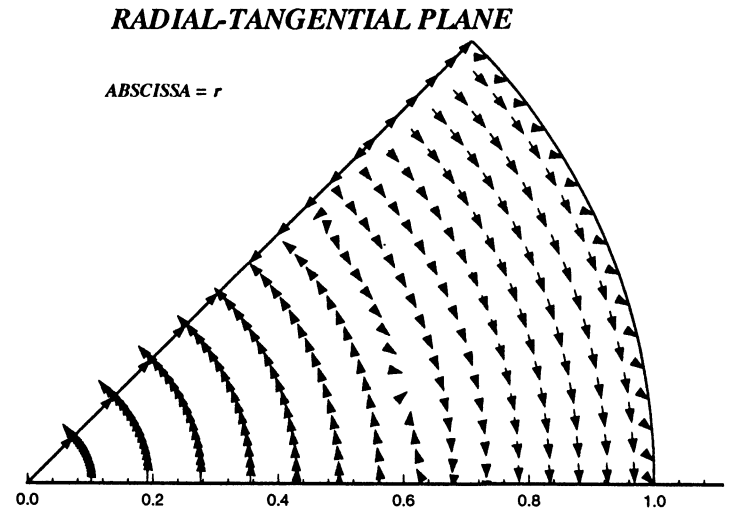
Figure-B5-9. Effect of the change in J on the velocity distribution
Clockwise from top left: J= 25, 52, and 80
45^0 slots, L/W=4, MR=2.96, DR=2.28, 8 orifices/row

AXIAL-TANGENTIAL PLANE

ABCSISSA = x/R
ORDINATE = z/S

NORMALIZED TEMPERATURE

$T_{STO1} = 1$

0.90
0.80
0.70
0.60
0.50
0.40
0.30
0.20
0.10

$T_{JET} = 0$

AXIAL-TANGENTIAL PLANE

ABCSISSA = x/R
ORDINATE = z/S

NORMALIZED TEMPERATURE

$T_{STO1} = 1$

0.90
0.80
0.70
0.60
0.50
0.40
0.30
0.20
0.10

$T_{JET} = 0$

The axial-tangential plane is nearest the outer wall of the mixer

AXIAL-TANGENTIAL PLANE

ABCSISSA = x/R
ORDINATE = z/S

NORMALIZED TEMPERATURE

$T_{STO1} = 1$

0.90
0.80
0.70
0.60
0.50
0.40
0.30
0.20
0.10

$T_{JET} = 0$
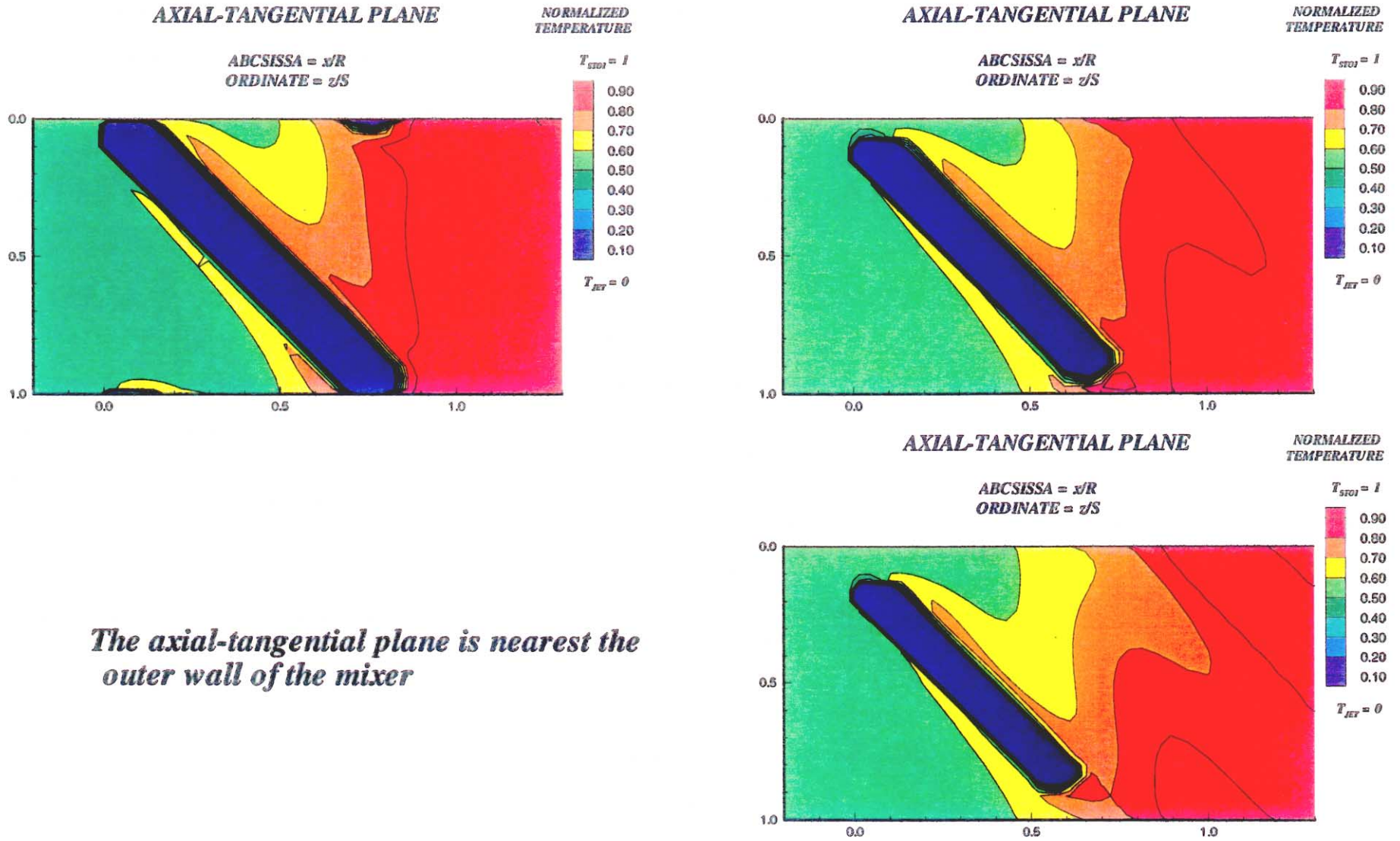
Figure-B6-1. Effect of the change in J on the temperature distribution
Clockwise from top left: J= 25, 52, and 80
45^0 slots, L/W=8, MR=2.96, DR=2.28, 8 orifices/row

AXIAL-TANGENTIAL PLANE

NORMALIZED
◇
MAINSTREAM = 1.0

ABCSISSA = x/R
ORDINATE = z/S

0.90
0.80
0.70
0.60
0.50
0.40
0.30
0.20
0.10

AXIAL-TANGENTIAL PLANE

NORMALIZED
◇
MAINSTREAM = 1.0

ABCSISSA = x/R
ORDINATE = z/S

0.90
0.80
0.70
0.60
0.50
0.40
0.30
0.20
0.10

JET = 0.0

JET = 0.0

The axial-tangential plane is nearest the outer wall of the mixer

AXIAL-TANGENTIAL PLANE

NORMALIZED
◇
MAINSTREAM = 1.0

ABCSISSA = x/R
ORDINATE = z/S

0.90
0.80
0.70
0.60
0.50
0.40
0.30
0.20
0.10

JET = 0.0
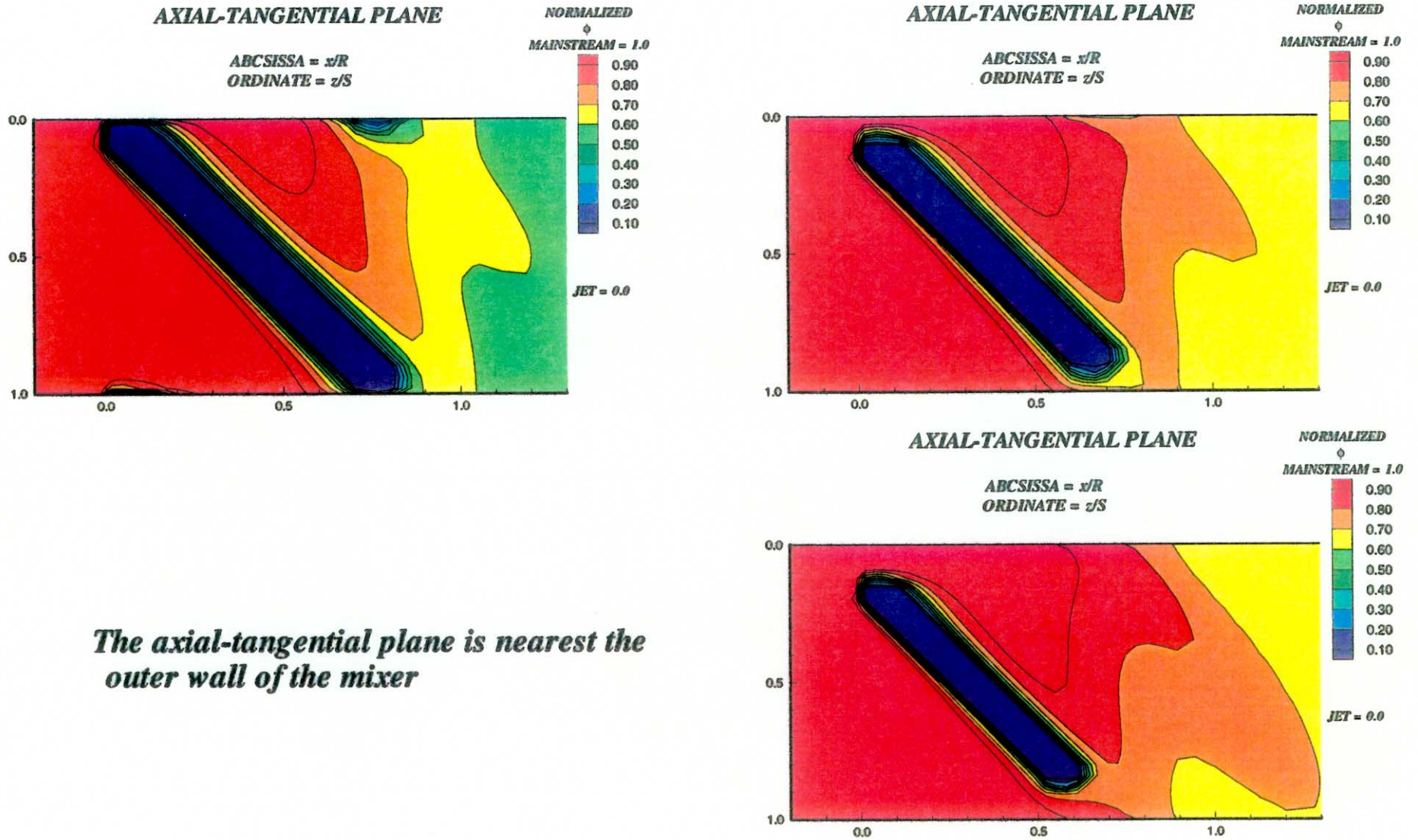
Figure-B6-2. Effect of the change in J on the equivalence ratio distribution
Clockwise from top left: J= 25, 52, and 80
45⁰ slots, L/W=8, MR=2.96, DR=2.28, 8 orifices/row

AXIAL-TANGENTIAL PLANE

ABCSISSA = x/R
ORDINATE = z/S

AXIAL-TANGENTIAL PLANE

ABCSISSA = x/R
ORDINATE = z/S

AXIAL-TANGENTIAL PLANE

ABCSISSA = x/R
ORDINATE = z/S
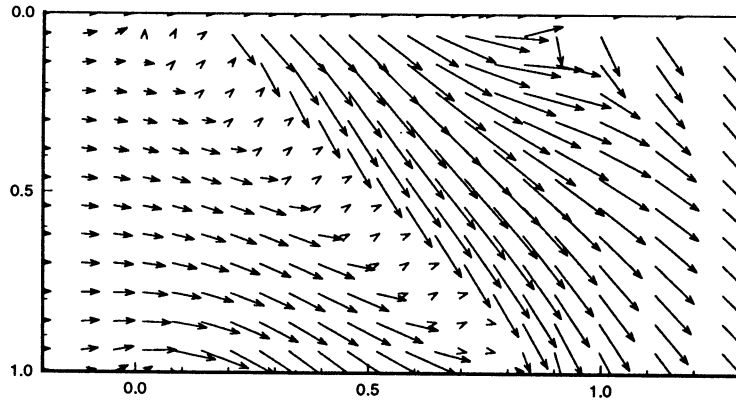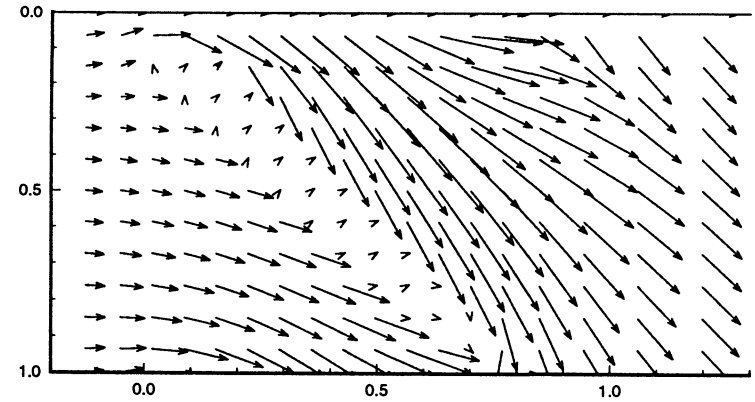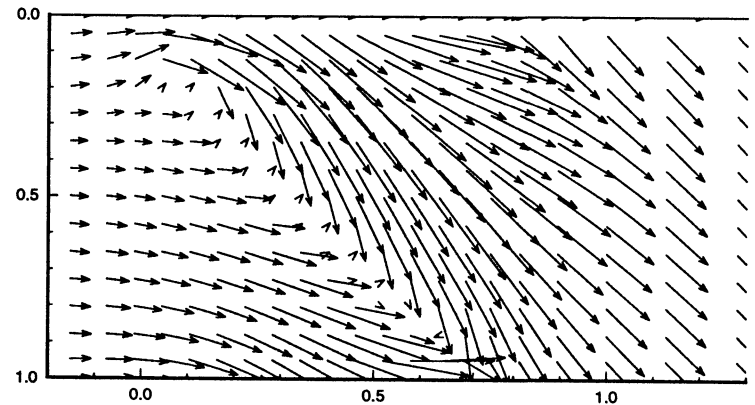
The axial-tangential plane is nearest the outer wall of the mixer

Figure-B6-3. Effect of the change in J on the velocity distribution Clockwise from top left: J= 25, 52, and 80 45⁰ slots, L/W=8, MR=2.96, DR=2.28, 8 orifices/row

AXIAL-RADIAL PLANE

NORMALIZED
TEMPERATURE

ABSCISSA = x/R
ORDINATE = r

$T_{STOI} = 1$
0.90
0.80
0.70
0.60
0.50
0.40
0.30
0.20
0.10

$T_{JET} = 0$

AXIAL-RADIAL PLANE

NORMALIZED
TEMPERATURE

ABSCISSA = x/R
ORDINATE = r

$T_{STOI} = 1$
0.90
0.80
0.70
0.60
0.50
0.40
0.30
0.20
0.10

$T_{JET} = 0$

AXIAL-RADIAL PLANE

NORMALIZED
TEMPERATURE

ABSCISSA = x/R
ORDINATE = r

$T_{STOI} = 1$
0.90
0.80
0.70
0.60
0.50
0.40
0.30
0.20
0.10

$T_{JET} = 0$
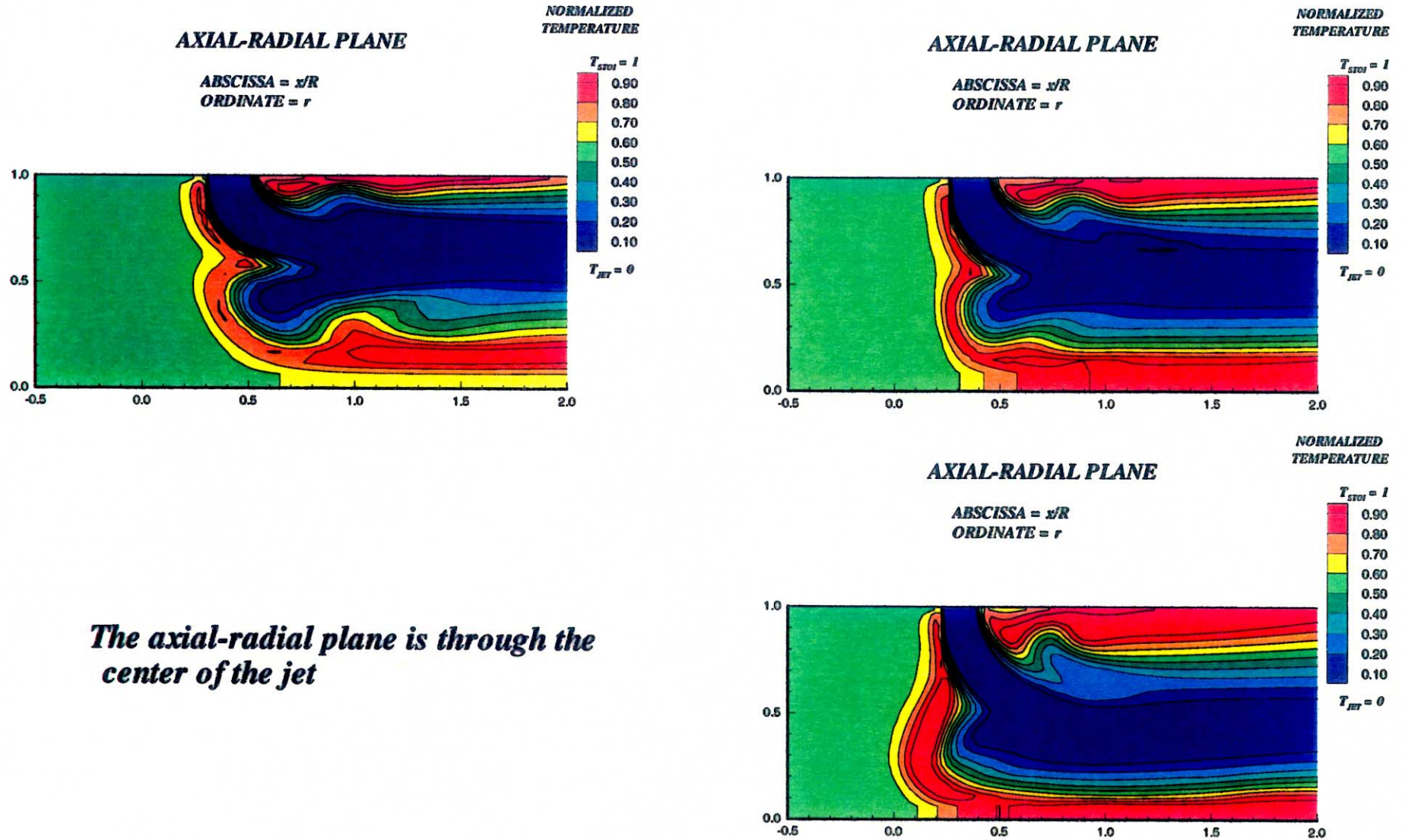
The axial-radial plane is through the center of the jet

Figure-B6-4. Effect of the change in J on the temperature distribution
Clockwise from top left: J= 25, 52, and 80
45^0 slots, L/W=8, MR=2.96, DR=2.28, 8 orifices/row
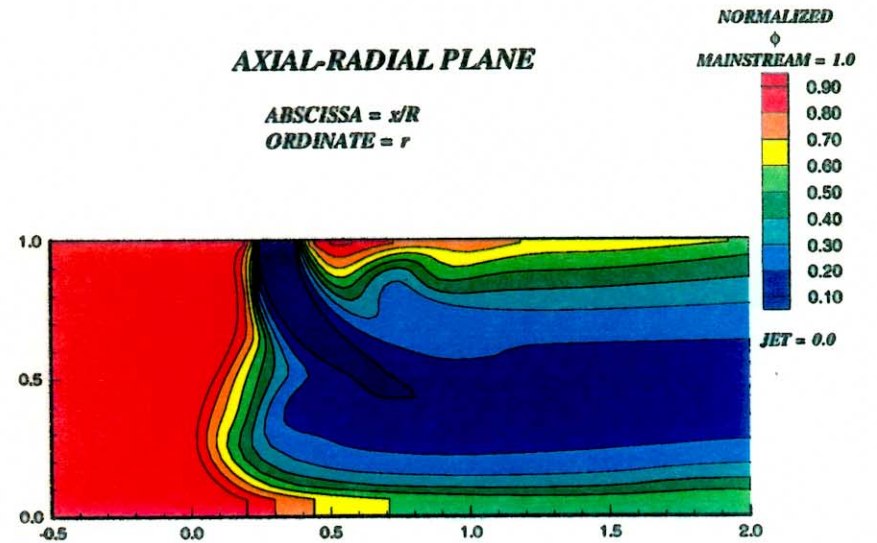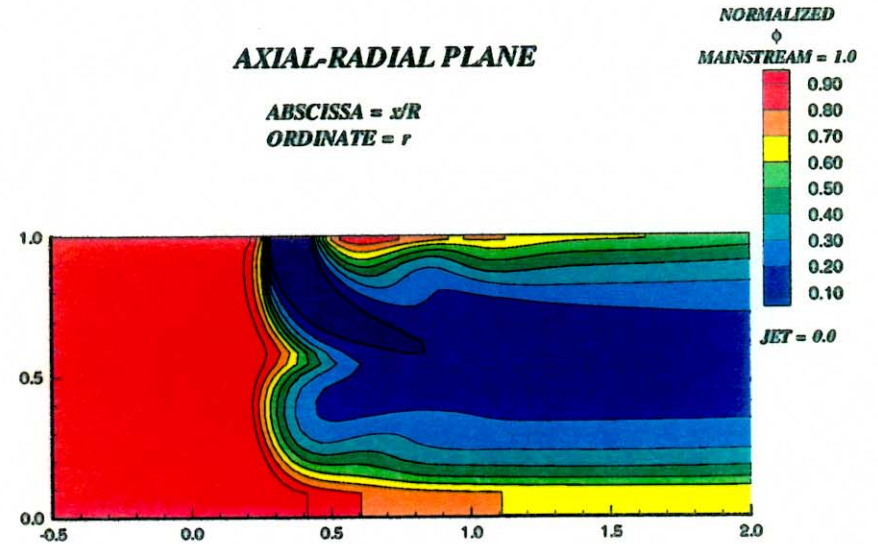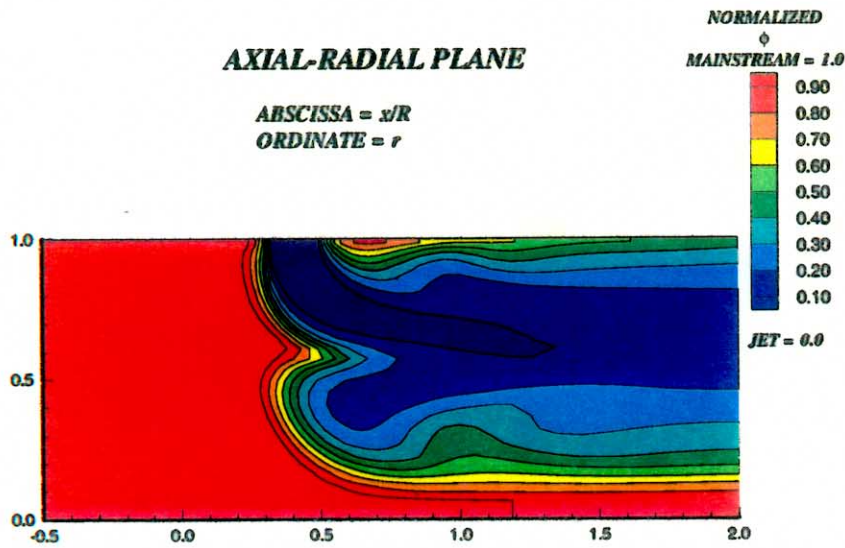
The axial-radial plane is through the
center of the jet

Figure-B6-5. Effect of the change in J on the equivalence ratio distribution
Clockwise from top left: J= 25, 52, and 80
45⁰ slots, L/W=8, MR=2.96, DR=2.28, 8 orifices/row

AXIAL-RADIAL PLANE

ABSCISSA = x/R
ORDINATE = r
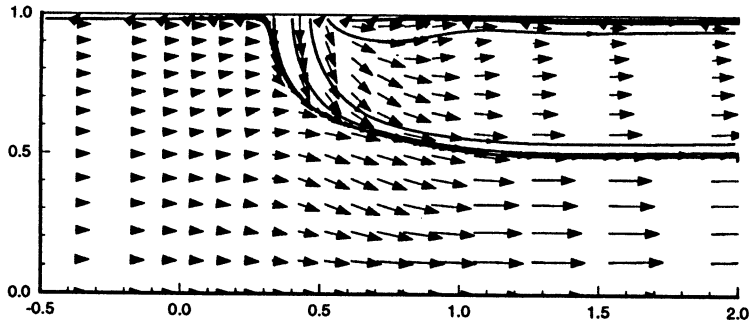
AXIAL-RADIAL PLANE

ABSCISSA = x/R
ORDINATE = r
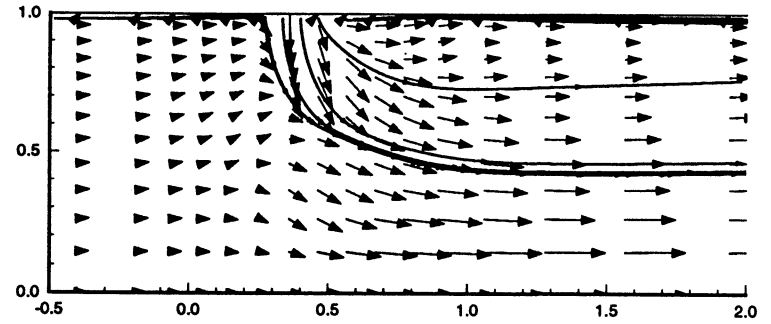
AXIAL-RADIAL PLANE

ABSCISSA = x/R
ORDINATE = r
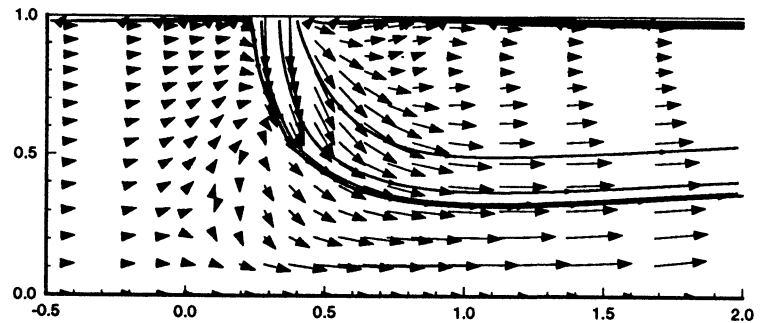
The axial-radial plane is through the center of the jet

Figure-B6-6. Effect of the change in J on the velocity distribution
Clockwise from top left: J= 25, 52, and 80
45° slots, L/W= 8, MR= 2.96, DR= 2.28, 8 orifices/row
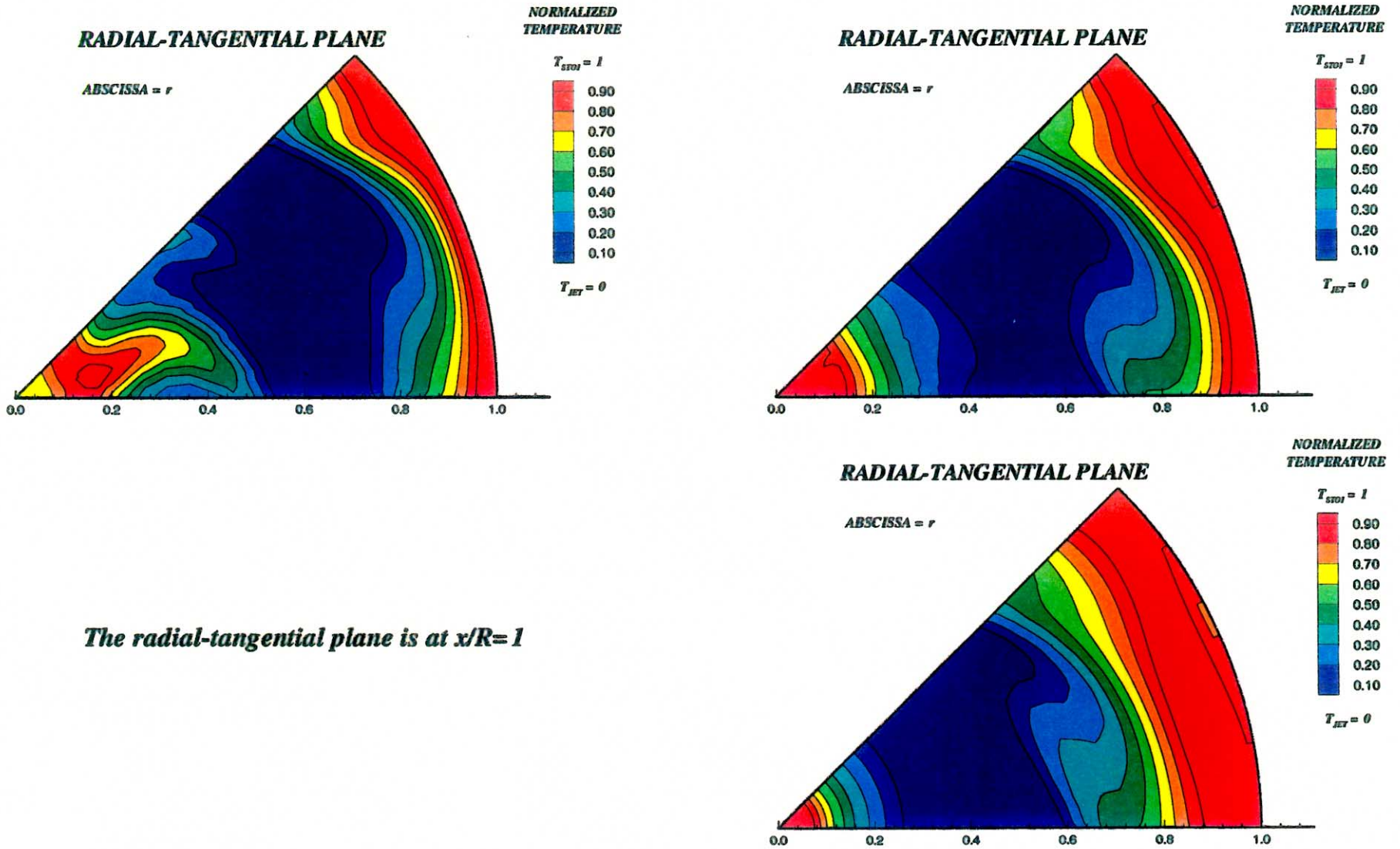
Figure-B6-7. Effect of the change in J on the temperature distribution
Clockwise from top left: J= 25, 52, and 80
45⁰ slots, L/W=8, MR=2.96, DR=2.28, 8 orifices/row
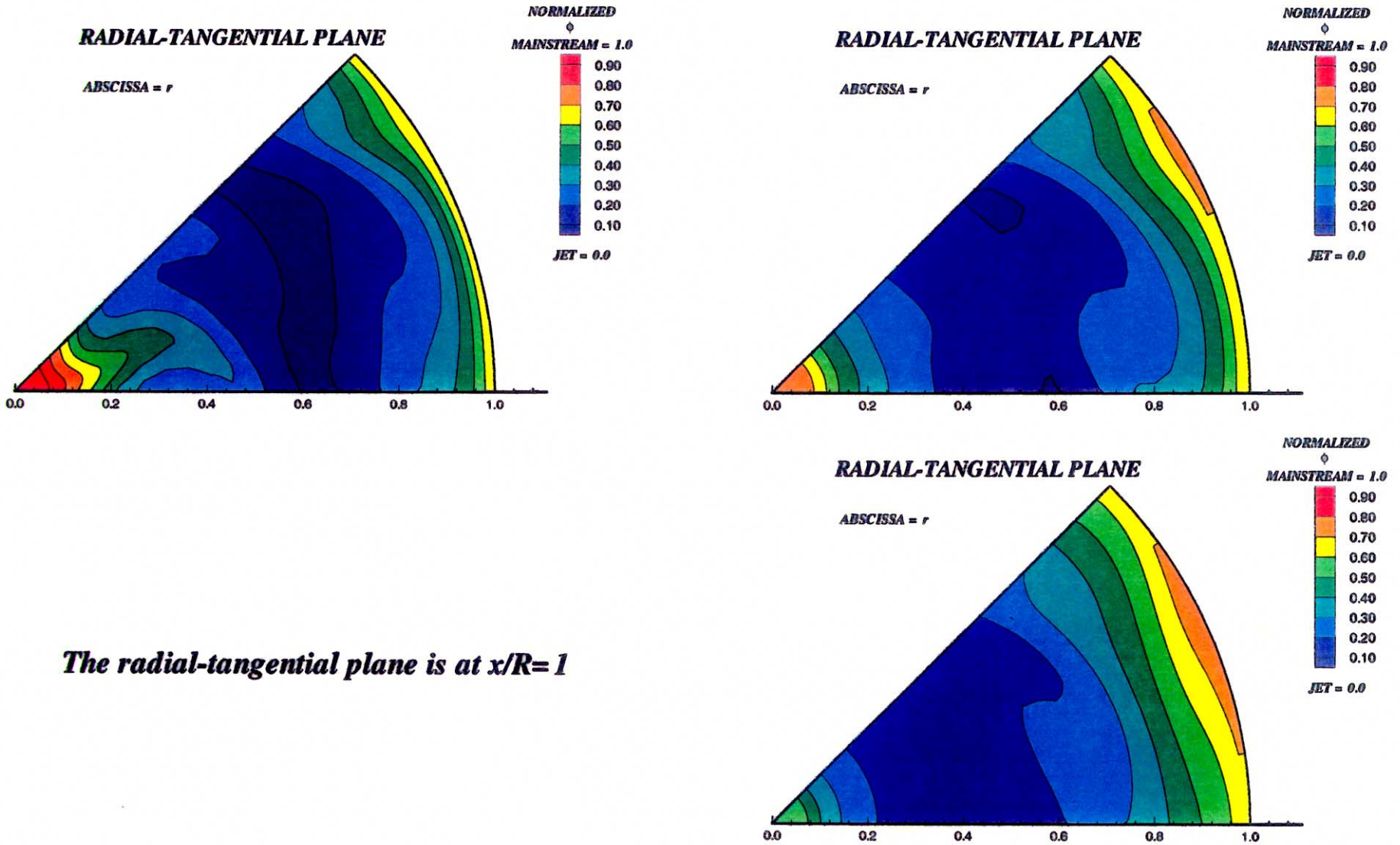
Figure-B6-8. Effect of the change in J on the equivalence ratio distribution
Clockwise from top left: J= 25, 52, and 80
45° slots, L/W= 8, MR= 2.96, DR= 2.28, 8 orifices/row

RADIAL-TANGENTIAL PLANE

ABSCISSA = r

RADIAL-TANGENTIAL PLANE

ABSCISSA = r

The radial-tangential plane is at x/R=1

RADIAL-TANGENTIAL PLANE

ABSCISSA = r
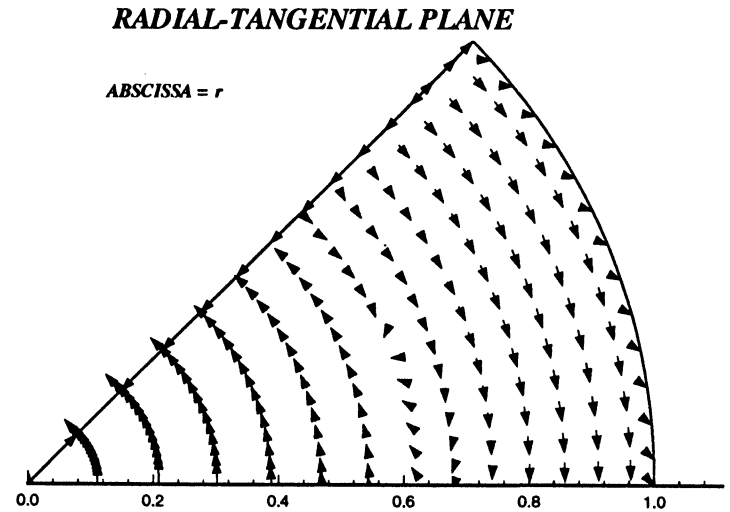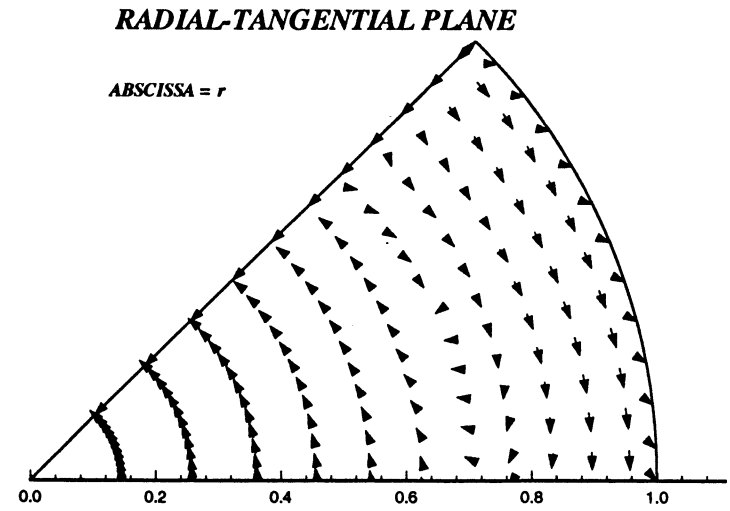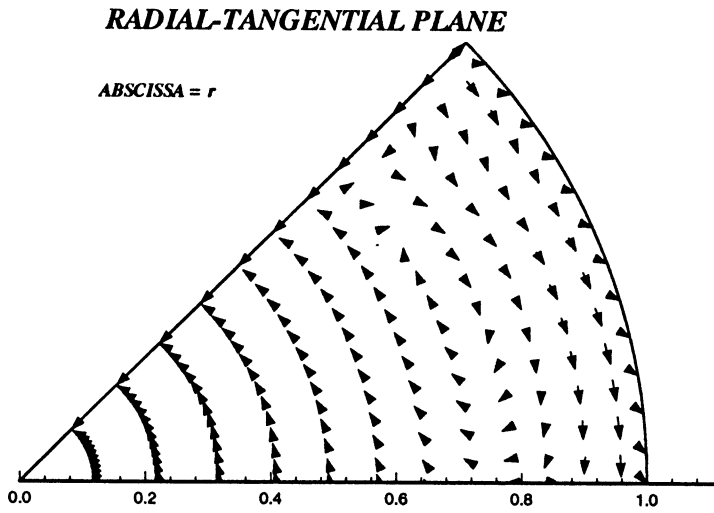
Figure-B6-9. Effect of the change in J on the velocity distribution
Clockwise from top left: J= 25, 52, and 80
45⁰ slots, L/W=8, MR=2.96, DR=2.28, 8 orifices/row

AXIAL-TANGENTIAL PLANE

ABCSISSA = x/R
ORDINATE = z/S

NORMALIZED TEMPERATURE

$T_{STOI} = 1$

0.90
0.80
0.70
0.60
0.50
0.40
0.30
0.20
0.10

$T_{JET} = 0$

AXIAL-TANGENTIAL PLANE

ABCSISSA = x/R
ORDINATE = z/S

NORMALIZED TEMPERATURE

$T_{STOI} = 1$

0.90
0.80
0.70
0.60
0.50
0.40
0.30
0.20
0.10

$T_{JET} = 0$

AXIAL-TANGENTIAL PLANE

ABCSISSA = x/R
ORDINATE = z/S

NORMALIZED TEMPERATURE

$T_{STOI} = 1$

0.90
0.80
0.70
0.60
0.50
0.40
0.30
0.20
0.10

$T_{JET} = 0$
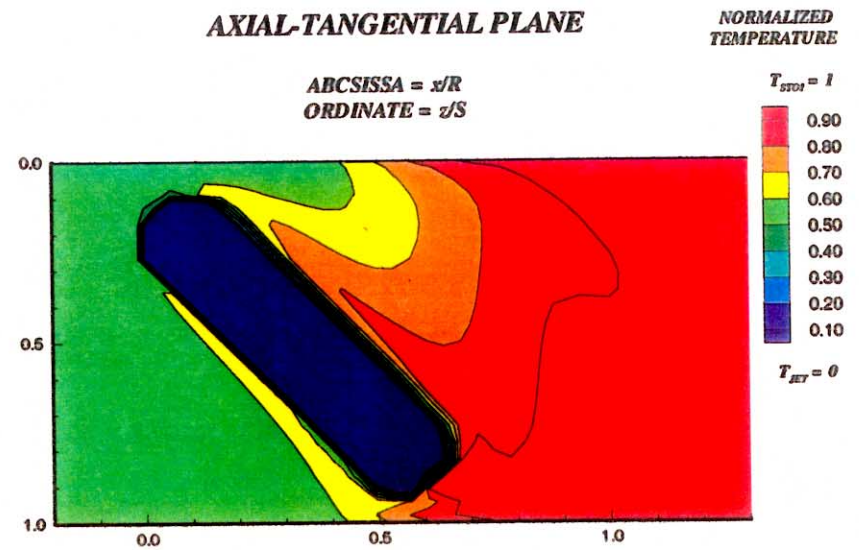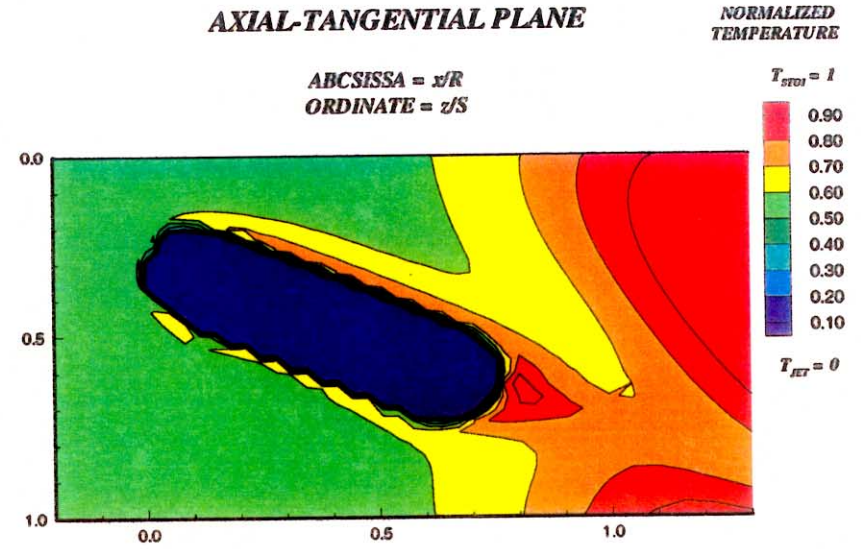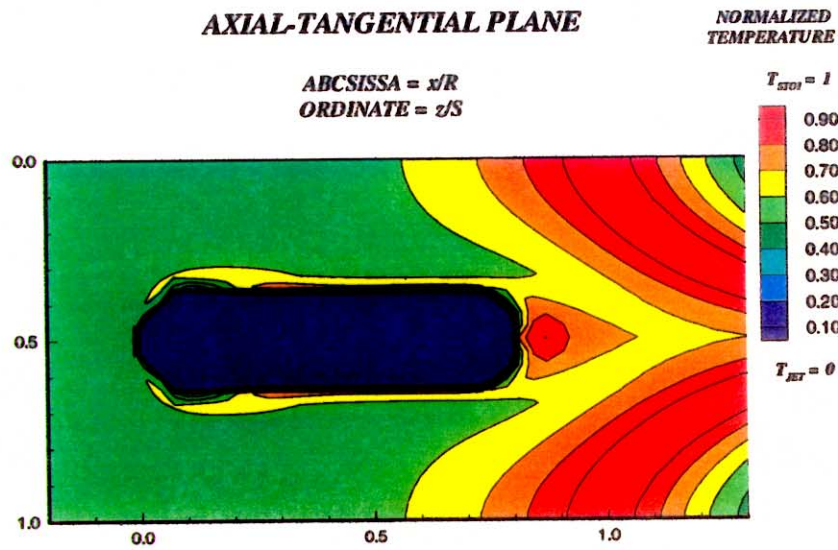
The axial-tangential plane is nearest the outer wall of the mixer

***Figure-B7-1. Effect of the change in slot slant angle on the temperature distribution
Clockwise from top left: 0^0 (in-line), 22.5^0, and 45^0
J=25, MR=2.96, DR=2.28, 8 orifices/row, slot L/W=4***
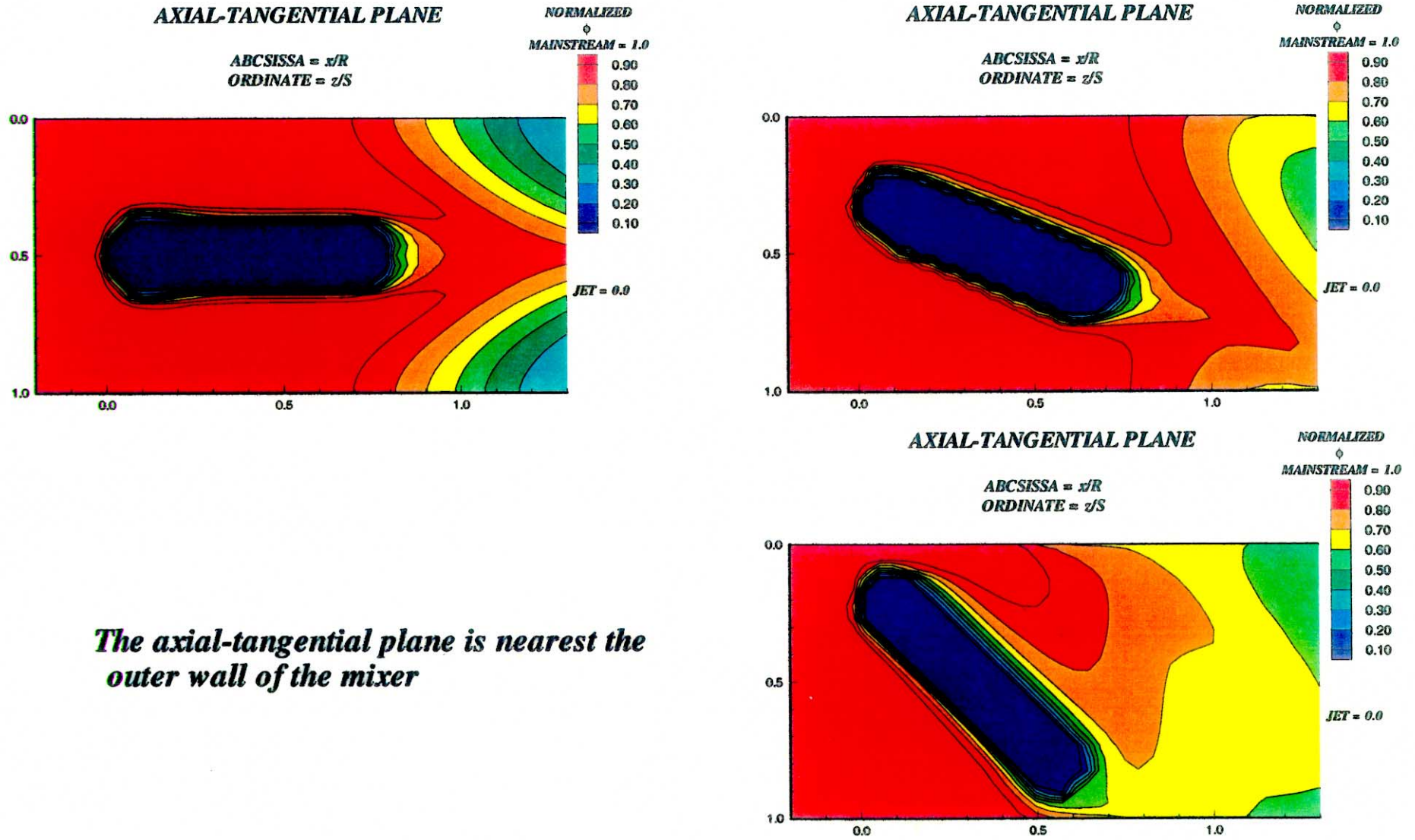
The axial-tangential plane is nearest the outer wall of the mixer

Figure-B7-2. Effect of the change in slot slant angle on the equivalence ratio distribution Clockwise from top left: 0° (in-line), 22.5°, and 45° J=25, MR=2.96, DR=2.28, 8 orifices/row, slot L/W=4

AXIAL-TANGENTIAL PLANE

ABCSISSA = x/R
ORDINATE = z/S

AXIAL-TANGENTIAL PLANE

ABCSISSA = x/R
ORDINATE = z/S

AXIAL-TANGENTIAL PLANE

ABCSISSA = x/R
ORDINATE = z/S
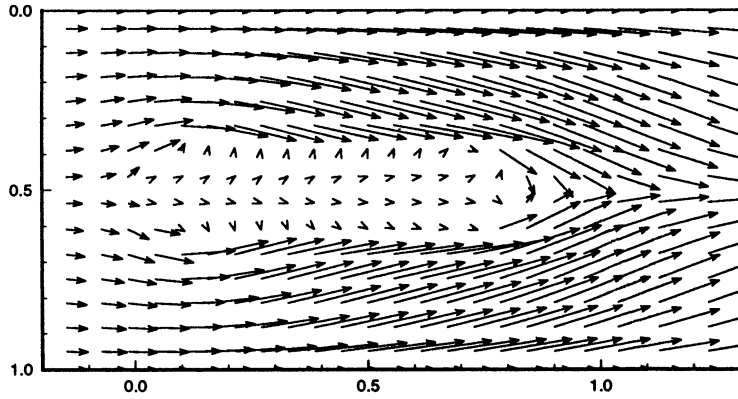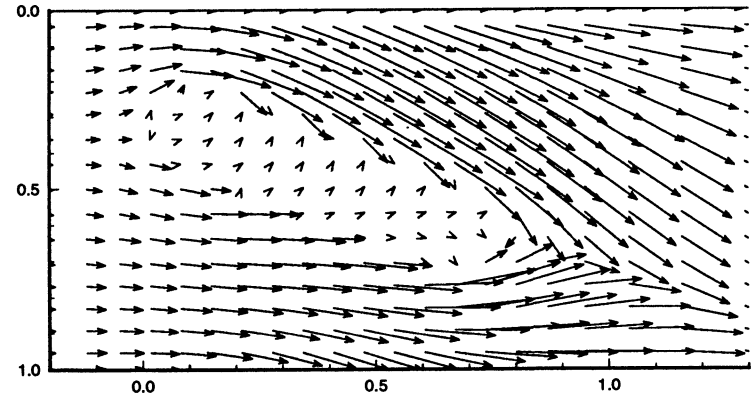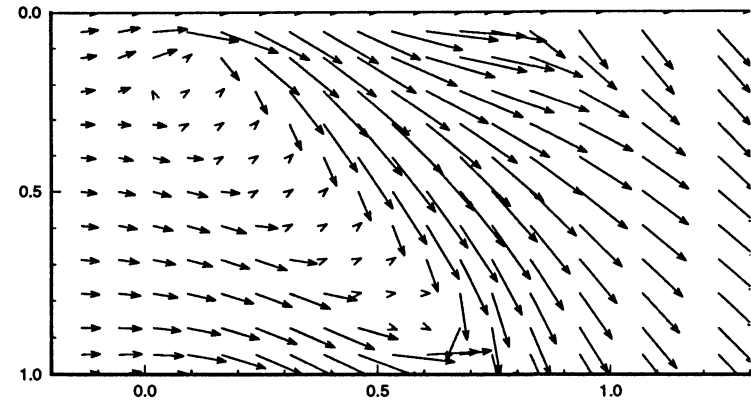
The axial-tangential plane is nearest the outer wall of the mixer

Figure-B7-3. Effect of the change in slot slant angle on the velocity distribution
Clockwise from top left: 0^0 (in-line), 22.5^0, and 45^0
J=25, MR=2.96, DR=2.28, 8 orifices/row, slot L/W=4

AXIAL-RADIAL PLANE

ABSCISSA = x/R
ORDINATE = r

NORMALIZED TEMPERATURE

$T_{STOI} = 1$

0.90
0.80
0.70
0.60
0.50
0.40
0.30
0.20
0.10

$T_{JET} = 0$

AXIAL-RADIAL PLANE

ABSCISSA = x/R
ORDINATE = r

NORMALIZED TEMPERATURE

$T_{STOI} = 1$

0.90
0.80
0.70
0.60
0.50
0.40
0.30
0.20
0.10

$T_{JET} = 0$

The axial-radial plane is through the center of the jet

AXIAL-RADIAL PLANE

ABSCISSA = x/R
ORDINATE = r

NORMALIZED TEMPERATURE

$T_{STOI} = 1$

0.90
0.80
0.70
0.60
0.50
0.40
0.30
0.20
0.10

$T_{JET} = 0$
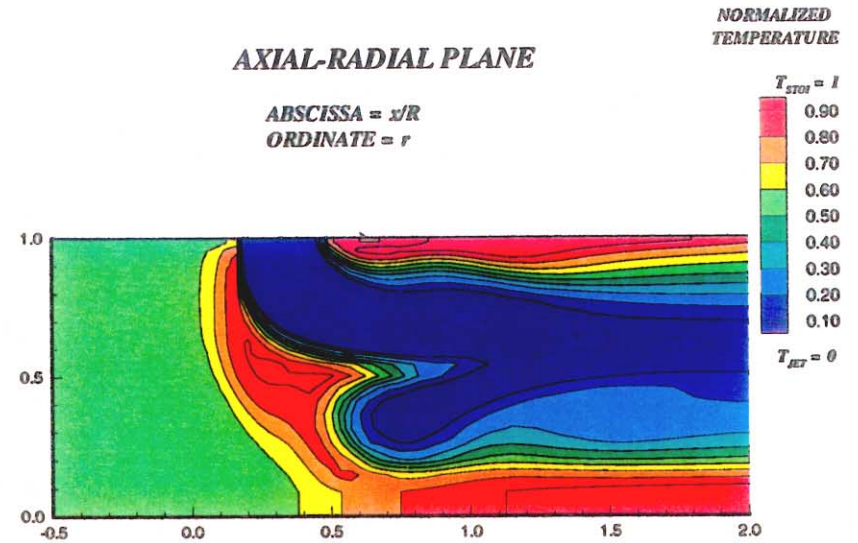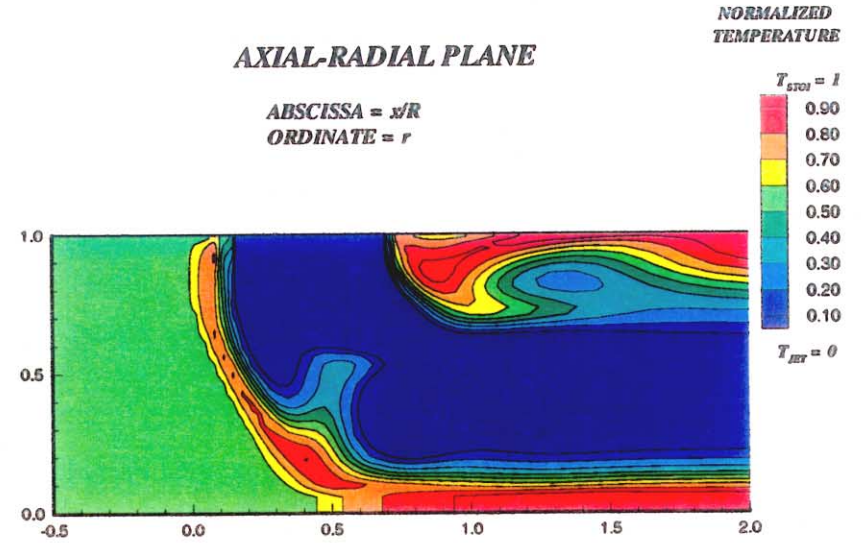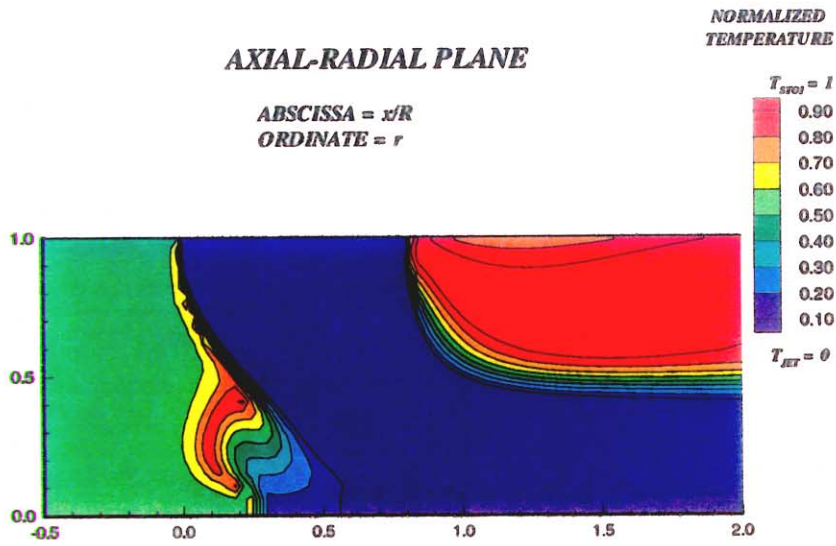
Figure-B7-4. Effect of the change in slot slant angle on the temperature distribution
Clockwise from top left: 0^0 (in-line), 22.5^0, and 45^0
J=25, MR=2.96, DR=2.28, 8 orifices/row, slot L/W=4
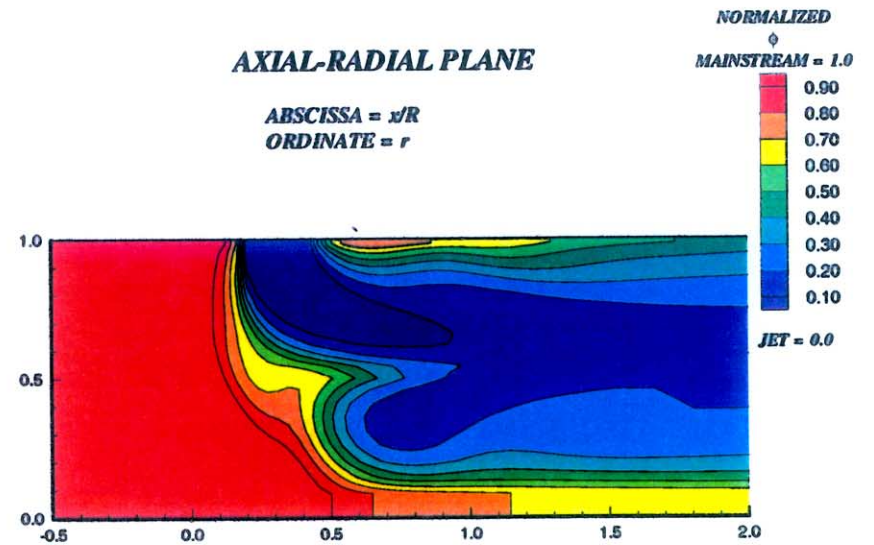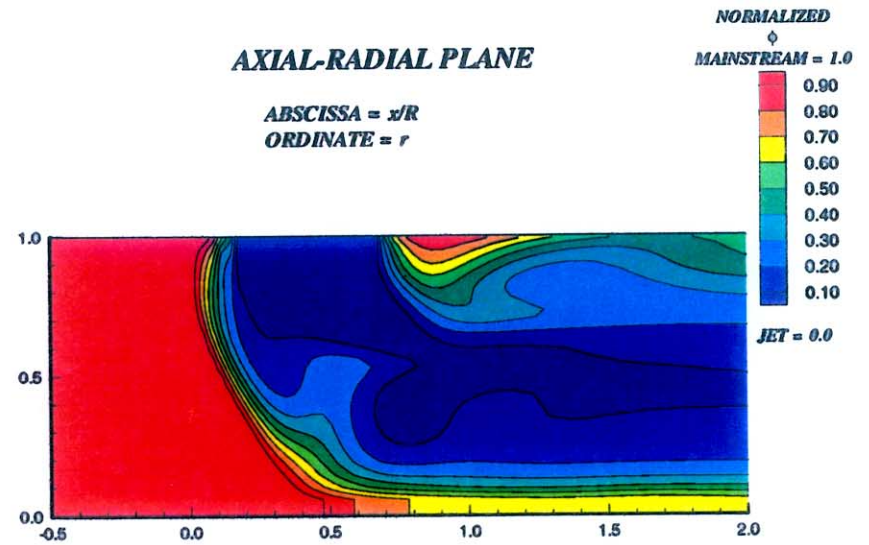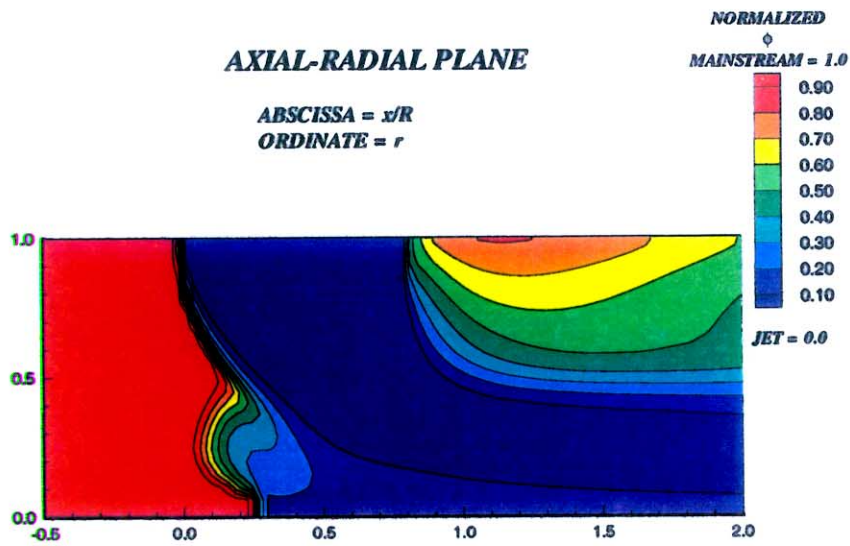
The axial-radial plane is through the center of the jet

Figure-B7-5. Effect of the change in slot slant angle on the equivalence ratio distribution
Clockwise from top left: 0^0 (in-line), 22.5^0, and 45^0
J=25, MR=2.96, DR=2.28, 8 orifices/row, slot L/W=4

AXIAL-RADIAL PLANE

ABSCISSA = x/R
ORDINATE = r
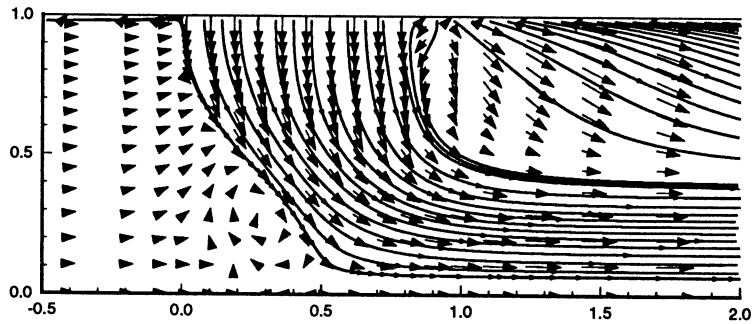
AXIAL-RADIAL PLANE

ABSCISSA = x/R
ORDINATE = r
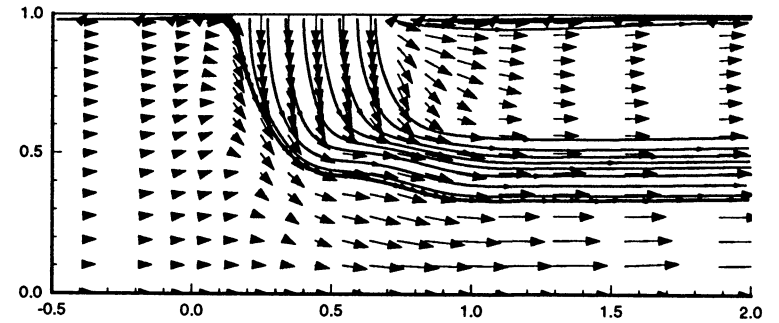
**AXIAL-RADIAL PLANE**

ABSCISSA = x/R
ORDINATE = r
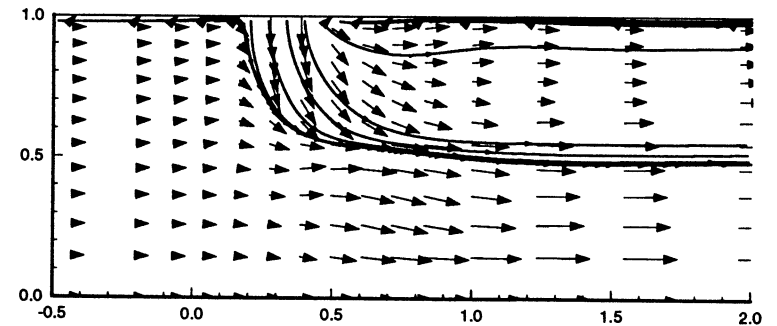
The axial-radial plane is through the center of the jet

Figure-B7-6. Effect of the change in slot slant angle on the velocity distribution
Clockwise from top left: 0^0 (in-line), 22.5^0, and 45^0
*J=25, MR=2.96, DR=2.28, 8 orifices/row, slot L/W=4*

RADIAL-TANGENTIAL PLANE

ABSCISSA = r

NORMALIZED TEMPERATURE

$T_{STOI} = 1$

0.90
0.80
0.70
0.60
0.50
0.40
0.30
0.20
0.10

$T_{JET} = 0$

RADIAL-TANGENTIAL PLANE

ABSCISSA = r

NORMALIZED TEMPERATURE

$T_{STOI} = 1$

0.90
0.80
0.70
0.60
0.50
0.40
0.30
0.20
0.10

$T_{JET} = 0$

The radial-tangential plane is at x/R=1

RADIAL-TANGENTIAL PLANE

ABSCISSA = r

NORMALIZED TEMPERATURE

$T_{STOI} = 1$

0.90
0.80
0.70
0.60
0.50
0.40
0.30
0.20
0.10

$T_{JET} = 0$
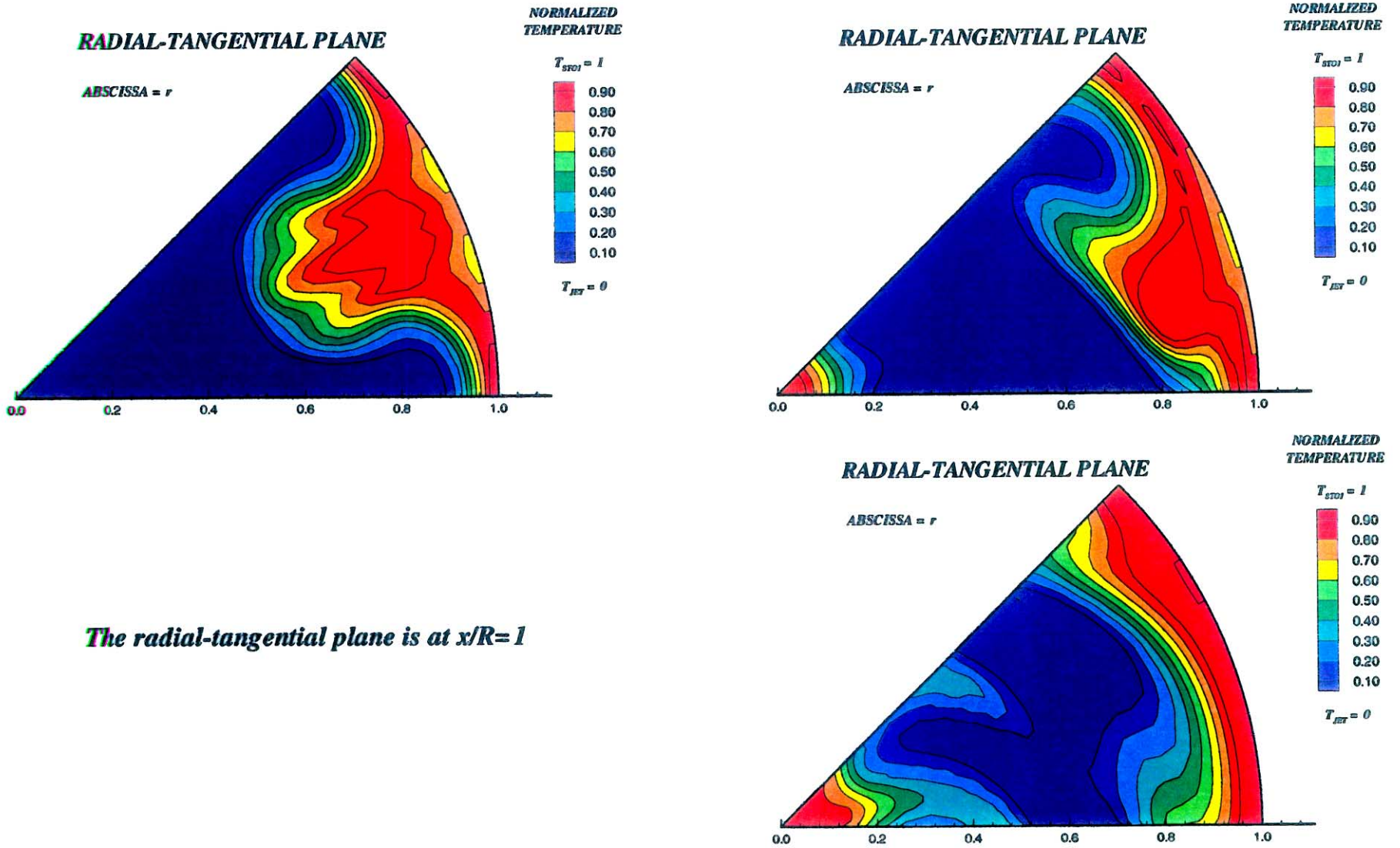
Figure-B7-7. Effect of the change in slot slant angle on the temperature distribution
Clockwise from top left: 0^0 (in-line), 22.5^0, and 45^0
J=25, MR=2.96, DR=2.28, 8 orifices/row, slot L/W=4
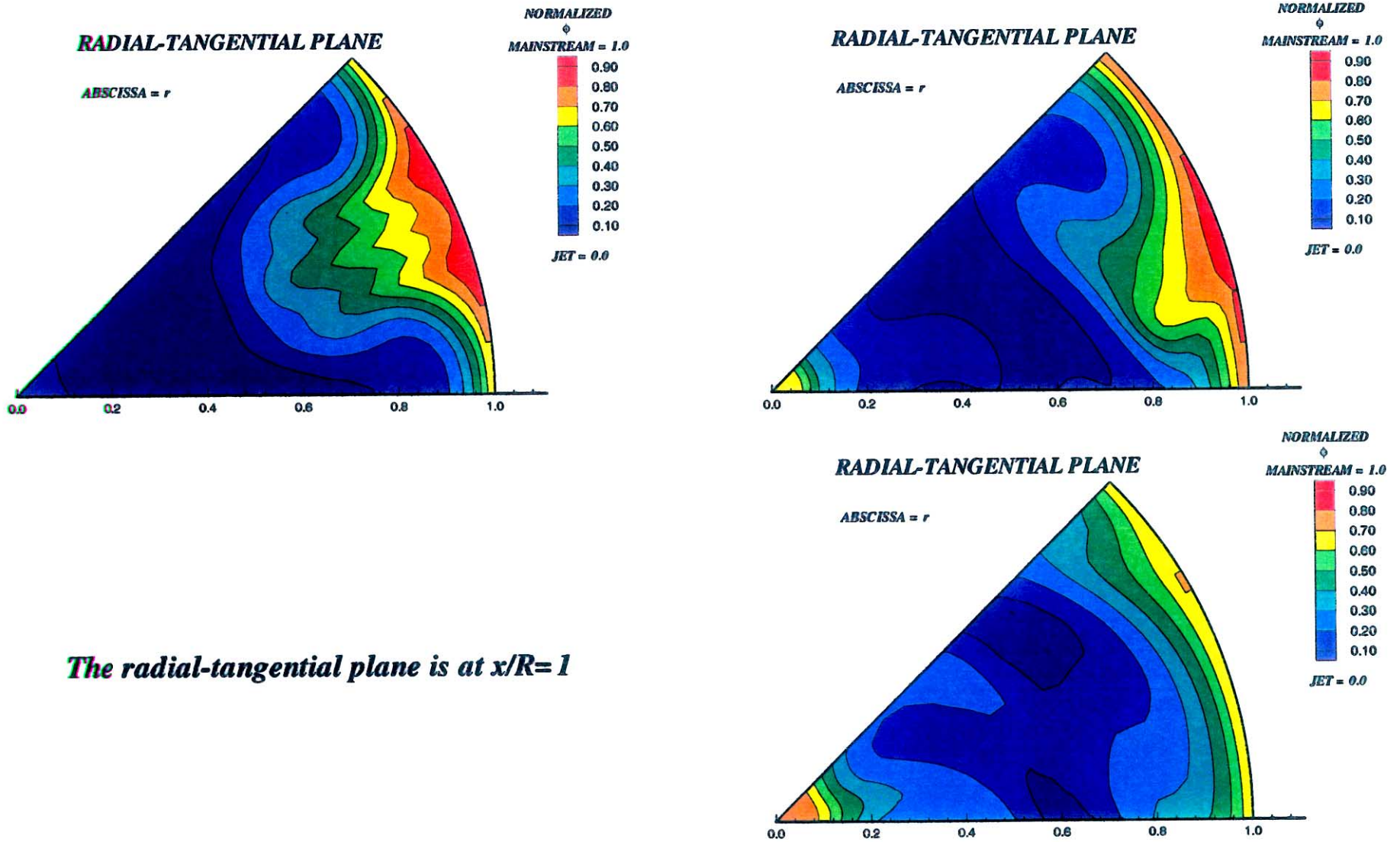
The radial-tangential plane is at x/R= 1

Figure-B7-8. Effect of the change in slot slant angle on the equivalence ratio distribution
Clockwise from top left: 0° (in-line), 22.5°, and 45°
J=25, MR=2.96, DR=2.28, 8 orifices/row, slot L/W=4

RADIAL-TANGENTIAL PLANE

ABSCISSA = r

RADIAL-TANGENTIAL PLANE

ABSCISSA = r

RADIAL-TANGENTIAL PLANE

ABSCISSA = r
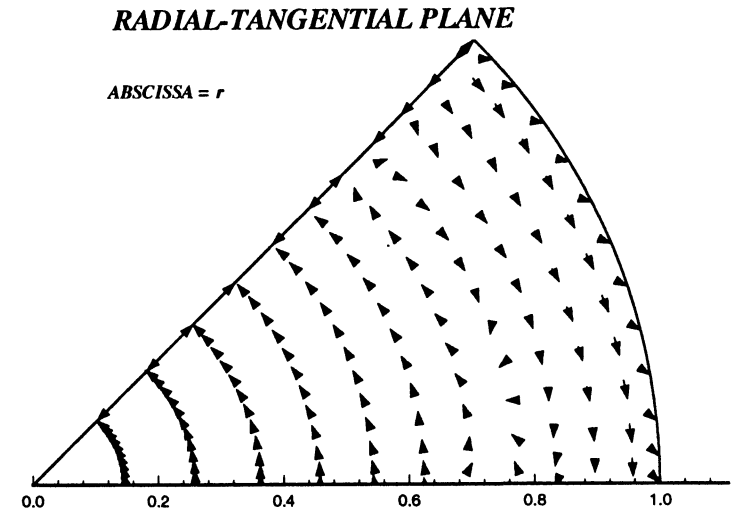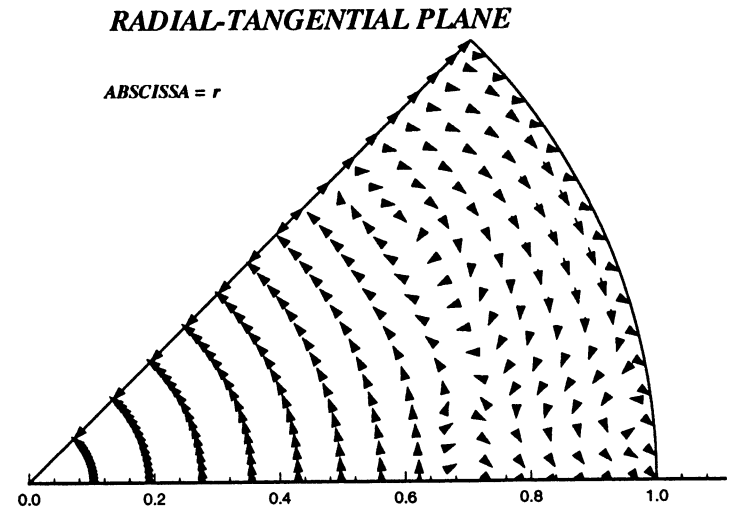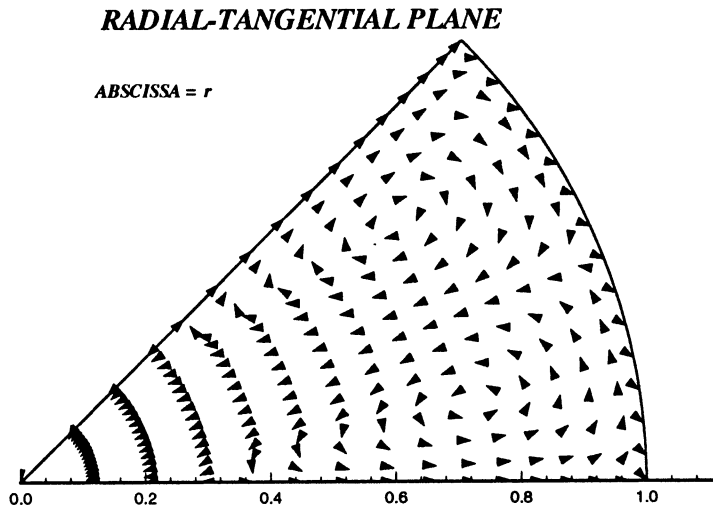
The radial-tangential plane is at x/R=1

Figure-B7-9. Effect of the change in slot slant angle on the velocity distribution
Clockwise from top left: 0^0 (in-line), 22.5^0, and 45^0
J=25, MR=2.96, DR=2.28, 8 orifices/row, slot L/W=4

Axial-tangential plane nearest the outer wall of the mixer

NORMALIZED TEMPERATURE

ABCSISSA = x/R
ORDINATE = z/S

$T_{STOI} = 1$

0.90
0.80
0.70
0.60
0.50
0.40
0.30
0.20
0.10

$T_{JET} = 0$

AXIAL-TANGENTIAL PLANE

NORMALIZED TEMPERATURE

ABCSISSA = x/R
ORDINATE = z/S

$T_{STOI} = 1$

0.90
0.80
0.70
0.60
0.50
0.40
0.30
0.20
0.10

$T_{JET} = 0$

AXIAL-TANGENTIAL PLANE

NORMALIZED TEMPERATURE

ABCSISSA = x/R
ORDINATE = z/S

$T_{STOI} = 1$

0.90
0.80
0.70
0.60
0.50
0.40
0.30
0.20
0.10

$T_{JET} = 0$

AXIAL-TANGENTIAL PLANE

NORMALIZED TEMPERATURE

ABCSISSA = x/R
ORDINATE = z/S

$T_{STOI} = 1$

0.90
0.80
0.70
0.60
0.50
0.40
0.30
0.20
0.10

$T_{JET} = 0$

Figure-B8-1. Effect of the change in slot slant angle on the temperature distribution
Clockwise from top left: 0^0 (in-line), 22.5^0, 45^0, and 67.5^0
J=52, MR=2.96, DR=2.28, 8 orifices/row, slot L/W=4
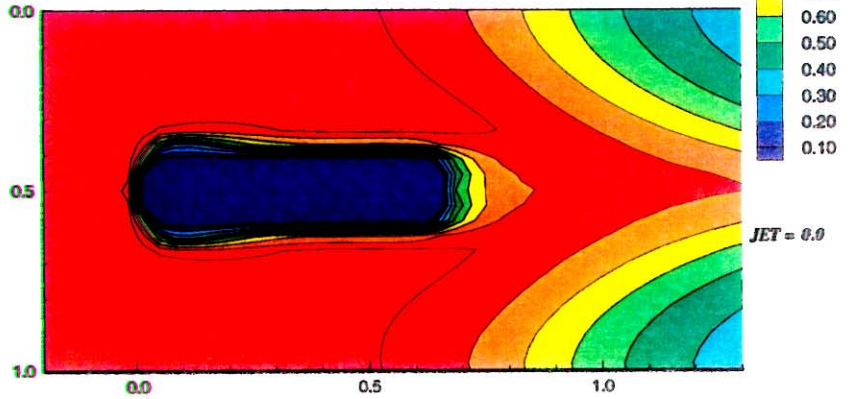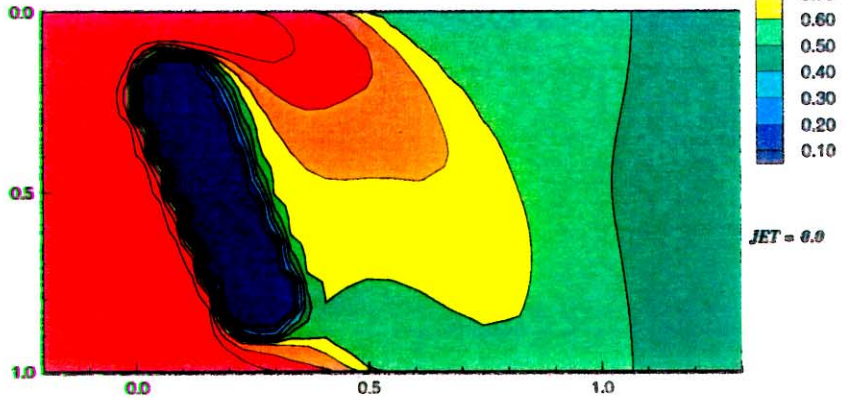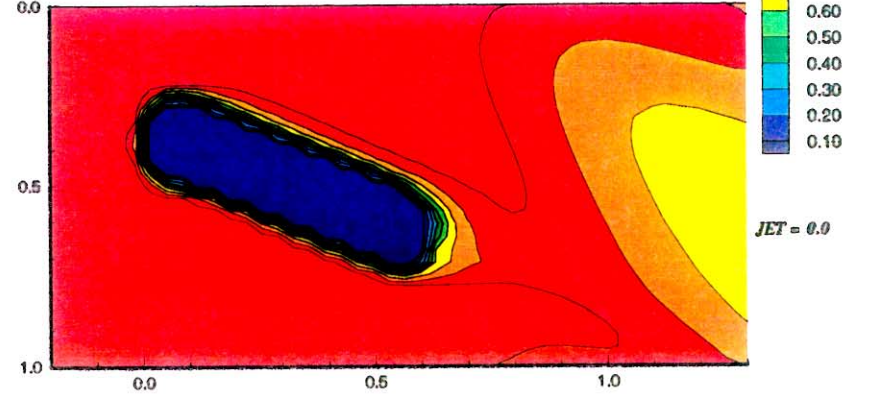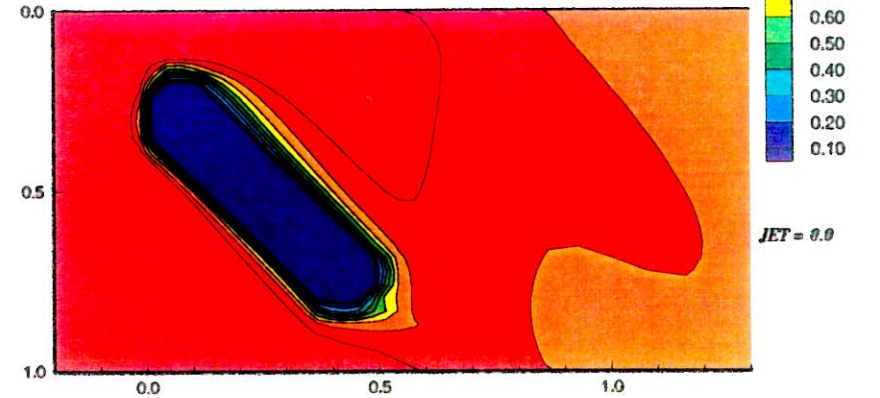
Figure-B8-2. *Effect of the change in slot slant angle on the equivalence ratio distribution*
Clockwise from top left: 0° (in-line), 22.5°, 45°, and 67.5°
J=52, MR=2.96, DR=2.28, 8 orifices/row, slot L/W=4

**axial-tangential plane nearest**
the outer wall of the mixer

ABCSISSA = x/R
ORDINATE = z/S
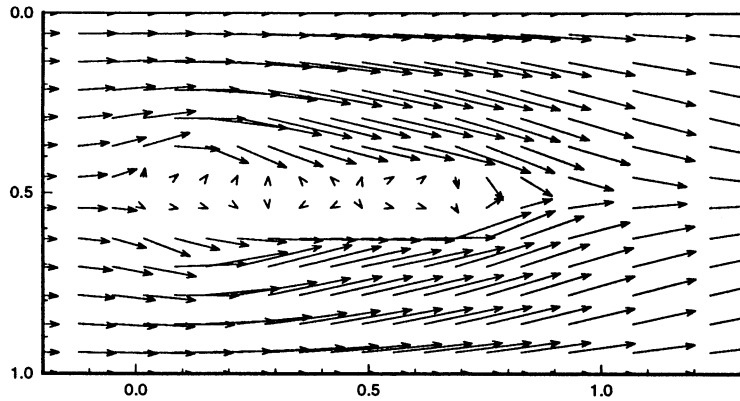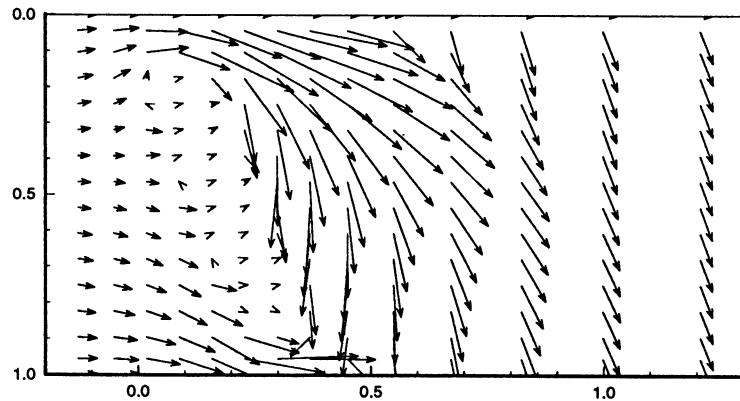
AXIAL-TANGENTIAL PLANE

ABCSISSA = x/R
ORDINATE = z/S

AXIAL-TANGENTIAL PLANE

ABCSISSA = x/R
ORDINATE = z/S
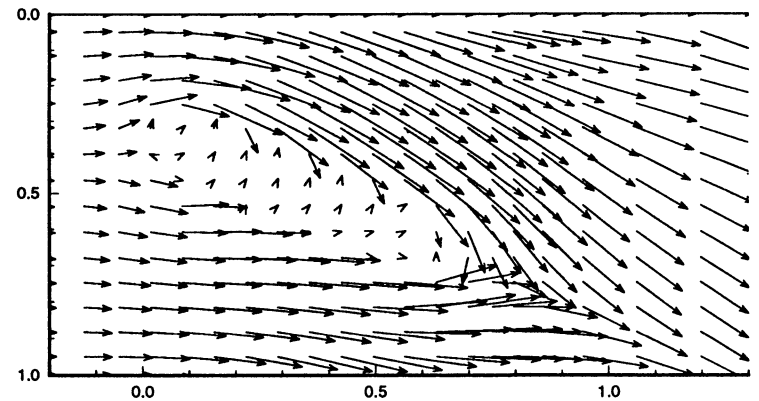
AXIAL-TANGENTIAL PLANE

ABCSISSA = x/R
ORDINATE = z/S
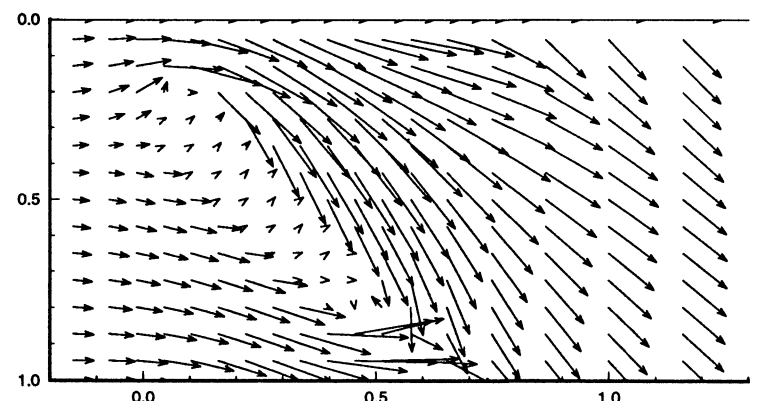
Figure-B8-3. Effect of the change in slot slant angle on the velocity distribution
Clockwise from top left: 0^0 (in-line), 22.5^0, 45^0, and 67.5^0
J=52, MR=2.96, DR=2.28, 8 orifices/row, slot L/W=4

Axial-radial plane through the center of the jet

NORMALIZED TEMPERATURE

ABSCISSA = x/R
ORDINATE = r

$T_{STOI} = 1$

0.90
0.80
0.70
0.60
0.50
0.40
0.30
0.20
0.10

$T_{JET} = 0$

AXIAL-RADIAL PLANE

NORMALIZED TEMPERATURE

ABSCISSA = x/R
ORDINATE = r

$T_{STOI} = 1$

0.90
0.80
0.70
0.60
0.50
0.40
0.30
0.20
0.10

$T_{JET} = 0$

AXIAL-RADIAL PLANE

NORMALIZED TEMPERATURE

ABSCISSA = x/R
ORDINATE = r

$T_{STOI} = 1$

0.90
0.80
0.70
0.60
0.50
0.40
0.30
0.20
0.10

$T_{JET} = 0$

AXIAL-RADIAL PLANE

NORMALIZED TEMPERATURE

ABSCISSA = x/R
ORDINATE = r

$T_{STOI} = 1$

0.90
0.80
0.70
0.60
0.50
0.40
0.30
0.20
0.10

$T_{JET} = 0$
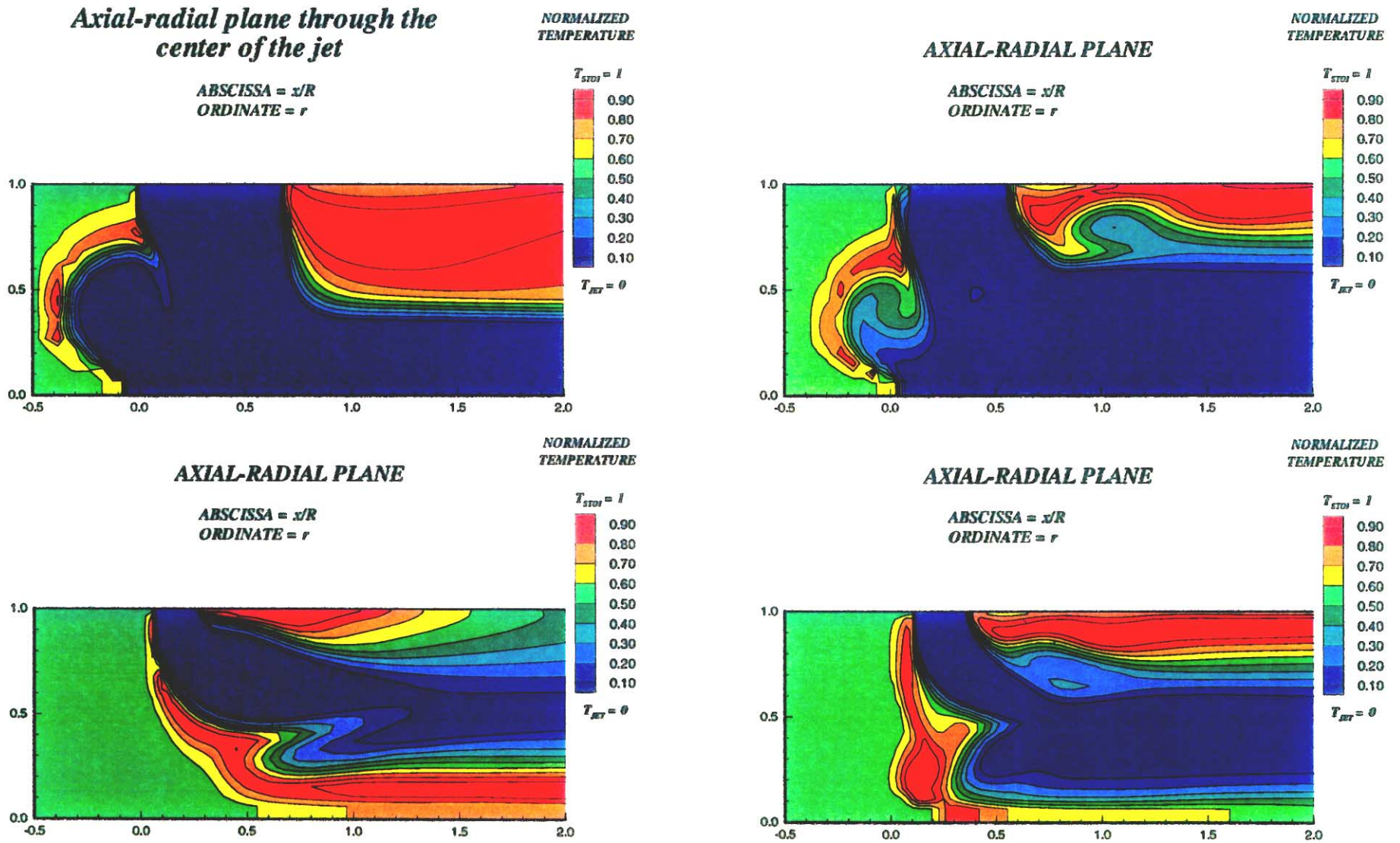
Figure-B8-4. Effect of the change in slot slant angle on the temperature distribution
Clockwise from top left: 0^0 (in-line), 22.5^0, 45^0, and 67.5^0
J=52, MR=2.96, DR=2.28, 8 orifices/row, slot L/W=4

axial-radial plane through the center of the jet

NORMALIZED
◊
MAINSTREAM = 1.0

ABSCISSA = x/R
ORDINATE = r

0.90
0.80
0.70
0.60
0.50
0.40
0.30
0.20
0.10

JET = 0.0

AXIAL-RADIAL PLANE

NORMALIZED
◊
MAINSTREAM = 1.0

ABSCISSA = x/R
ORDINATE = r

0.90
0.80
0.70
0.60
0.50
0.40
0.30
0.20
0.10

JET = 0.0

AXIAL-RADIAL PLANE

NORMALIZED
◊
MAINSTREAM = 1.0

ABSCISSA = x/R
ORDINATE = r

0.90
0.80
0.70
0.60
0.50
0.40
0.30
0.20
0.10

JET = 0.0

AXIAL-RADIAL PLANE

NORMALIZED
◊
MAINSTREAM = 1.0

ABSCISSA = x/R
ORDINATE = r

0.90
0.80
0.70
0.60
0.50
0.40
0.30
0.20
0.10

JET = 0.0
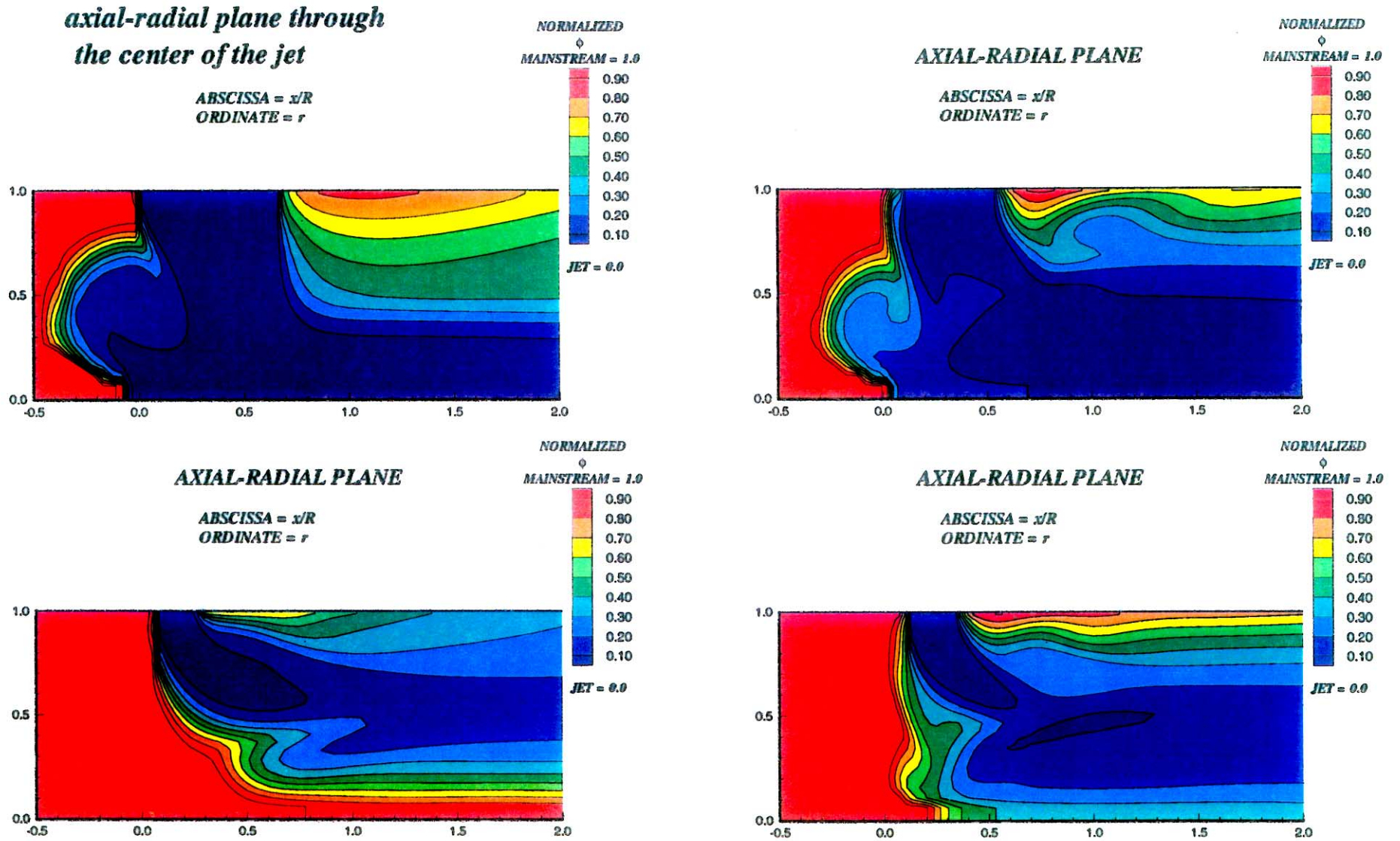
Figure-B8-5. Effect of the change in slot slant angle on the equivalence ratio distribution
Clockwise from top left: 0° (in-line), 22.5°, 45°, and 67.5°
J=52, MR=2.96, DR=2.28, 8 orifices/row, slot L/W=4

**axial-radial plane through
the center of the jet**

AXISSA = x/R
ORDINATE = r
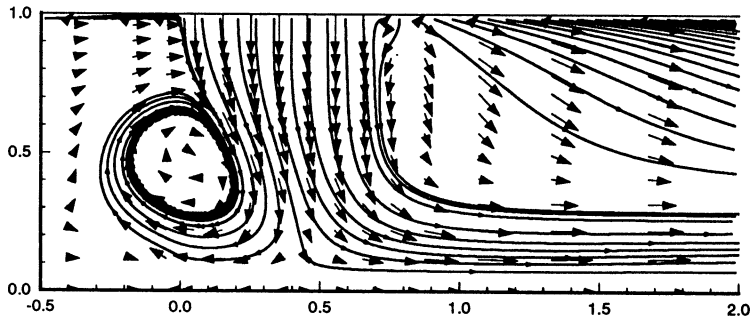
AXIAL-RADIAL PLANE

ABSCISSA = x/R
ORDINATE = r
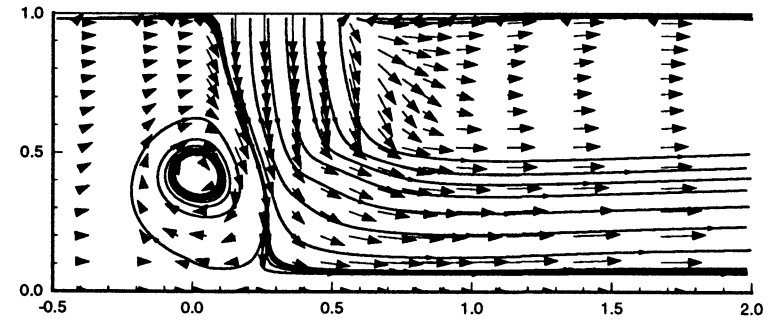
AXIAL-RADIAL PLANE

ABSCISSA = x/R
ORDINATE = r
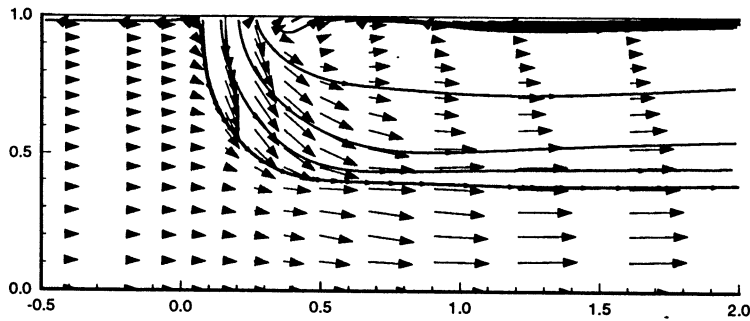
AXIAL-RADIAL PLANE

ABSCISSA = x/R
ORDINATE = r
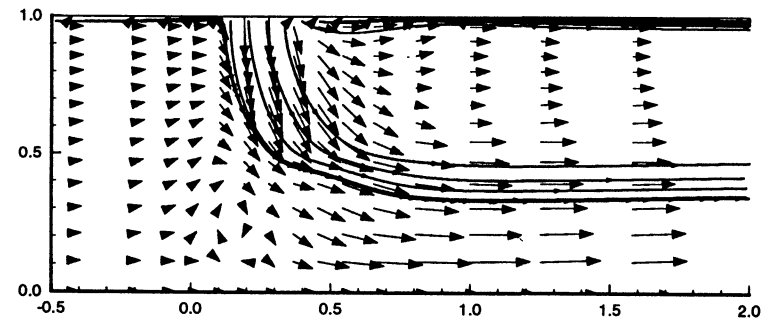
*Figure-B8-6. Effect of the change in slot slant angle on the velocity distribution
Clockwise from top left: 0^0 (in-line), 22.5^0, 45^0, and 67.5^0
J= 52, MR= 2.96, DR= 2.28, 8 orifices/row, slot L/W= 4*
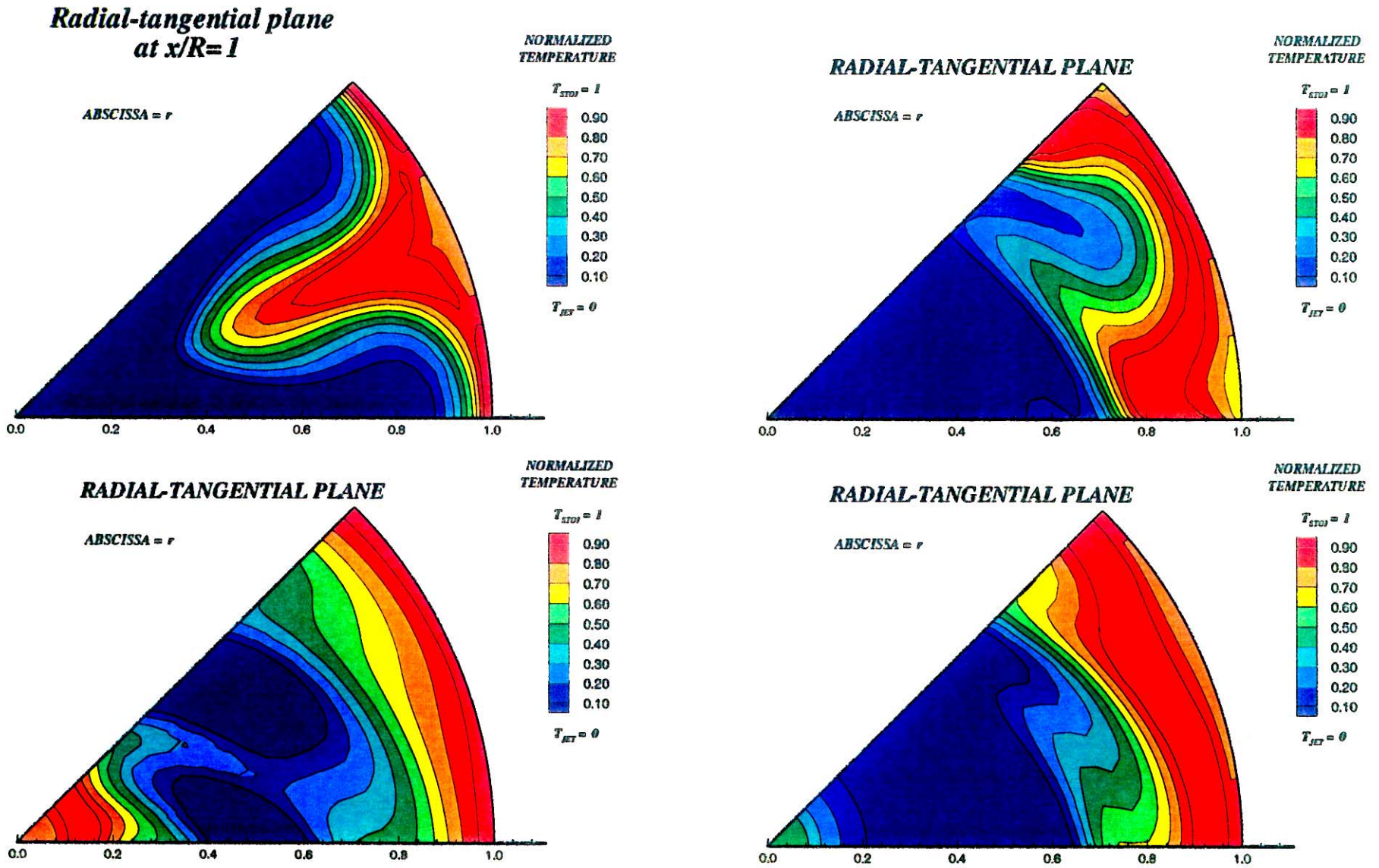
Figure-B8-7. Effect of the change in slot slant angle on the temperature distribution
Clockwise from top left: 0^0 (in-line), 22.5^0, 45^0, and 67.5^0
J=52, MR=2.96, DR=2.28, 8 orifices/row, slot L/W=4

radial-tangential plane at x/R=1

ABSCISSA = r

NORMALIZED
◇
MAINSTREAM = 1.0

0.90
0.80
0.70
0.60
0.50
0.40
0.30
0.20
0.10

JET = 0.0

RADIAL-TANGENTIAL PLANE

ABSCISSA = r

NORMALIZED
◇
MAINSTREAM = 1.0

0.90
0.80
0.70
0.60
0.50
0.40
0.30
0.20
0.10

JET = 0.0

RADIAL-TANGENTIAL PLANE

ABSCISSA = r

NORMALIZED
◇
MAINSTREAM = 1.0

0.90
0.80
0.70
0.60
0.50
0.40
0.30
0.20
0.10

JET = 0.0

RADIAL-TANGENTIAL PLANE

ABSCISSA = r

NORMALIZED
◇
MAINSTREAM = 1.0

0.90
0.80
0.70
0.60
0.50
0.40
0.30
0.20
0.10

JET = 0.0
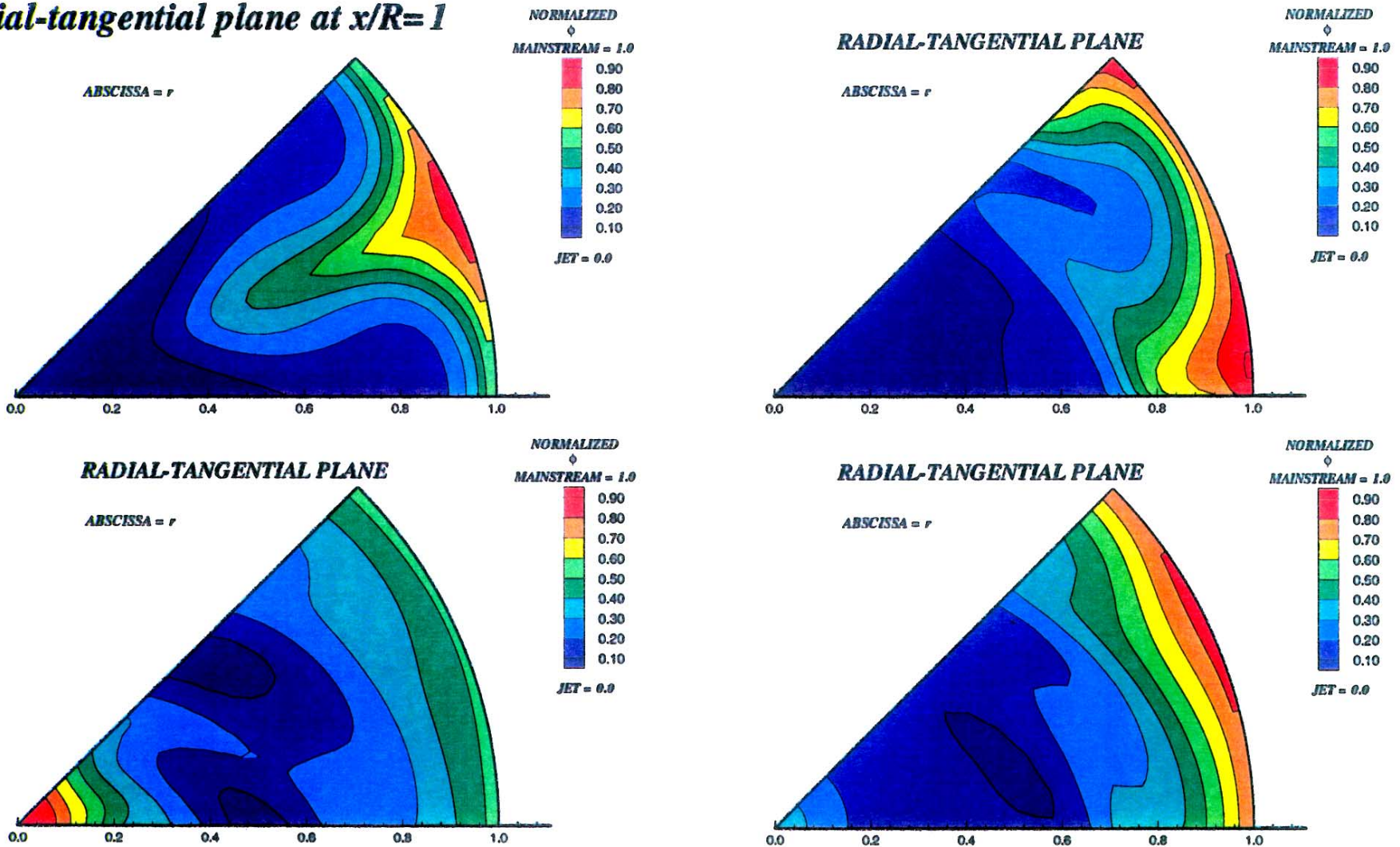
Figure-B8-8. Effect of the change in slot slant angle on the equivalence ratio distribution
Clockwise from top left: 0^0 (in-line), 22.5^0, 45^0, and 67.5^0
J=52, MR=2.96, DR=2.28, 8 orifices/row, slot L/W=4

Radial-tangential plane at x/R=1

ABSCISSA = r

RADIAL-TANGENTIAL PLANE

ABSCISSA = r

RADIAL-TANGENTIAL PLANE

ABSCISSA = r

RADIAL-TANGENTIAL PLANE

ABSCISSA = r
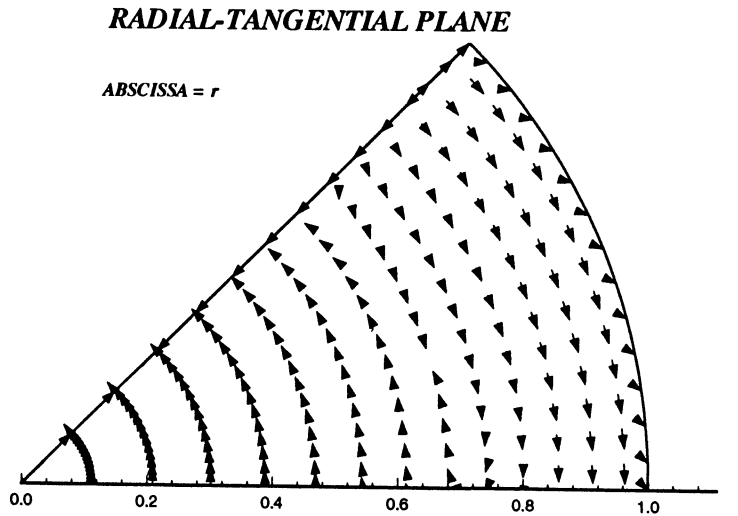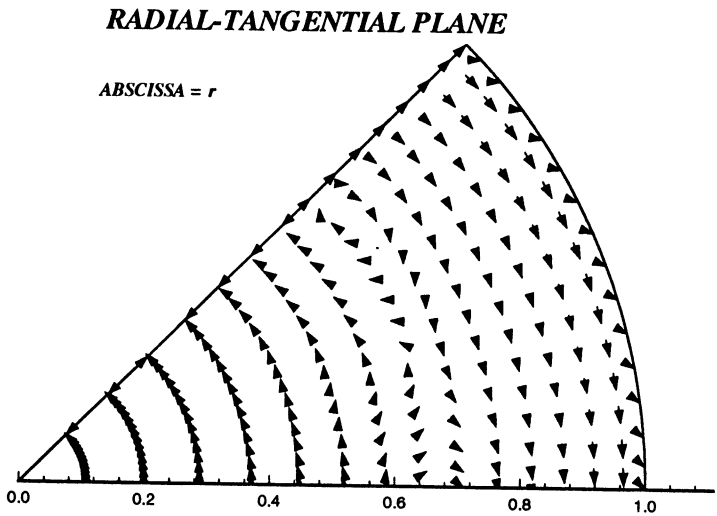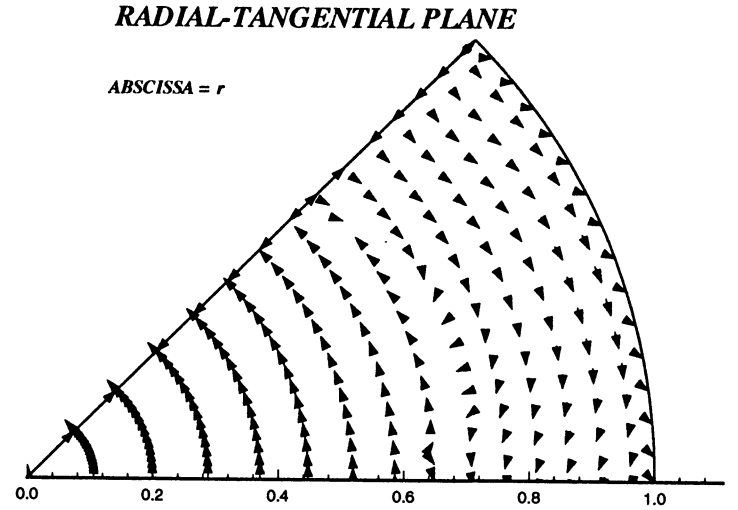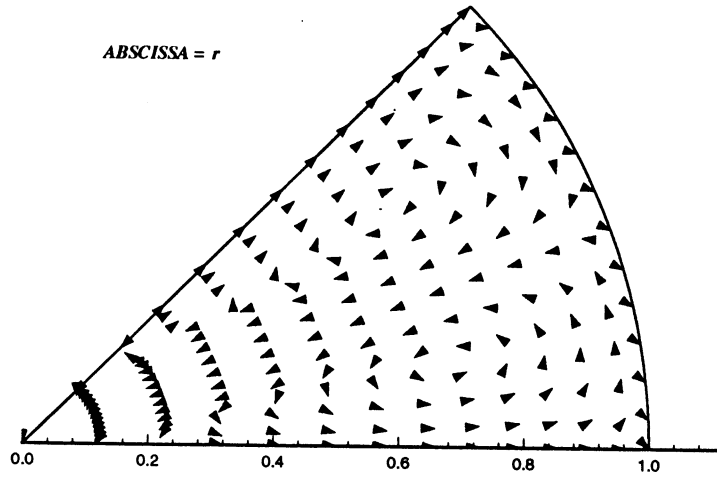
Figure-B8-9. Effect of the change in slot slant angle on the velocity distribution
Clockwise from top left: 0° (in-line), 22.5°, 45°, and 67.5°
J=52, MR=2.96, DR=2.28, 8 orifices/row, slot L/W=4
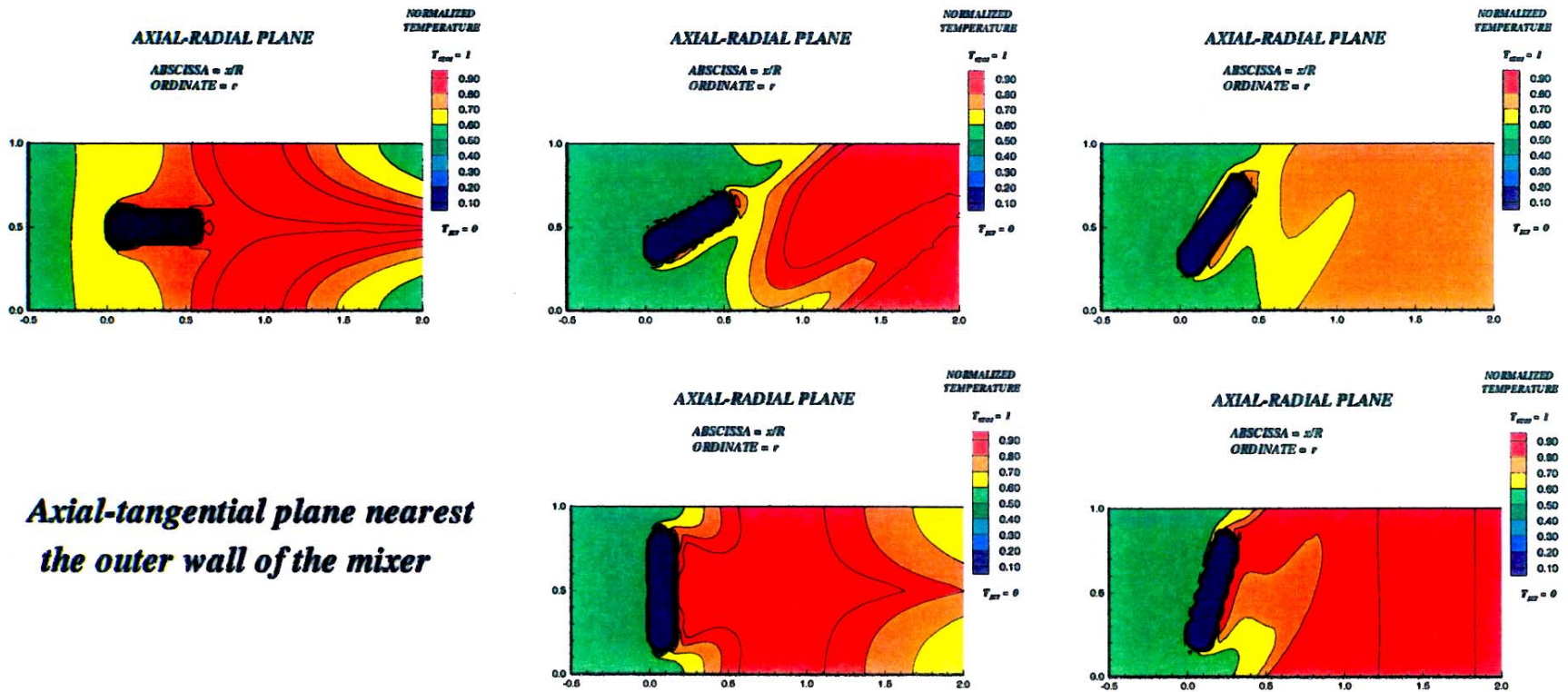
Axial-tangential plane nearest the outer wall of the mixer

Figure-B9-1. Effect of the change in slot slant angle on the temperature distribution

Clockwise from top left: slot slant angles of 0° (in-line), 22.5°, 45°, 67.5°, and 90° (transverse to the flow)

J=80, MR=2.96, DR=2.28, 8 orifices/row
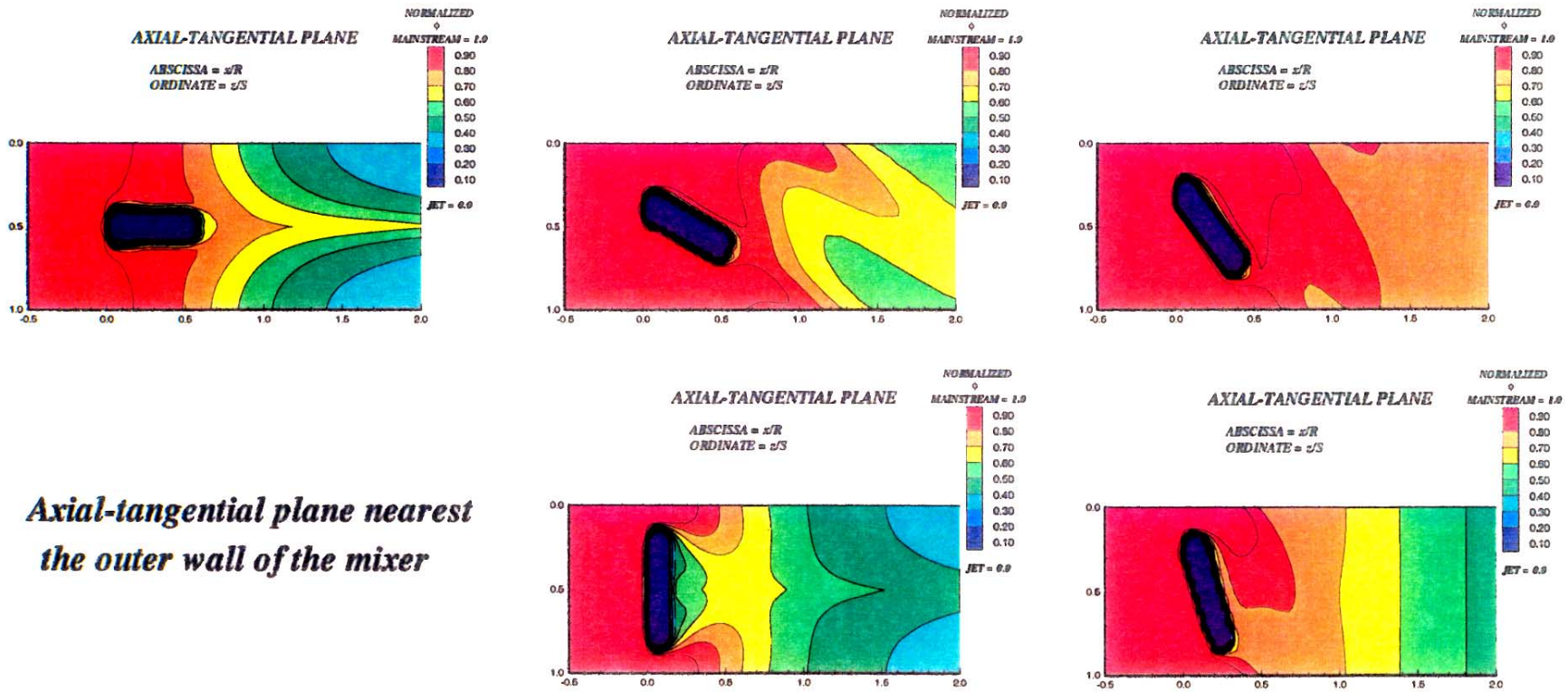
Axial-tangential plane nearest the outer wall of the mixer

Figure-B9-2. *Effect of the change in slot slant angle on the equivalence ratio distribution*

Clockwise from top left: slot slant angles of 0^0 (in-line), 22.5^0, 45^0, 67.5^0, and 90^0 (transverse to the flow)

J=80, MR=2.96, DR=2.28, 8 orifices/row

AXIAL-TANGENTIAL PLANE

ABSCISSA = x/R
ORDINATE = z/S

AXIAL-TANGENTIAL PLANE

ABSCISSA = x/R
ORDINATE = z/S

AXIAL-TANGENTIAL PLANE

ABSCISSA = x/R
ORDINATE = z/S

AXIAL-TANGENTIAL PLANE

ABSCISSA = x/R
ORDINATE = z/S

AXIAL-TANGENTIAL PLANE

ABSCISSA = x/R
ORDINATE = z/S

*Axial-tangential plane nearest
the outer wall of the mixer*

Figure-B9-3. Effect of the change in slot slant angle on the velocity distribution

Clockwise from top left: slot slant angles of 0^0 (in-line), 22.5^0, 45^0, 67.5^0, and 90^0 (transverse to the flow)

J=80, MR=2.96, DR=2.28, 8 orifices/row

Figure-B9-4. Effect of the change in slot slant angle on the temperature distribution

Clockwise from top left: slot slant angles of 0^0 (in-line), 22.5^0, 45^0, 67.5^0, and 90^0 (transverse to the flow)

J=80, MR=2.96, DR=2.28, 8 orifices/row

Axial-radial plane through the center of the jet

Figure-B9-5. Effect of the change in slot slant angle on the equivalence ratio distribution
Clockwise from top left: slot slant angles of 0⁰ (in-line), 22.5⁰, 45⁰, 67.5⁰, and 90⁰ (transverse to the flow)
J=80, MR=2.96, DR=2.28, 8 orifices/row

AXIAL-RADIAL PLANE

ABSCISSA = x/R
ORDINATE = r

AXIAL-RADIAL PLANE

ABSCISSA = x/R
ORDINATE = r

AXIAL-RADIAL PLANE

ABSCISSA = x/R
ORDINATE = r

Axial-radial plane through the center of the jet

AXIAL-RADIAL PLANE

ABSCISSA = x/R
ORDINATE = r

AXIAL-RADIAL PLANE

ABSCISSA = x/R
ORDINATE = r

Figure-B9-6. Effect of the change in slot slant angle on the velocity distribution

Clockwise from top left: slot slant angles of 0^0 (in-line), 22.5^0, 45^0, 67.5^0, and 90^0 (transverse to the flow)

J=80, MR=2.96, DR=2.28, 8 orifices/row

Figure-B9-7. Effect of the change in slot slant angle on the temperature distribution

Clockwise from top left: slot slant angles of 0⁰ (in-line), 22.5⁰, 45⁰, 67.5⁰, and 90⁰ (transverse to the flow)

J=80, MR=2.96, DR=2.28, 8 orifices/row

Radial-tangential plane at x/R=1

Figure-B9-8. *Effect of the change in slot slant angle on the equivalence ratio distribution*
Clockwise from top left: slot slant angles of 0⁰ (in-line), 22.5⁰, 45⁰, 67.5⁰, and 90⁰ (transverse to the flow)
J=80, MR=2.96, DR=2.28, 8 orifices/row

Figure-B9-9. Effect of the change in slot slant angle on the velocity distribution

Clockwise from top left: slot slant angles of 0^0 (in-line), 22.5^0, 45^0, 67.5^0, and 90^0 (transverse to the flow)

$J=80$, $MR=2.96$, $DR=2.28$, 8 orifices/row

APPENDIX-C

NOx production, f/a, and temperature distribution results from the hybrid model for configuration numbers 19 through 36.

    a) TOP -- local NOx distribution in log scale, gr NOx / {sec m³}

    b) MIDDLE -- f/a distribution

    c) BOTTOM -- temperature distribution, K

CONF #	FIG #
19	C1
20	C2
21	C3
22	C4
23	C5
24	C6
25	C7
26	C8
27	C9
28	C10
29	C11
30	C12
31	C13
32	C14
33	C15
34	C16
35	C17
36	C18

LOCAL NO$_x$ PRODUCTION RATE
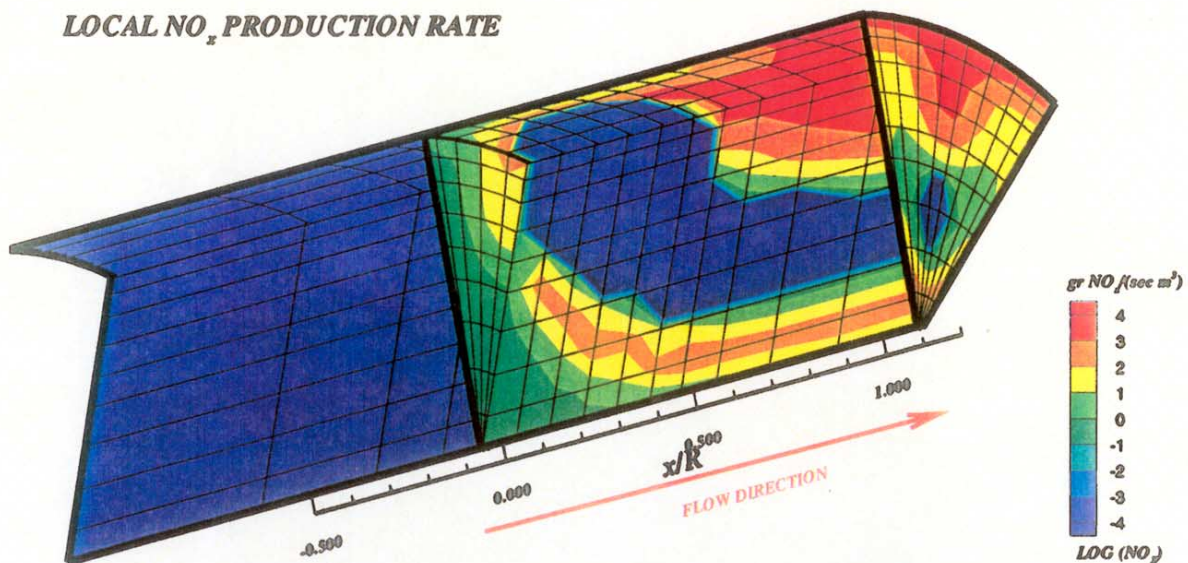
FUEL / AIR RATIO DISTRIBUTION
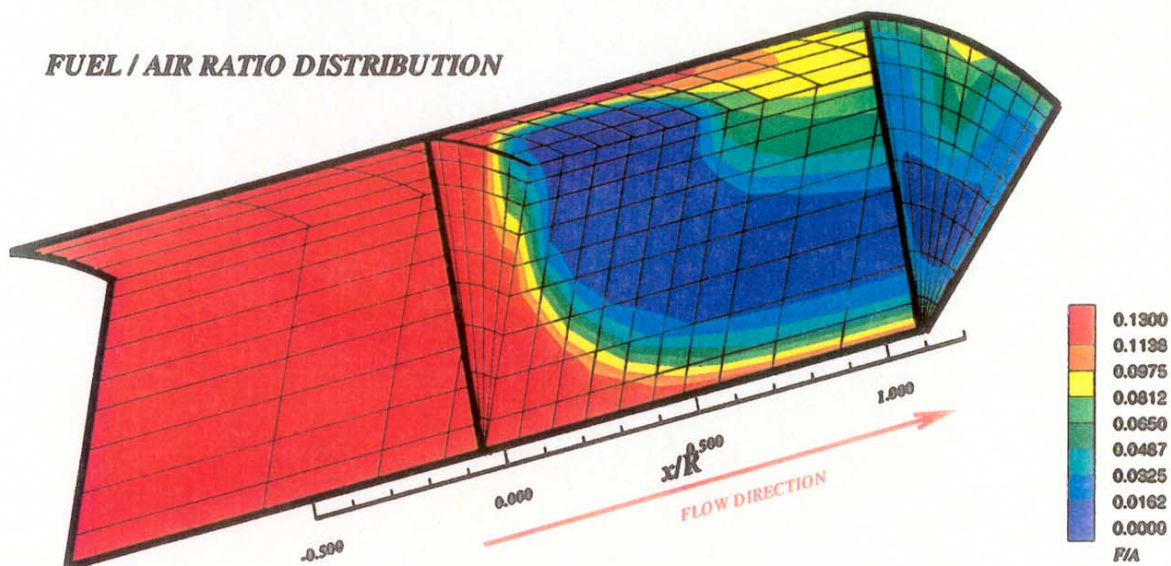
GAS TEMPERATURE DISTRIBUTION
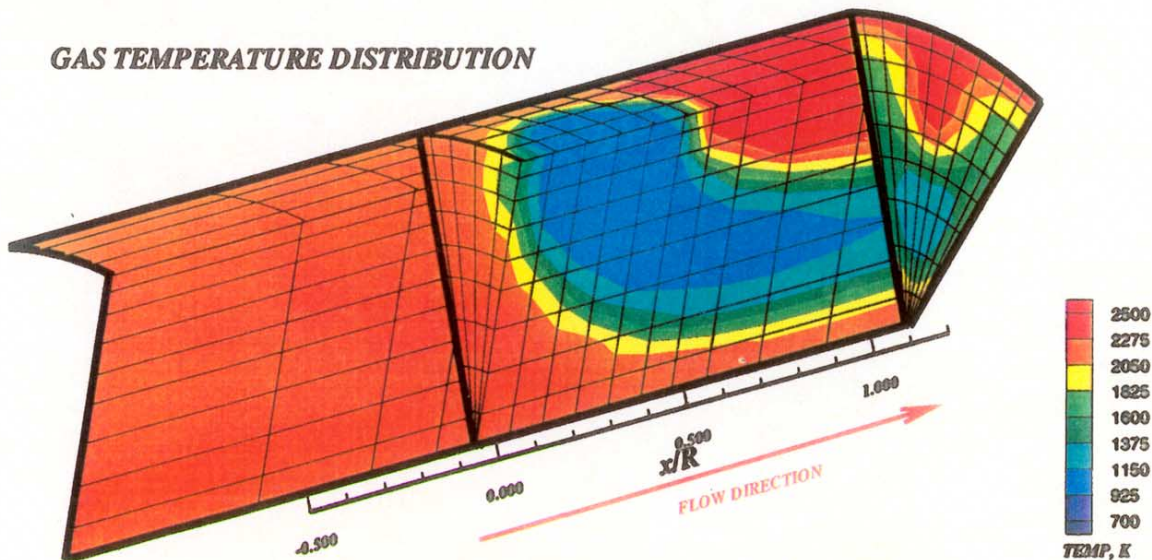
Figure-C1. Configuration #19 mixing performance and NO$_x$ production
J=26.7, MR=2.96, DR=2.28, phi rz=1.80, phi lz=0.416, 8 round holes/row

LOCAL NO$_x$ PRODUCTION RATE
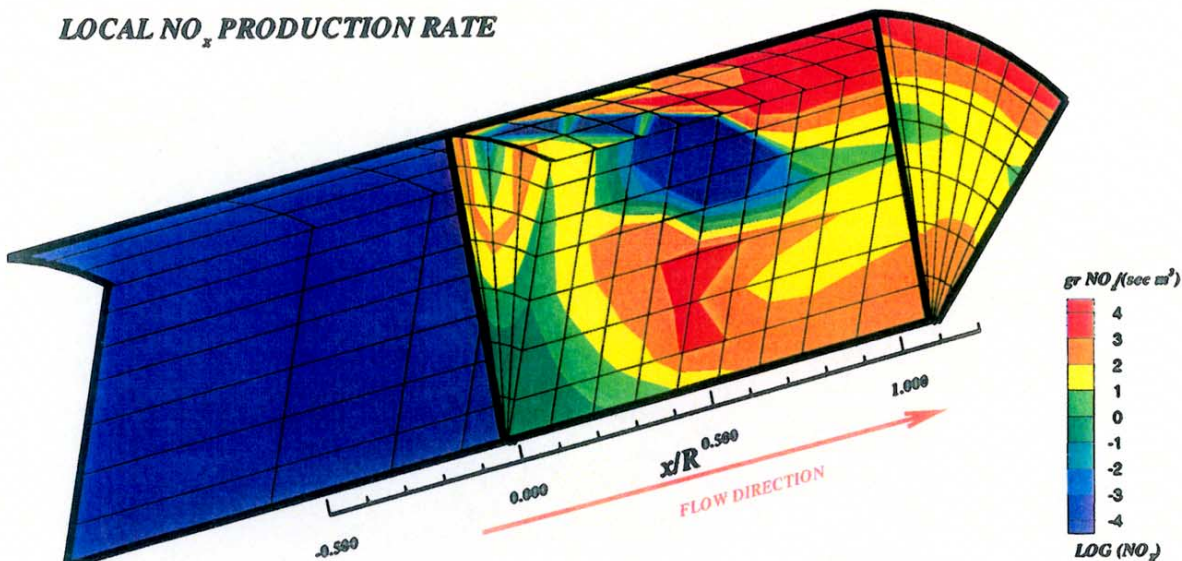
FUEL / AIR RATIO DISTRIBUTION
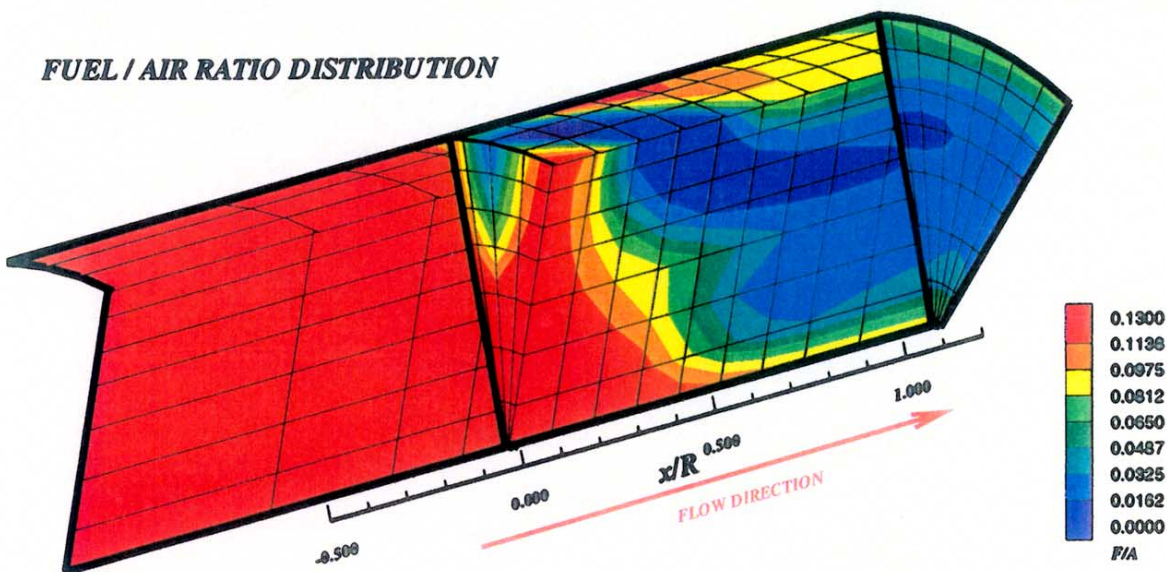
GAS TEMPERATURE DISTRIBUTION
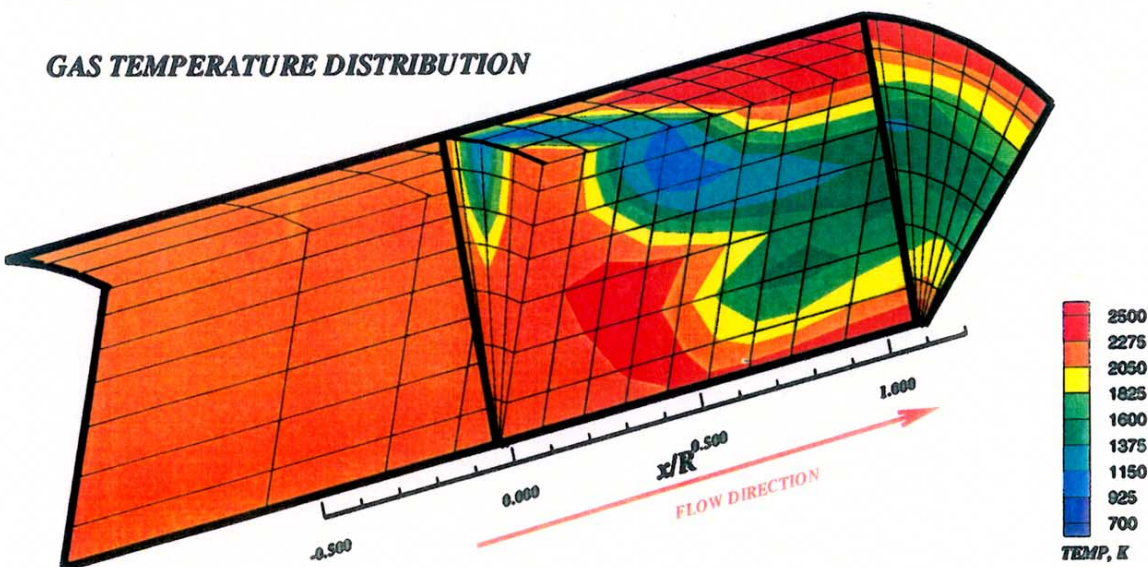
*Figure-C2. Configuration #20 mixing performance and NO$_x$ production
J = 30.5, MR = 2.96, DR = 2.28, phi rz = 1.80, phi lz = 0.416, 45° slot, L/W = 4, 8/row*
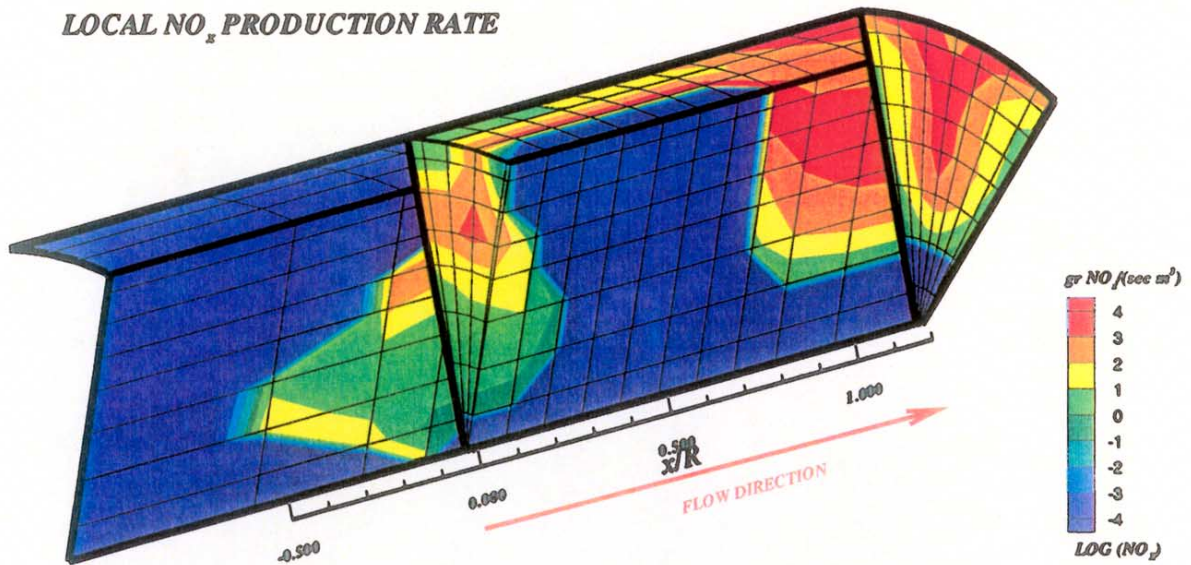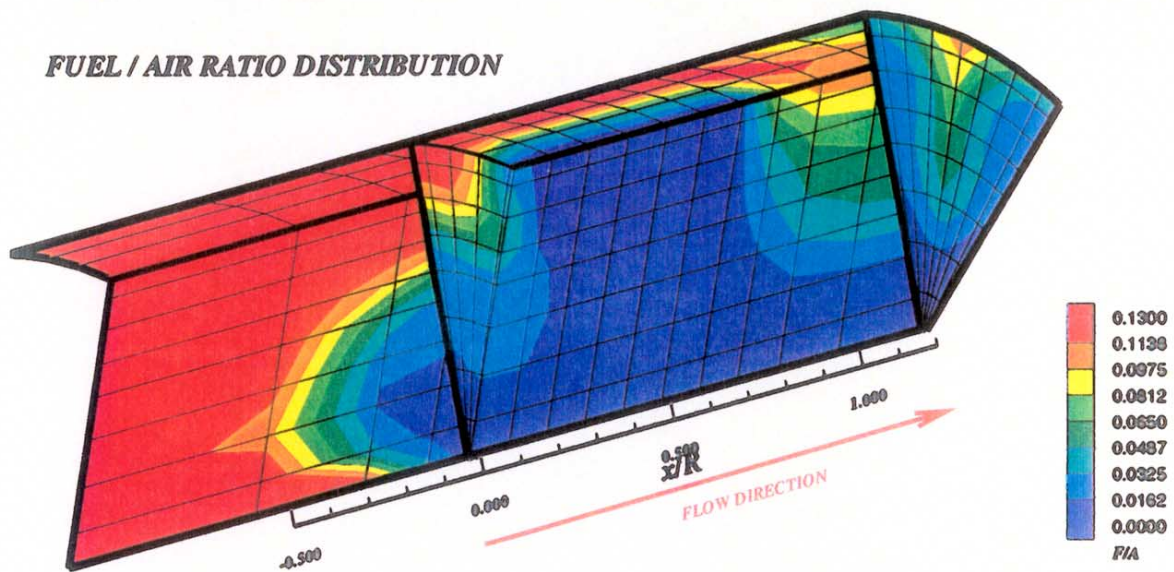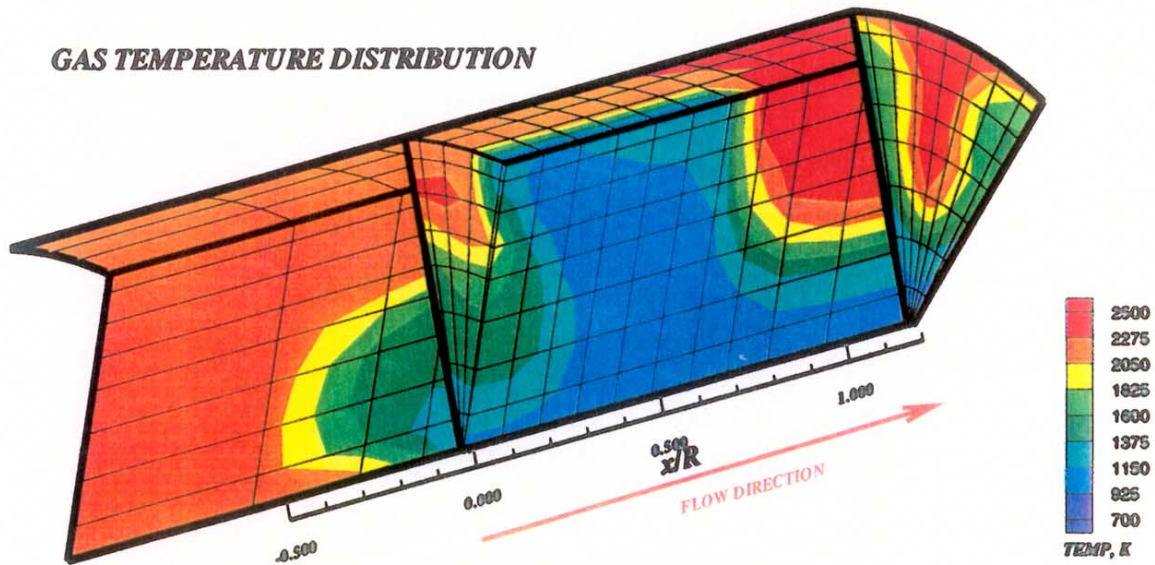
Figure-C3. Configuration #21 mixing performance and NO_x production
J=51.1, MR=2.96, DR=2.28, phi rz=1.80, phi lz=0.416, Aligned slot, L/W=4, 8/row
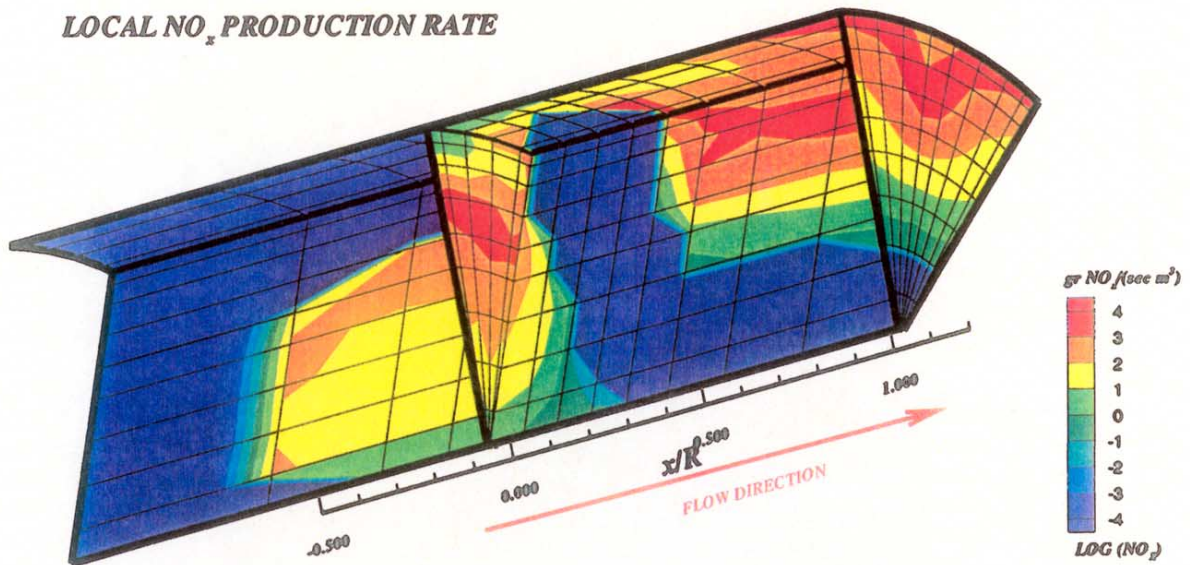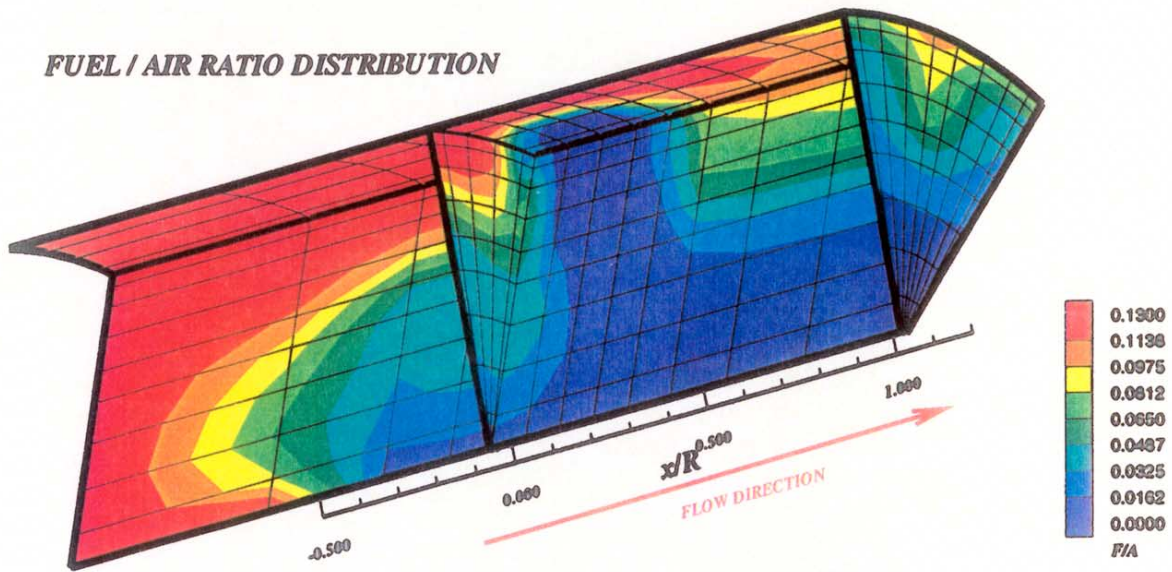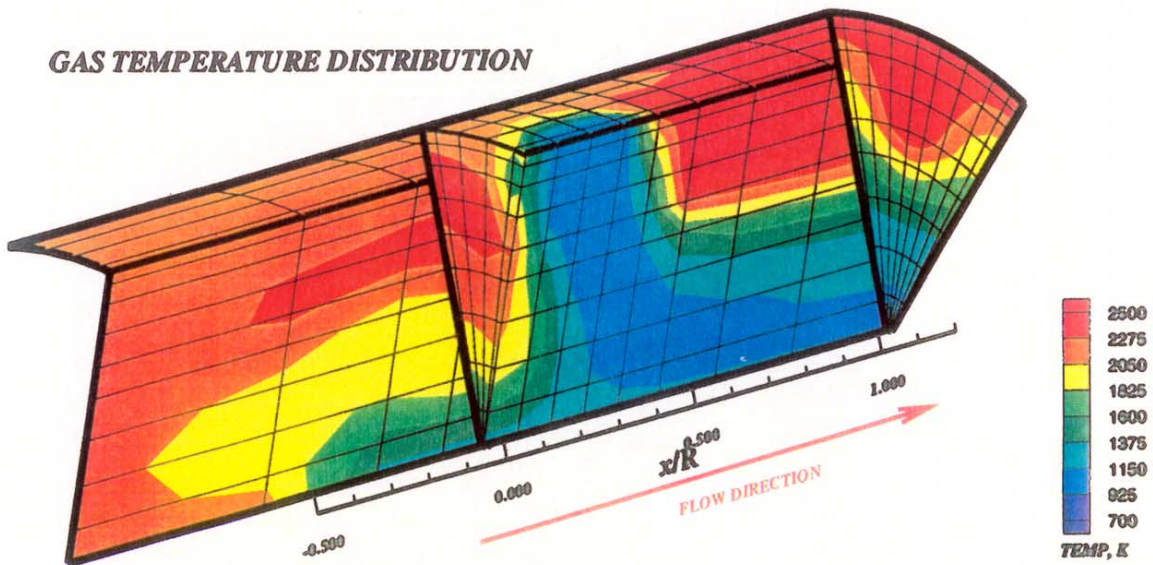
Figure-C4. Configuration #22 mixing performance and NO$_x$ production
J=84.1, MR=2.96, DR=2.28, phi rz=1.80, phi lz=0.416, round holes, 8/row

LOCAL NO_x PRODUCTION RATE
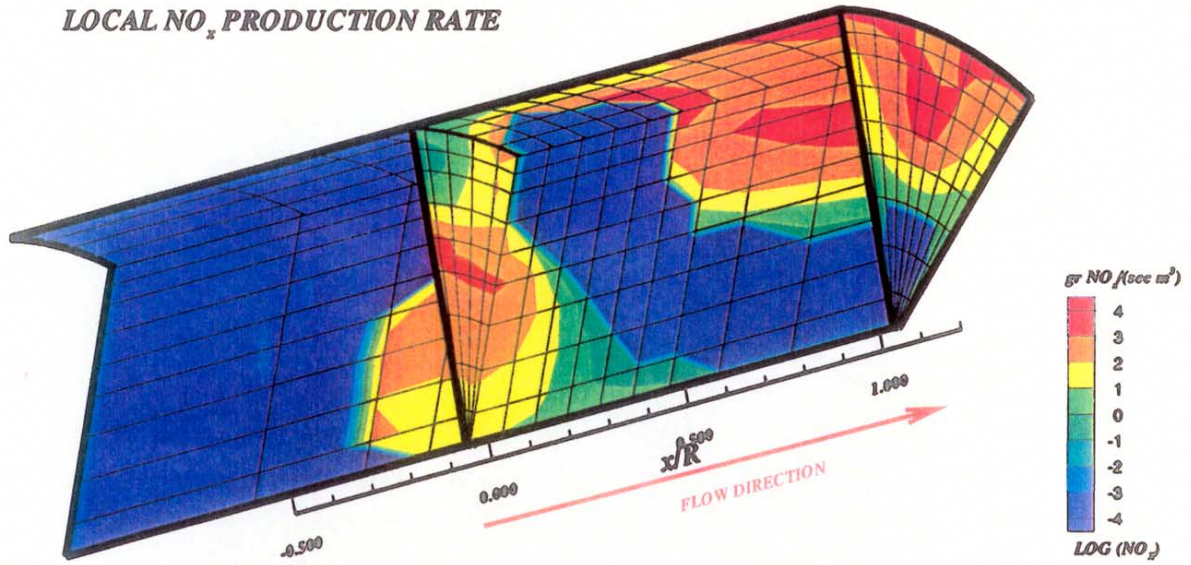
FUEL / AIR RATIO DISTRIBUTION
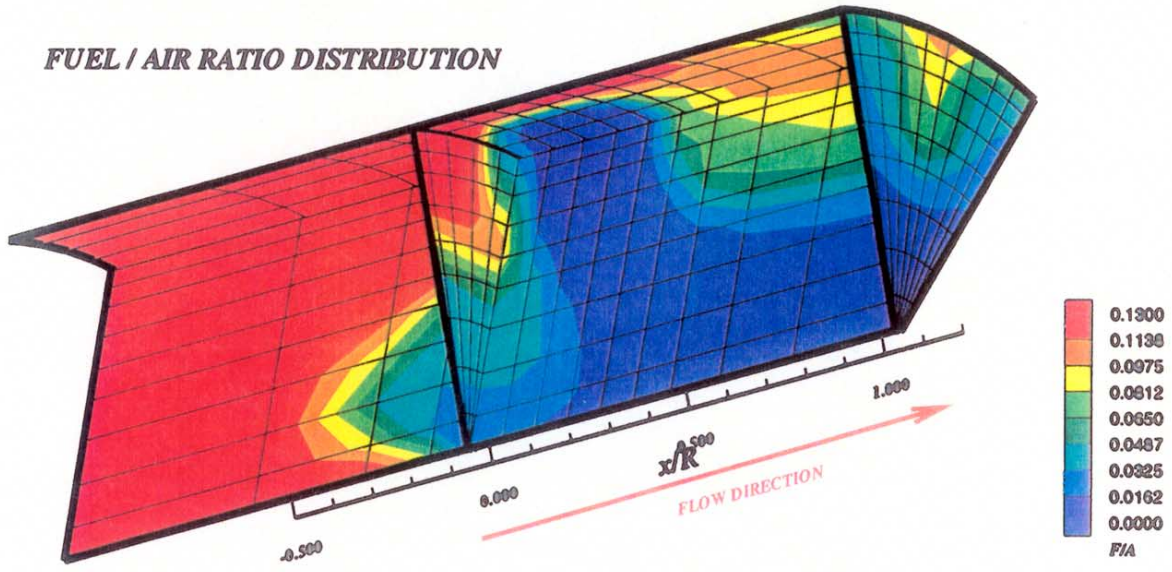
GAS TEMPERATURE DISTRIBUTION
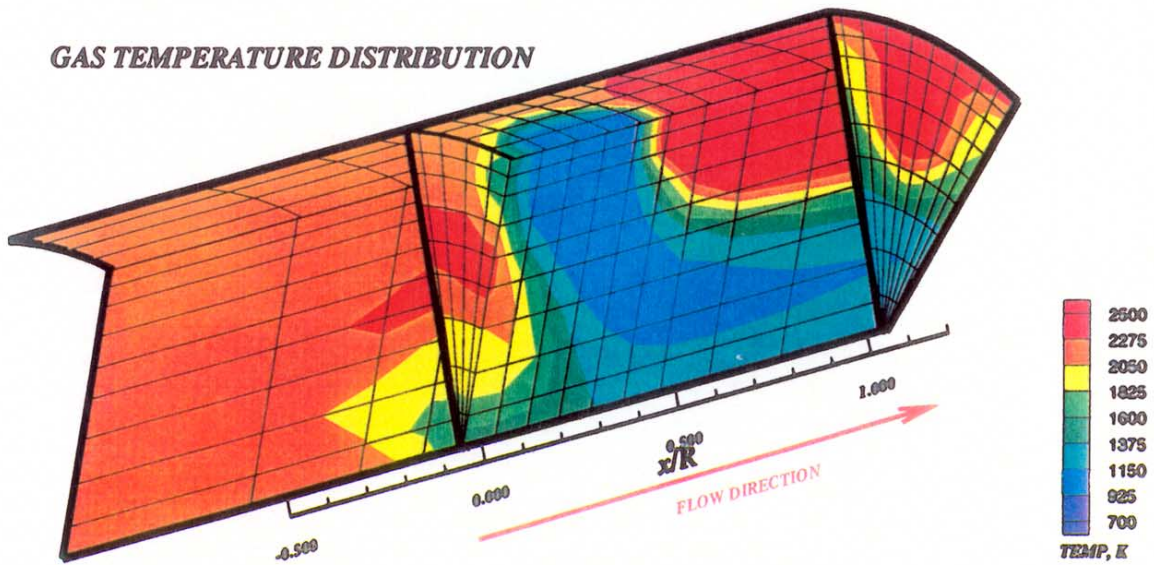
Figure-C5. Configuration #23 mixing performance and NO_x production
J=55.3, MR=2.96, DR=2.28, phi rz=1.80, phi lz=0.416, round holes, 8/row

LOCAL NO$_x$ PRODUCTION RATE
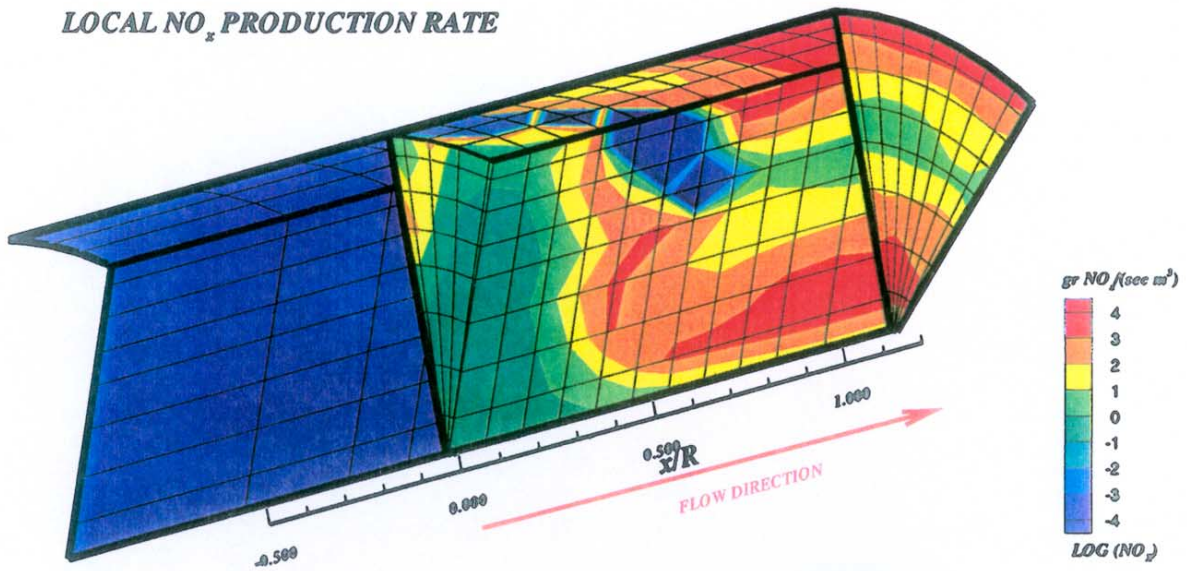
FUEL / AIR RATIO DISTRIBUTION
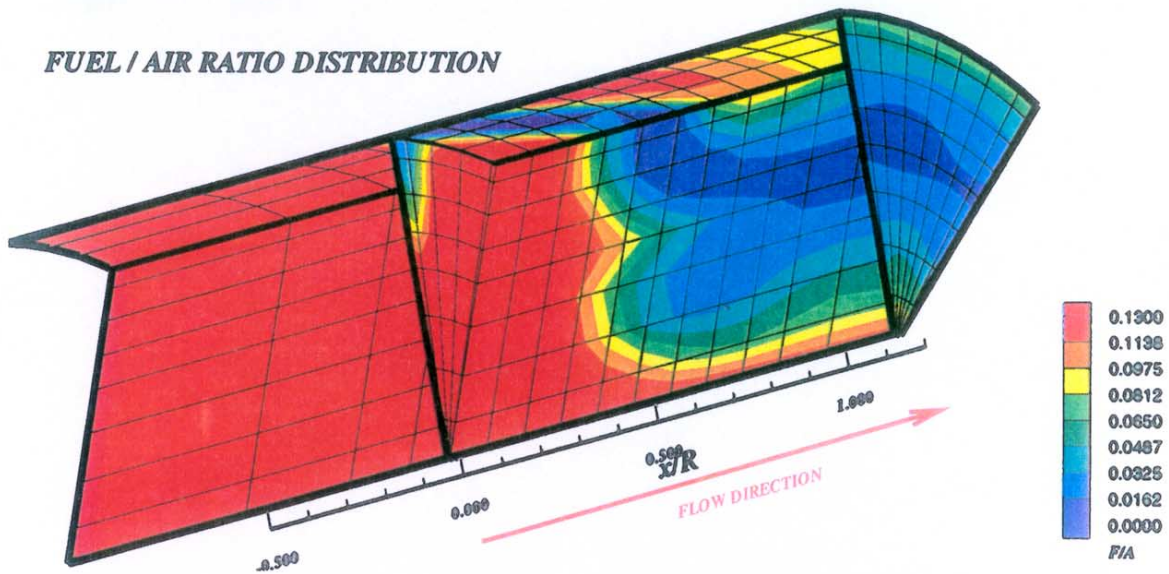
GAS TEMPERATURE DISTRIBUTION
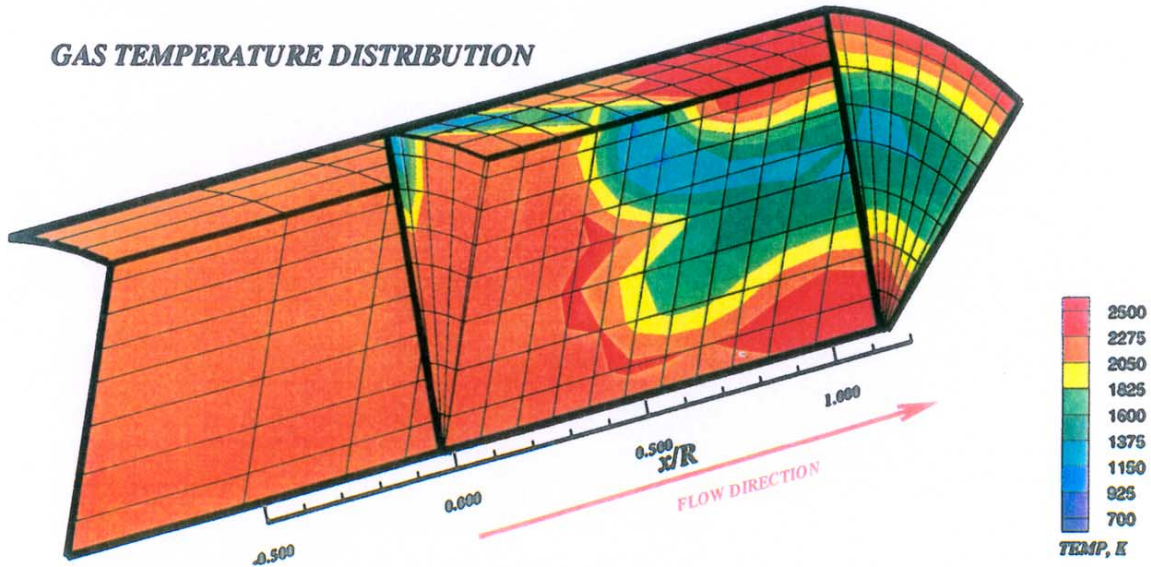
Figure-C6. Configuration #24 mixing performance and NO$_x$ production
J=28.1, MR=2.96, DR=2.28, phi rz=1.80, phi lz=0.416, 45^0 slot, L/W=8, 8/row

LOCAL NO$_x$ PRODUCTION RATE
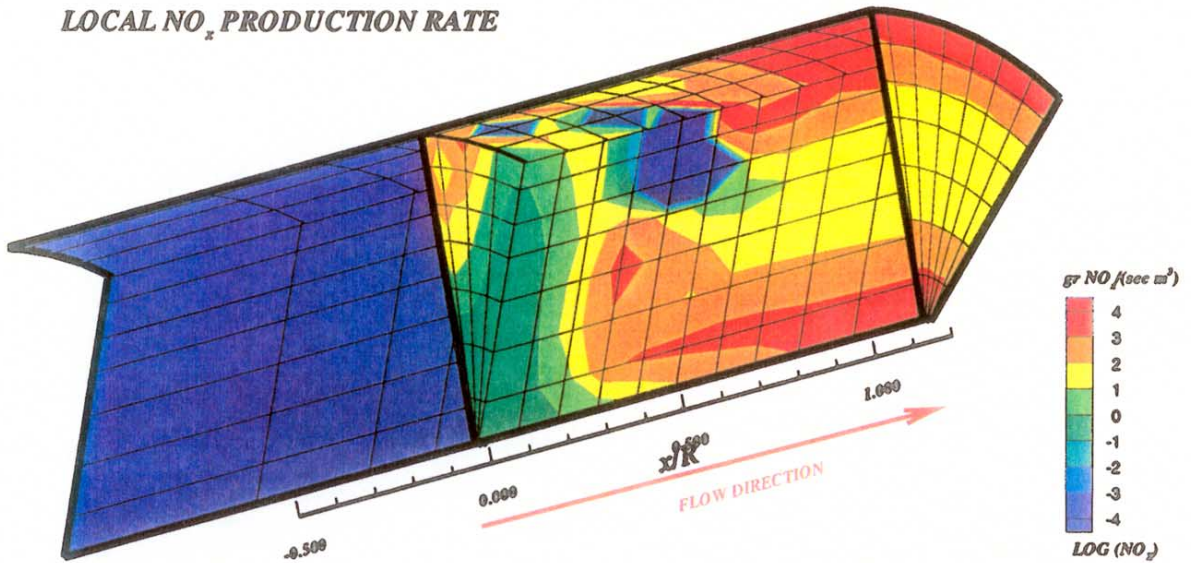
FUEL / AIR RATIO DISTRIBUTION
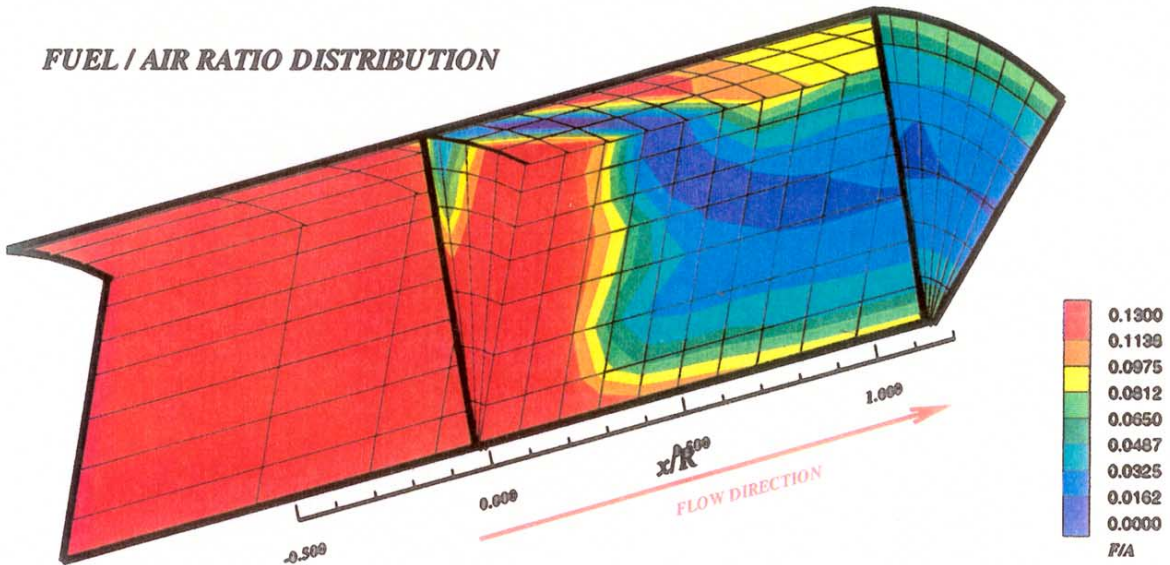
GAS TEMPERATURE DISTRIBUTION
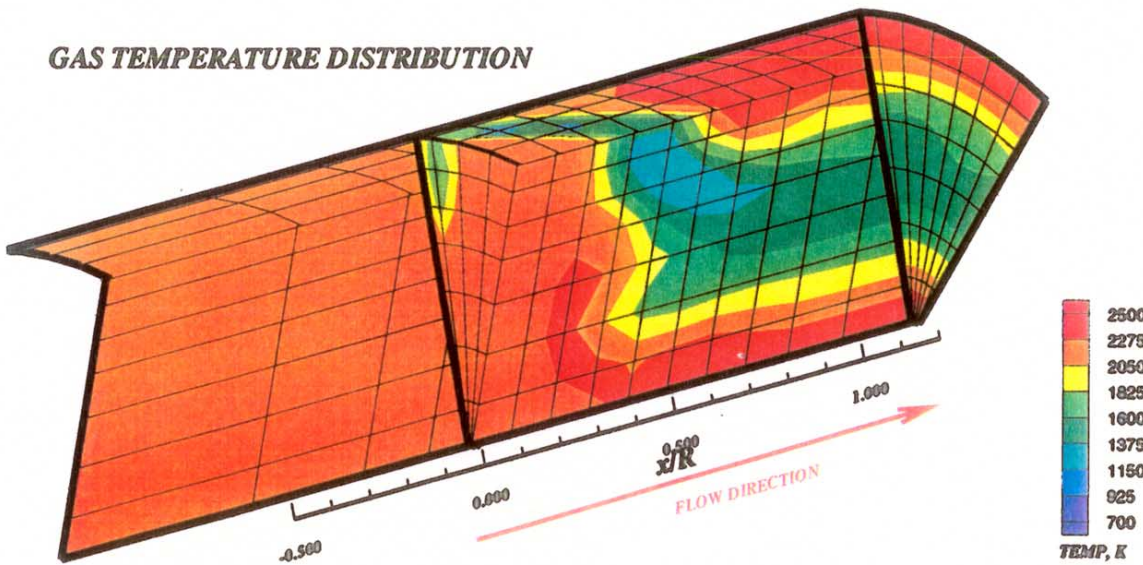
Figure-C7. Configuration #25 mixing performance and NO$_x$ production
J=50.9, MR=2.96, DR=2.28, phi rz=1.80, phi lz=0.416, 45° slot, L/W=8, 8/row

LOCAL NO$_x$ PRODUCTION RATE
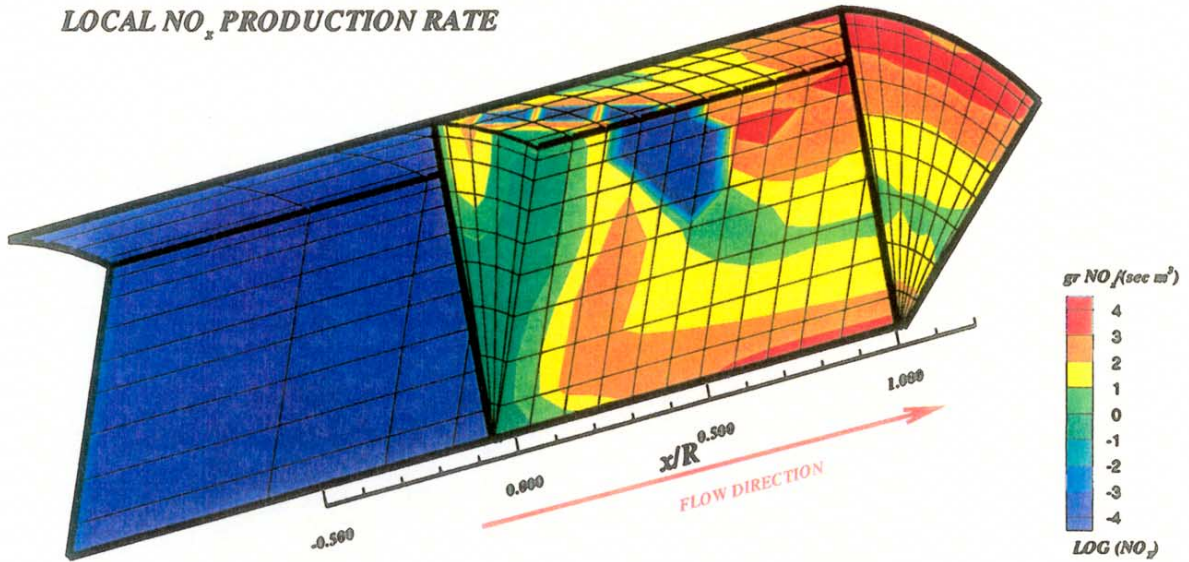
FUEL / AIR RATIO DISTRIBUTION
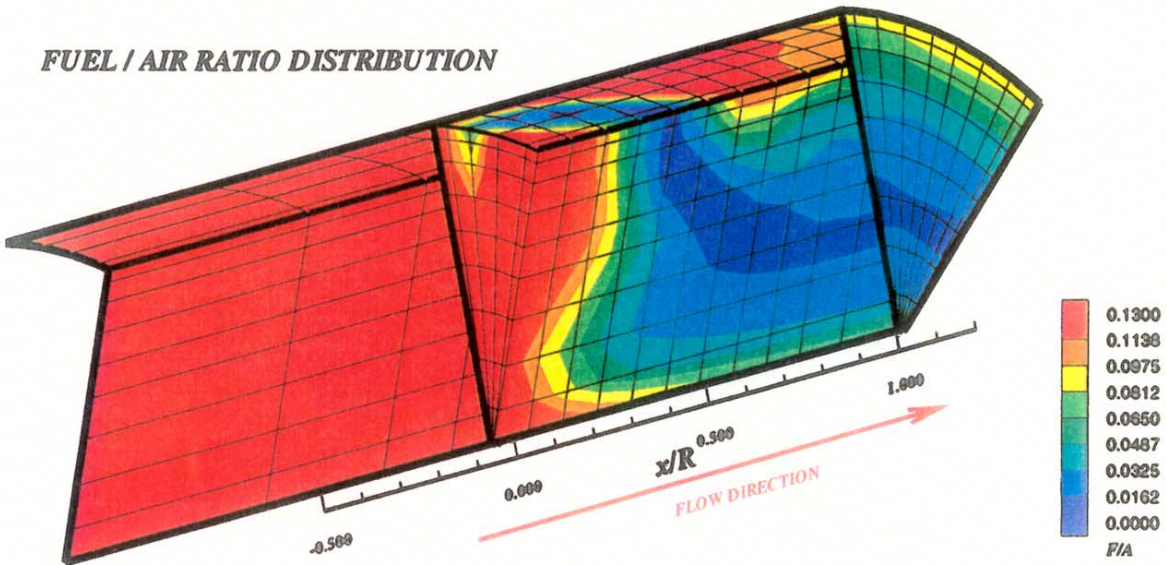
GAS TEMPERATURE DISTRIBUTION
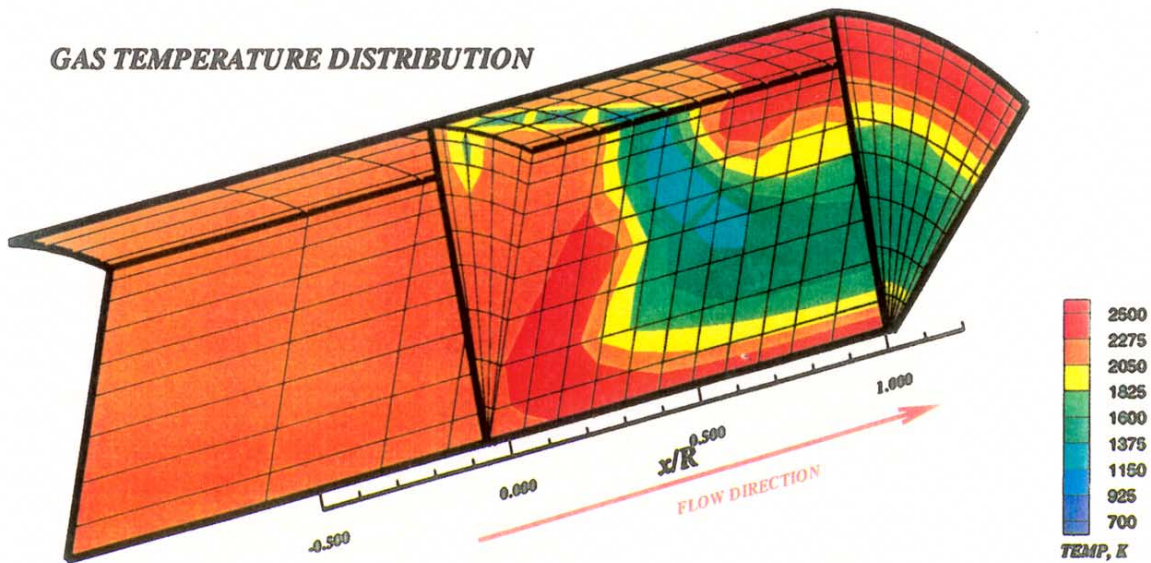
Figure-C8. Configuration #26 mixing performance and NO$_x$ production
J=88.4, MR=2.96, DR=2.28, phi rz=1.80, phi lz=0.416, 45° slot, L/W=8, 8/row

LOCAL NO$_x$ PRODUCTION RATE
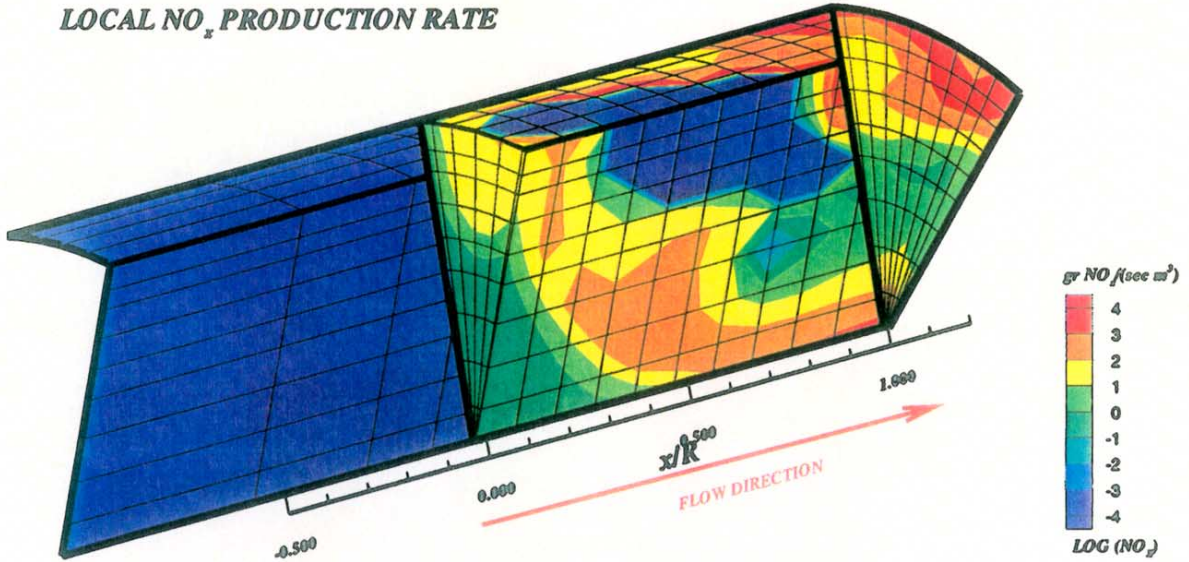
**FUEL / AIR RATIO DISTRIBUTION**
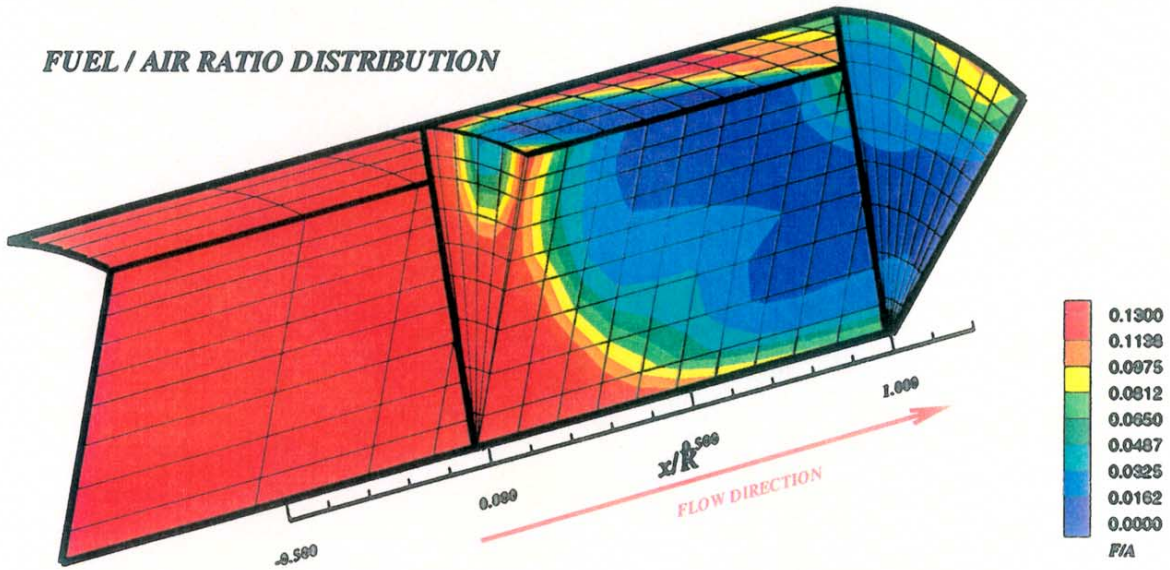
GAS TEMPERATURE DISTRIBUTION
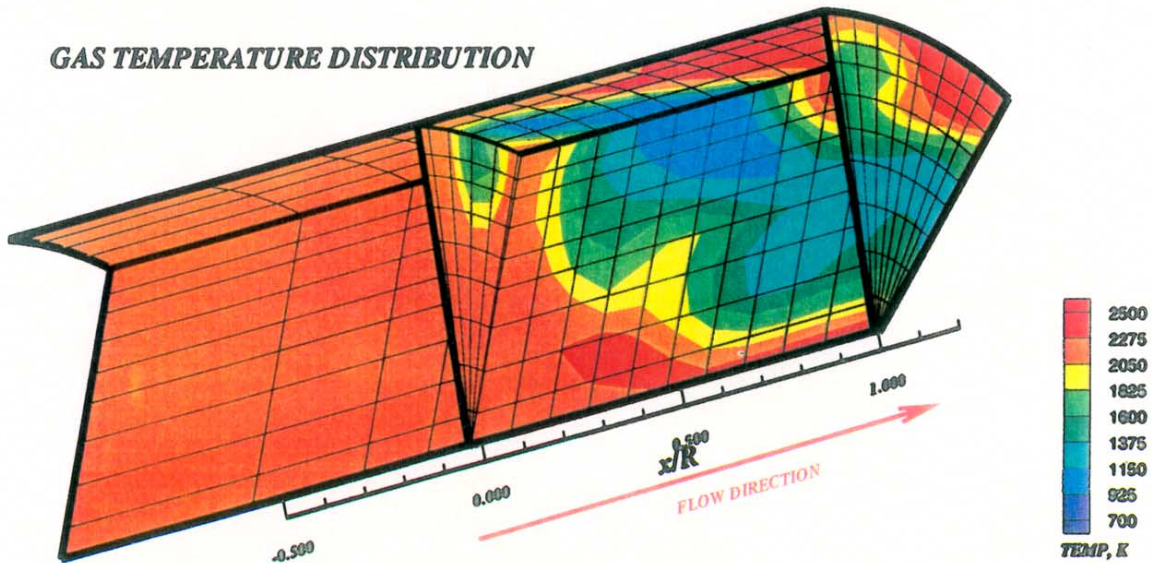
Figure-C9. Configuration #27 mixing performance and NO$_x$ production
J=28.0, MR=2.96, DR=2.28, phi rz=1.80, phi lz=0.416, 22.5° slot, L/W=4, 8/row
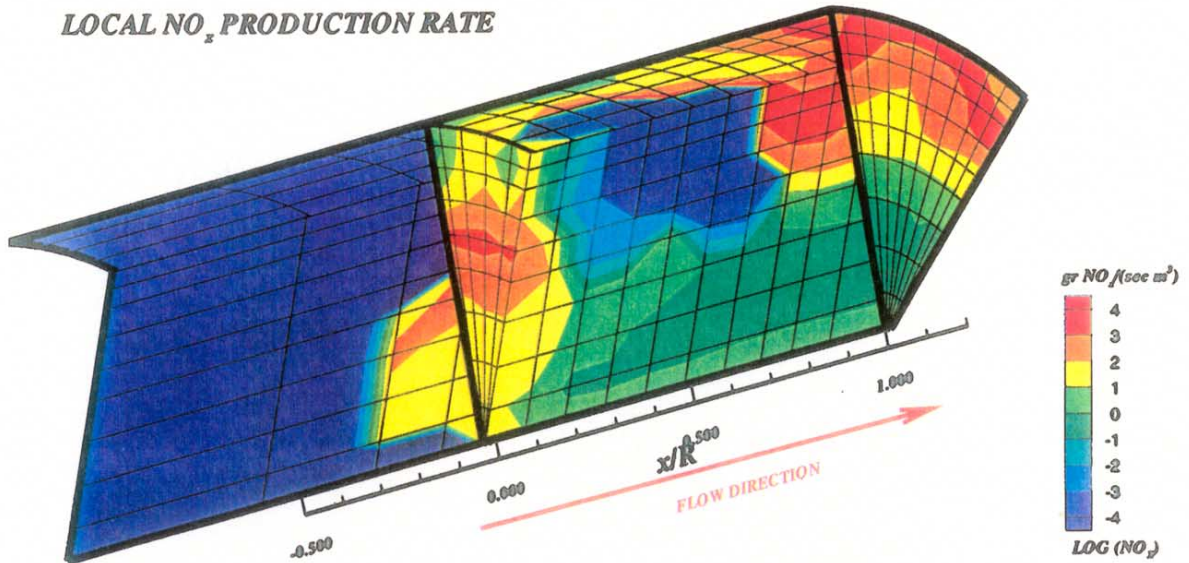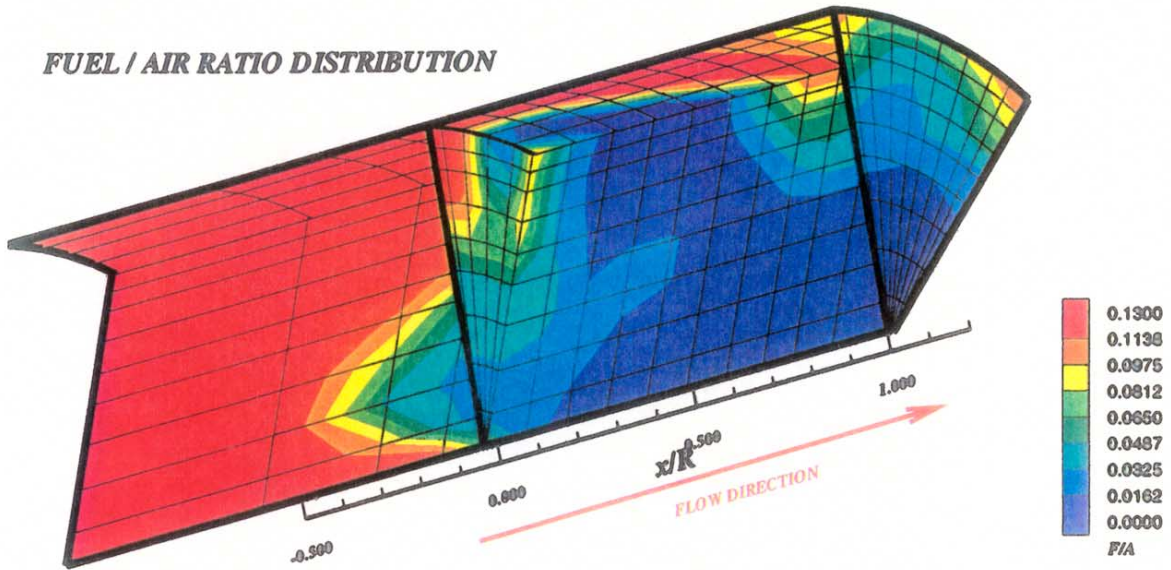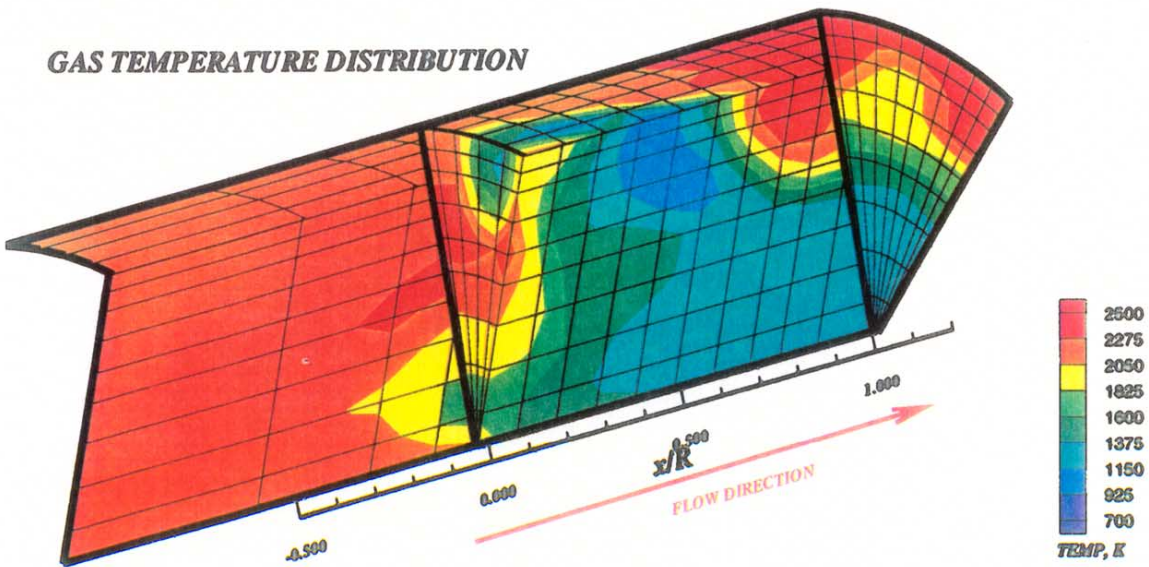
Figure-C10. Configuration #28 mixing performance and NO$_x$ production
J=53.2, MR=2.96, DR=2.28, phi rz=1.80, phi lz=0.416, 22.5° slot, L/W=4, 8/row
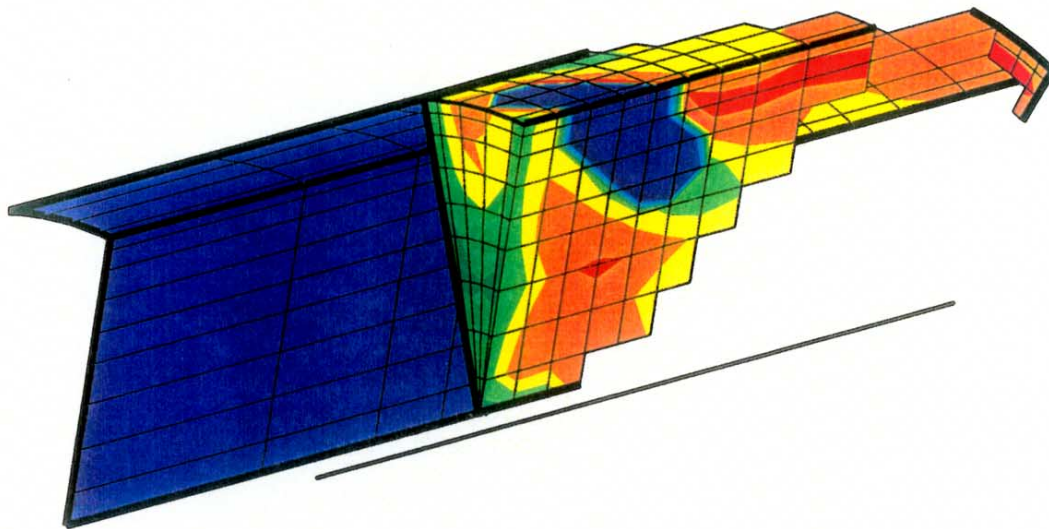
FUEL / AIR RATIO DISTRIBUTION
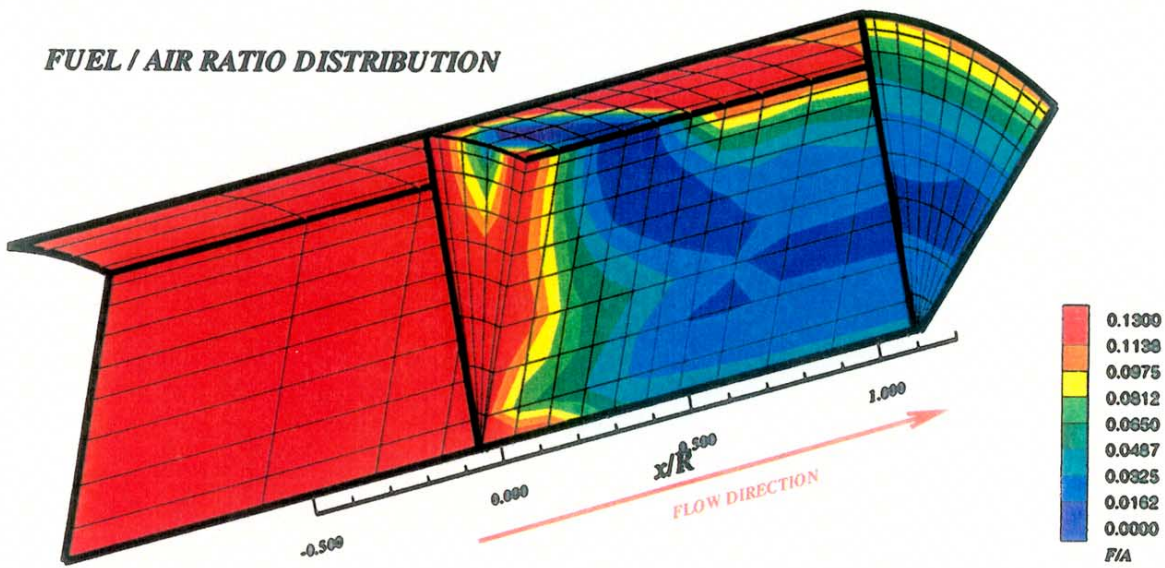
GAS TEMPERATURE DISTRIBUTION
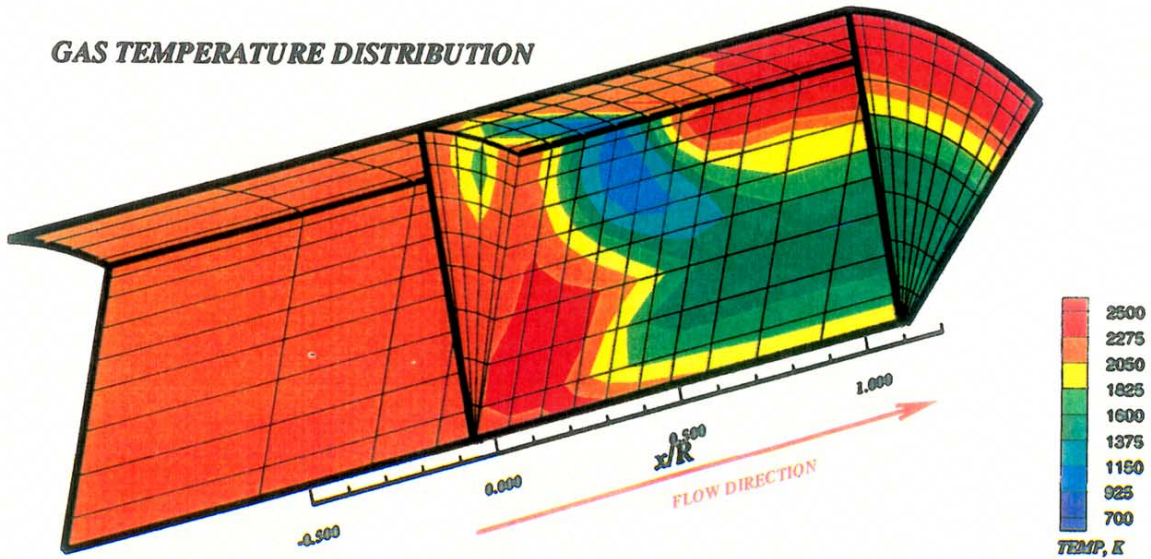
Figure-C11. Configuration #29 mixing performance and NO$_x$ production
J=57.6, MR=2.96, DR=2.28, phi rz=1.80, phi lz=0.416, 45^0 slot, L/W=4, 8/row

LOCAL NO$_z$ PRODUCTION RATE

FUEL / AIR RATIO DISTRIBUTION

GAS TEMPERATURE DISTRIBUTION
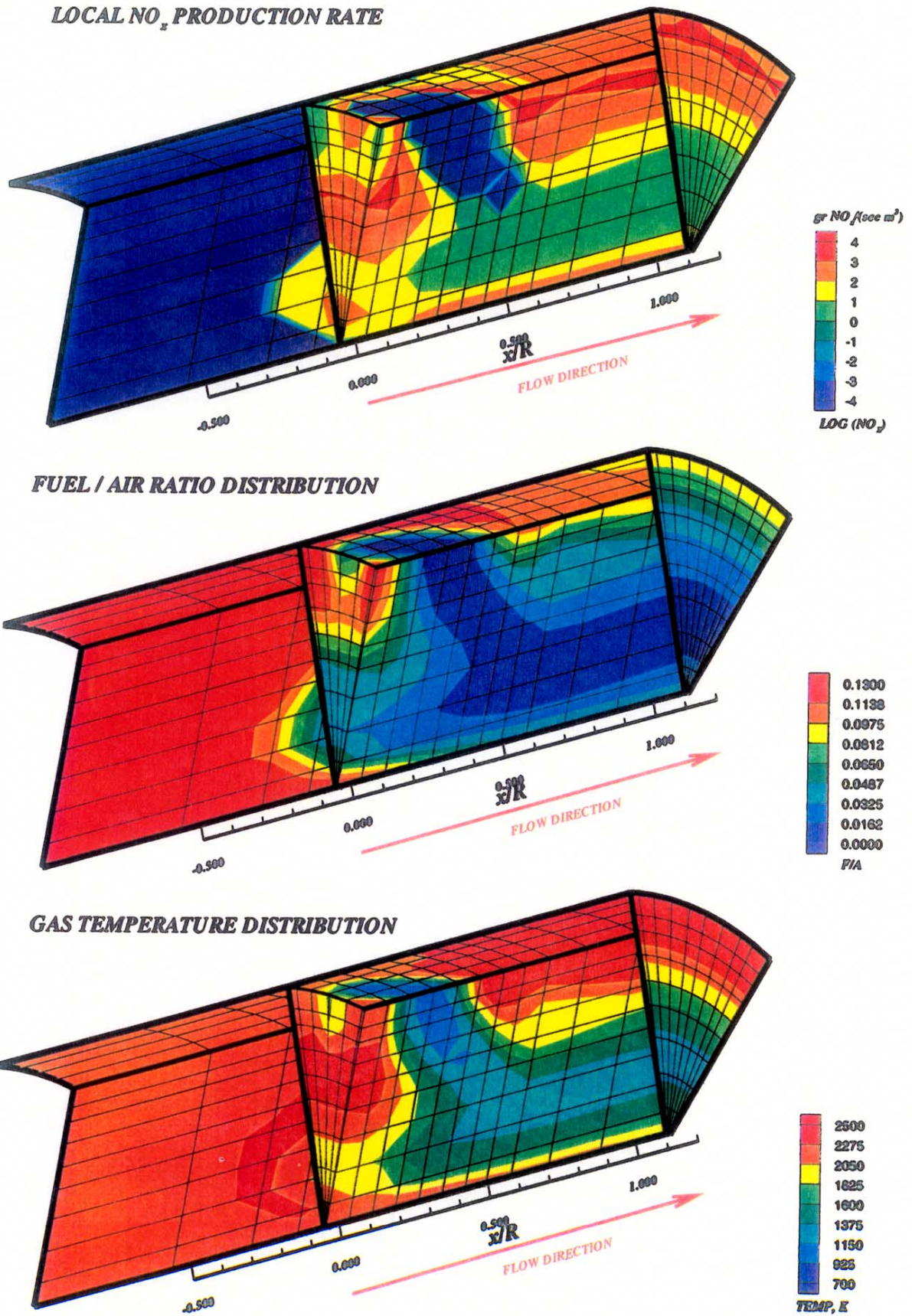
Figure-C12. Configuration #30 mixing performance and NO$_z$ production
*J=92.9, MR=2.96, DR=2.28, phi rz=1.80, phi lz=0.416, 45° slot, L/W=4, 8/row*

LOCAL NO$_x$ PRODUCTION RATE

gr NO $_x$ (sec m^3)

4
3
2
1
0
-1
-2
-3
-4

LOG (NO$_x$)

x/R

FLOW DIRECTION

-0.500   0.000   0.500   1.000

FUEL / AIR RATIO DISTRIBUTION

0.1300
0.1138
0.0975
0.0812
0.0650
0.0487
0.0325
0.0162
0.0000

F/A

x/R

FLOW DIRECTION

-0.500   0.000   0.500   1.000

GAS TEMPERATURE DISTRIBUTION

2500
2275
2050
1825
1600
1375
1150
925
700

TEMP, K

x/R

FLOW DIRECTION

-0.500   0.000   0.500   1.000
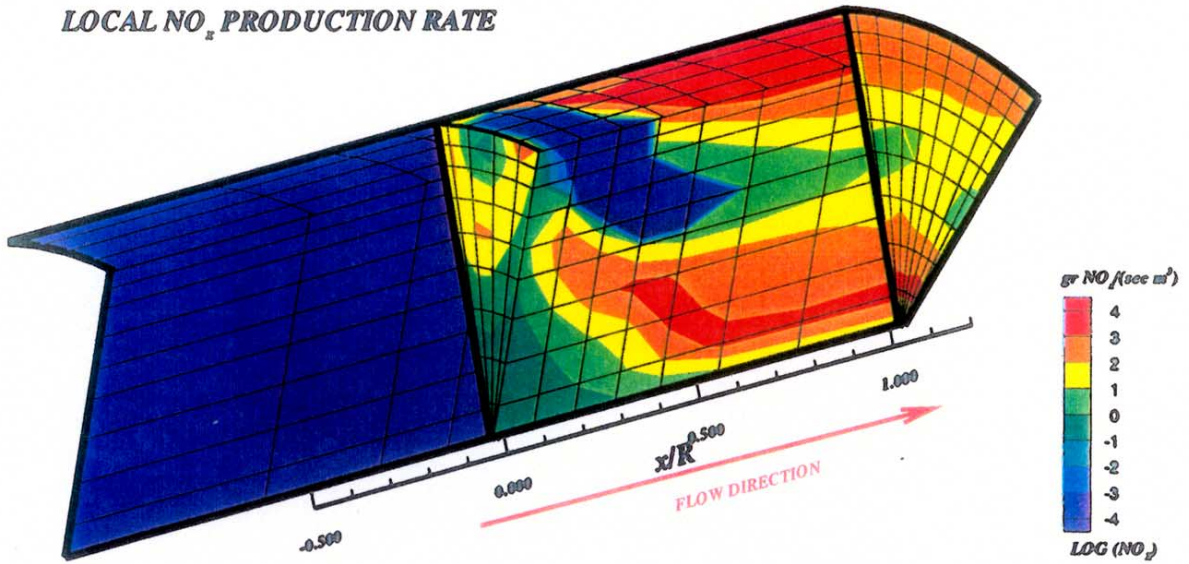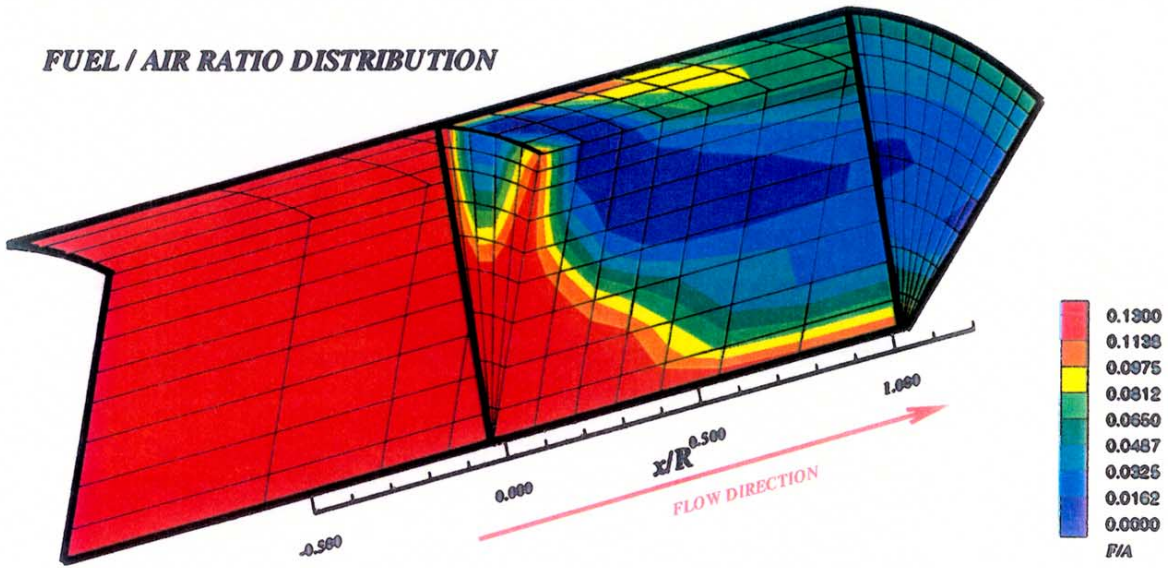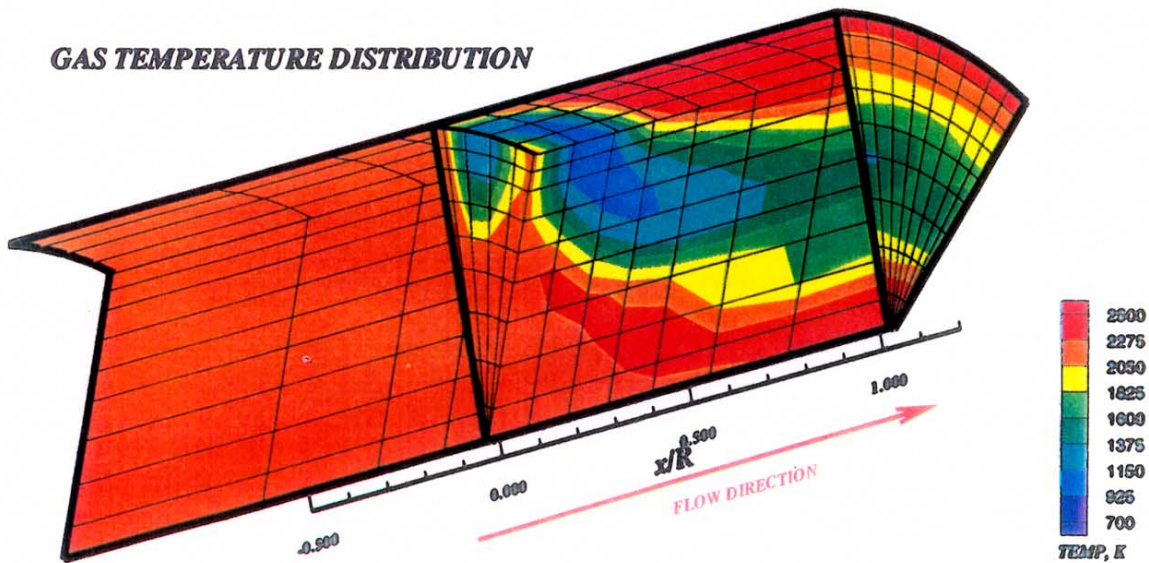
Figure-C13. Configuration #31 mixing performance and NO$_x$ production
J=59.9, MR=2.96, DR=2.28, phi rz=1.80, phi lz=0.416, 67.5^o slot, L/W=4, 8/row

LOCAL NO$_x$ PRODUCTION RATE
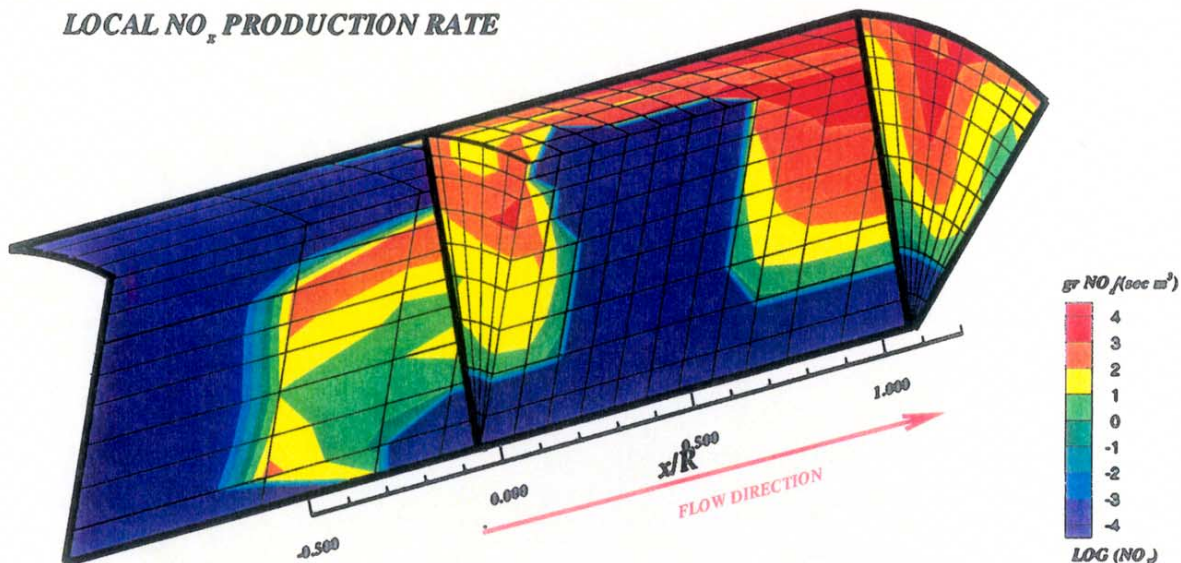
FUEL / AIR RATIO DISTRIBUTION
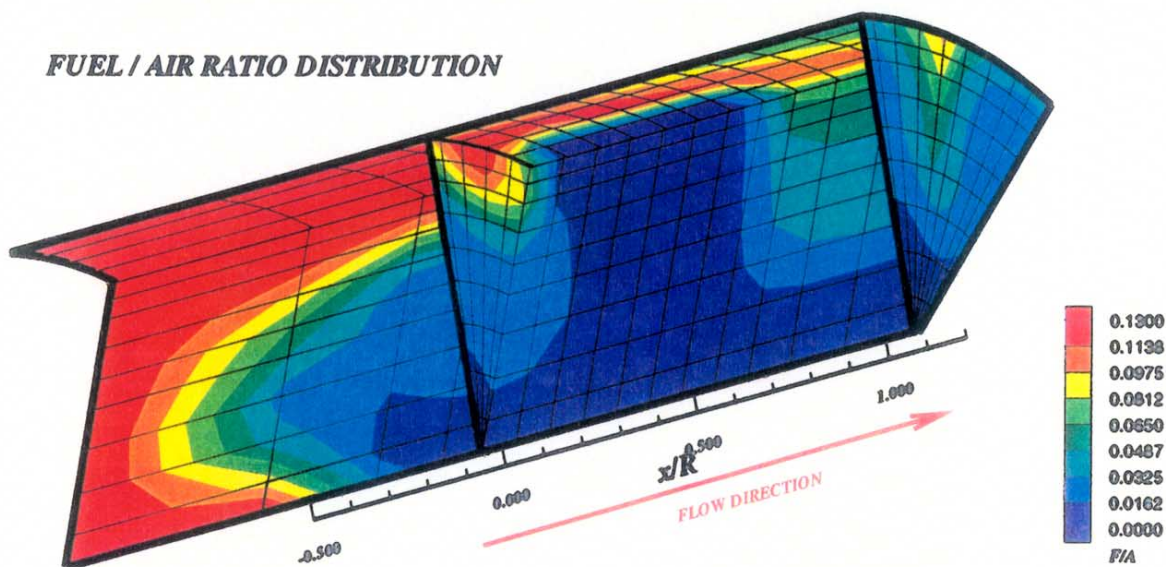
GAS TEMPERATURE DISTRIBUTION
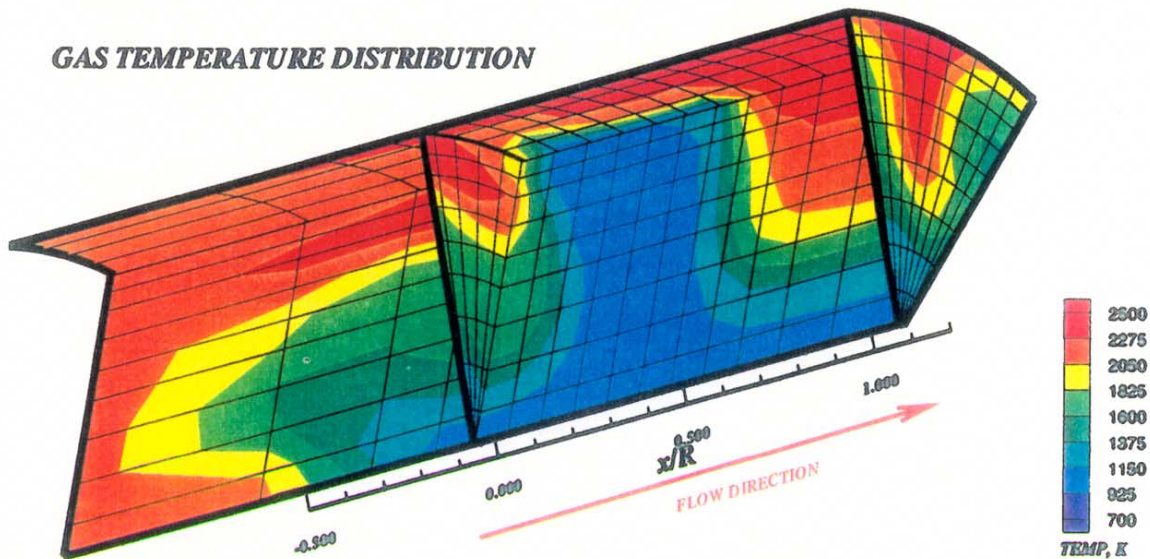
Figure-C14. Configuration #32 mixing performance and NO$_x$ production
J= 93.0, MR= 2.96, DR= 2.28, phi rz= 1.80, phi lz= 0.416, Aligned slot, L/W= 4, 8/row

LOCAL NO$_x$ PRODUCTION RATE
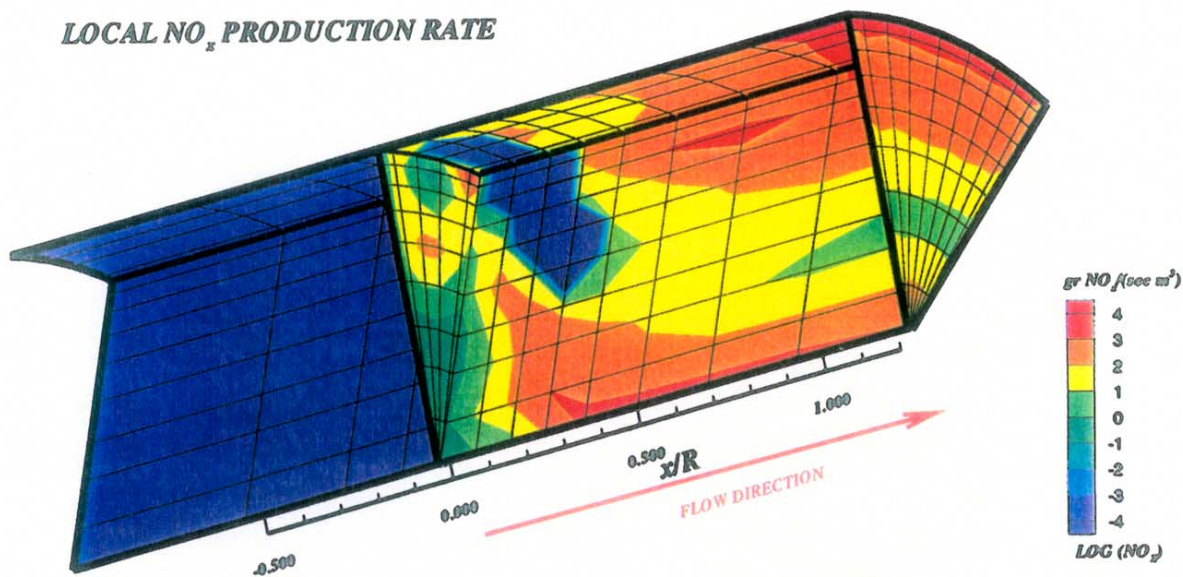
## FUEL / AIR RATIO DISTRIBUTION
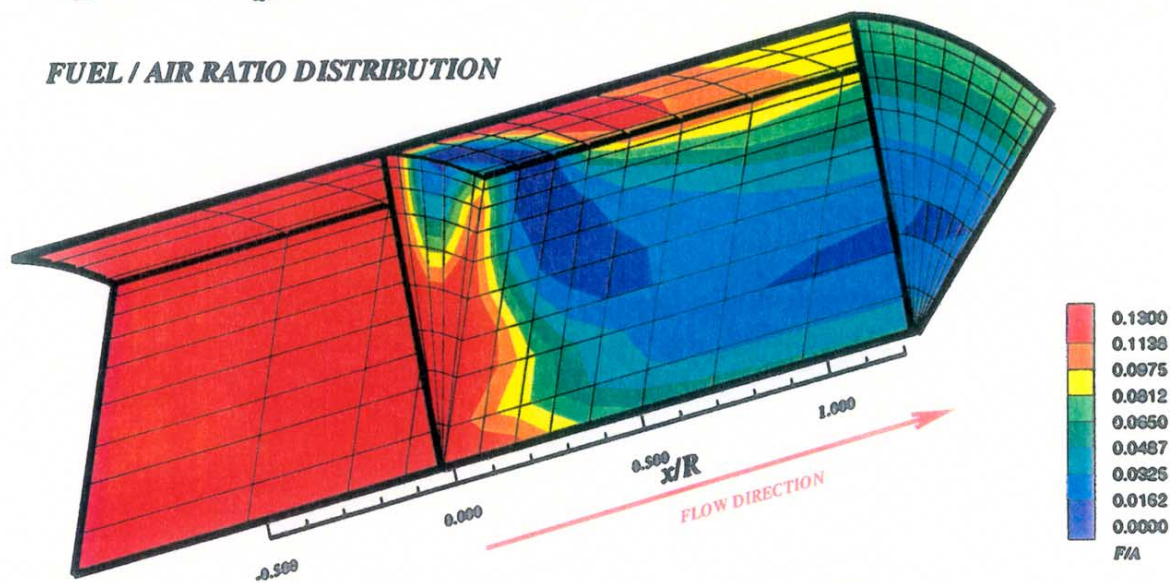
GAS TEMPERATURE DISTRIBUTION
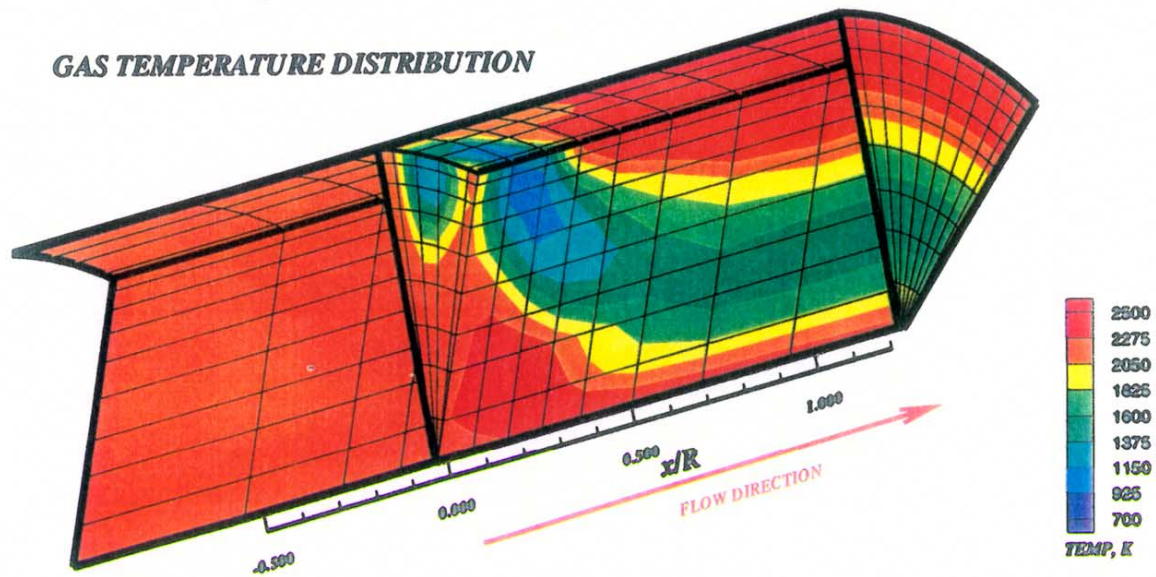
Figure-C15. Configuration #33 mixing performance and NO$_x$ production
J=99.3, MR=2.96, DR=2.28, phi rz=1.80, phi lz=0.416, 67.5° slot, L/W=4, 8/row

LOCAL NO₂ PRODUCTION RATE
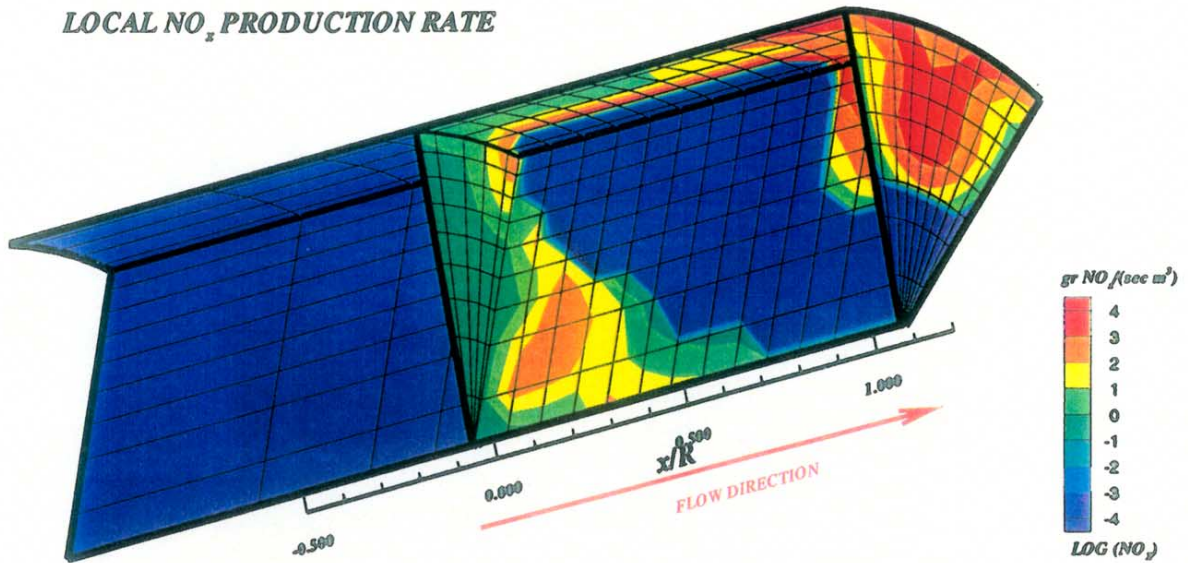
**FUEL / AIR RATIO DISTRIBUTION**
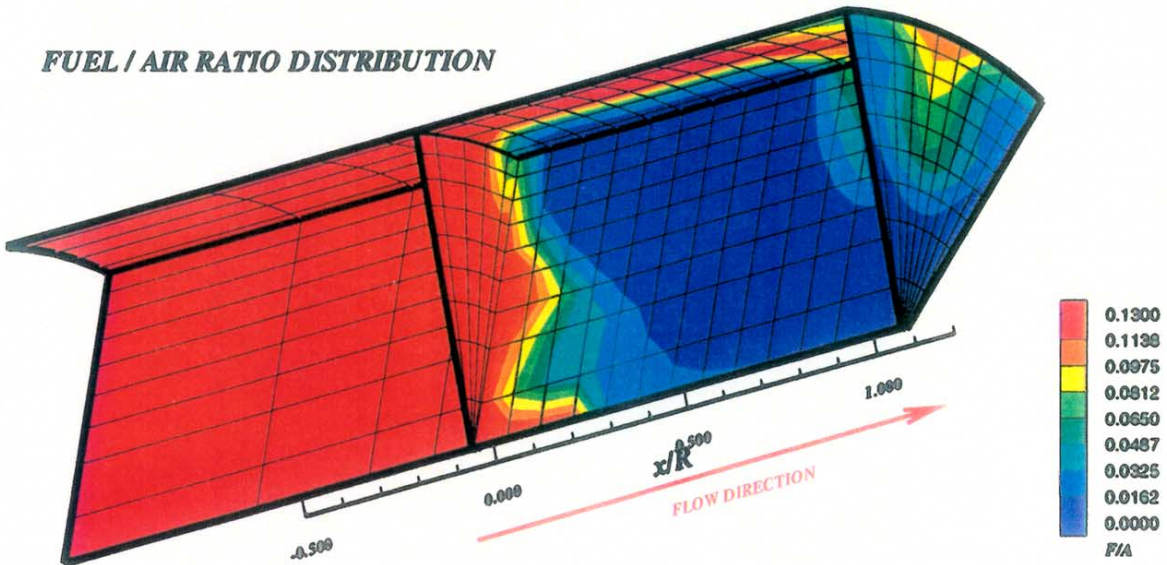
GAS TEMPERATURE DISTRIBUTION
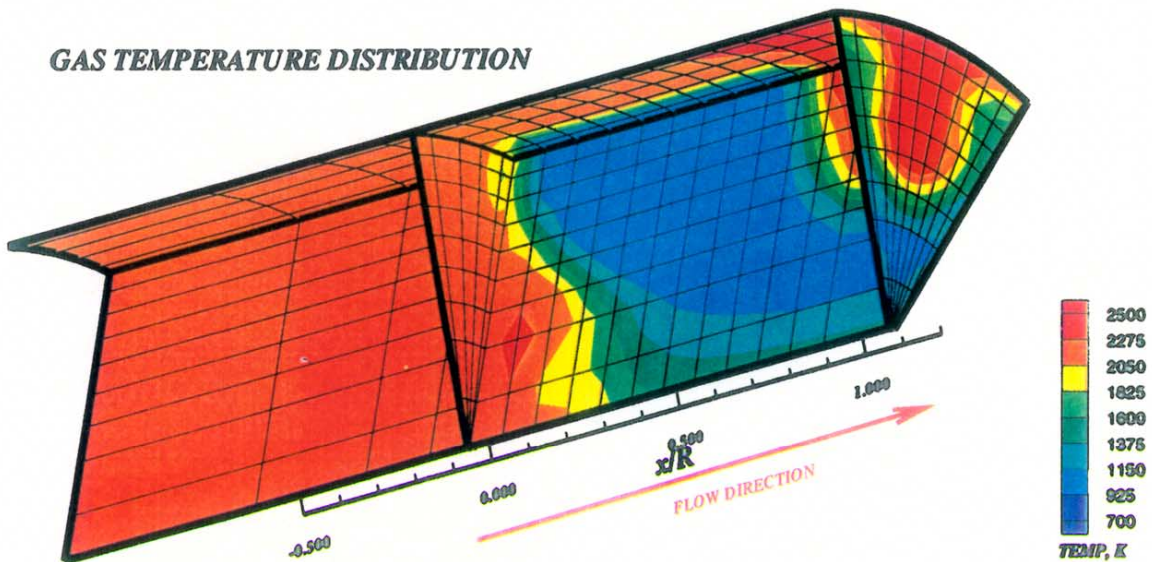
Figure-C16. Configuration #34 mixing performance and NO₂ production
J=26.0, MR=2.96, DR=2.28, phi rz=1.80, phi lz=0.416, Aligned slot, L/W=4, 8/row

LOCAL NO$_x$ PRODUCTION RATE
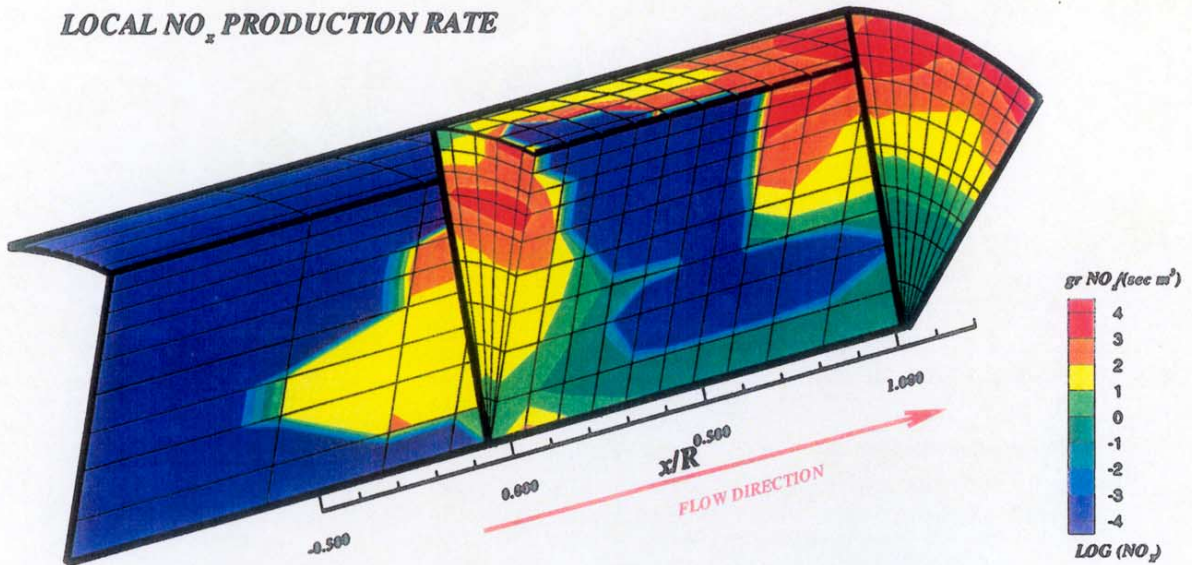
FUEL / AIR RATIO DISTRIBUTION
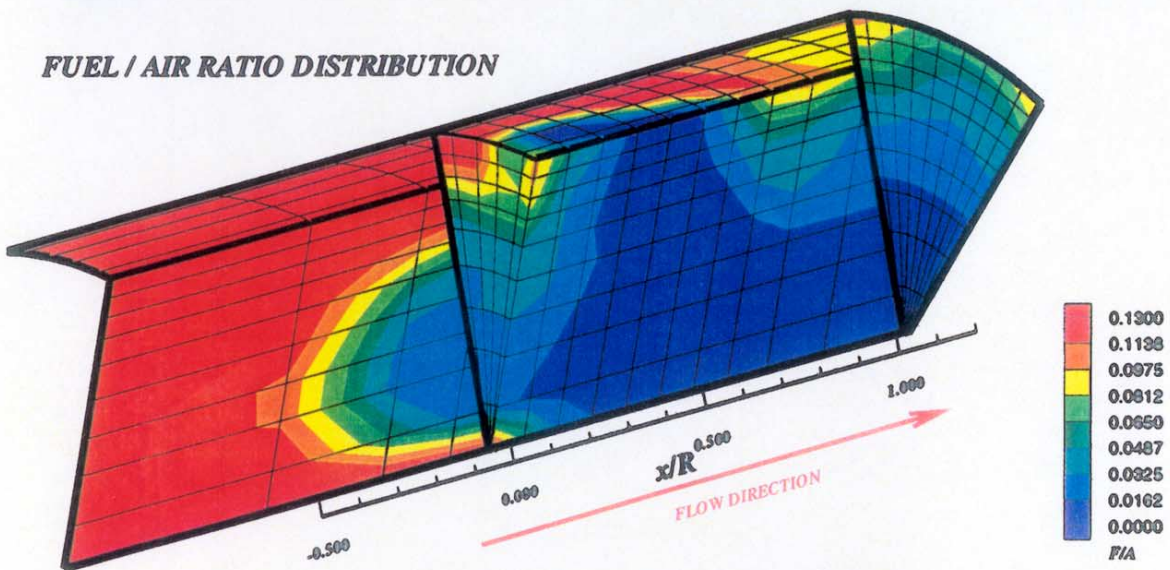
GAS TEMPERATURE DISTRIBUTION
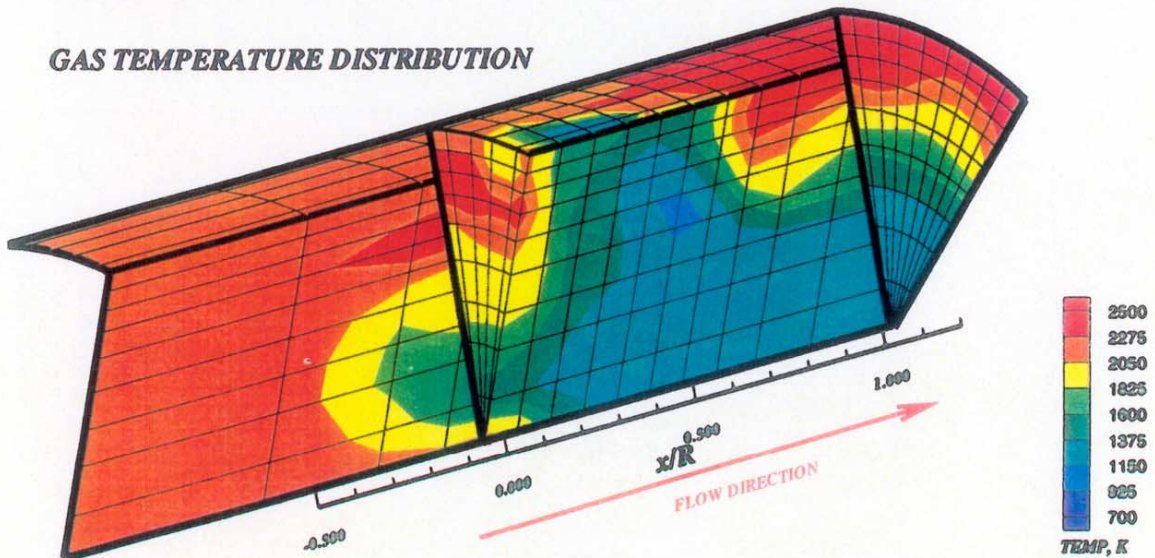
Figure-C17. Configuration #35 mixing performance and NO$_x$ production
J=88.1, MR=2.96, DR=2.28, phi rz=1.80, phi lz=0.416, 22.5° slot, L/W=4, 8/row

LOCAL NO$_x$ PRODUCTION RATE
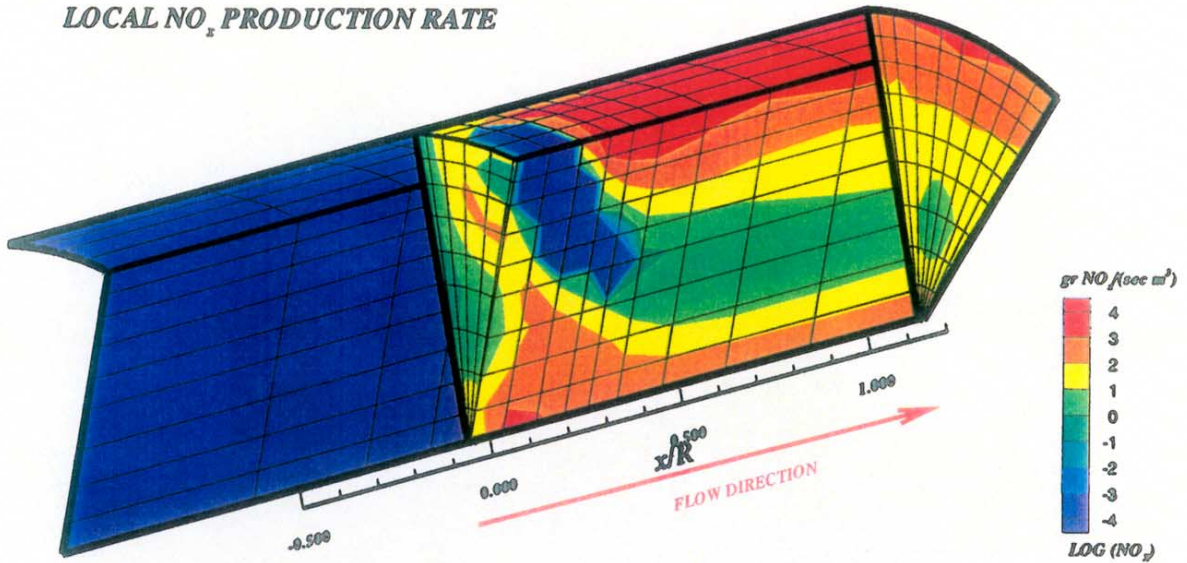
**FUEL / AIR RATIO DISTRIBUTION**
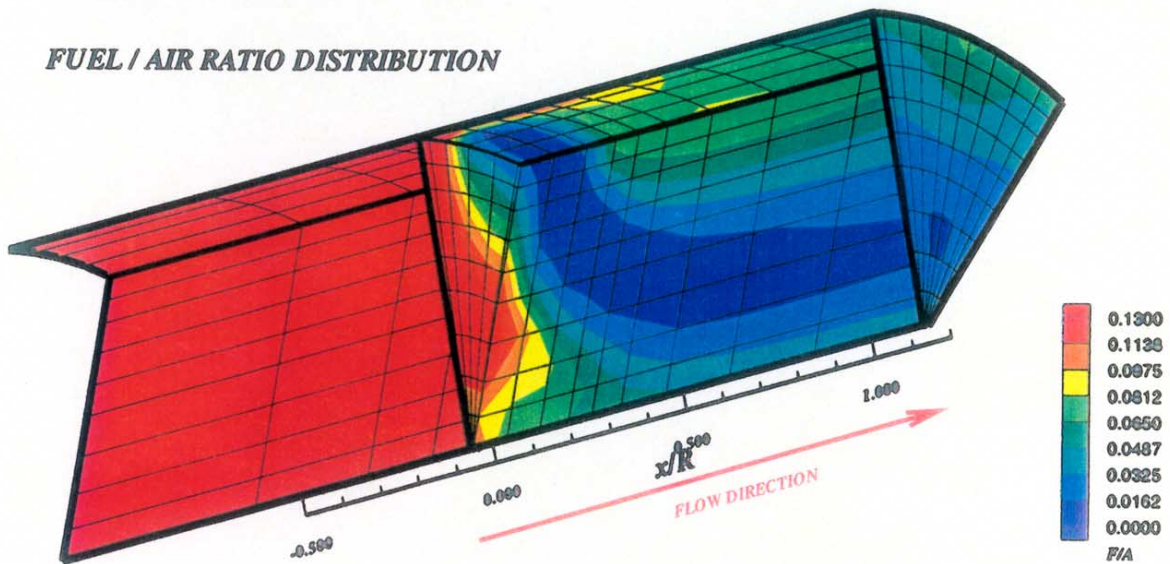
GAS TEMPERATURE DISTRIBUTION
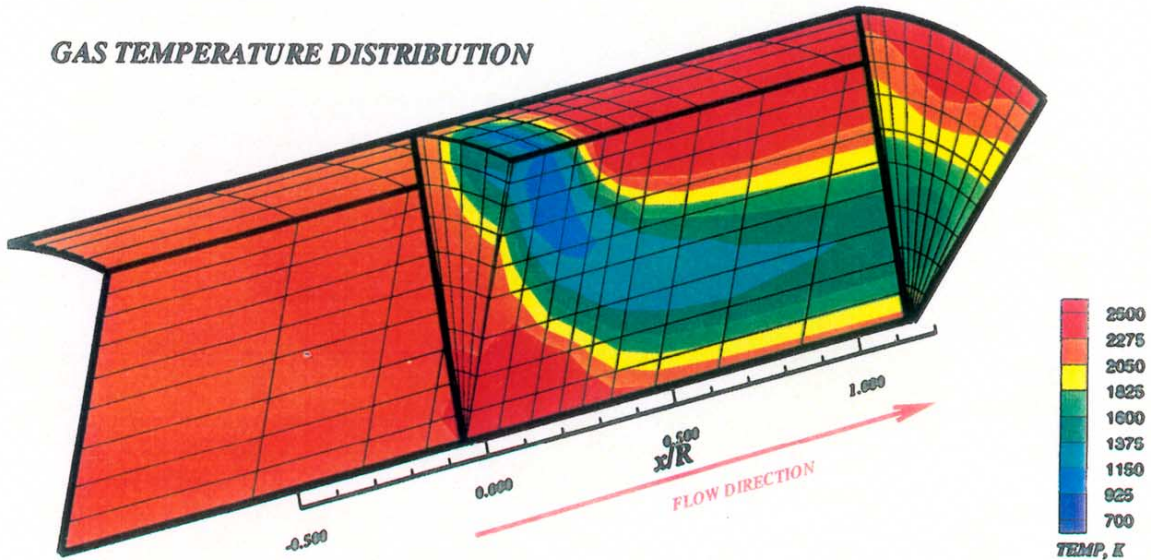
Figure-C18. Configuration #36 mixing performance and NO$_x$ production

J=106.2, MR=2.96, DR=2.28, phi rz=1.80, phi lz=0.416, Transverse slot, L/W=4, 8/row

APPENDIX-D

Interpolated iso-surfaces of constant NOx production (gr NOx / {sec m^3} for configuration numbers 19 through 36.

Each configuration is represented by two plots:

a) 3-D orthogonal view of the mixing section only (-1 ≤ x/R ≤ 5), and

b) 3-D orthogonal view of the entire computational domain (0 ≤ x/R ≤ 1)

	-1<x/R<5	0<x/R<1
CONF #	FIG #	FIG #
19	D1	D2
20	D3	D4
21	D5	D6
22	D7	D8
23	D9	D10
24	D11	D12
25	D13	D14
26	D15	D16
27	D17	D18
28	D19	D20
29	D21	D22
30	D23	D24
31	D25	D26
32	D27	D28
33	D29	D30
34	D31	D32
35	D33	D34
36	D35	D36

Figure-D37 shows the sub-volume grid of the entire mixing domain and partial domain (section of interest 0<x/R<1).
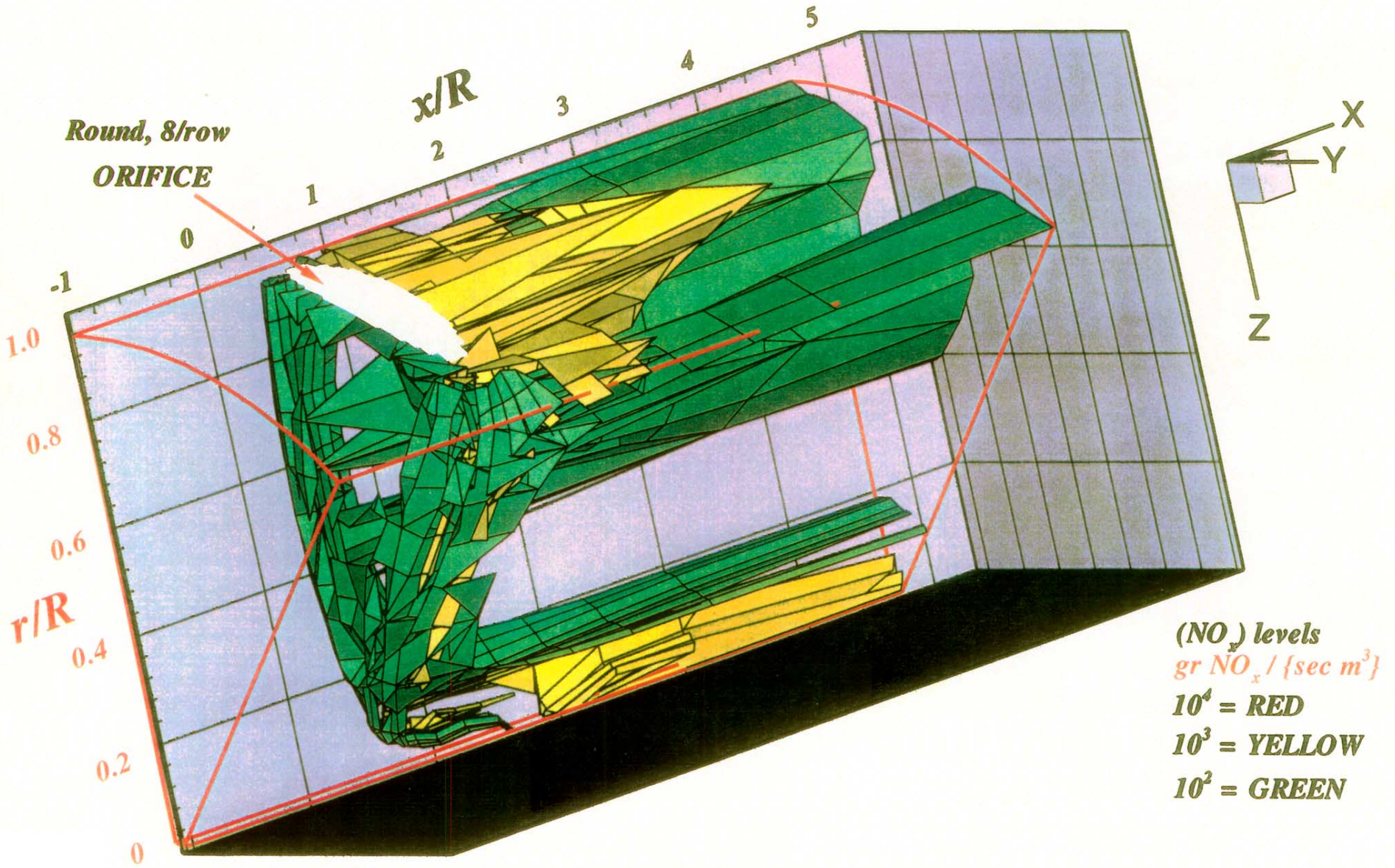
Figure-D1. Local NO_x production isopleths for configuration # 19
$J=26.7$, $MR=2.96$, $DR=2.28$, $Phi_{RZ}=1.80$, $Phi_{LZ}=0.416$

Round, 8/row
ORIFICE

x/R

r/R

(NO_x) levels
$gr\ NO_x / \{sec\ m^3\}$
$10^4 = $ RED
$10^3 = $ YELLOW
$10^2 = $ GREEN

ORIFICE

x/R

NO_x levels, log(gr NO_x /{sec m^3})

10^4 = RED

10^3 = YELLOW

10^2 = GREEN
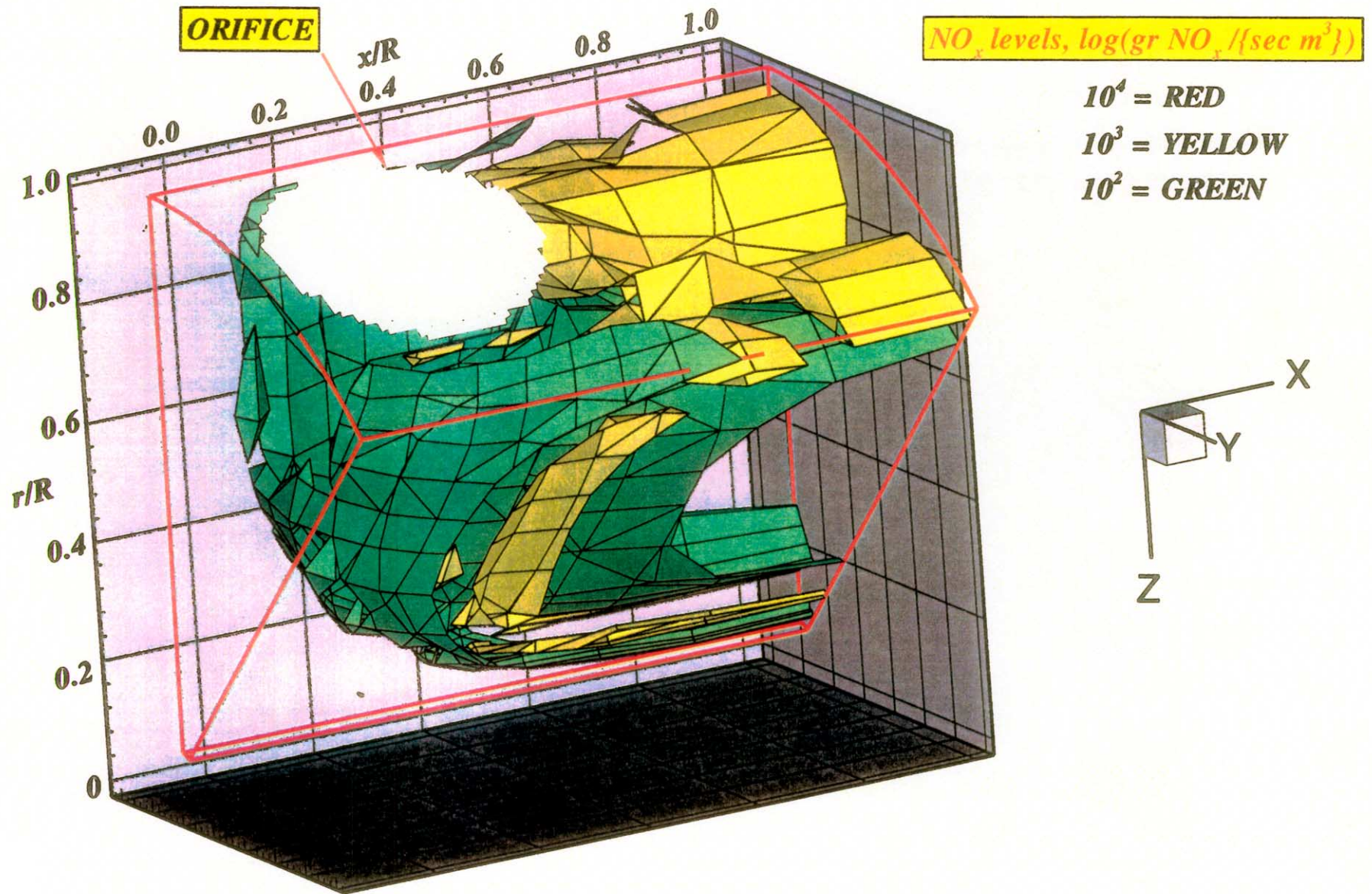
Figure-D2. Local NO_x production isopleths for configuration #19
J=26.7, MR=2.96, DR=2.28, phi rz=1.80, phi lz=0.416

45° slot, L/W=4

ORIFICE

x/R

5

4

3

2

1

0

-1

r/R

1.0

0.8

0.6

0.4

0.2

0

X

Y

Z

(NO$_x$) levels

gr NO$_x$ / {sec m^3}

10^4 = RED

10^3 = YELLOW

10^2 = GREEN
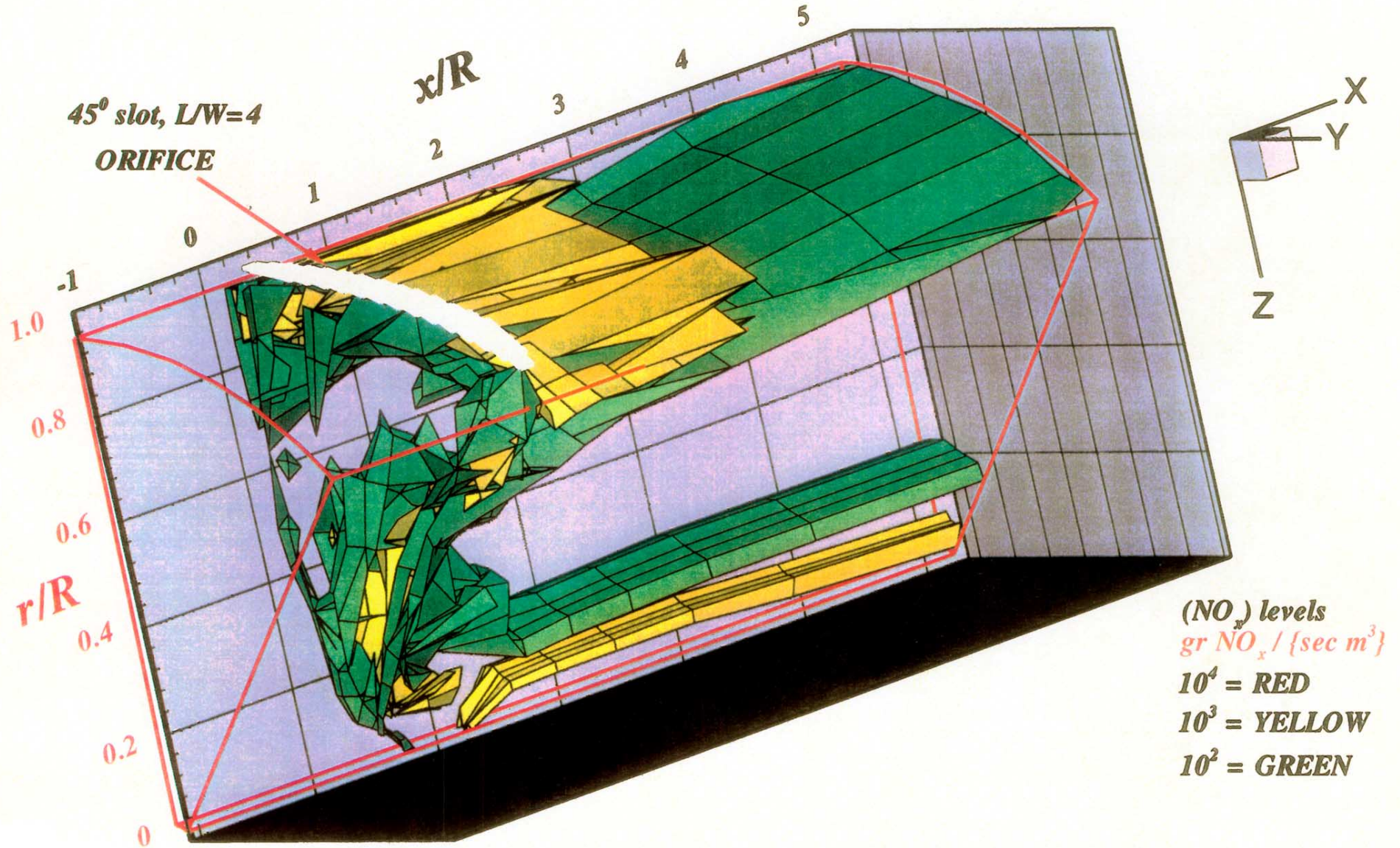
Figure-D3. Local NO$_x$ production isopleths for configuration # 20

**J=30.5, MR=2.96, DR=2.28, Phi$_{RZ}$ = 1.80, Phi$_{LZ}$ = 0.416**

ORIFICE

NO_x levels, $\log(gr\ NO_x/\{sec\ m^3\})$

10^4 = RED

10^3 = YELLOW

10^2 = GREEN
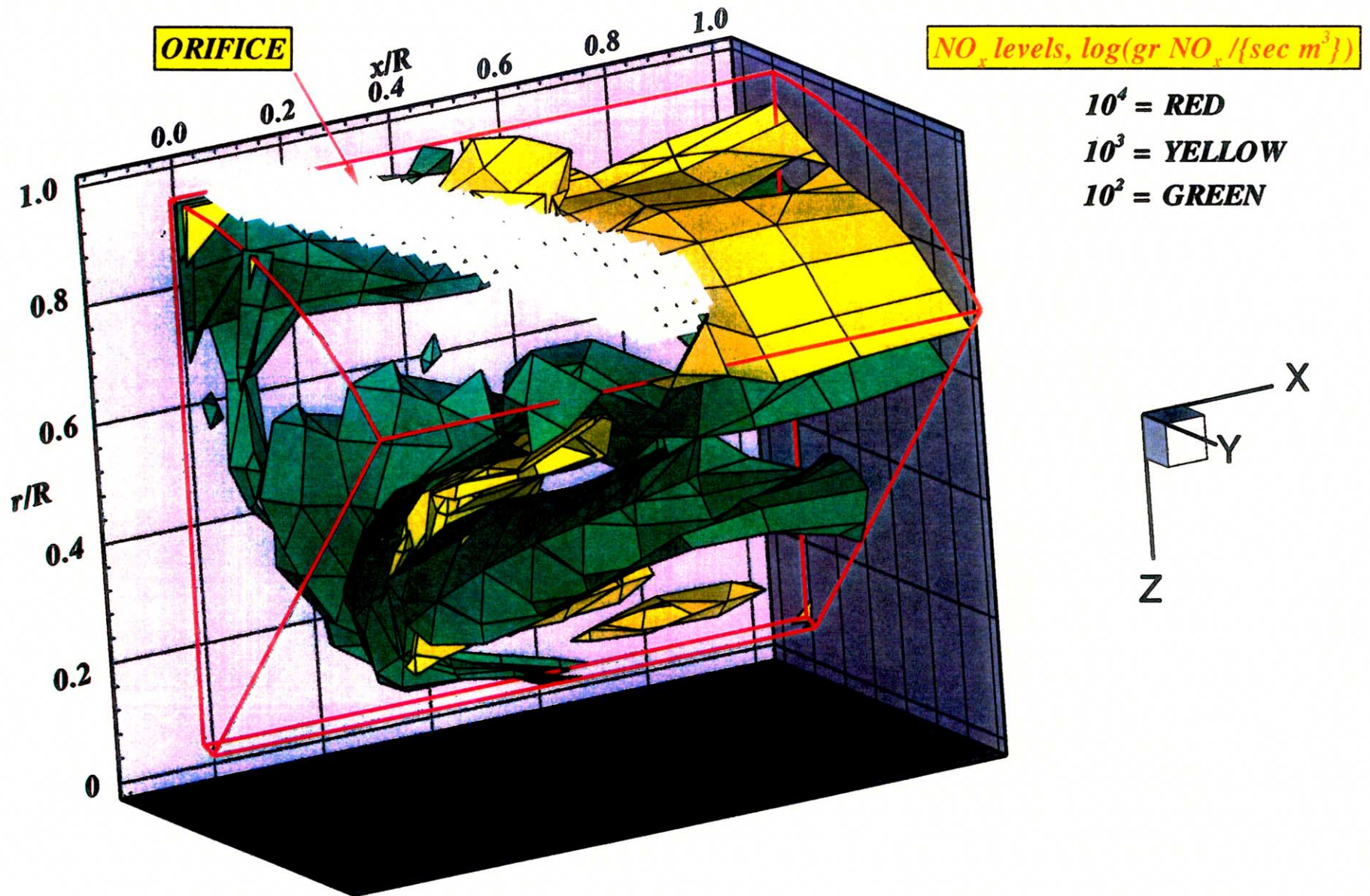
Figure-D4. Local NO_x production isopleths for configuration #19
J=30.5, MR=2.96, DR=2.28, phi rz=1.80, phi lz=0.416

Aligned slot, L/W=4, 8/row

ORIFICE

x/R

r/R

(NO_x) levels

$gr\ NO_x\ /\ \{sec\ m^3\}$

$10^4 = RED$

$10^3 = YELLOW$

$10^2 = GREEN$
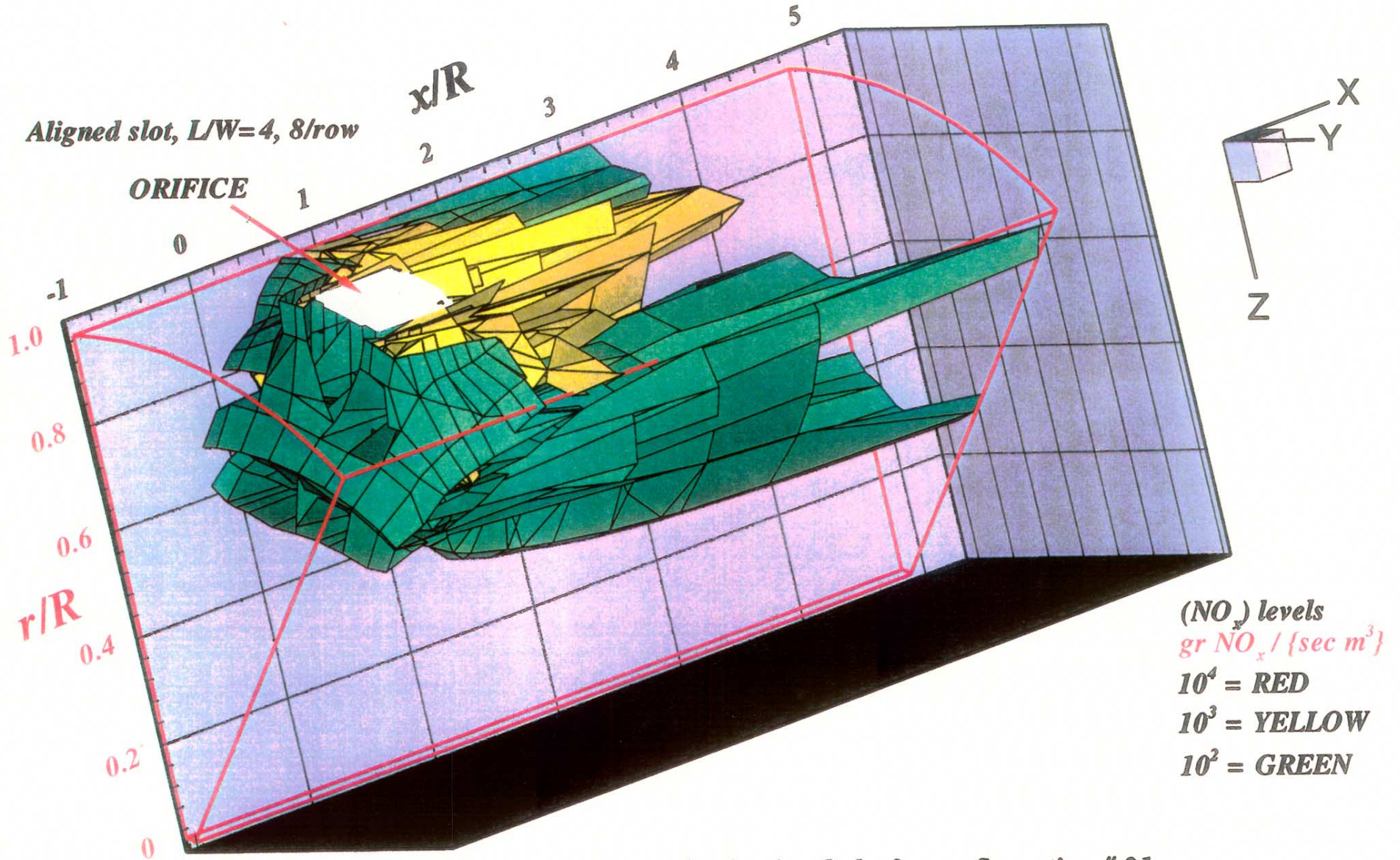
**Figure-D5. Local NO_x production isopleths for configuration # 21**
J=51.1, MR=2.96, DR=2.28, Phi_{RZ} = 1.80, Phi_{LZ} = 0.416

x/R

ORIFICE

NO$_x$ levels, log(gr NO$_x$ /{sec m^3})

10^4 = RED

10^3 = YELLOW

10^2 = GREEN

X

Y

Z

r/R
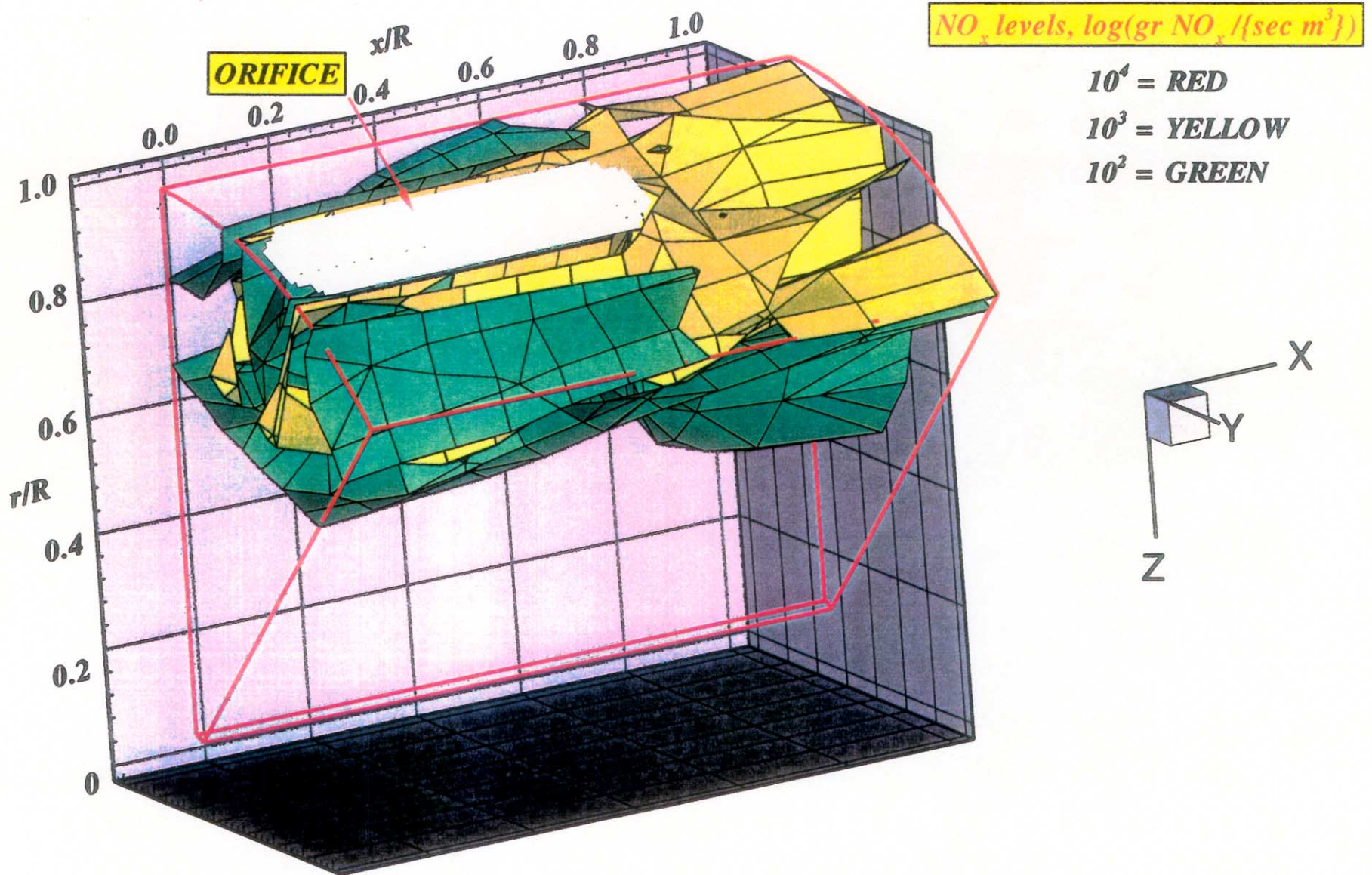
Figure-D6. Local NO$_x$ production isopleths for configuration #21
J=51.1, MR=2.96, DR=2.28, phi rz=1.80, phi lz=0.416

Round, 8/row
ORIFICE

x/R

X
Y
Z

r/R

(NO$_x$) levels
gr NO$_x$ / {sec m^3}
10^4 = RED
10^3 = YELLOW
10^2 = GREEN
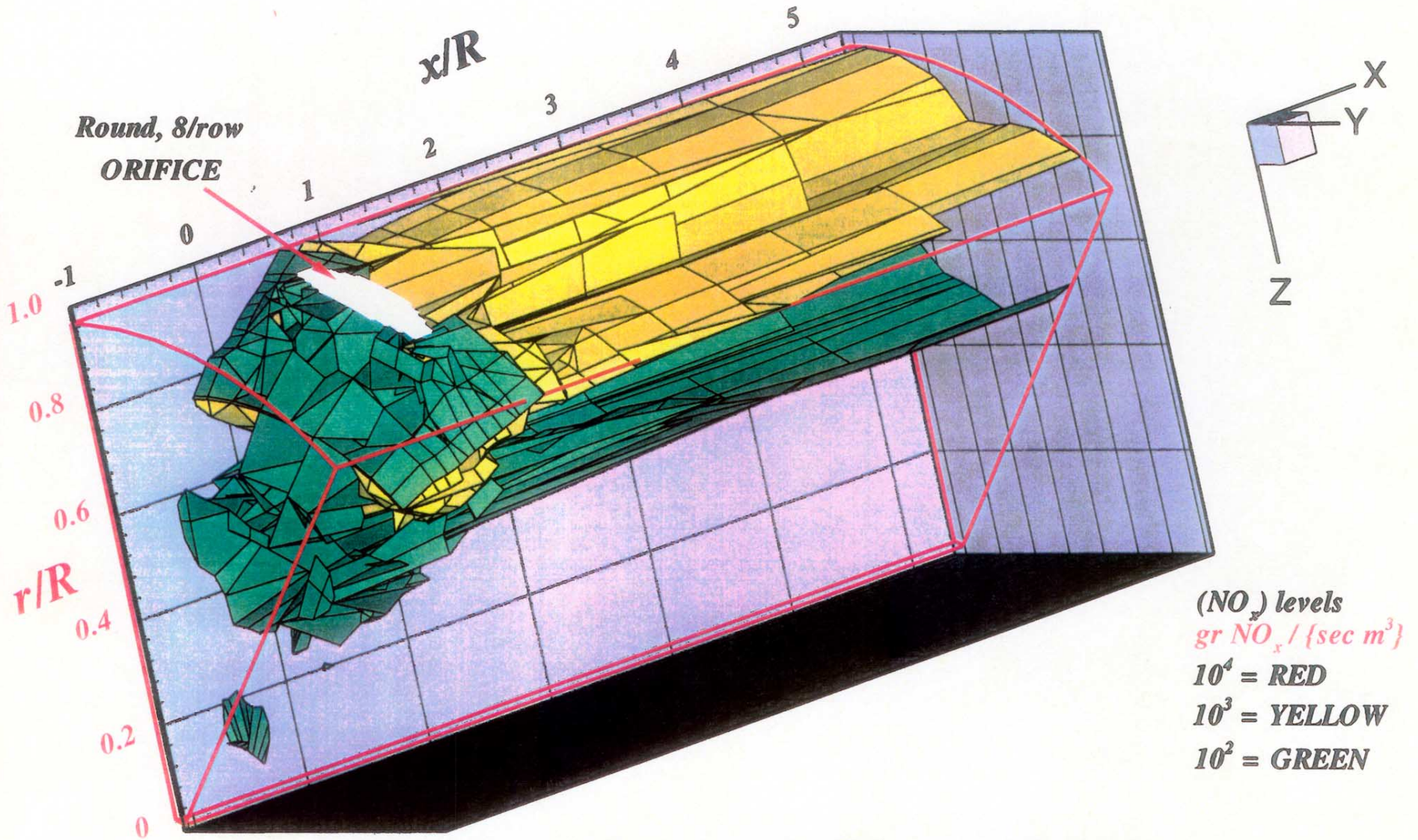
**Figure-D7. Local NO$_x$ production isopleths for configuration # 22
J=84.1, MR=2.96, DR=2.28, Phi$_{RZ}$ = 1.80, Phi$_{LZ}$ = 0.416**

ORIFICE

x/R

1.0
0.8
0.6
0.4
0.2
0.0

r/R

1.0
0.8
0.6
0.4
0.2
0

NO_x levels, log(gr NO_x /{sec m^3})

10^4 = RED

10^3 = YELLOW

10^2 = GREEN

X

Y

Z
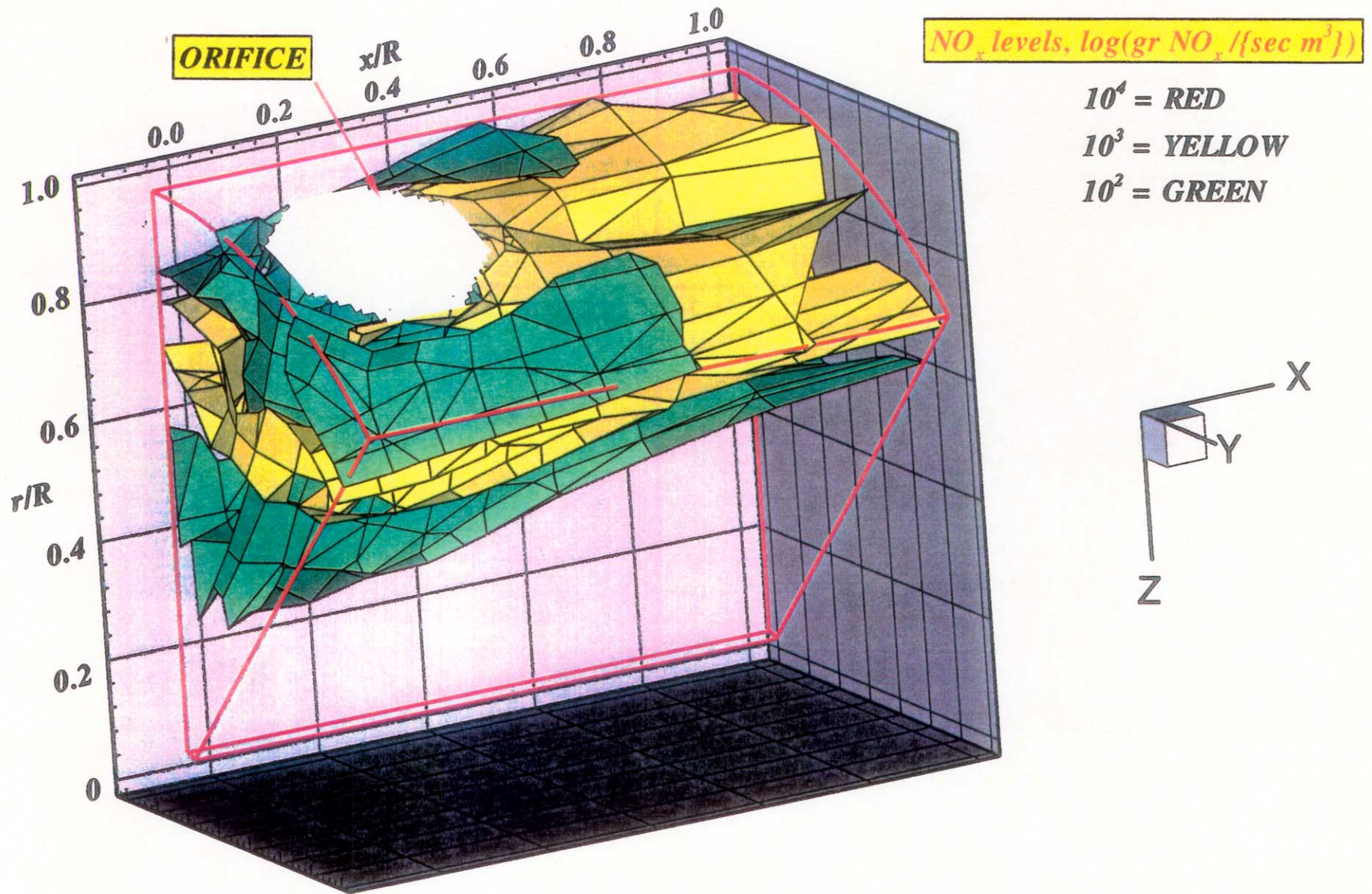
Figure-D8. Local NO_x production isopleths for configuration #22
J=84.1, MR=2.96, DR=2.28, phi rz=1.80, phi lz=0.416

Figure-D9. *Local NO$_x$ production isopleths for configuration # 23*
*J=55.3, MR=2.96, DR=2.28, Phi$_{RZ}$ = 1.80, Phi$_{LZ}$ = 0.416*

ORIFICE

NO_x levels, $log(gr\ NO_x/\{sec\ m^3\})$

10^4 = **RED**

10^3 = **YELLOW**

10^2 = **GREEN**

x/R

0.0 0.2 0.4 0.6 0.8 1.0

1.0

0.8

r/R 0.6

0.4

0.2

0

X

Y

Z
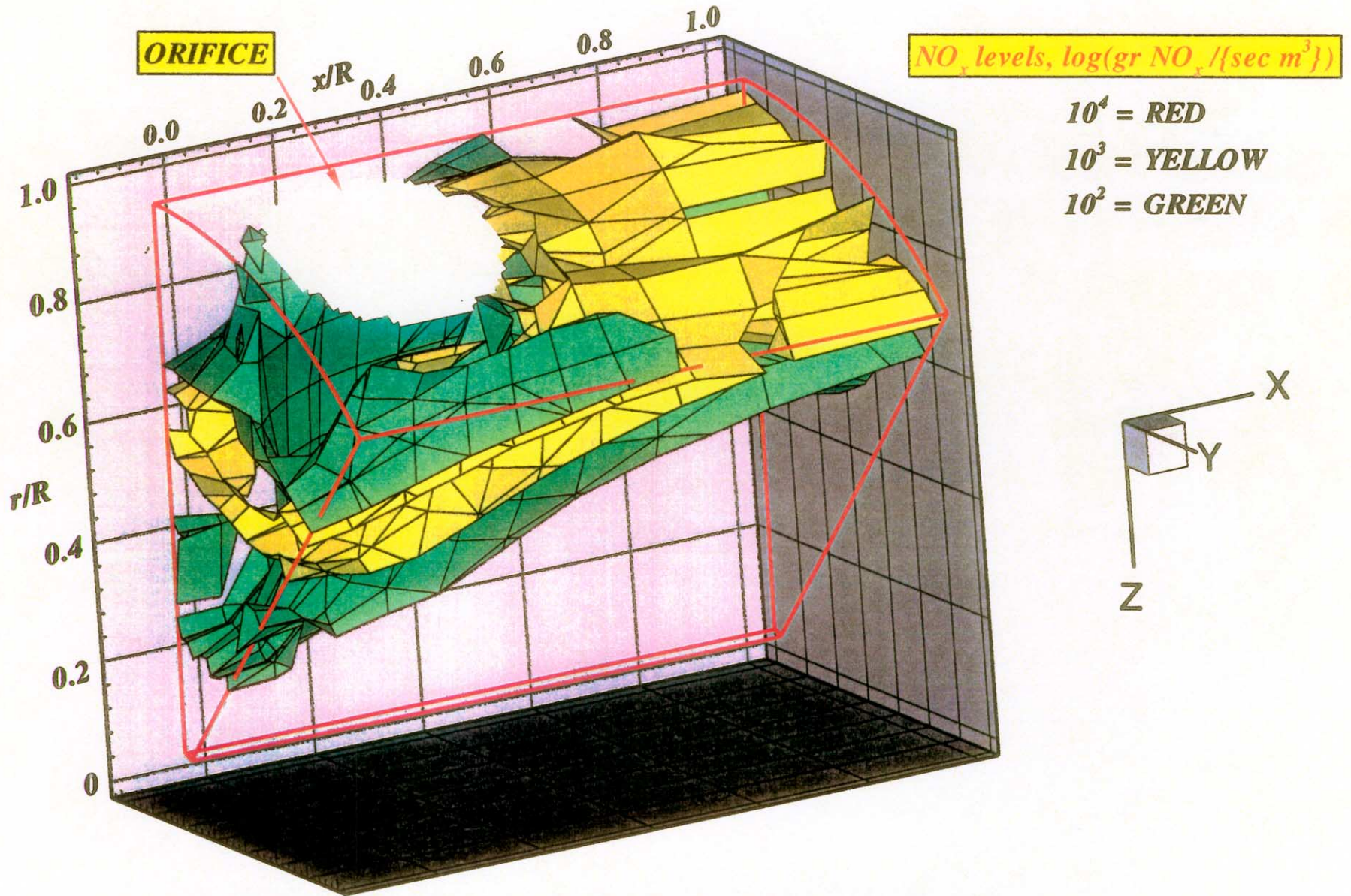
Figure-D10. Local NO_x production isopleths for configuration #23
J=55.3, MR=2.96, DR=2.28, phi rz=1.80, phi lz=0.416

45⁰ slot, L/W=8, 8/row
ORIFICE

x/R

5

4

3

2

1

0

-1

X

Y

Z

r/R

1.0

0.8

0.6

0.4

0.2

0

(NO$_x$) levels
gr NO$_x$ / {sec m^3}

10^4 = RED
10^3 = YELLOW
10^2 = GREEN
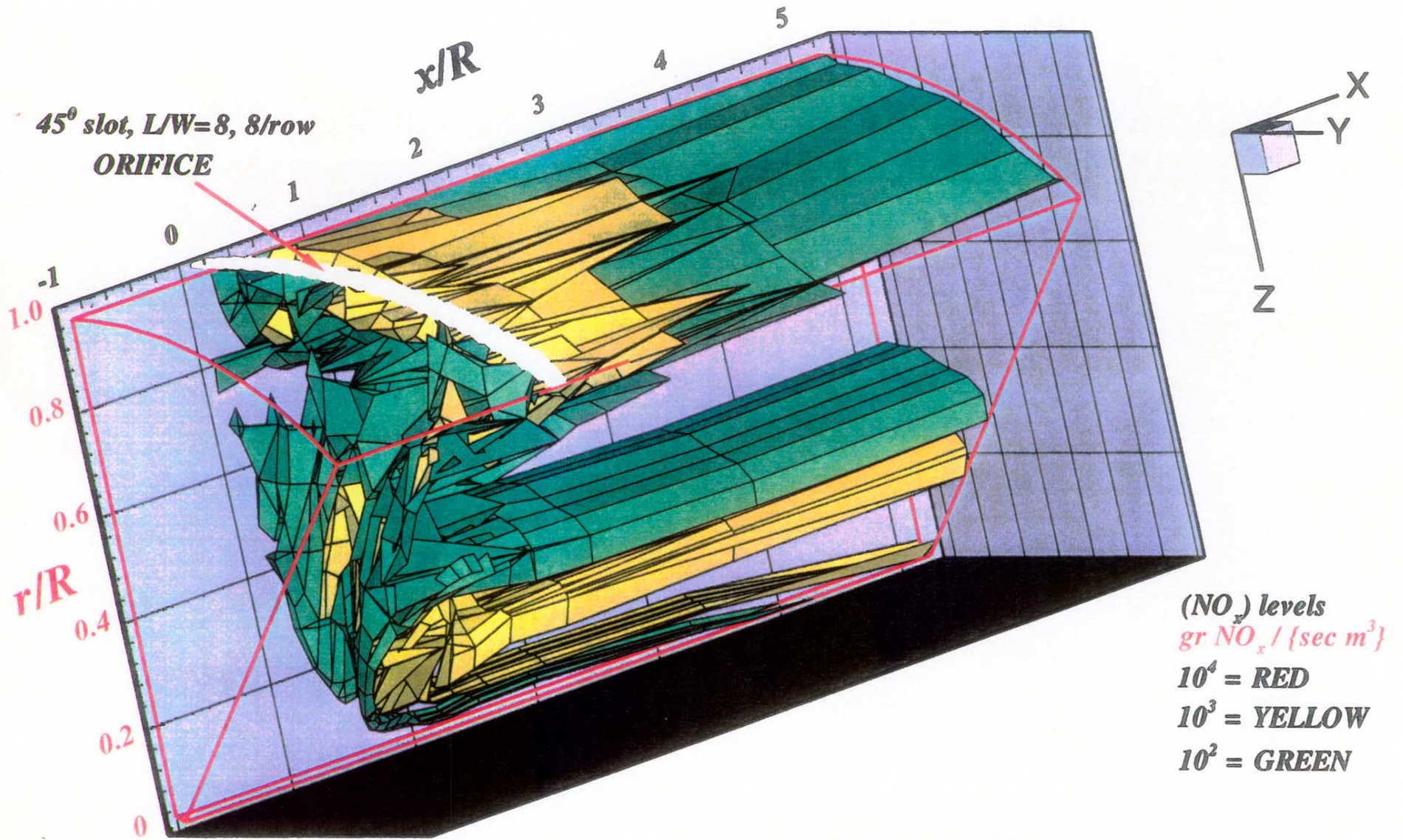
Figure-D11. Local NO$_x$ production isopleths for configuration # 24
J=28.1, MR=2.96, DR=2.28, Phi$_{RZ}$ = 1.80, Phi$_{LZ}$ = 0.416

ORIFICE

x/R
0.0   0.2   0.4   0.6   0.8   1.0

NOₓ levels, log(gr NOₓ /{sec m³})

10^4 = RED

10^3 = YELLOW

10^2 = GREEN

r/R
1.0
0.8
0.6
0.4
0.2
0

X
Y
Z
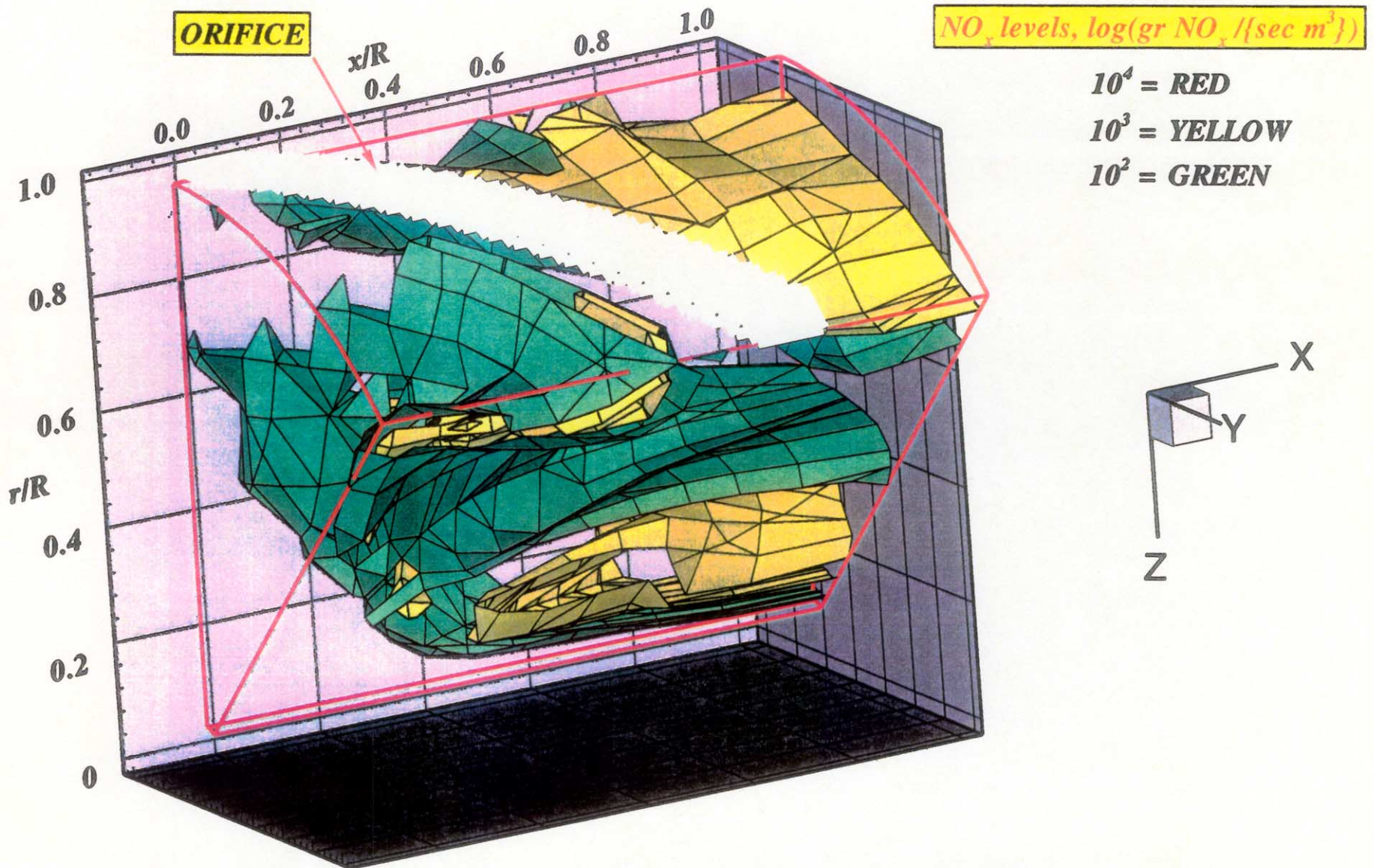
Figure-D12. Local NOₓ production isopleths for configuration #24
J=28.1, MR=2.96, DR=2.28, phi rz=1.80, phi lz=0.416
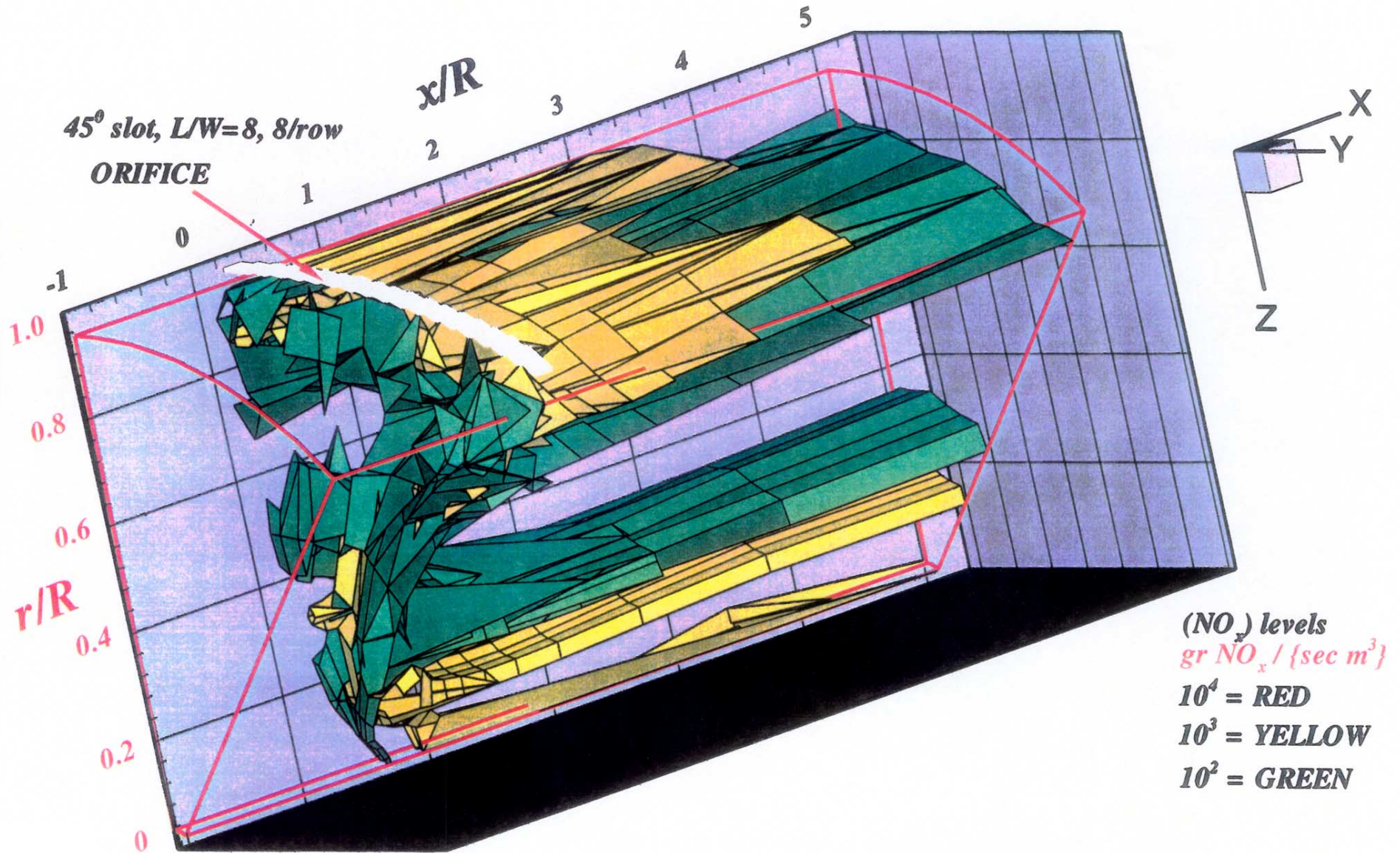
Figure-D13. Local NO_x production isopleths for configuration # 25
$J=50.9$, $MR=2.96$, $DR=2.28$, $Phi_{RZ} = 1.80$, $Phi_{LZ} = 0.416$

ORIFICE

x/R

1.0

0.8

0.6

0.4

0.2

0.0

r/R

1.0

0.8

0.6

0.4

0.2

0

NO_x levels, $log(gr\ NO_x\ /\{sec\ m^3\})$

10^4 = RED

10^3 = YELLOW

10^2 = GREEN

X

Y

Z
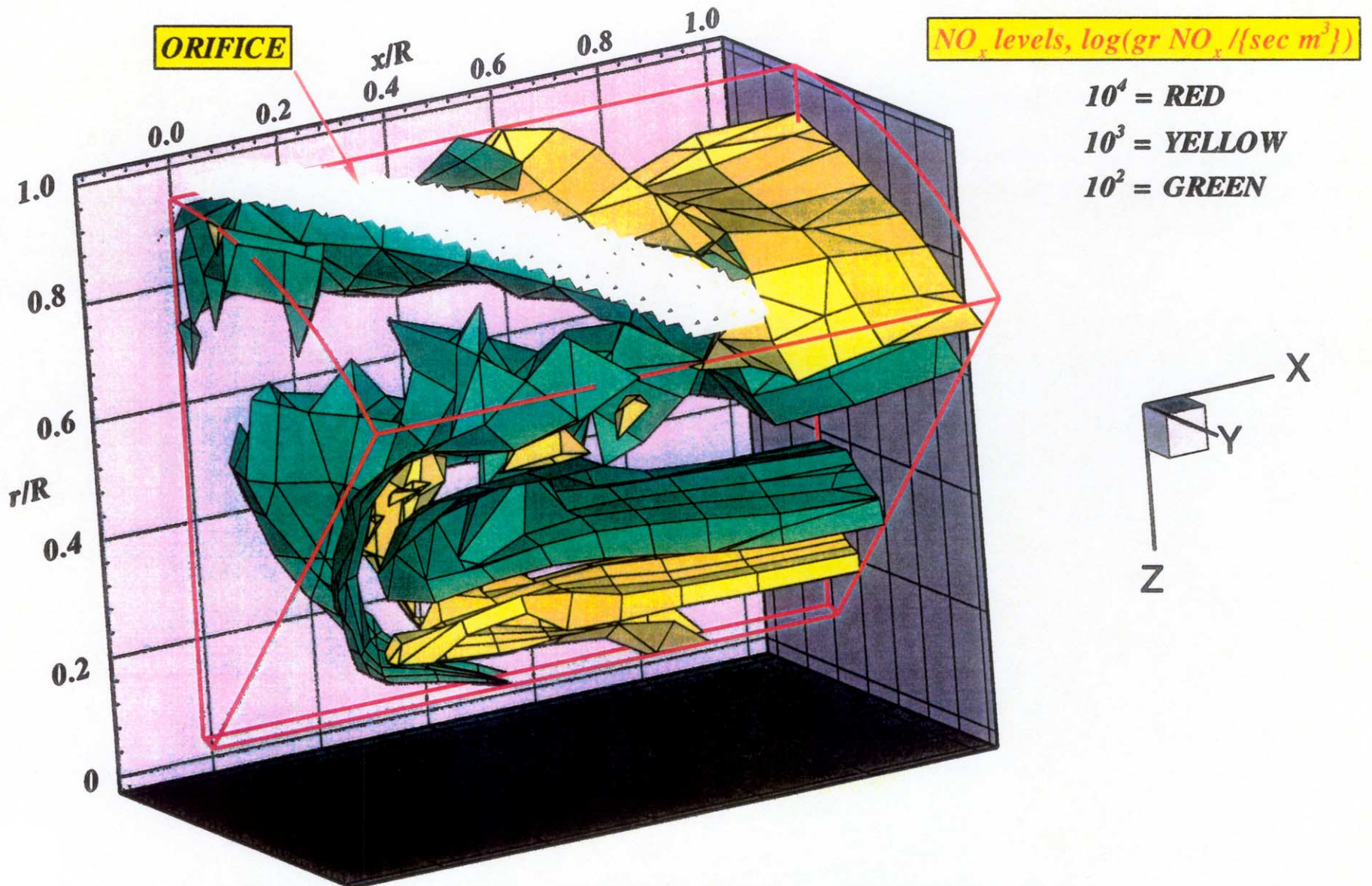
Figure-D14. Local NO_x production isopleths for configuration #25
J=50.9, MR=2.96, DR=2.28, phi rz=1.80, phi lz=0.416
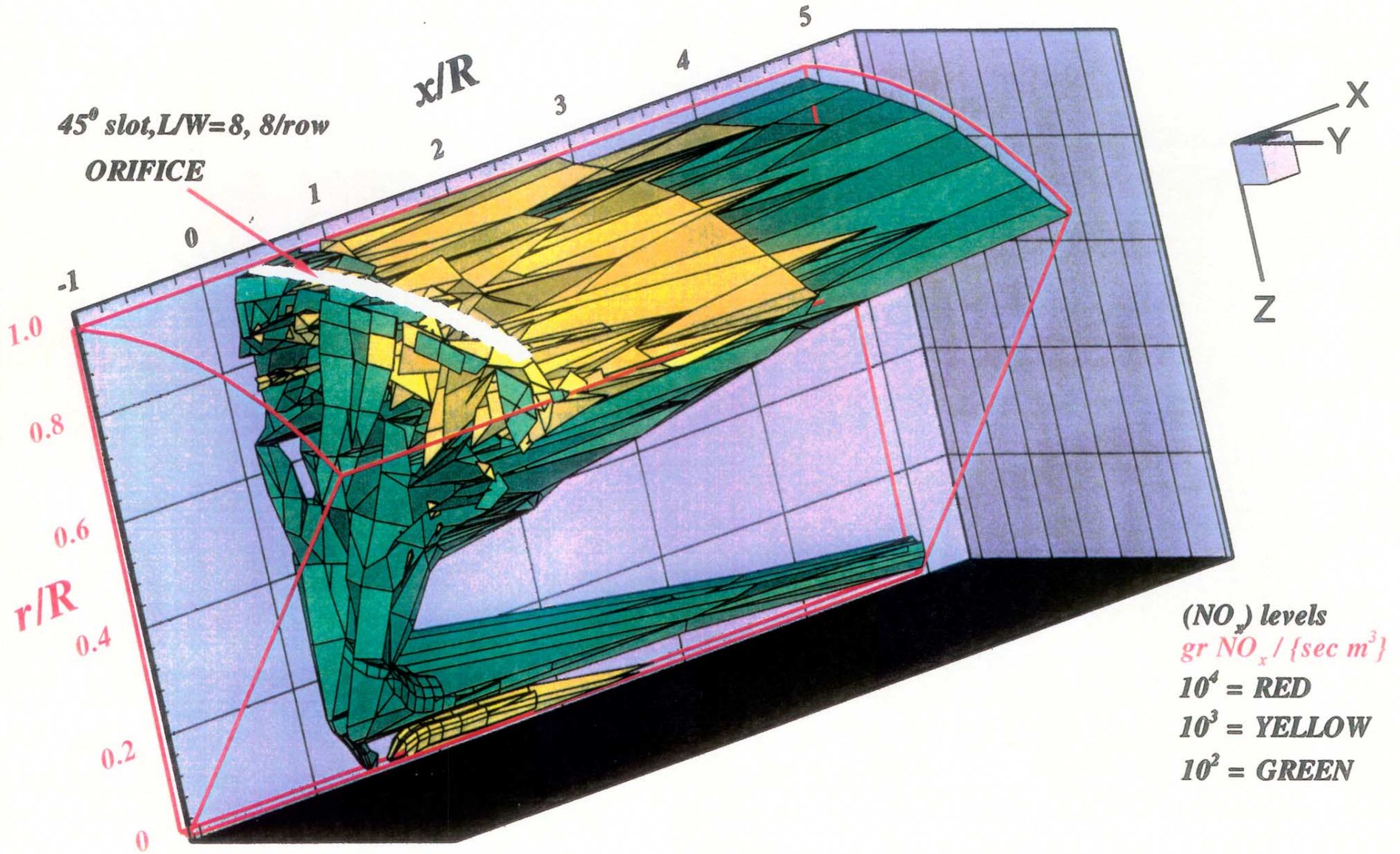
Figure-D15. Local NOₓ production isopleths for configuration # 26
J=88.4, MR=2.96, DR=2.28, Phi$_{RZ}$ = 1.80, Phi$_{LZ}$ = 0.416

ORIFICE

x/R

0.0   0.2   0.4   0.6   0.8   1.0

r/R

1.0

0.8

0.6

0.4

0.2

0

NO_x levels, $\log(gr\ NO_x/\{sec\ m^3\})$

10^4 = RED

10^3 = YELLOW

10^2 = GREEN

X

Y

Z
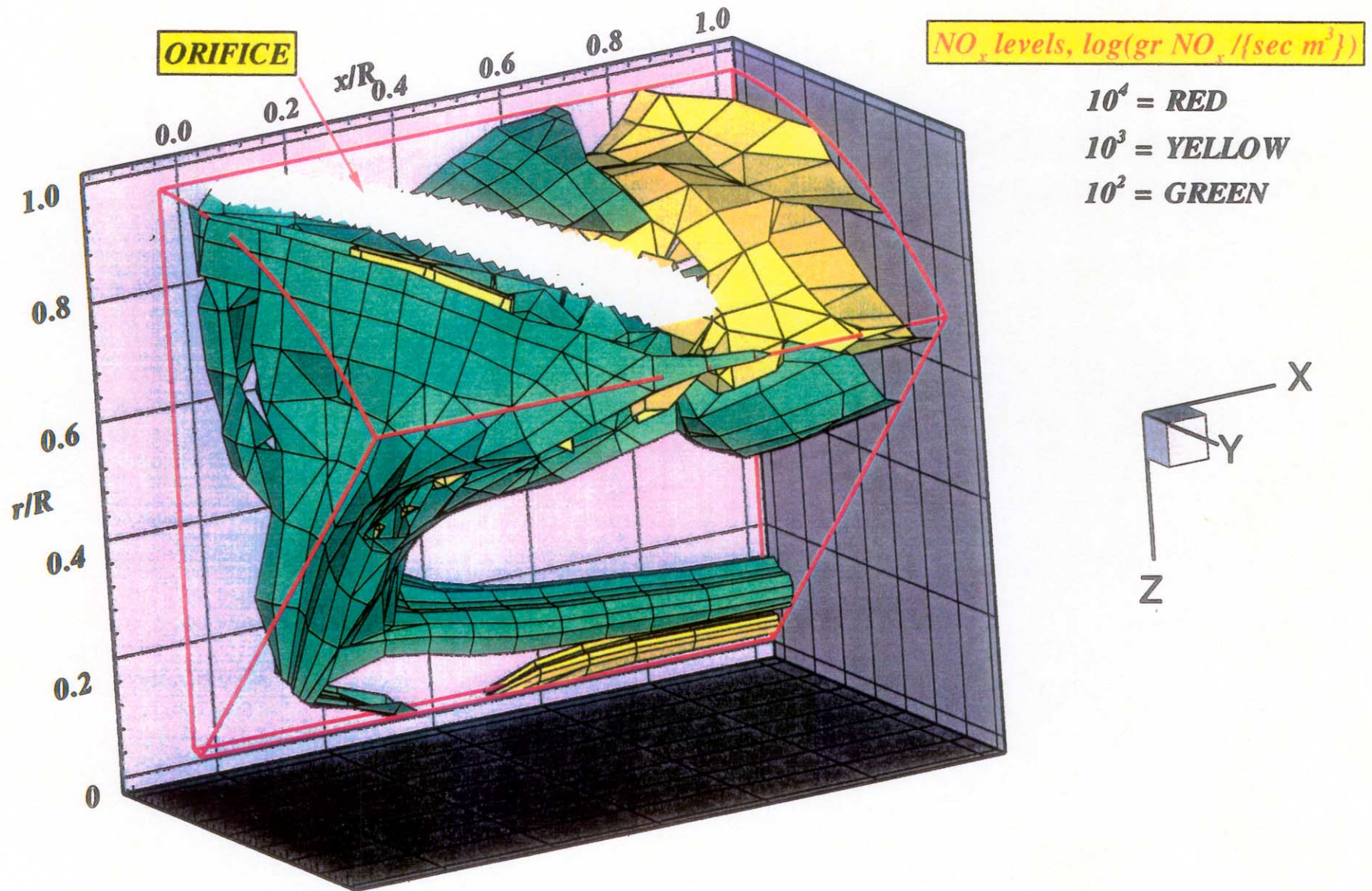
Figure-D16. Local NO_x production isopleths for configuration #26
J=88.4, MR=2.96, DR=2.28, phi rz=1.80, phi lz=0.416

22.5° *slot, L/W=4, 8/row*

ORIFICE

x/R

5

4

3

2

1

0

-.1

X

Y

Z

r/R

1.0

0.8

0.6

0.4

0.2

0

(NO$_x$) levels

gr NO$_x$ / {sec m^3}

10^4 = RED

10^3 = YELLOW

10^2 = GREEN
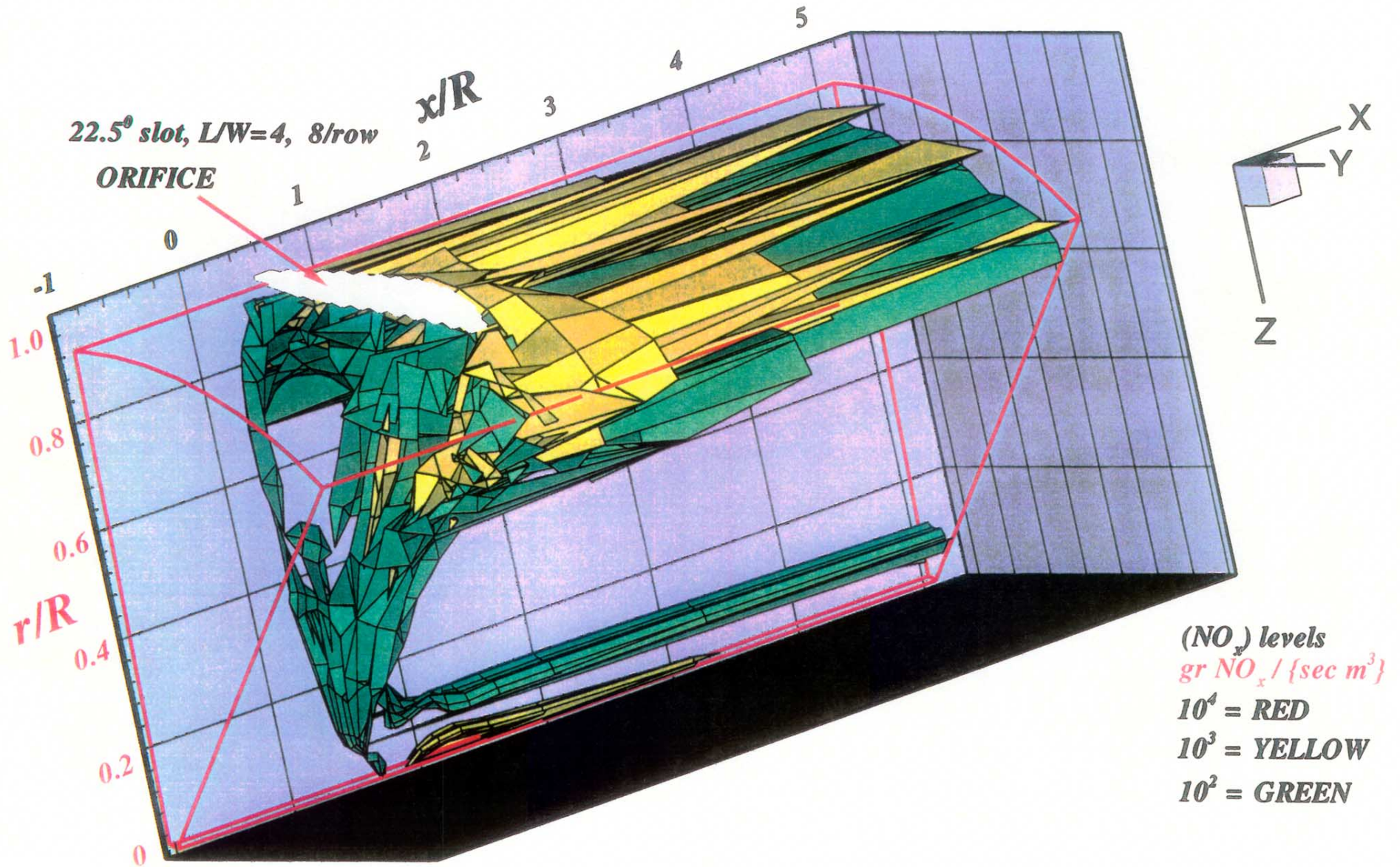
Figure-D17. Local NO$_x$ production isopleths for configuration # 27
J=28.0, MR=2.96, DR=2.28, Phi$_{RZ}$ = 1.80, Phi$_{LZ}$ = 0.416

ORIFICE

NO_x levels, $\log(gr\ NO_x/\{sec\ m^3\})$

10^4 = RED

10^3 = YELLOW

10^2 = GREEN
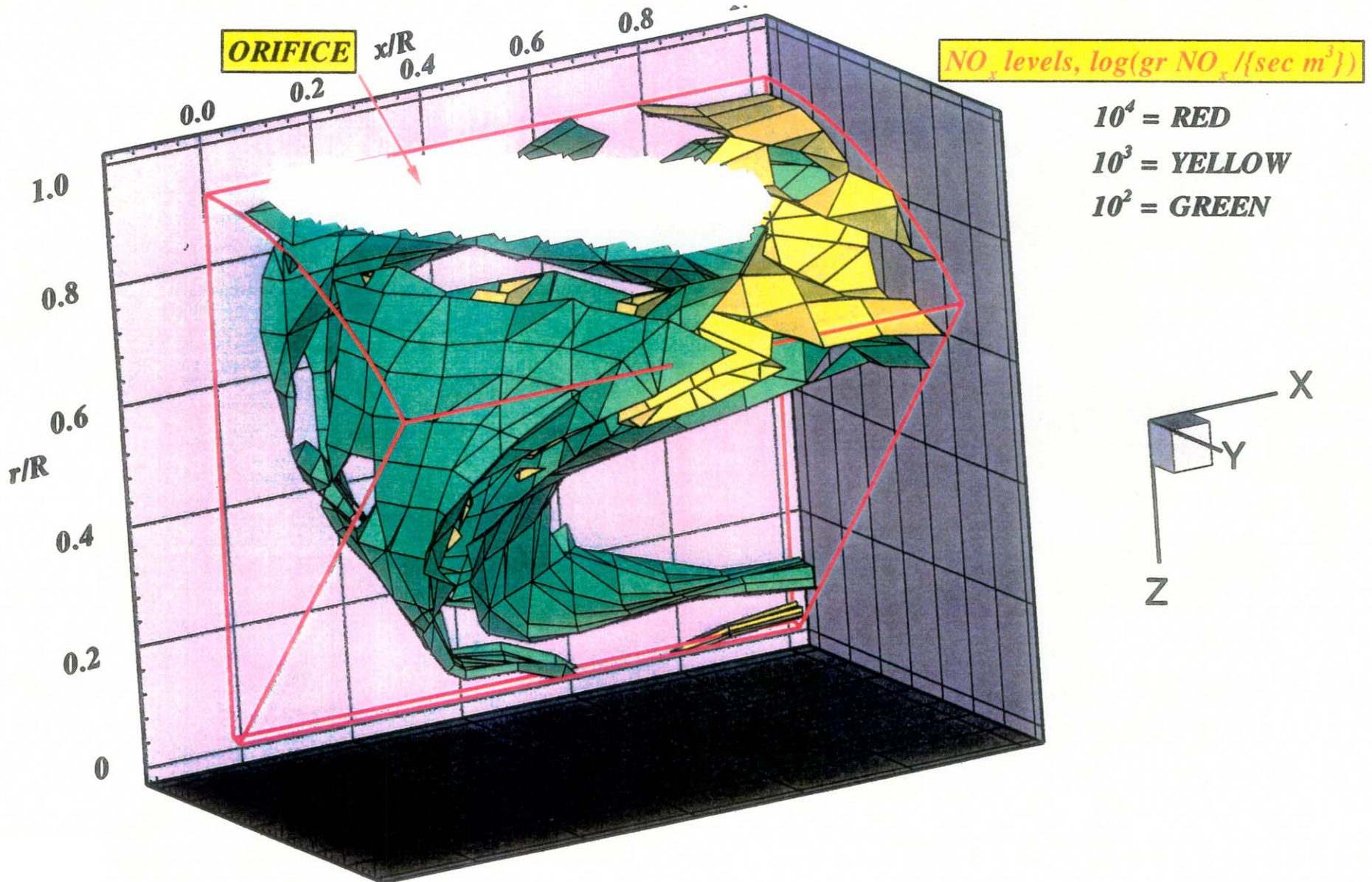
Figure-D18. Local NO_x production isopleths for configuration #27
J=28.0, MR=2.96, DR=2.28, phi rz=1.80, phi lz=0.416
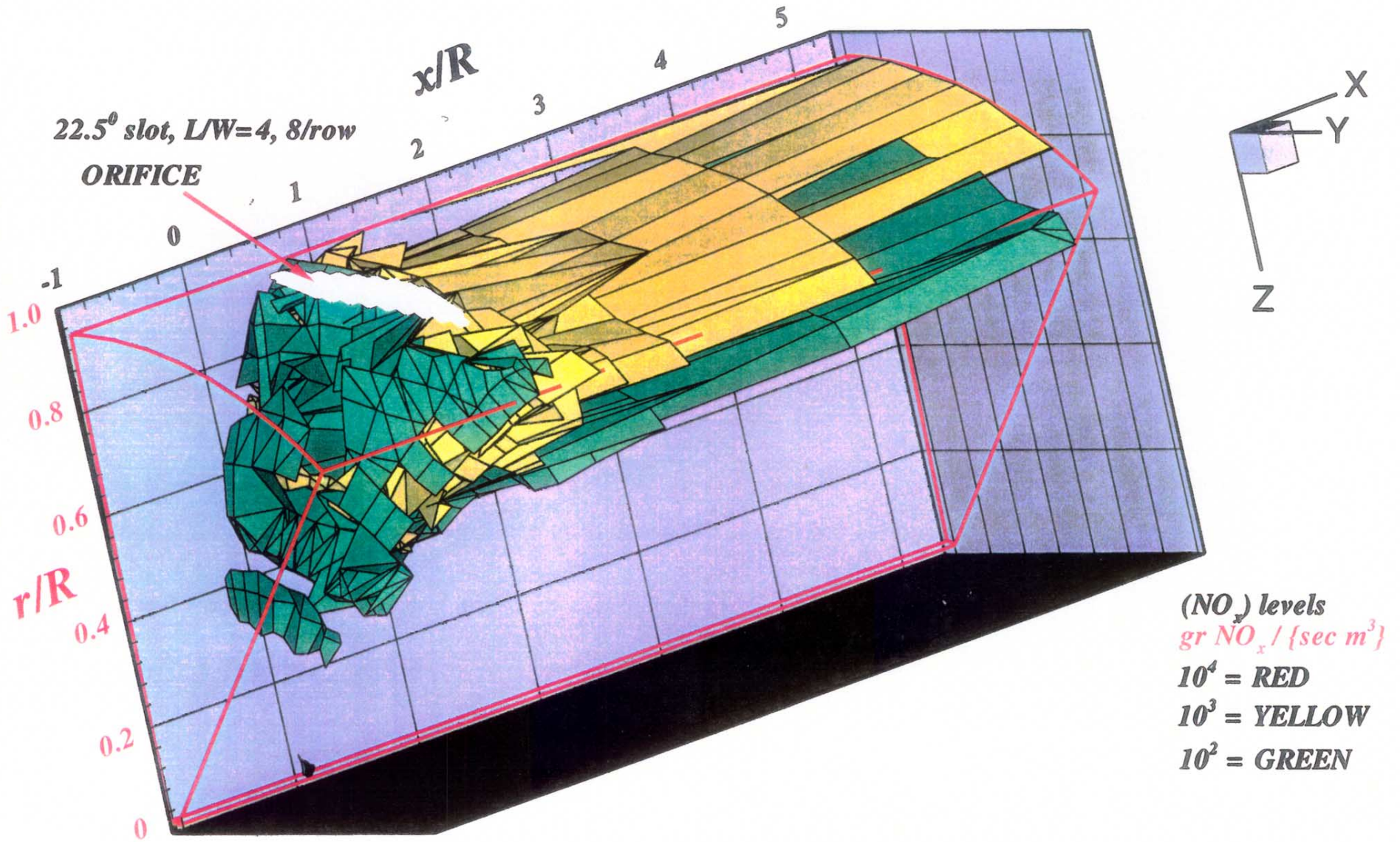
Figure-D19. Local NO$_x$ production isopleths for configuration # 28
**J=53.2, MR=2.96, DR=2.28, Phi$_{RZ}$ = 1.80, Phi$_{LZ}$ = 0.416**

ORIFICE

x/R

r/R

NO_x levels, $\log(gr\ NO_x\ /\{sec\ m^3\})$

10^4 = RED

10^3 = YELLOW

10^2 = GREEN

X

Y

Z
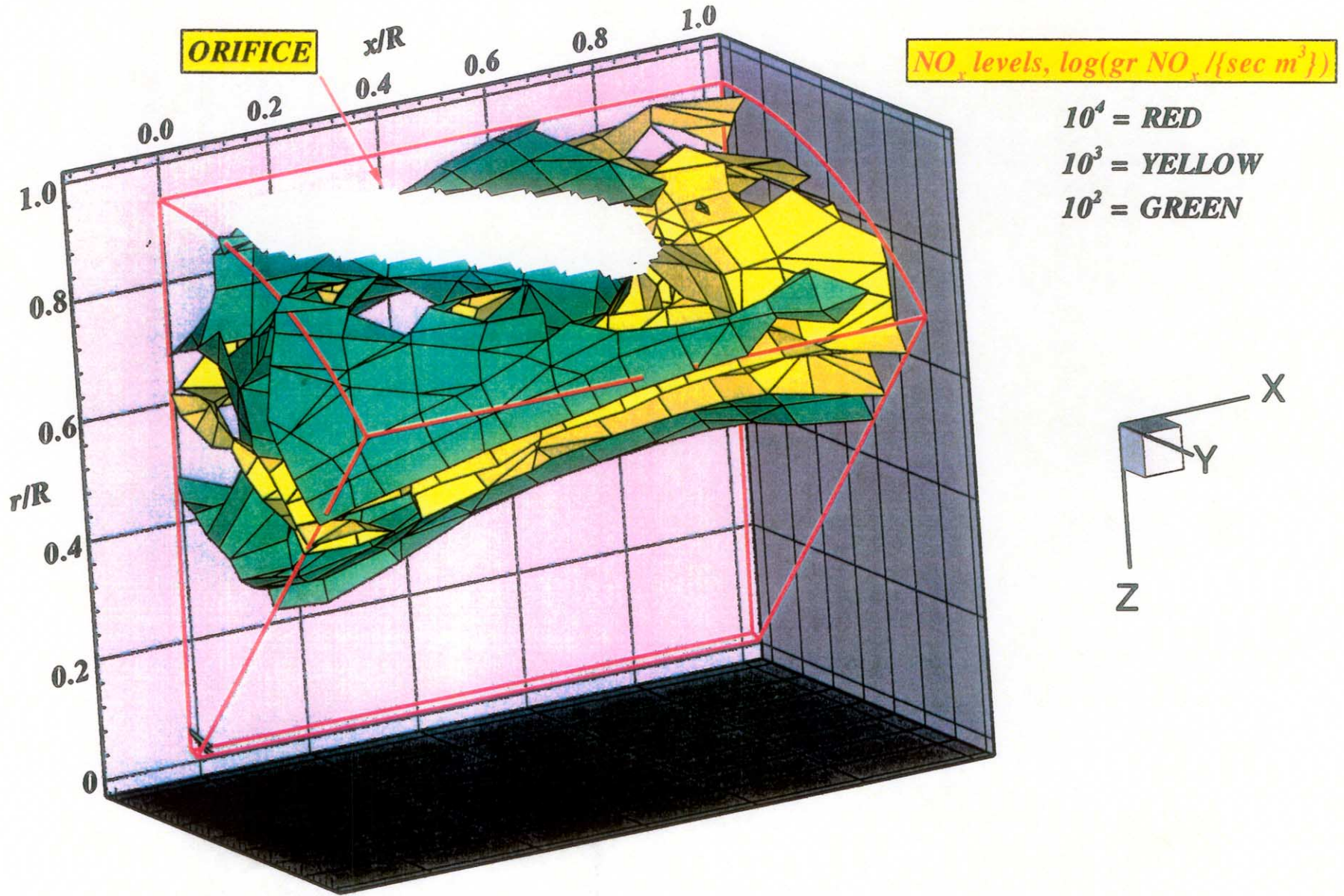
Figure-D20. Local NO_x production isopleths for configuration #28
J=53.2, MR=2.96, DR=2.28, phi rz=1.80, phi lz=0.416

45.0° slot, L/W=4, 8/row
ORIFICE

x/R

X
Y
Z

r/R

(NO$_x$) levels
gr NO$_x$ / {sec m^3}
10^4 = RED
10^3 = YELLOW
10^2 = GREEN
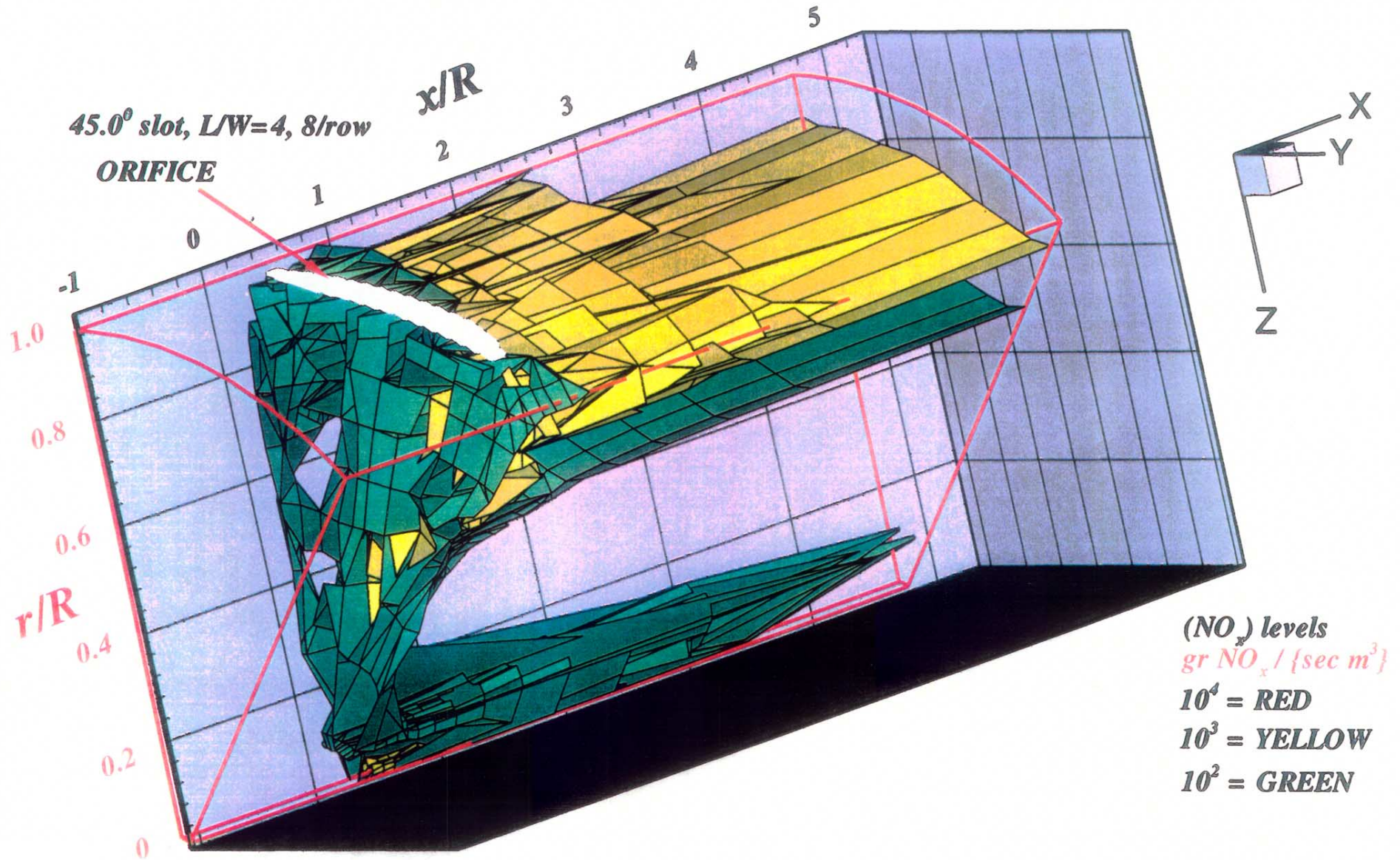
Figure-D21. Local NO$_x$ production isopleths for configuration # 29
J=57.6, MR=2.96, DR=2.28, Phi$_{RZ}$ = 1.80, Phi$_{LZ}$ = 0.416

ORIFICE

x/R

0.0   0.2   0.4   0.6   0.8   1.0

NO_x levels, $\log(gr\ NO_x\ /\{sec\ m^3\})$

10^4 = RED

10^3 = YELLOW

10^2 = GREEN

r/R

1.0   0.8   0.6   0.4   0.2   0

X

Y

Z
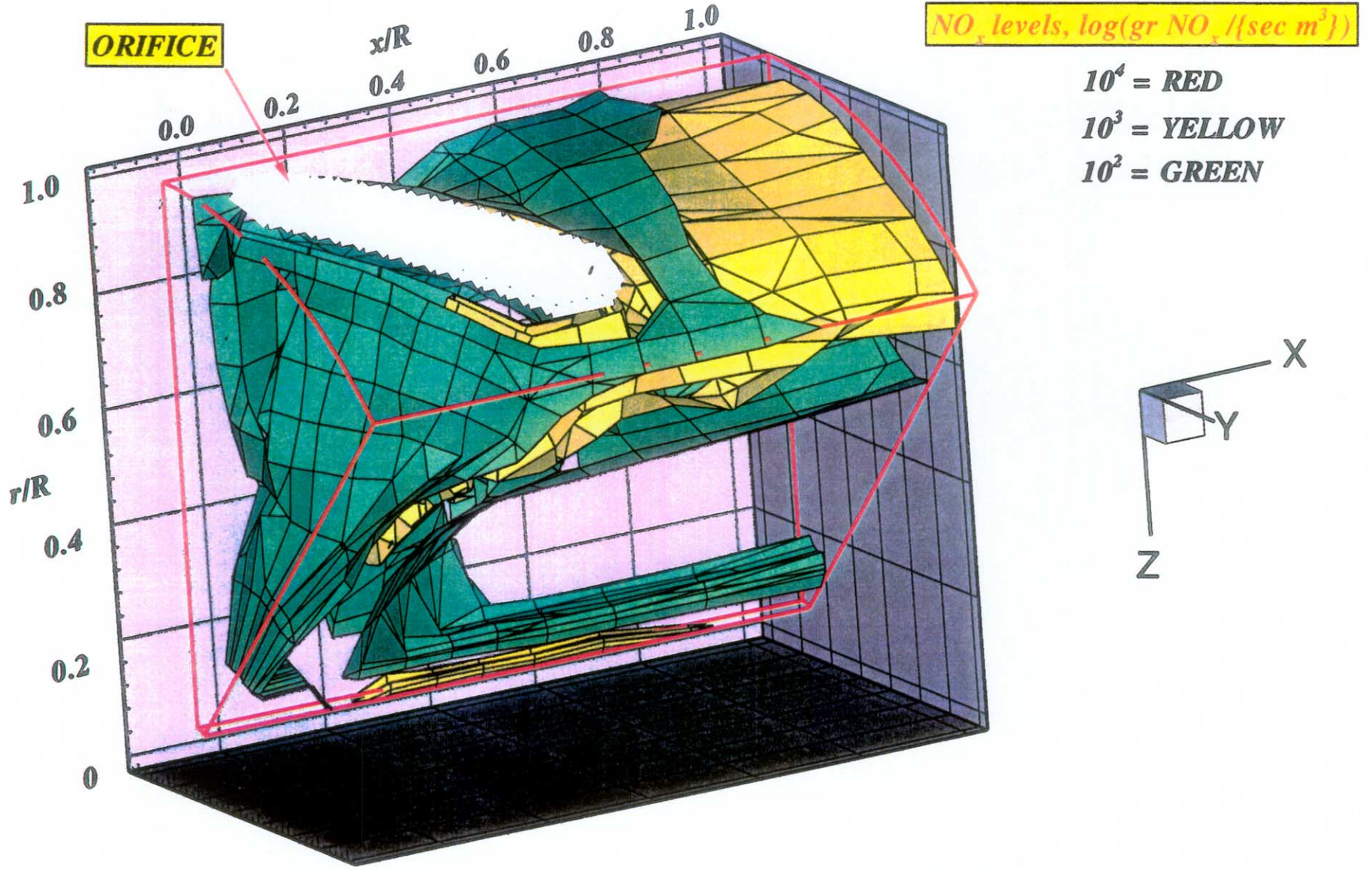
Figure-D22. Local NO_x production isopleths for configuration #29
J=57.6, MR=2.96, DR=2.28, phi rz=1.80, phi lz=0.416

45.0° slot, L/W=4, 8/row
ORIFICE

x/R

r/R

X

Y

Z

(NO_x) levels
$gr\ NO_x\ /\ \{sec\ m^3\}$

10^4 = RED
10^3 = YELLOW
10^2 = GREEN
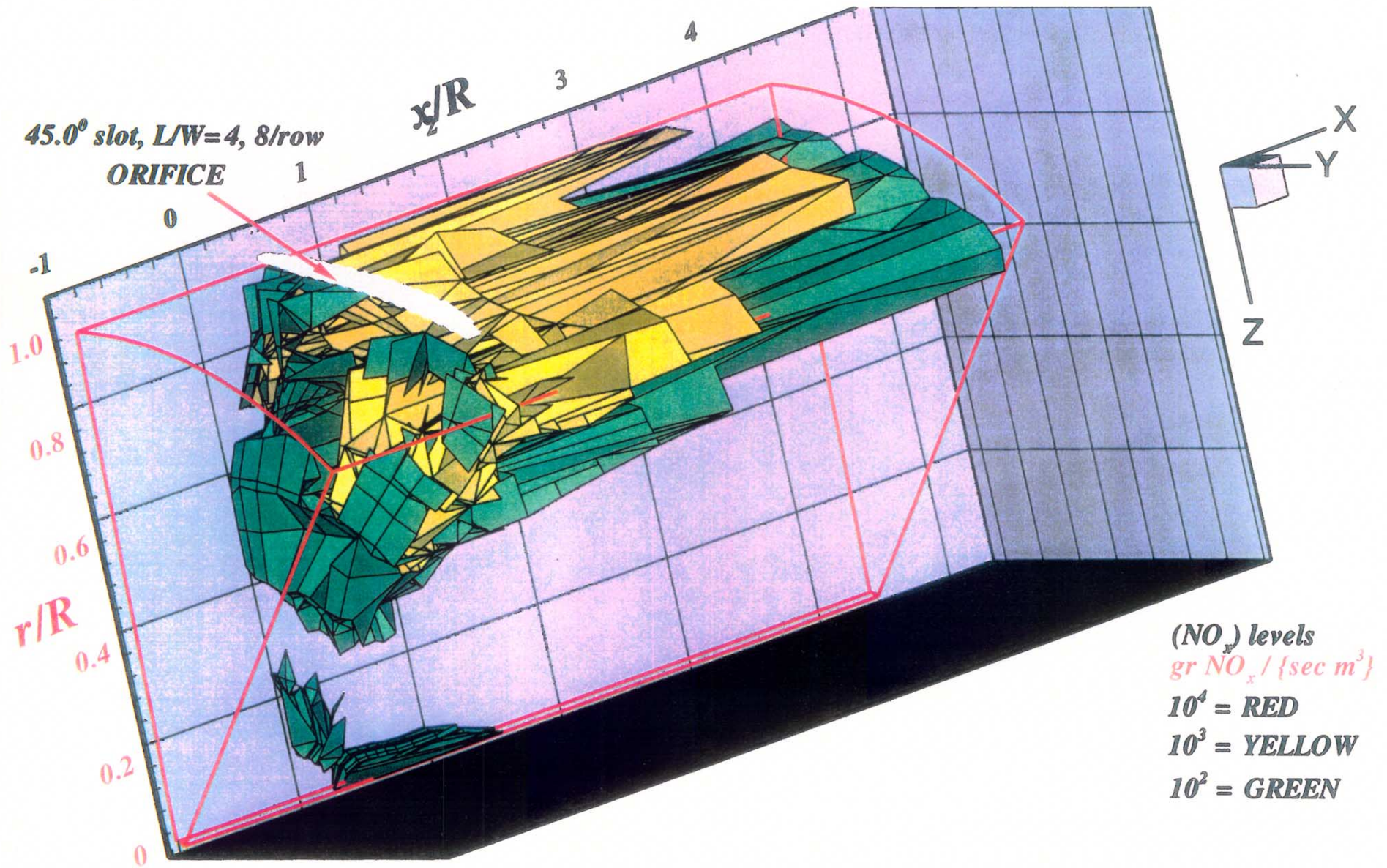
Figure-D23. Local NO_x production isopleths for configuration # 30
J=92.9, MR=2.96, DR=2.28, Phi_{RZ} = 1.80, Phi_{LZ} = 0.416

ORIFICE

x/R

0.0 0.2 0.4 0.6 0.8 1.0

r/R

1.0 0.8 0.6 0.4 0.2 0

NO_x levels, $\log(gr\ NO_x\ /\{sec\ m^3\})$

10^4 = RED

10^3 = YELLOW

10^2 = GREEN

X
Y
Z
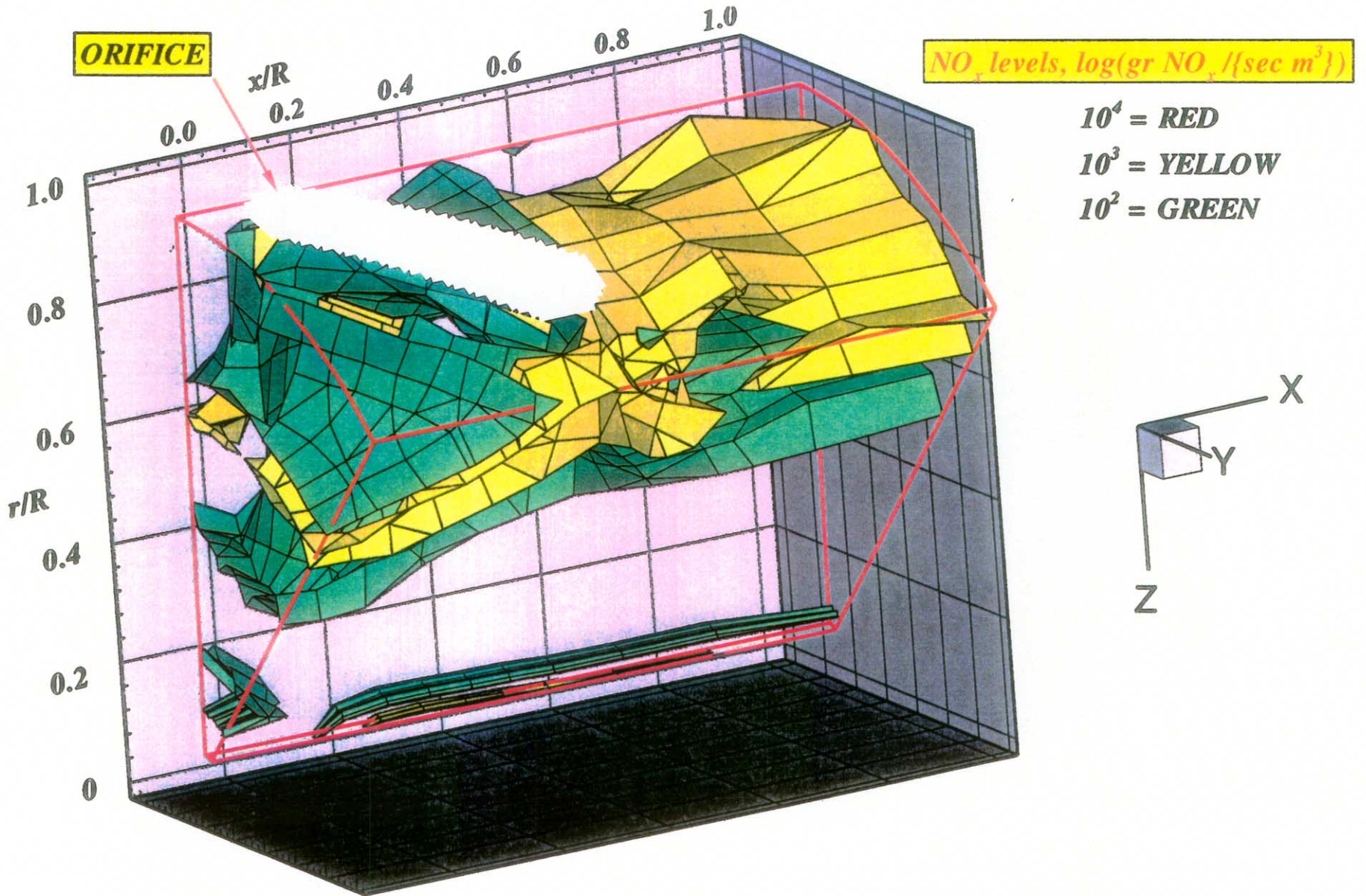
Figure-D24. Local NO_x production isopleths for configuration #30
J=92.9, MR=2.96, DR=2.28, phi rz=1.80, phi lz=0.416

67.5° slot, L/W=4, 8/row

ORIFICE

x/R

r/R

(NO$_x$) levels
gr NO$_x$ / {sec m^3}
10^4 = RED
10^3 = YELLOW
10^2 = GREEN
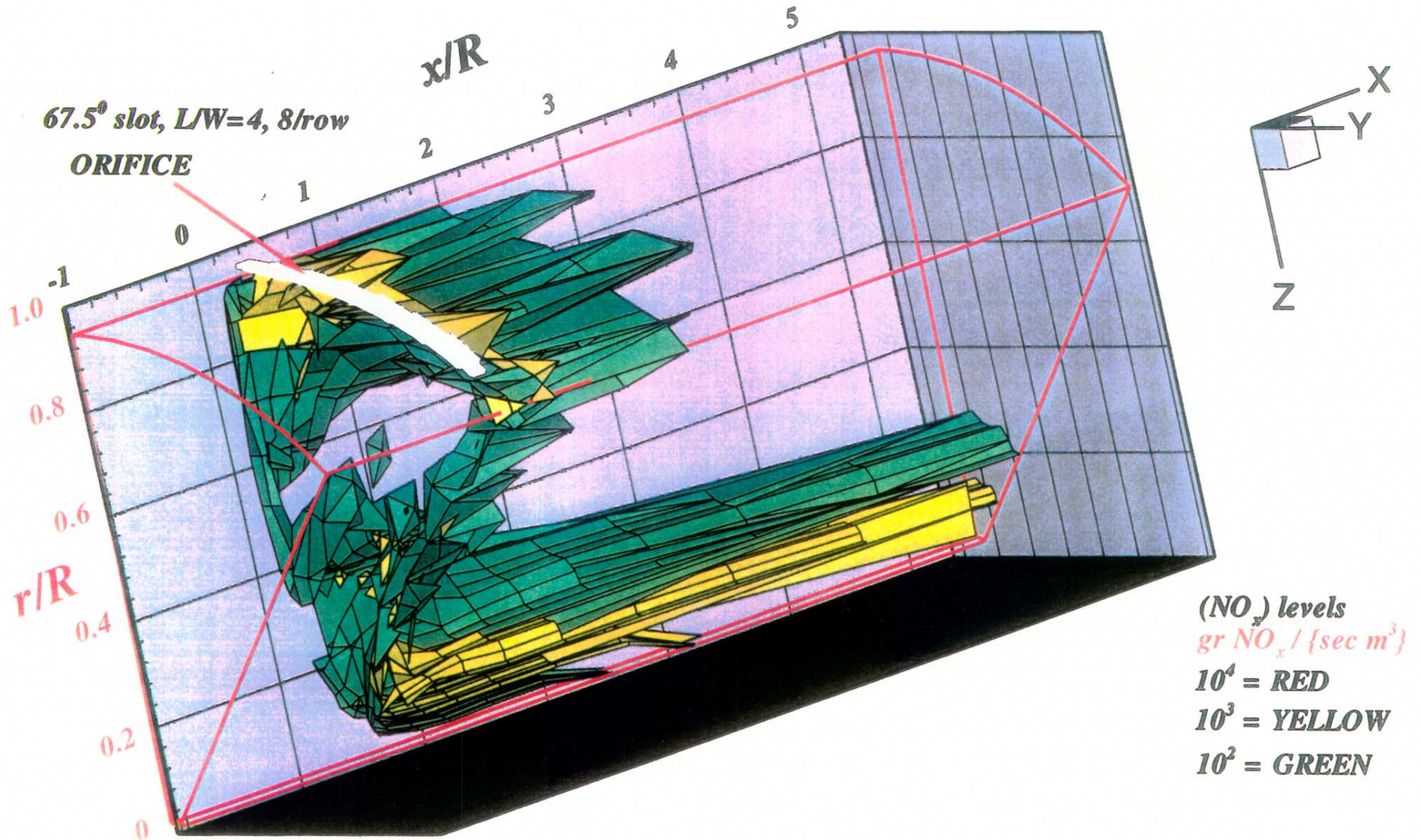
Figure-D25. Local NO$_x$ production isopleths for configuration # 31
**J=59.9, MR=2.96, DR=2.28, Phi$_{RZ}$ = 1.80, Phi$_{LZ}$ = 0.416**

ORIFICE

x/R

0.0 0.2 0.4 0.6 0.8 1.0

r/R

1.0 0.8 0.6 0.4 0.2 0

NO_x levels, $\log(gr\ NO_x\ /\{sec\ m^3\})$

$10^4 = RED$

$10^3 = YELLOW$

$10^2 = GREEN$

X

Y

Z
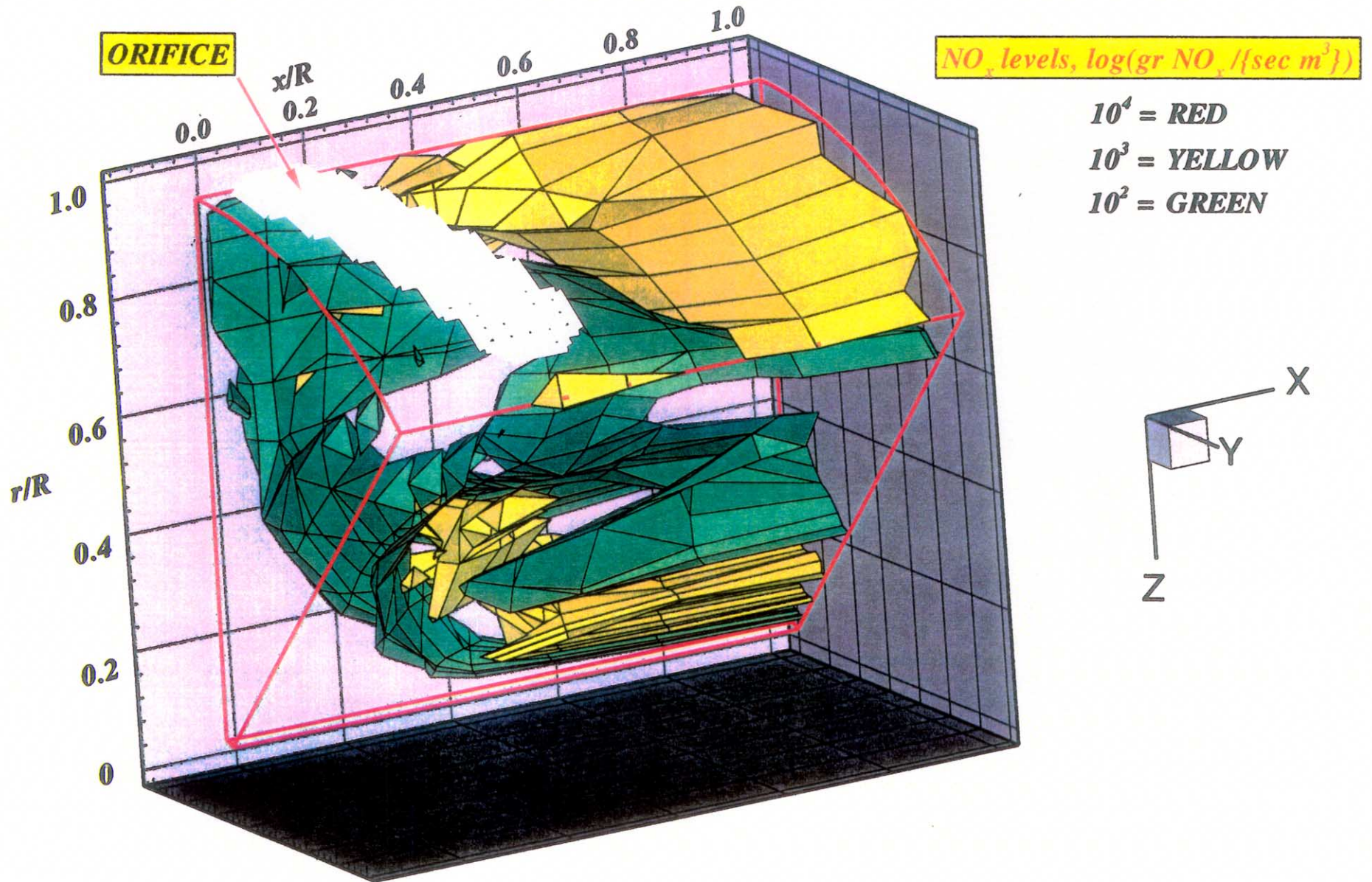
Figure-D26. Local NO_x production isopleths for configuration #31
J=59.9, MR=2.96, DR=2.28, phi rz=1.80, phi lz=0.416

Aligned slot, L/W=4, 8/row
ORIFICE

x/R

r/R

X
Y
Z

(NO$_x$) levels
gr NO$_x$ / {sec m^3}

10^4 = RED
10^3 = YELLOW
10^2 = GREEN
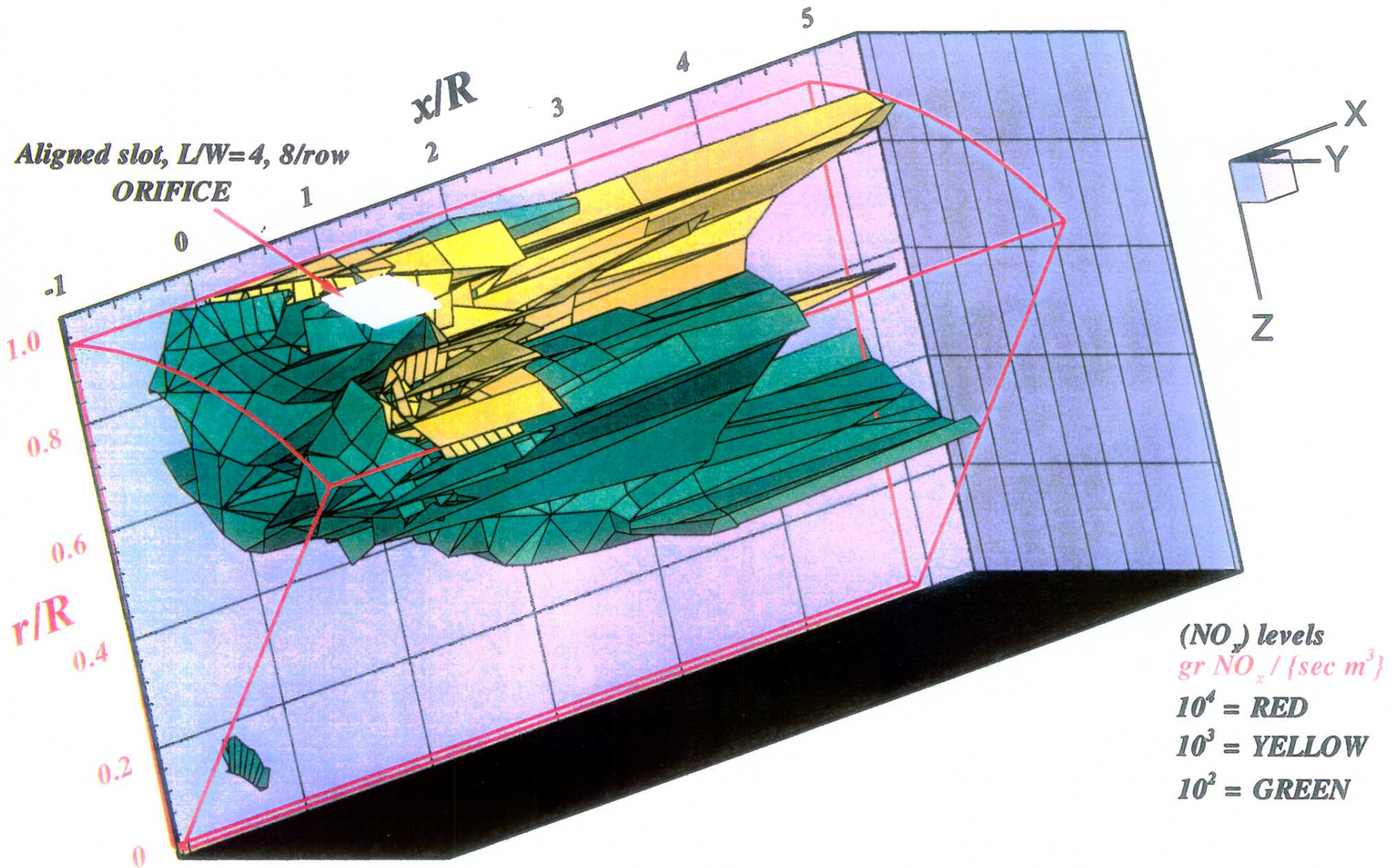
Figure-D27. Local NO$_x$ production isopleths for configuration # 32
J=93.0, MR=2.96, DR=2.28, Phi$_{RZ}$ = 1.80, Phi$_{LZ}$ = 0.416

ORIFICE

x/R

0.0 0.2 0.4 0.6 0.8 1.0

r/R

1.0 0.8 0.6 0.4 0.2 0

NO$_x$ levels, log(gr NO$_x$/{sec m^3})

10^4 = RED

10^3 = YELLOW

10^2 = GREEN

X

Y

Z
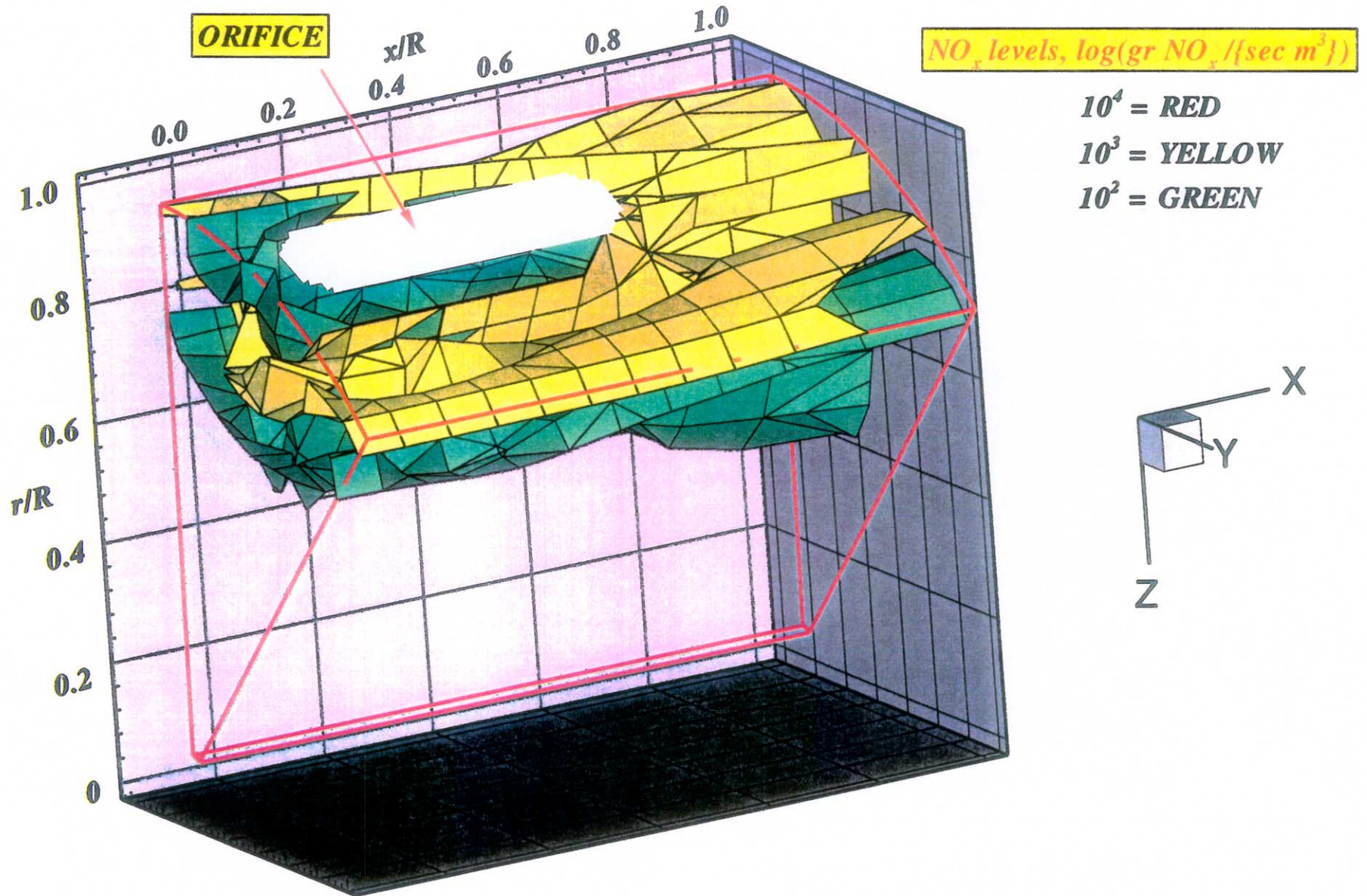
Figure-D28. Local NO$_x$ production isopleths for configuration #32
J=93.0, MR=2.96, DR=2.28, phi rz=1.80, phi lz=0.416

67.5$^\theta$ slot, L/W=4, 8/row
ORIFICE

x/R

r/R

5
4
3
2
1
0
-1

1.0
0.8
0.6
0.4
0.2
0

X
Y
Z

(NO$_x$) levels
gr NO$_x$ / {sec m^3}
10^4 = RED
10^3 = YELLOW
10^2 = GREEN
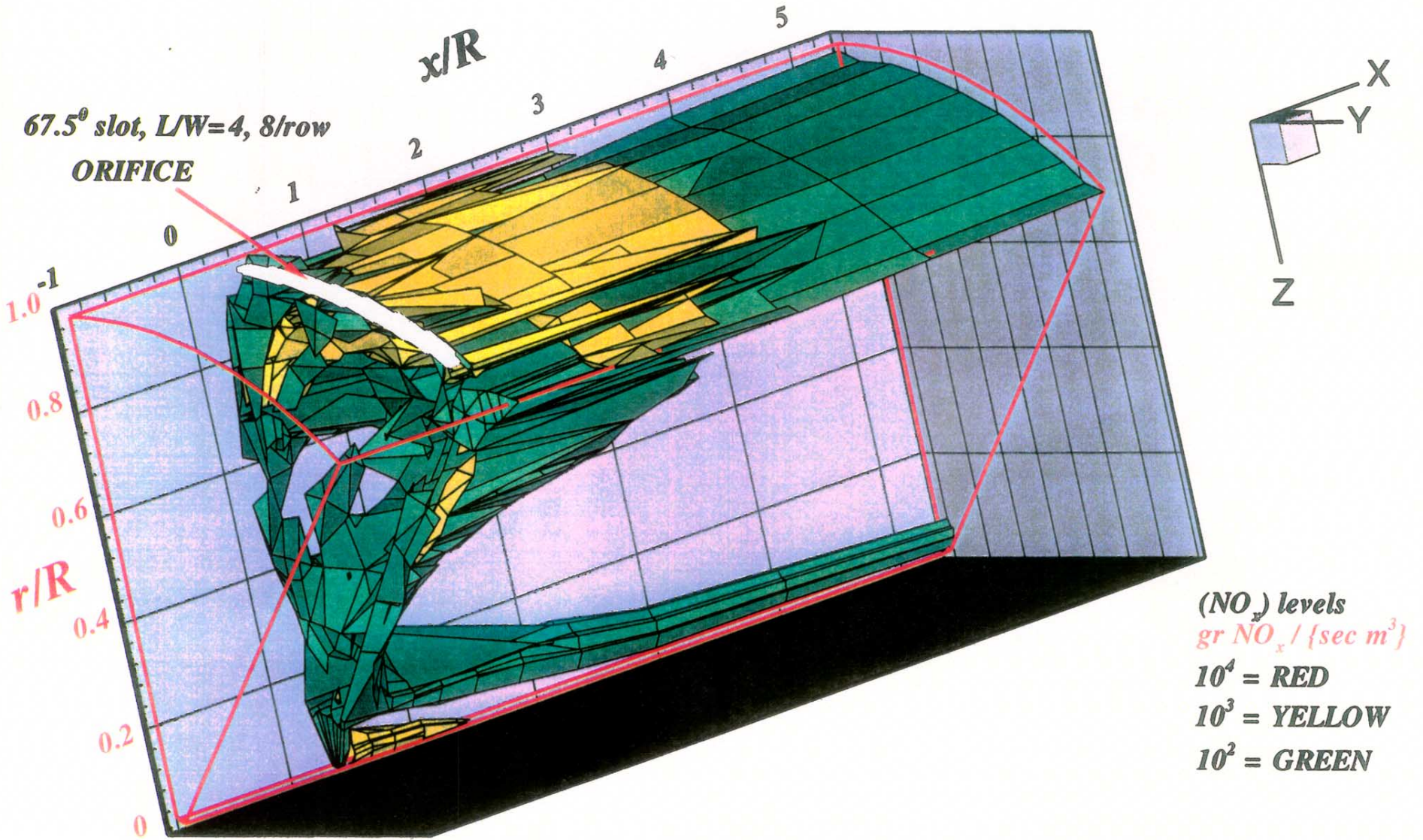
Figure-D29. Local NO$_x$ production isopleths for configuration # 33
J=99.3, MR=2.96, DR=2.28, Phi$_{RZ}$ = 1.80, Phi$_{LZ}$ = 0.416

ORIFICE

x/R

0.0   0.2   0.4   0.6   0.8   1.0

NO$_x$ levels, log(gr NO$_x$ /{sec m^3})

10^4 = RED

10^3 = YELLOW

10^2 = GREEN

r/R

1.0

0.8

0.6

0.4

0.2

0

X

Y

Z
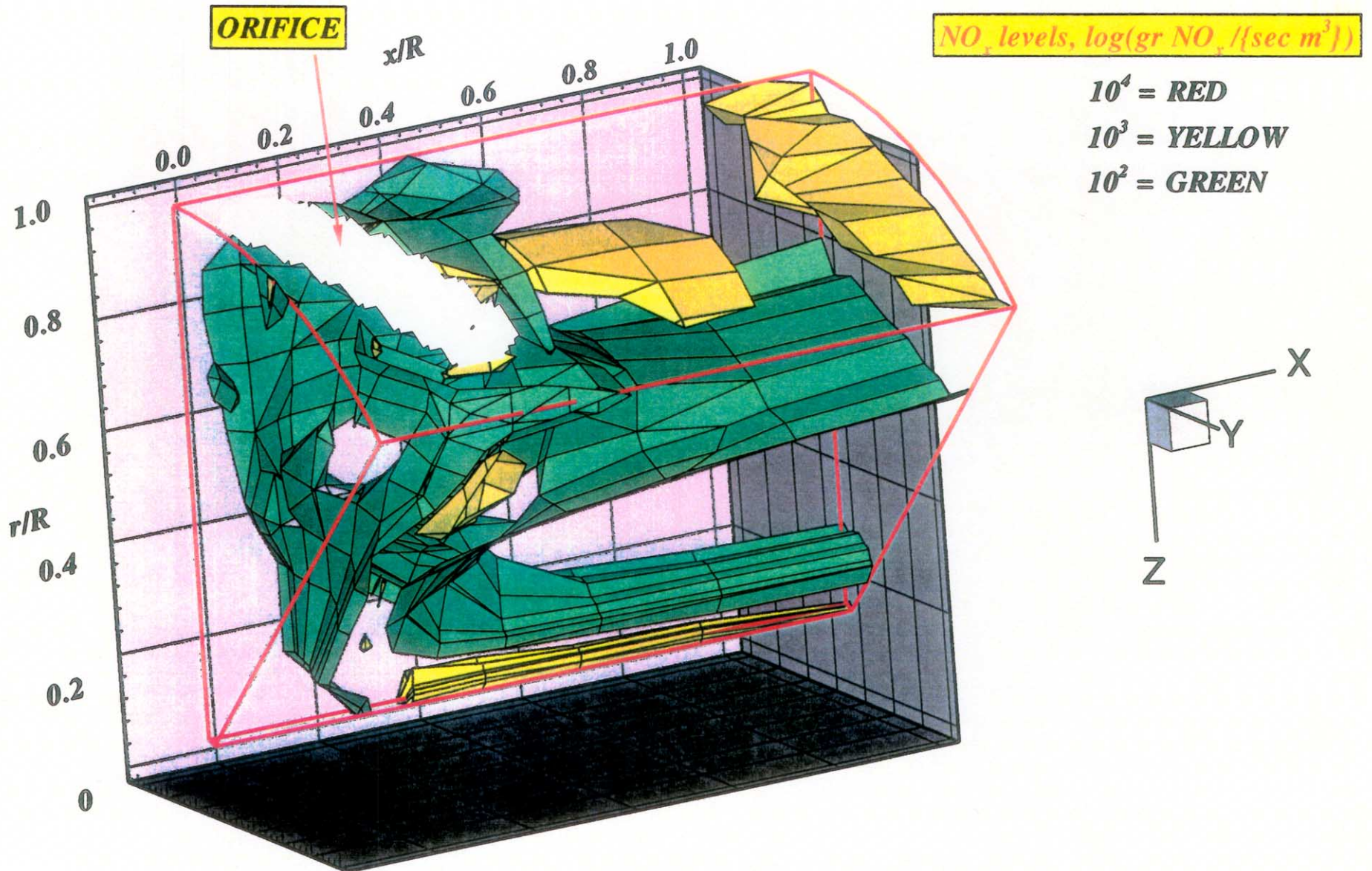
Figure-D30. Local NO$_x$ production isopleths for configuration #33
J=99.3, MR=2.96, DR=2.28, phi rz=1.80, phi lz=0.416

**Aligned slot, L/W=4, 8/row
ORIFICE**

x/R

r/R

(NO$_x$) levels
gr NO_x / {sec m^3}
10^4 = RED
10^3 = YELLOW
10^2 = GREEN

X
Y
Z
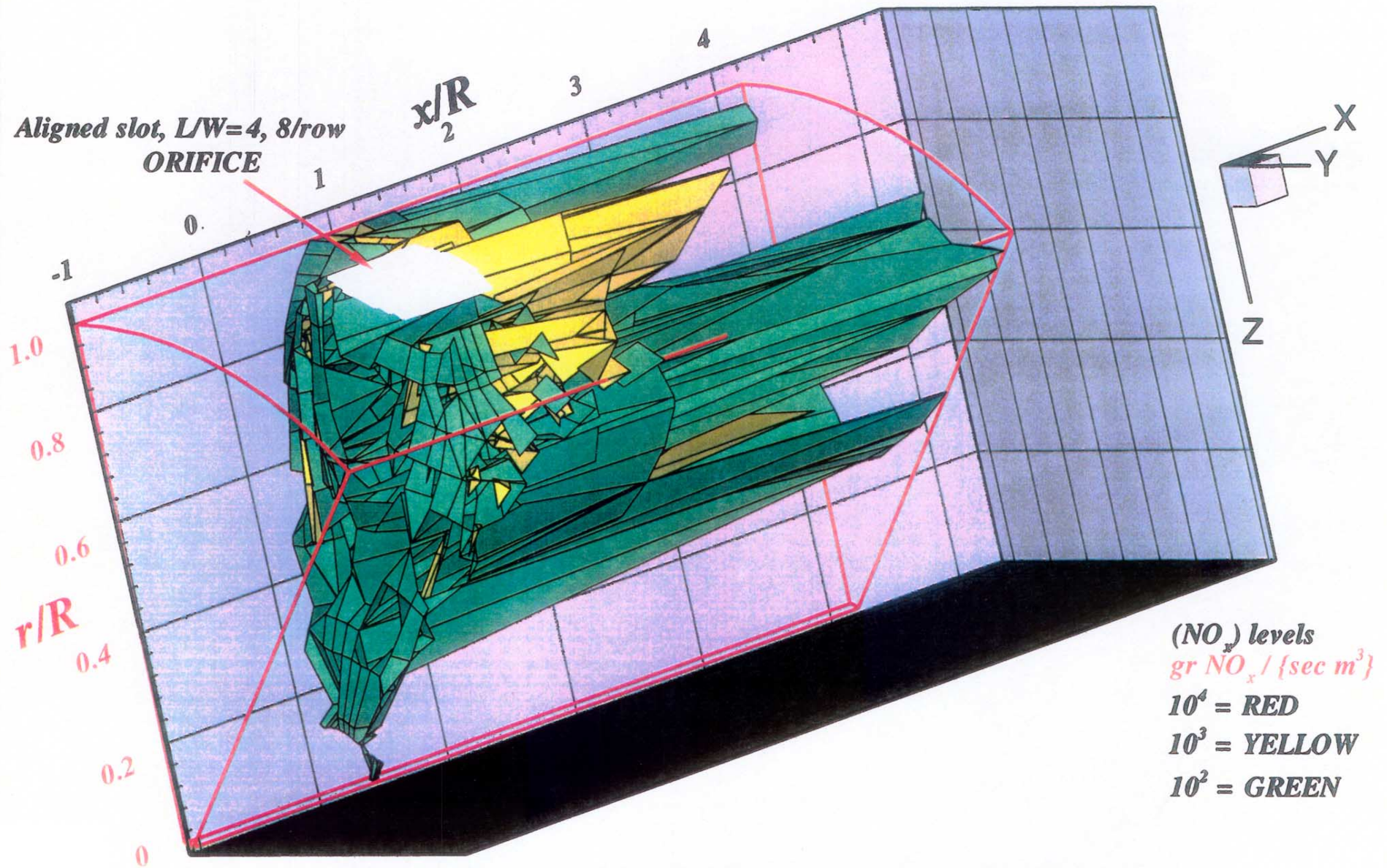
**Figure-D31. Local NO$_x$ production isopleths for configuration # 34
J=26.0, MR=2.96, DR=2.28, Phi$_{RZ}$ = 1.80, Phi$_{LZ}$ = 0.416**

ORIFICE

x/R

NO$_x$ levels, log(gr NO$_x$ /{sec m^3})

10^4 = RED

10^3 = YELLOW

10^2 = GREEN
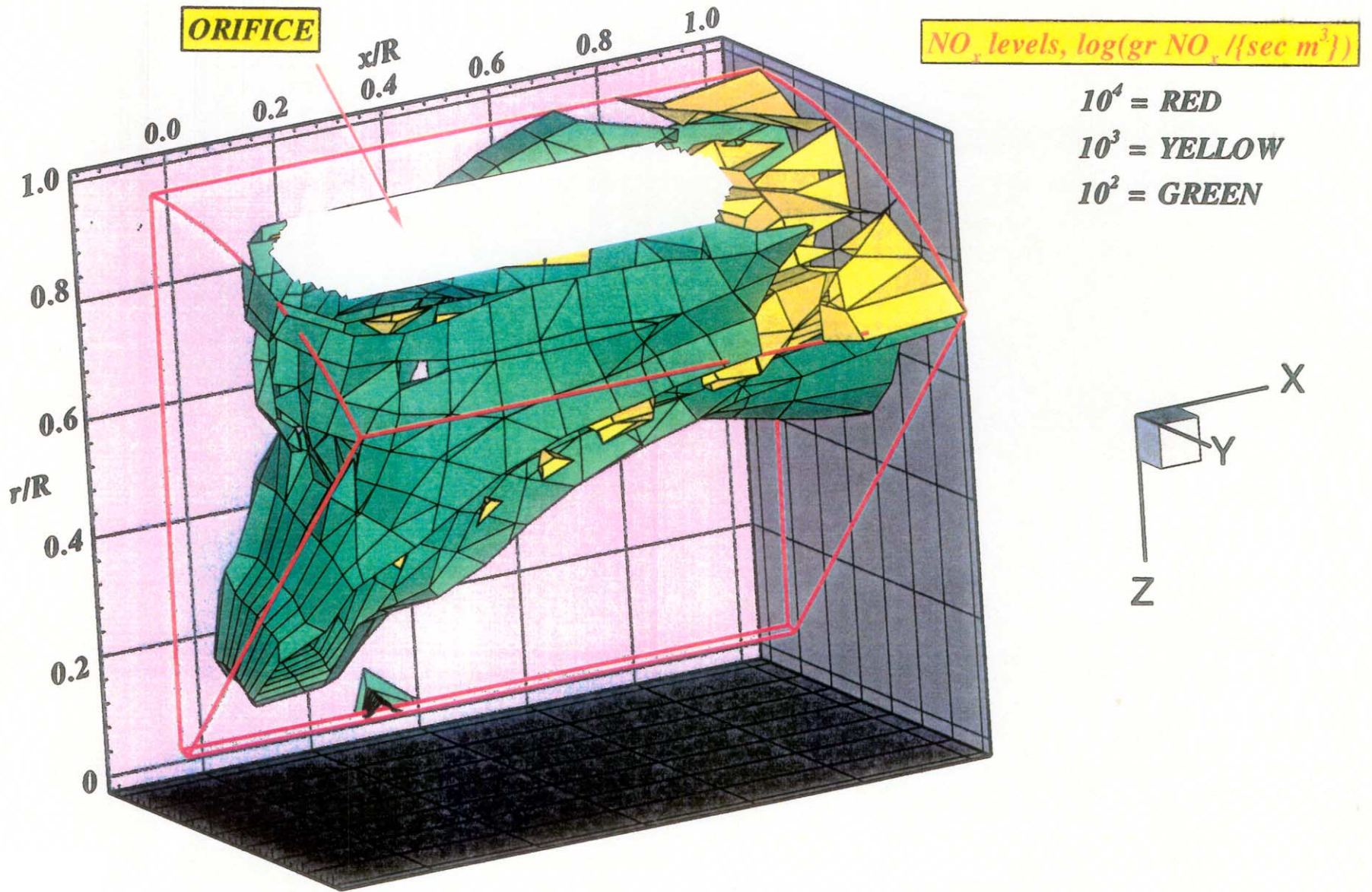
Figure-D32. Local NO$_x$ production isopleths for configuration #34
J=26.0, MR=2.96, DR=2.28, phi rz=1.80, phi lz=0.416

22.5⁰ slot, L/W=4, 8/row
ORIFICE

x/R

r/R

(NO$_x$) levels
gr NO$_x$ / {sec m^3}
10^4 = RED
10^3 = YELLOW
10^2 = GREEN
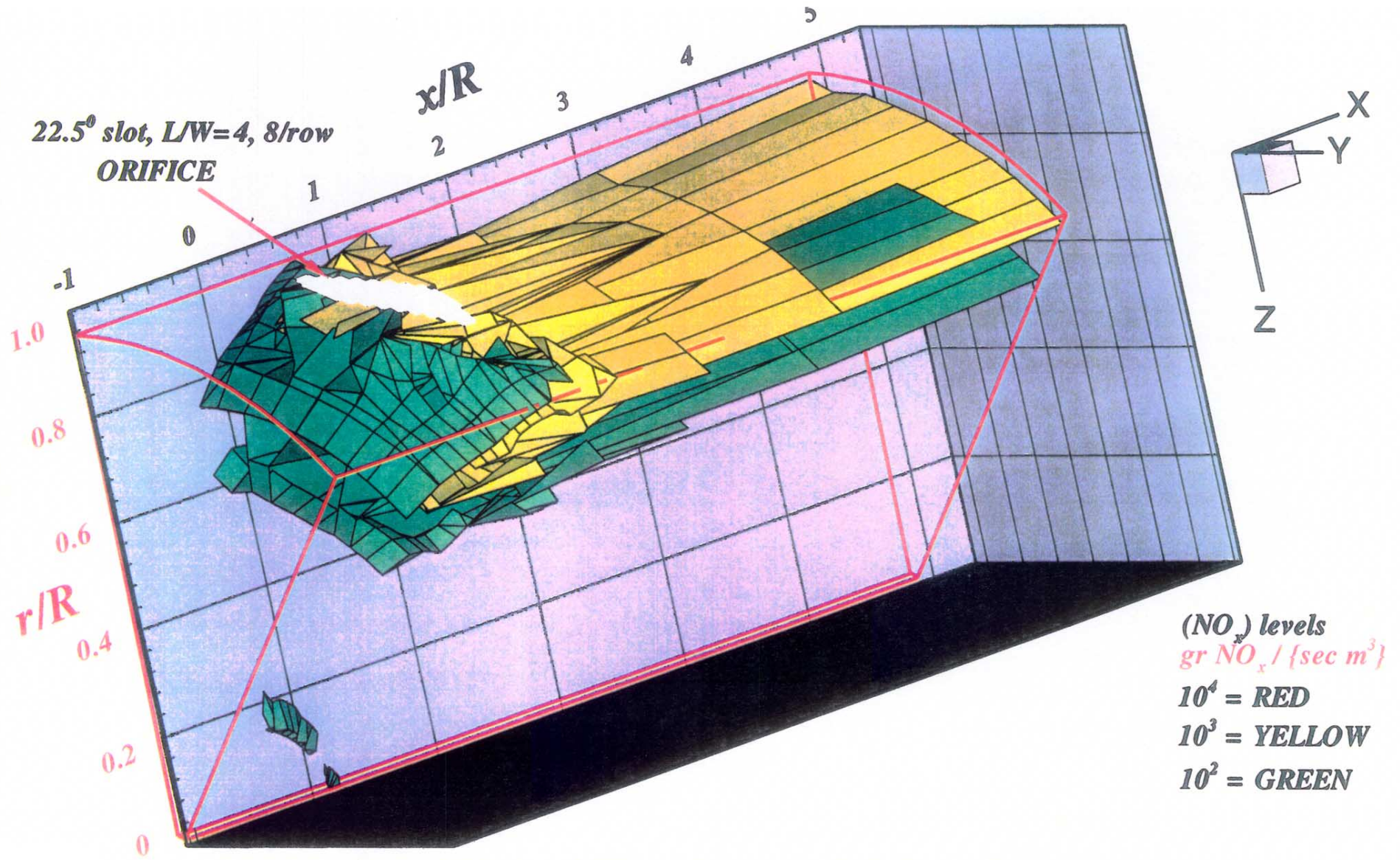
Figure-D33. Local NO$_x$ production isopleths for configuration # 35
J=88.1, MR=2.96, DR=2.28, Phi$_{RZ}$ = 1.80, Phi$_{LZ}$ = 0.416
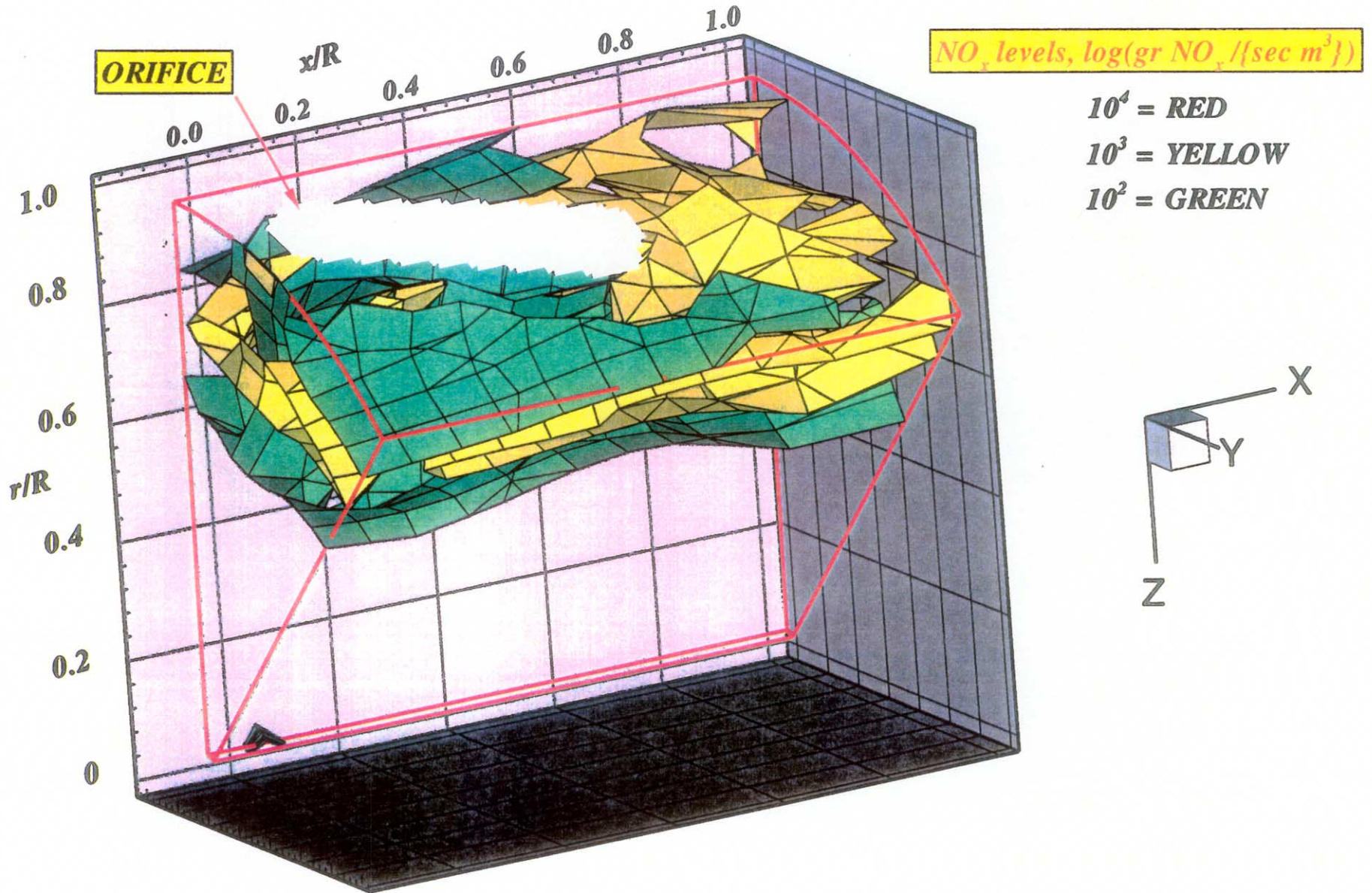
Figure-D34. Local NOₓ production isopleths for configuration #35
J=88.1, MR=2.96, DR=2.28, phi rz=1.80, phi lz=0.416

ORIFICE

NO_x levels, $log(gr\ NO_x\ /\{sec\ m^3\})$

10^4 = RED
10^3 = YELLOW
10^2 = GREEN

x/R

1.0
0.8
0.6
0.4
0.2
0.0

r/R

1.0
0.8
0.6
0.4
0.2
0

X
Y
Z

Transverse slot, L/W=4, 8/row
ORIFICE

x/R

r/R

(NO$_x$) levels
gr NO$_x$ / {sec m^3}
10^4 = RED
10^3 = YELLOW
10^2 = GREEN
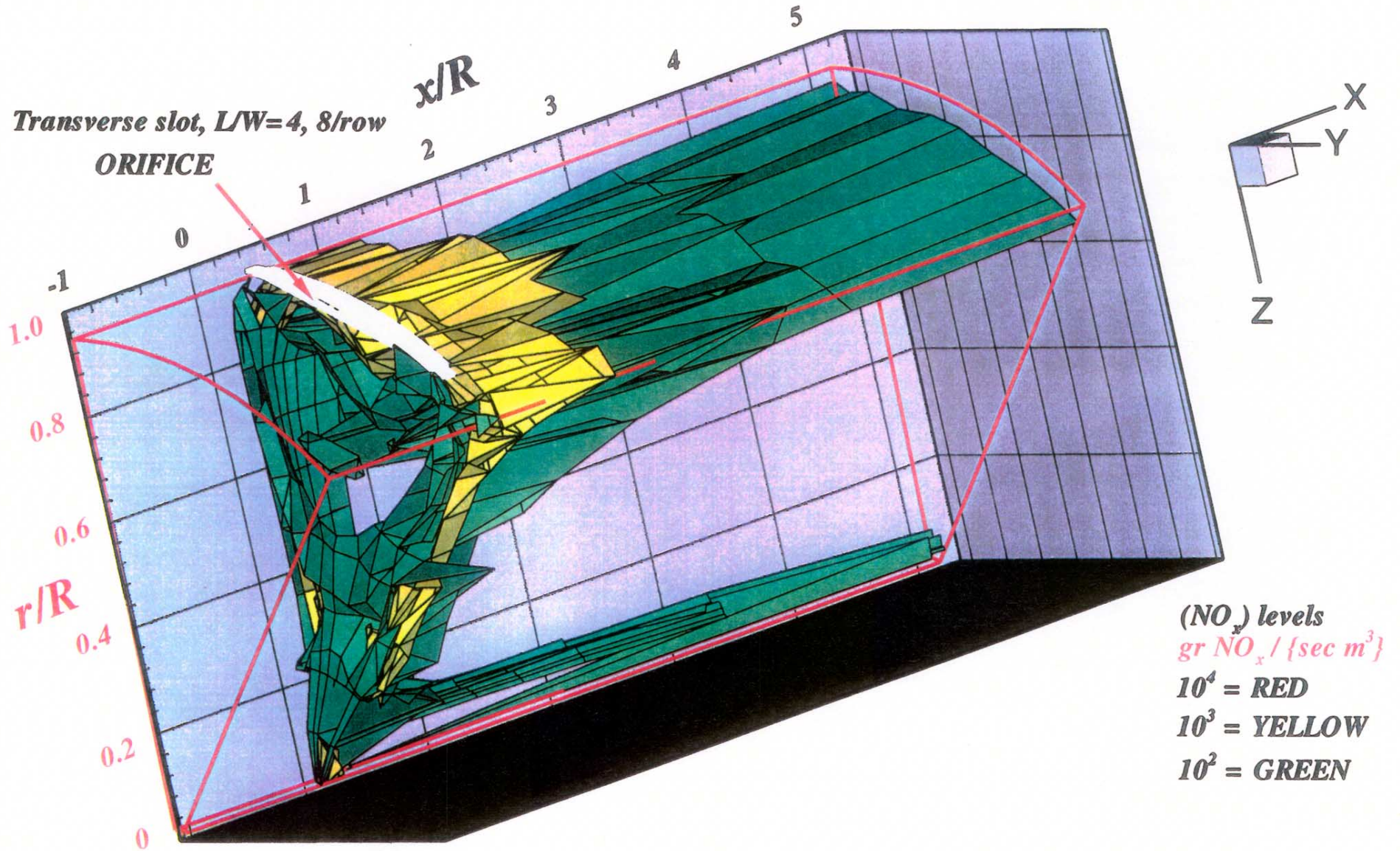
Figure-D35. Local NO$_x$ production isopleths for configuration # 36
J=106.2, MR=2.96, DR=2.28, Phi$_{RZ}$ = 1.80, Phi$_{LZ}$ = 0.416

ORIFICE

x/R

0.0 0.2 0.4 0.6 0.8 1.0

NO_x levels, log(gr NO_x /{sec m^3})

10^4 = **RED**

10^3 = **YELLOW**

10^2 = **GREEN**

r/R

1.0 0.8 0.6 0.4 0.2 0

X

Y

Z
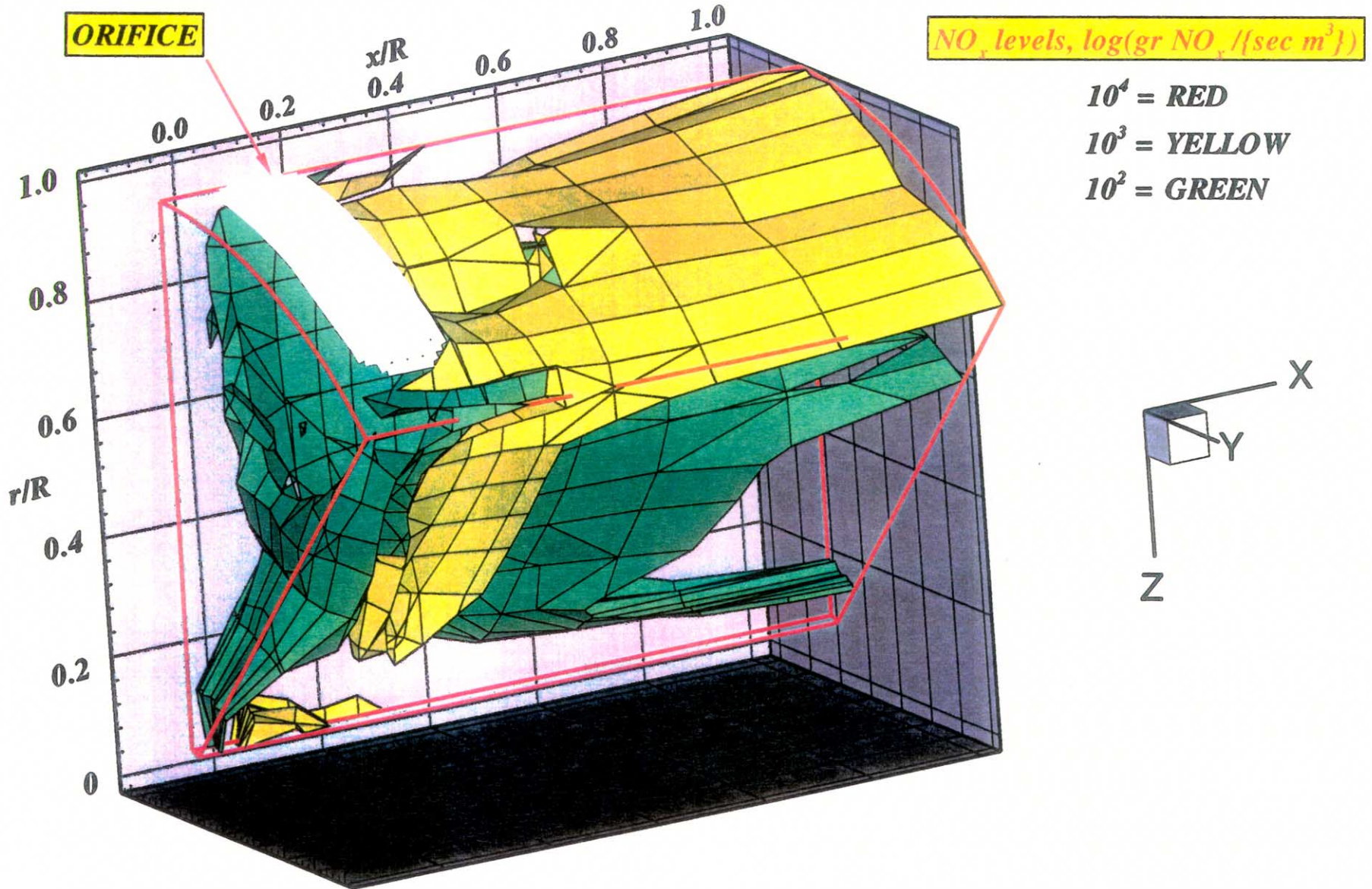
Figure-D36. Local NO$_x$ production isopleths for configuration #36
J=106.2, MR=2.96, DR=2.28, phi rz=1.80, phi lz=0.416
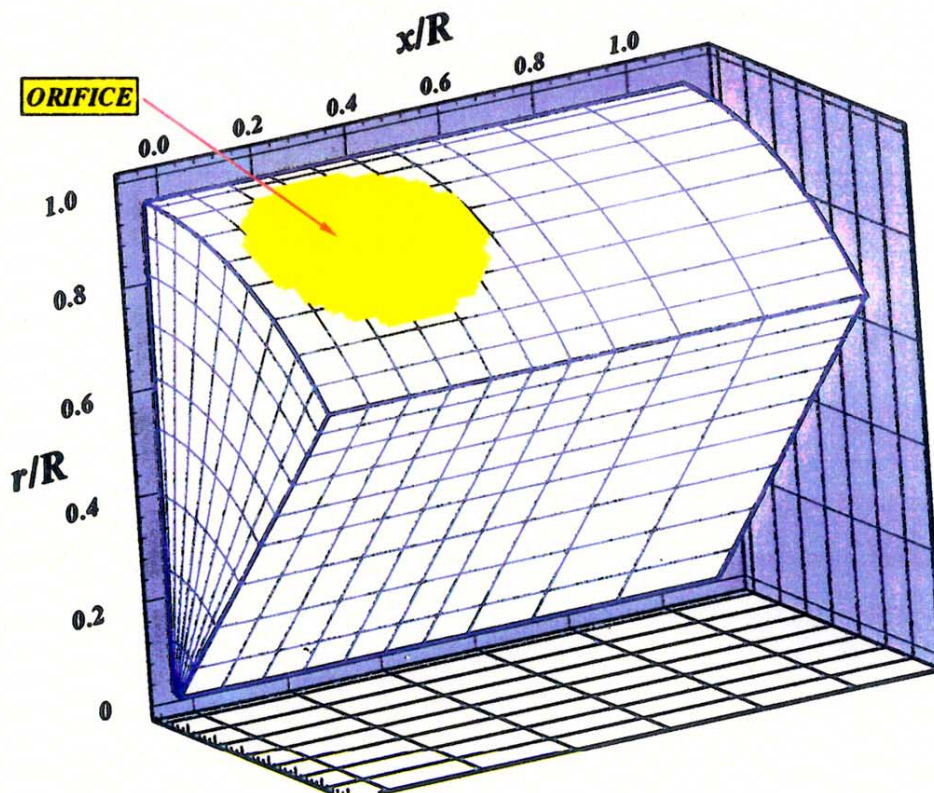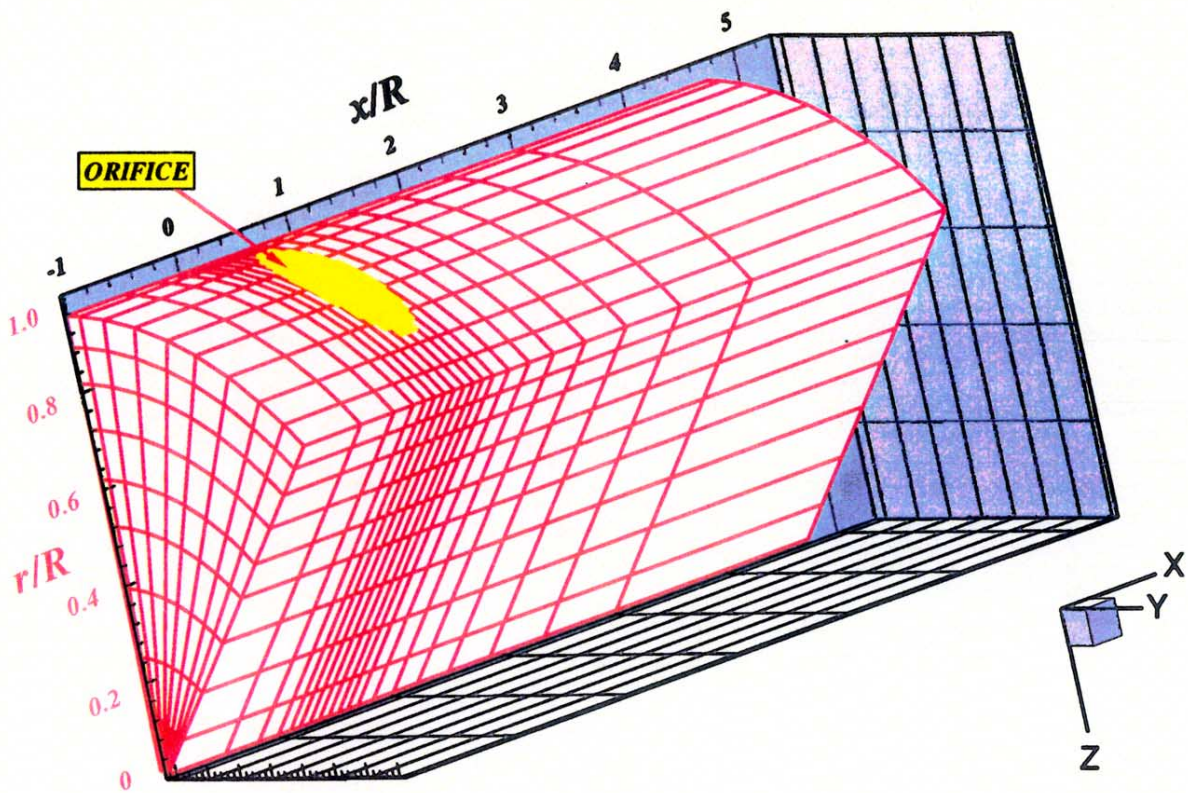
Figure-D37. *Computational grid for the NO$_x$ calculations*
top: entire analyzed sector
bottom: mixing sector (0 < x/R < 1)

APPENDIX-E

Stacked radial-tangential planes at x/R 0.08, 0.25, 0.5, 0.75, and 1.0 of temperature, local NOx production in gr NOx / {sec m³}, and normalized equivalence ratio for configurations # 19 through 36.

Configuration #	Fig-#
19	E1
20	E2
21	E3
22	E4
23	E5
24	E6
25	E7
26	E8
27	E9
28	E10
29	E11
30	E12
31	E13
32	E14
33	E15
34	E16
35	E17
36	E18

367

TEMP, K

2500
2300
2100
1900
1700
1500
1300
1100
900

LOCAL NO$_x$ PRODUCTION RATE

$log\{gr\ NO_x\ /\ (sec\ *\ m^3)\}$

4
3
2
1
0
-1
-2
-3
-4

NORMALIZED EQUIVALENCE RATIO

$\phi_{MAIN} = 1$
0.9
0.8
0.7
0.6
0.5
0.4
0.3
0.2
0.1
$\phi_{JET} = 0$
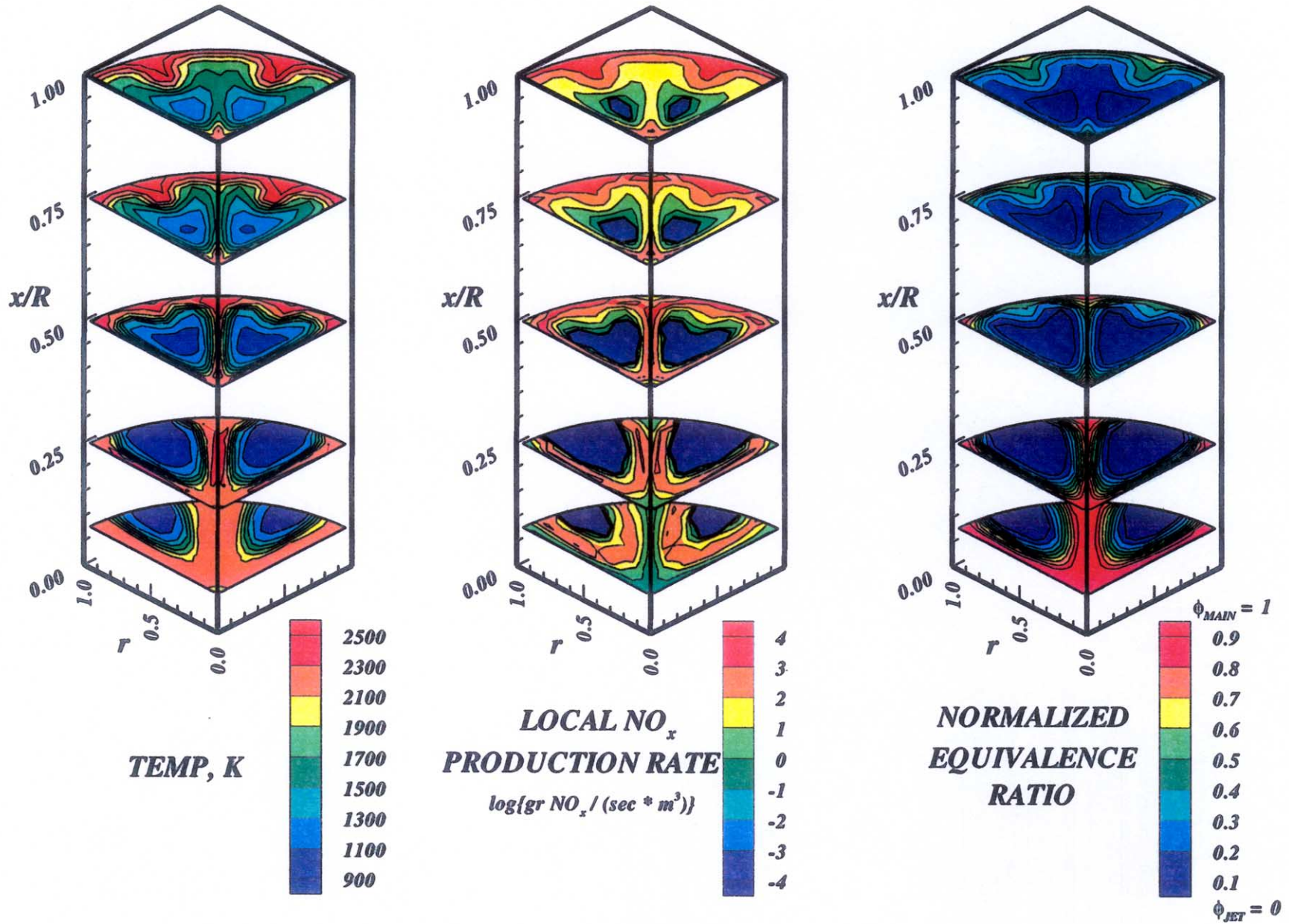
Figure-E1. Configuration #19, 8 round orifices / row
$J = 26.7$, $MR = 2.96$, $DR = 2.28$, $\phi_{RZ} = 1.80$, $\phi_{LZ} = 0.416$
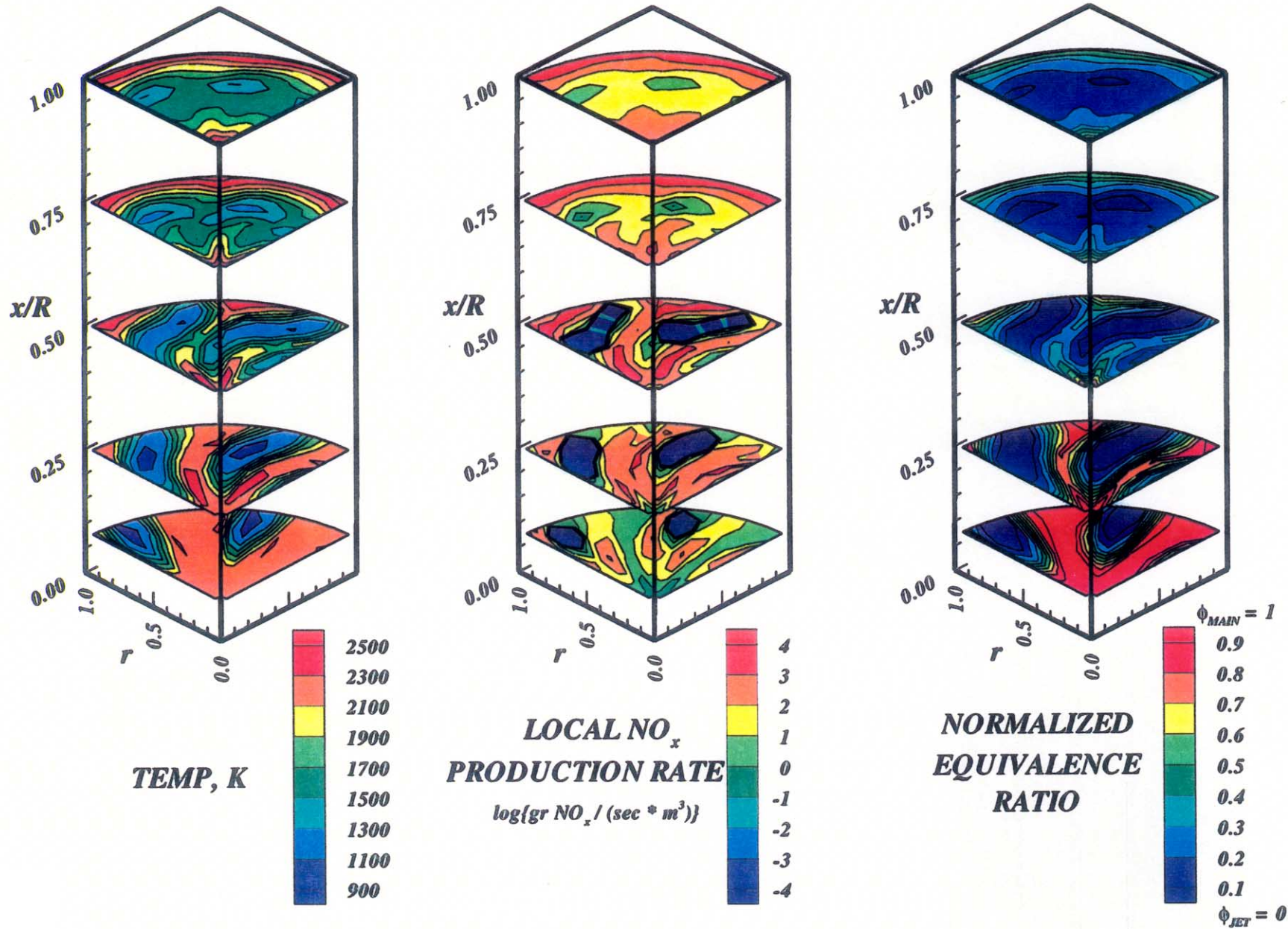
Figure-E2. Configuration #20, 8 round orifices / row
$J=30.5$, $MR=2.96$, $DR=2.28$, $\phi_{RZ}=1.80$, $\phi_{LZ}=0.416$
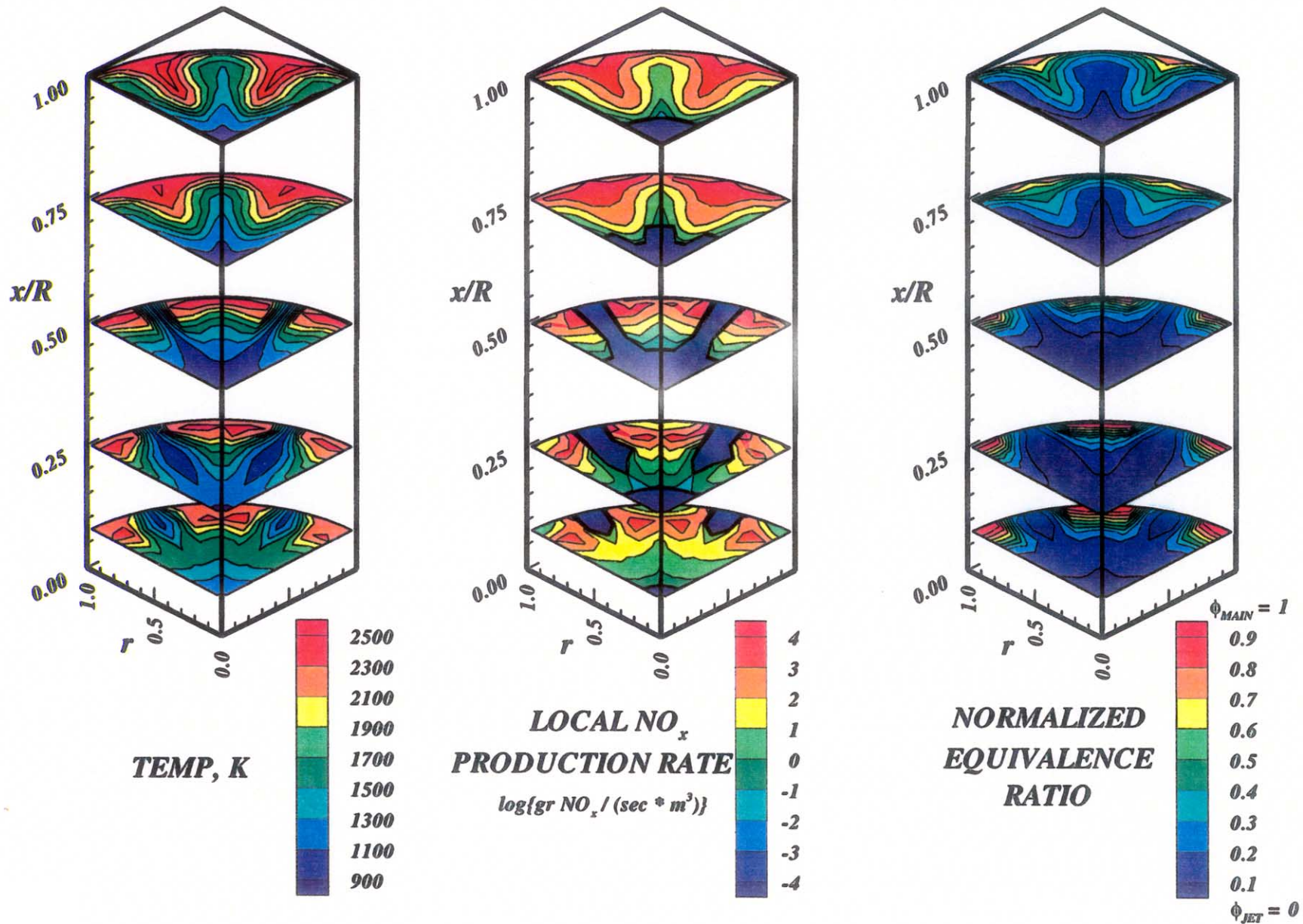
Figure-E3. Configuration #21, 8 round orifices / row
$J=51.1$, $MR=2.96$, $DR=2.28$, $\phi_{RZ}=1.80$, $\phi_{LZ}=0.416$
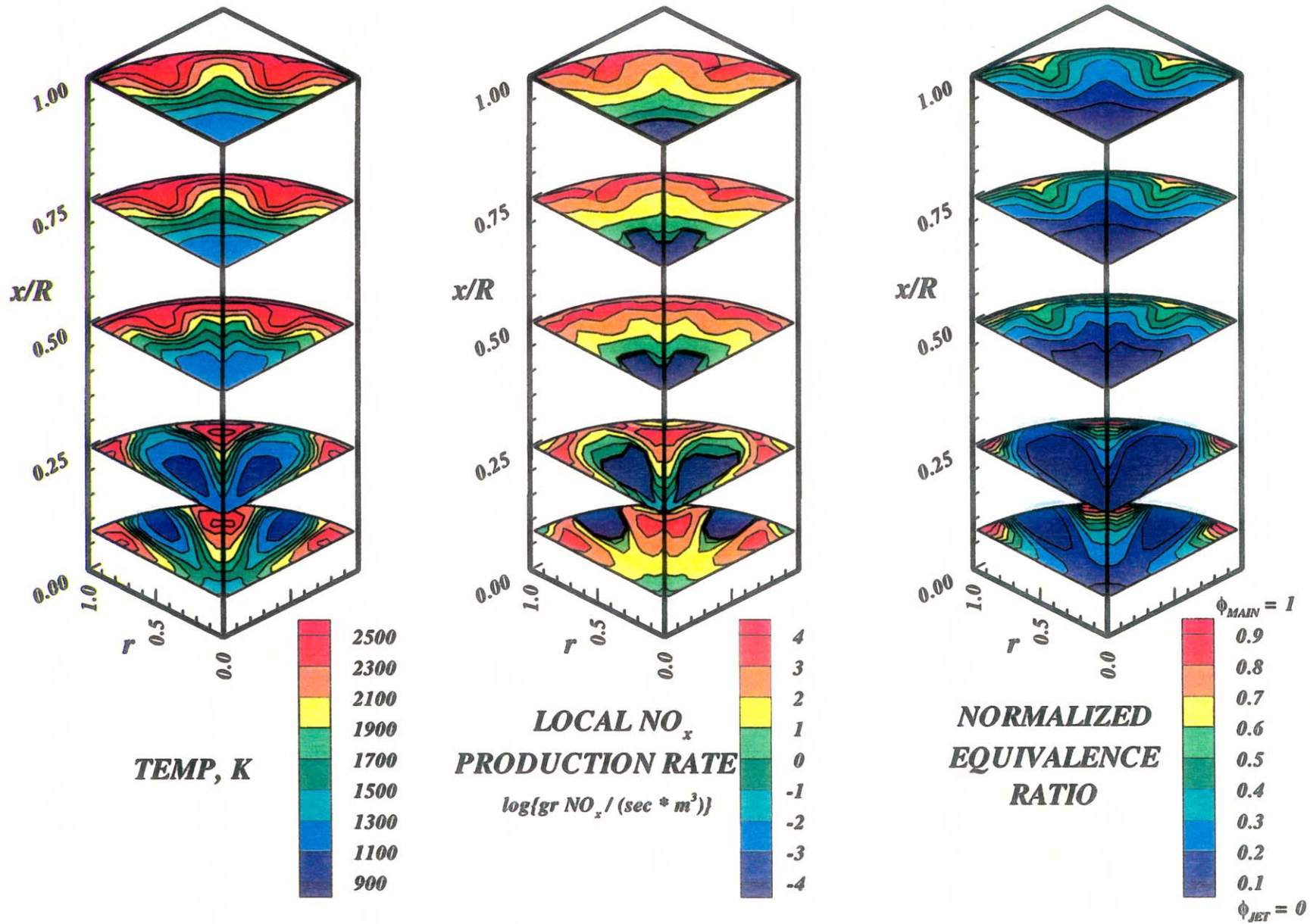
Figure-E4. Configuration #22, 8 round orifices / row
$J=84.1$, $MR=2.96$, $DR=2.28$, $\phi_{RZ}=1.80$, $\phi_{LZ}=0.416$
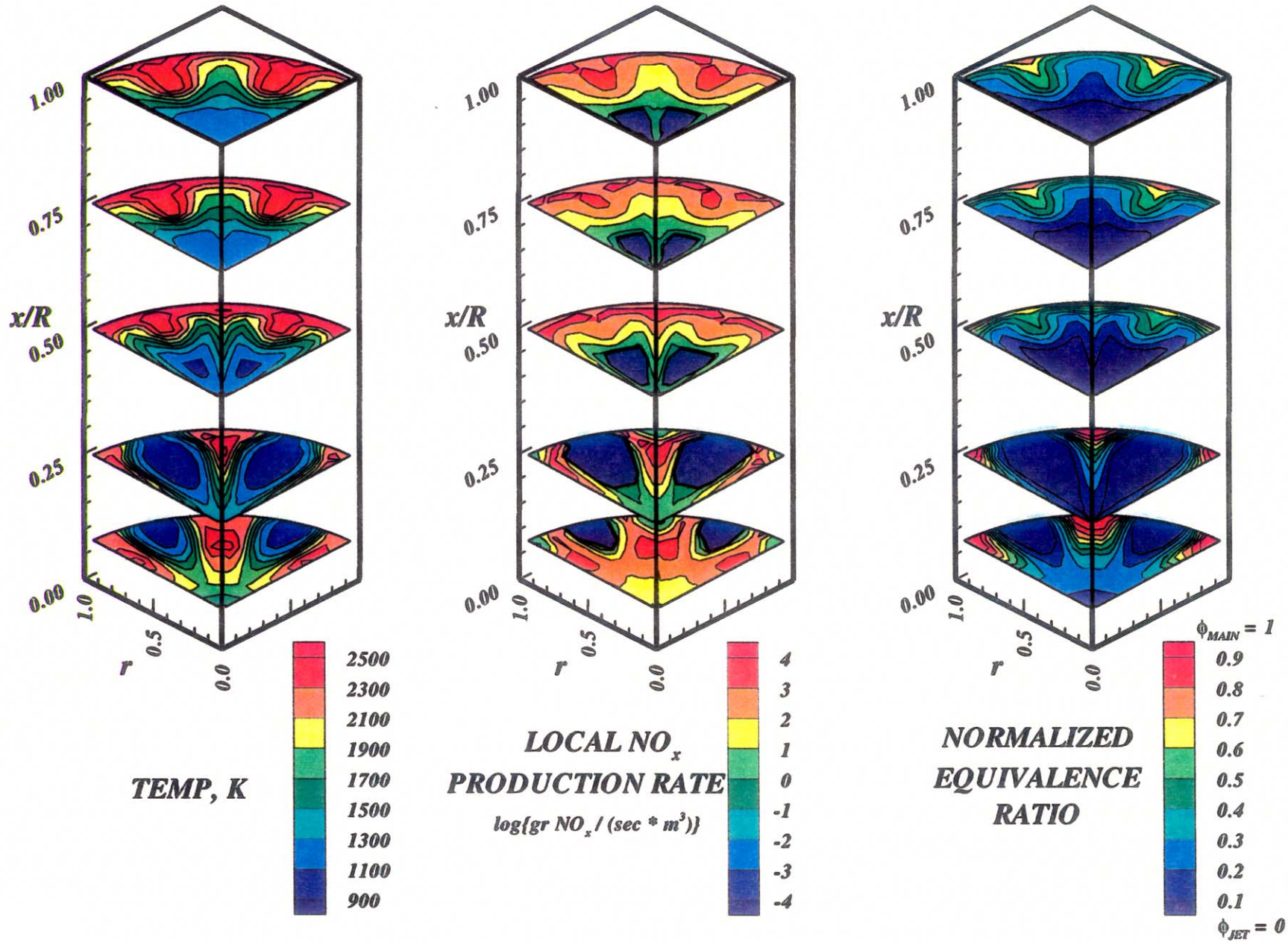
Figure-E5. Configuration #23, 8 round orifices / row
$J=55.3$, $MR=2.96$, $DR=2.28$, $\phi_{RZ}=1.80$, $\phi_{LZ}=0.416$
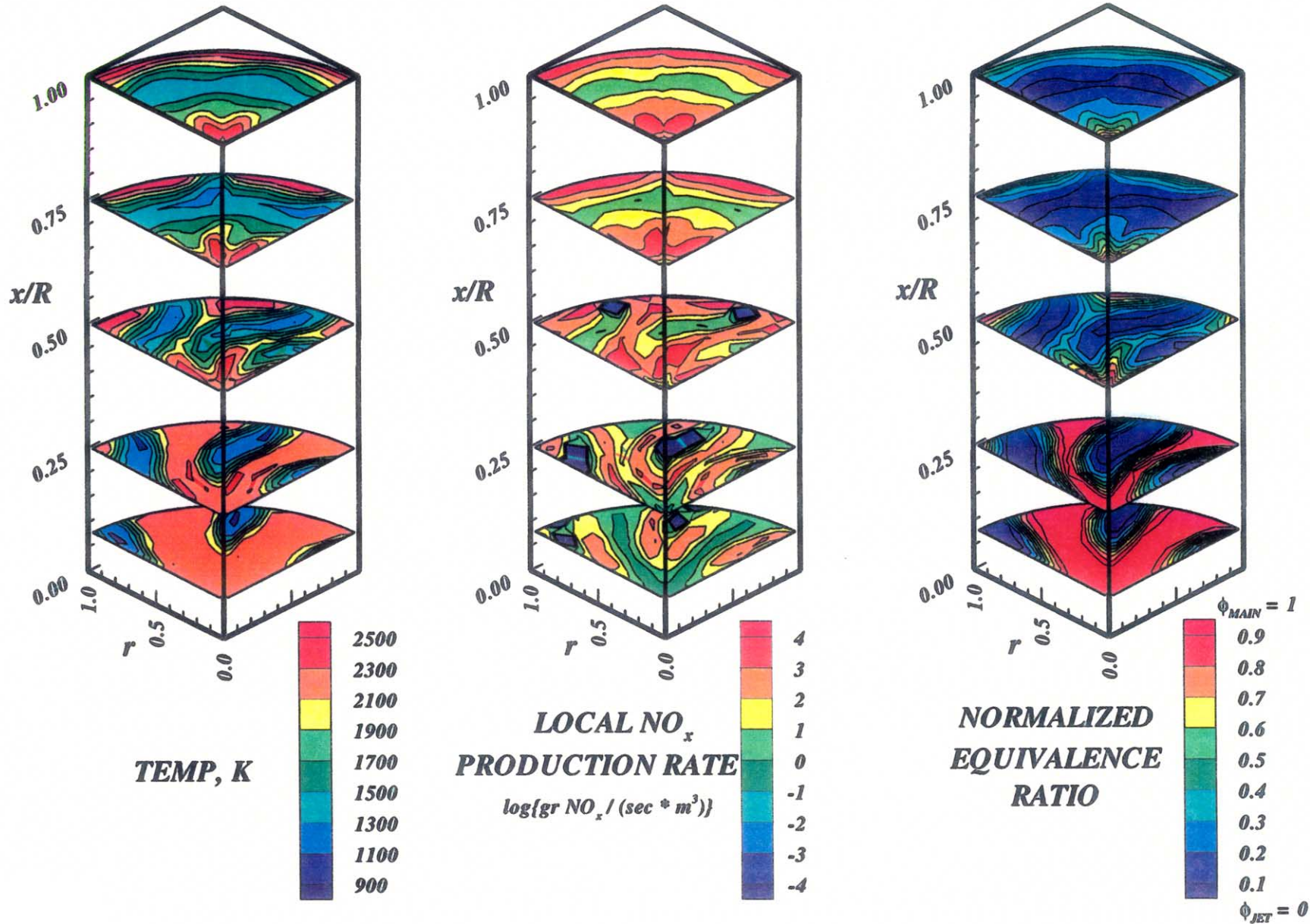
Figure-E6. Configuration #24, 8 round orifices / row
J=28.1, MR=2.96, DR=2.28, ϕ_{RZ}=1.80, ϕ_{LZ}=0.416
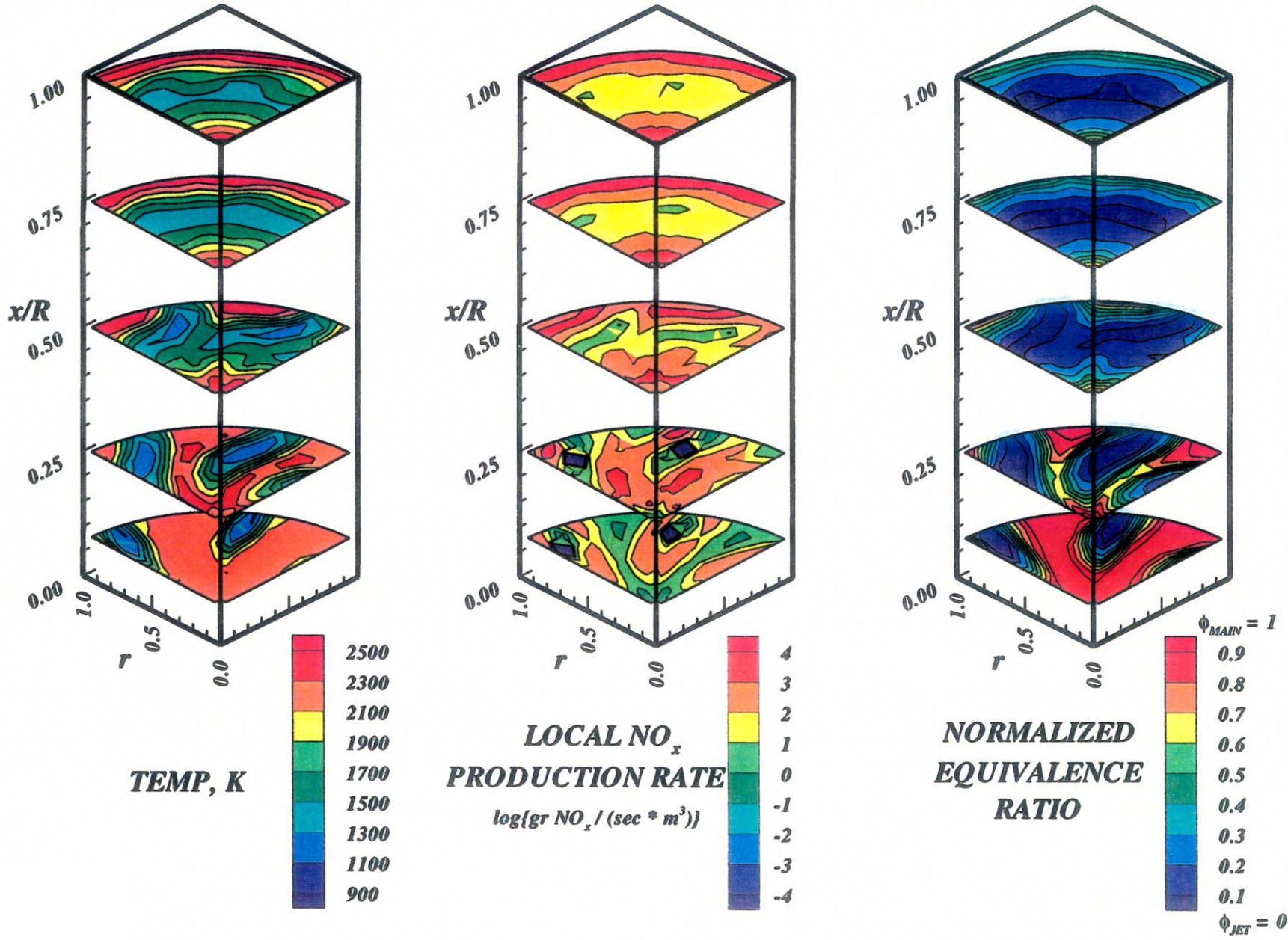
Figure-E7. Configuration #25, 8 round orifices / row
$J=50.9$, $MR=2.96$, $DR=2.28$, $\phi_{RZ}=1.80$, $\phi_{LZ}=0.416$
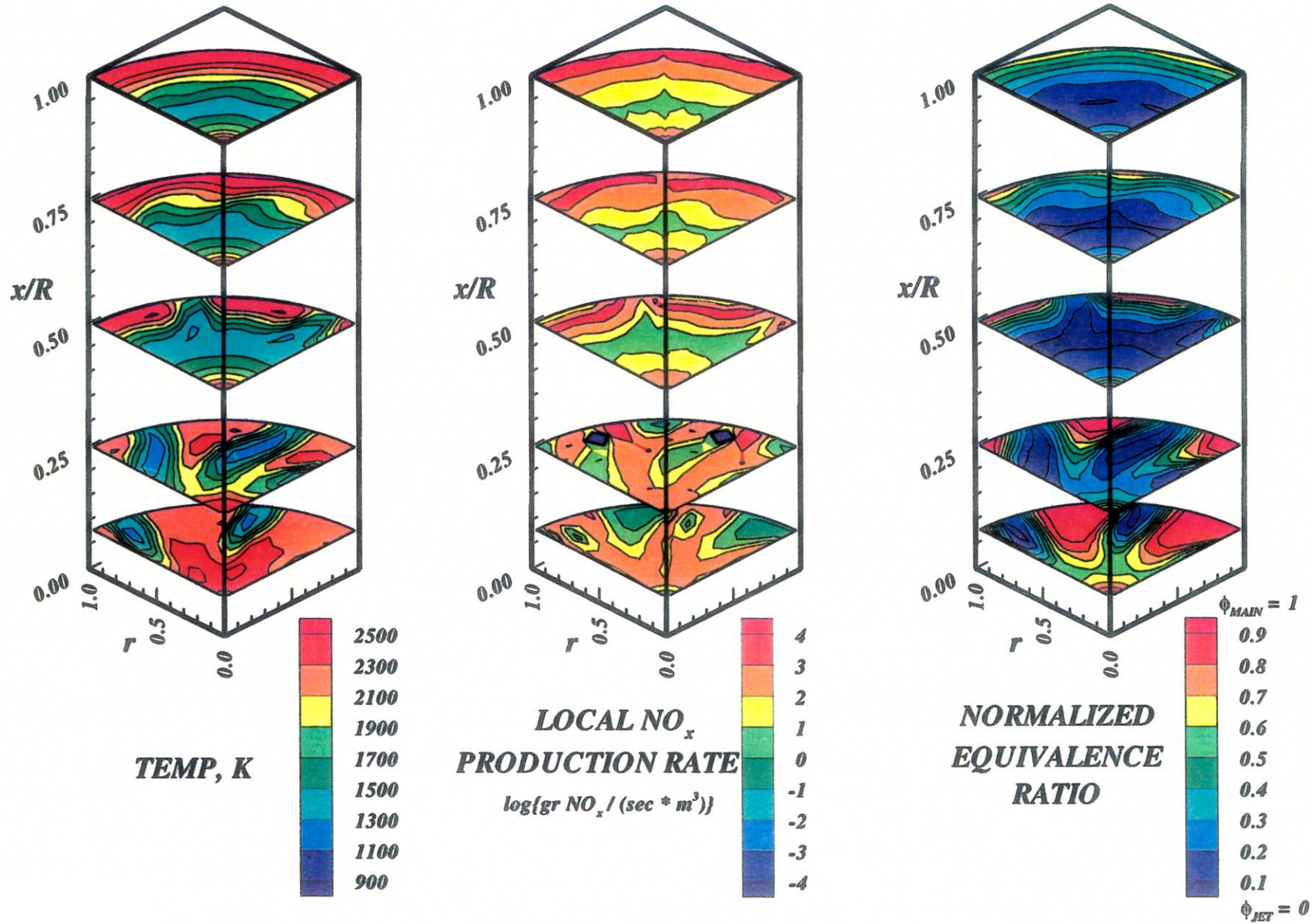
Figure-E8. Configuration #26, 8 round orifices / row
J=88.4, MR=2.96, DR=2.28, ϕ_{RZ}=1.80, ϕ_{LZ}=0.416
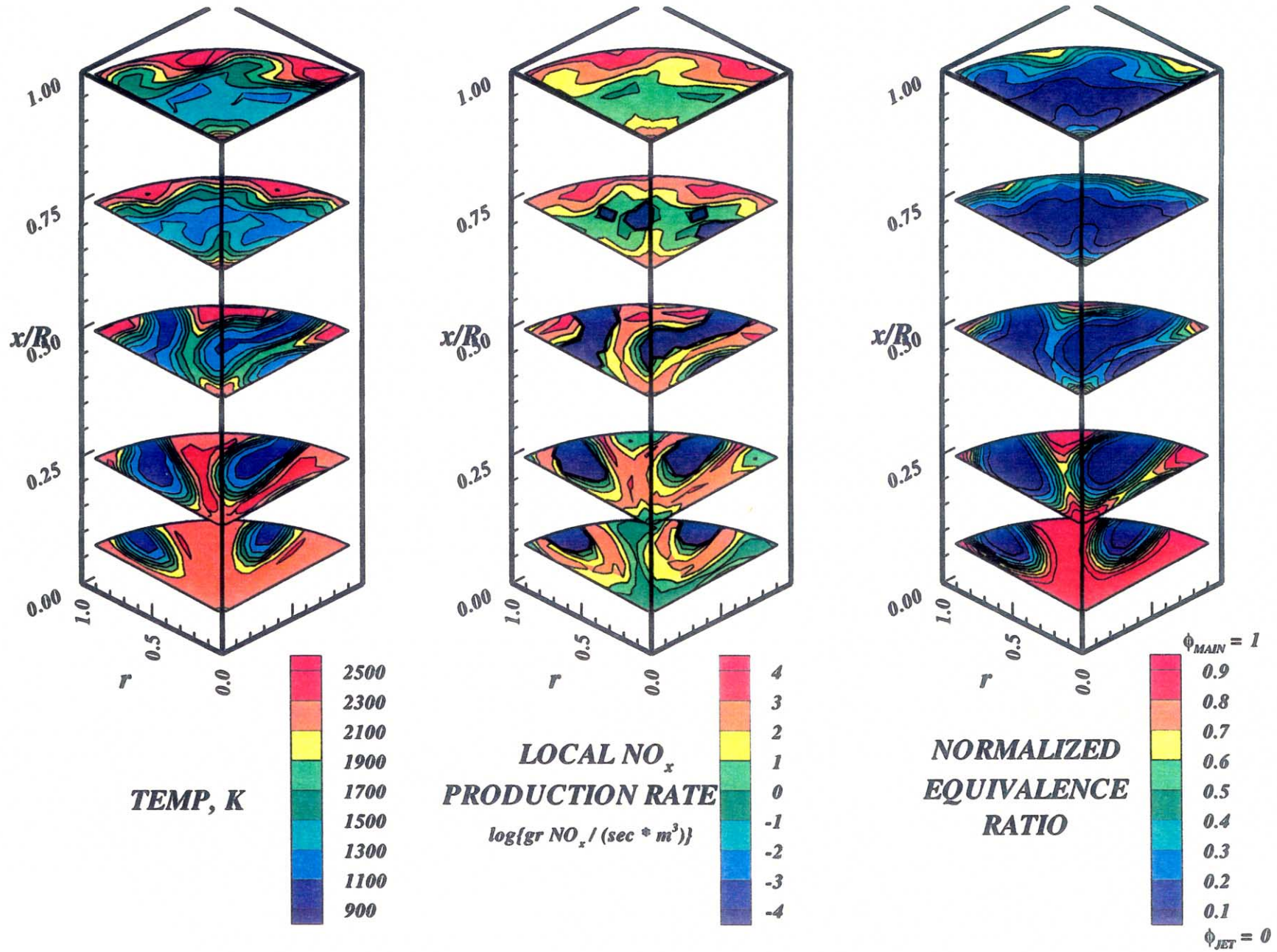
Figure-E9. Configuration #27, 8 round orifices / row
$J = 28.0$, $MR = 2.96$, $DR = 2.28$, $\phi_{RZ} = 1.80$, $\phi_{LZ} = 0.416$
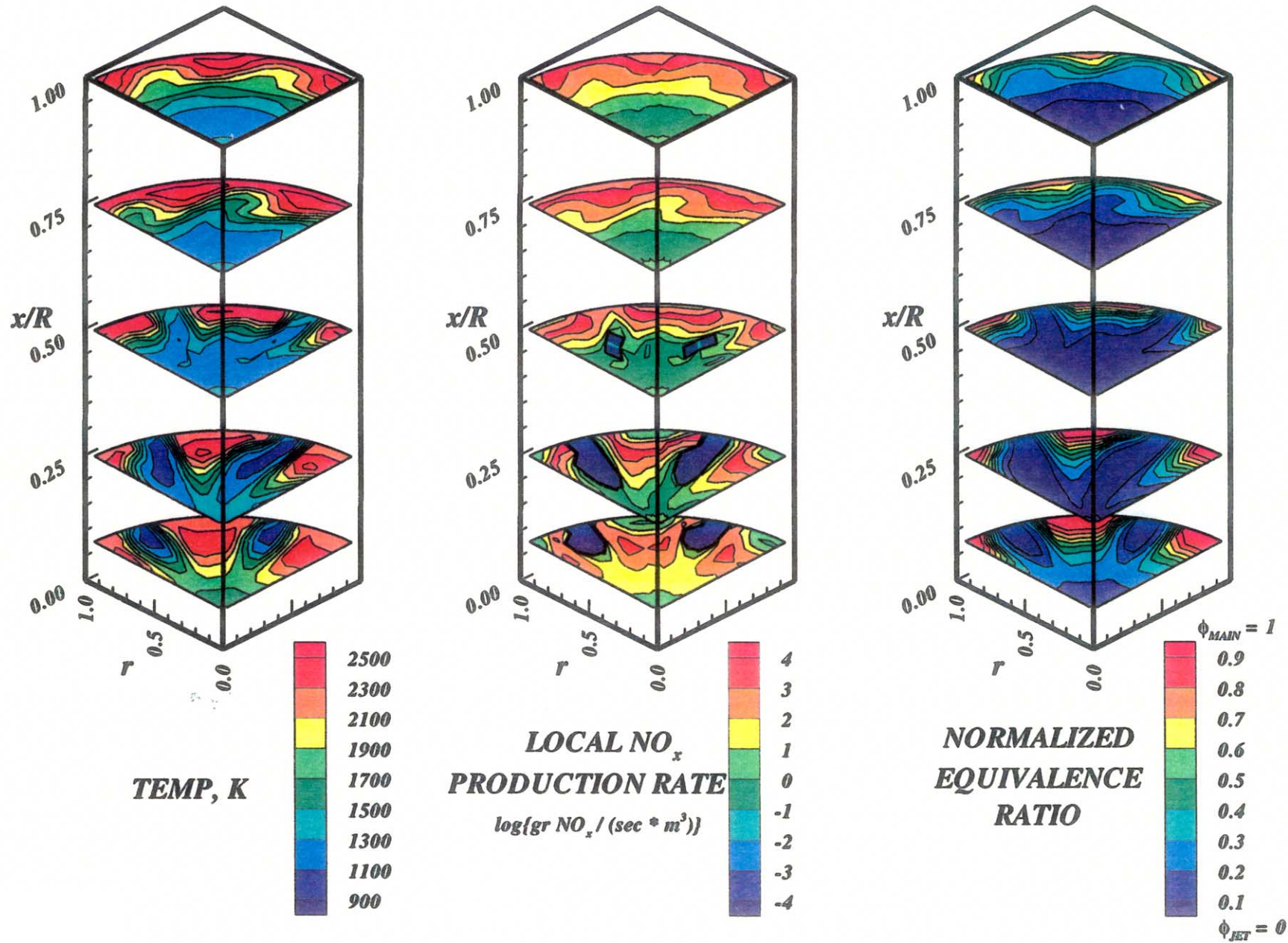
Figure-E10. Configuration #28, 8 round orifices / row
J=53.2, MR=2.96, DR=2.28, ϕ_{RZ}=1.80, ϕ_{LZ}=0.416
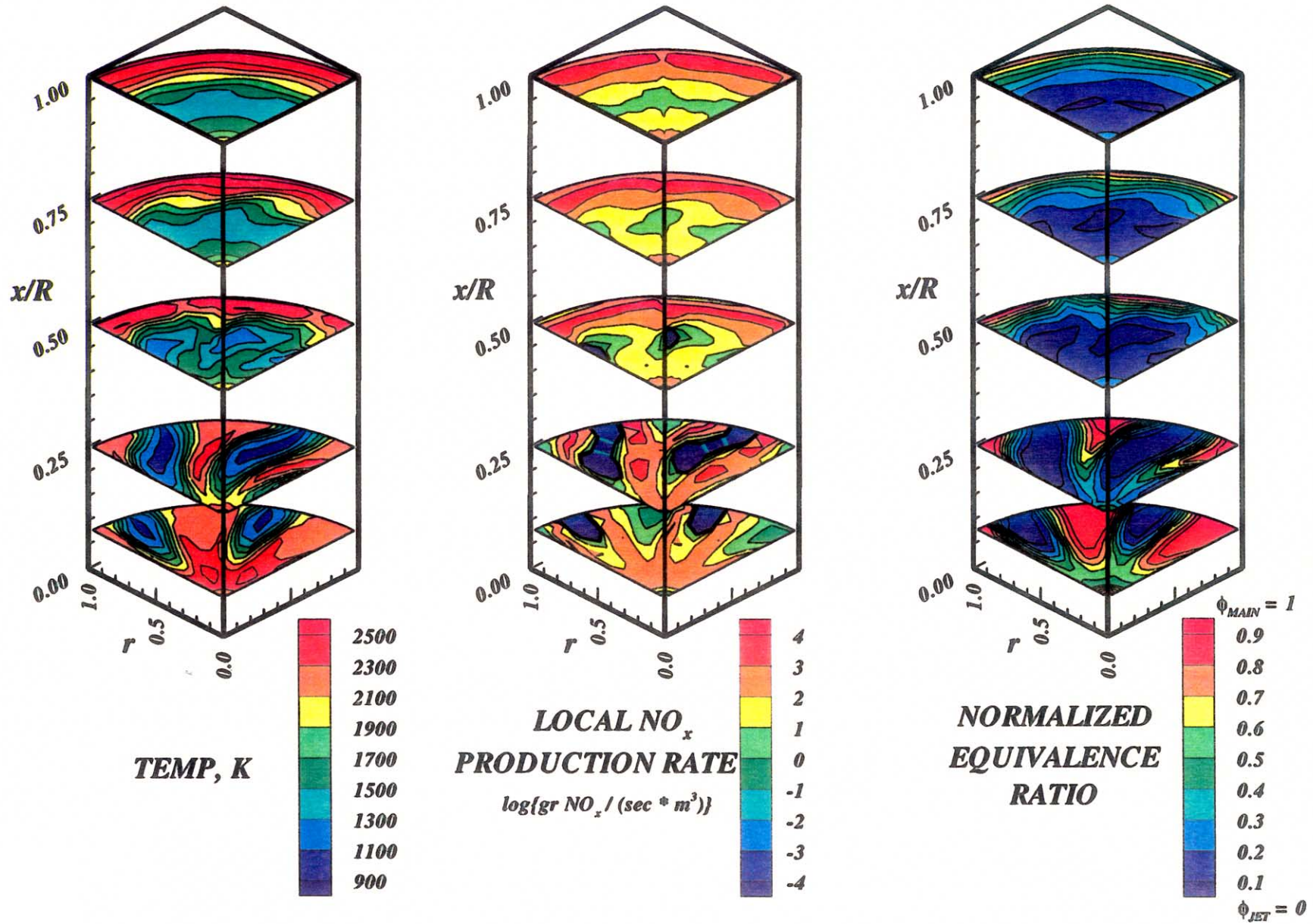
Figure-E11. Configuration #29, 8 round orifices / row
$J=57.6$, $MR=2.96$, $DR=2.28$, $\phi_{RZ}=1.80$, $\phi_{LZ}=0.416$
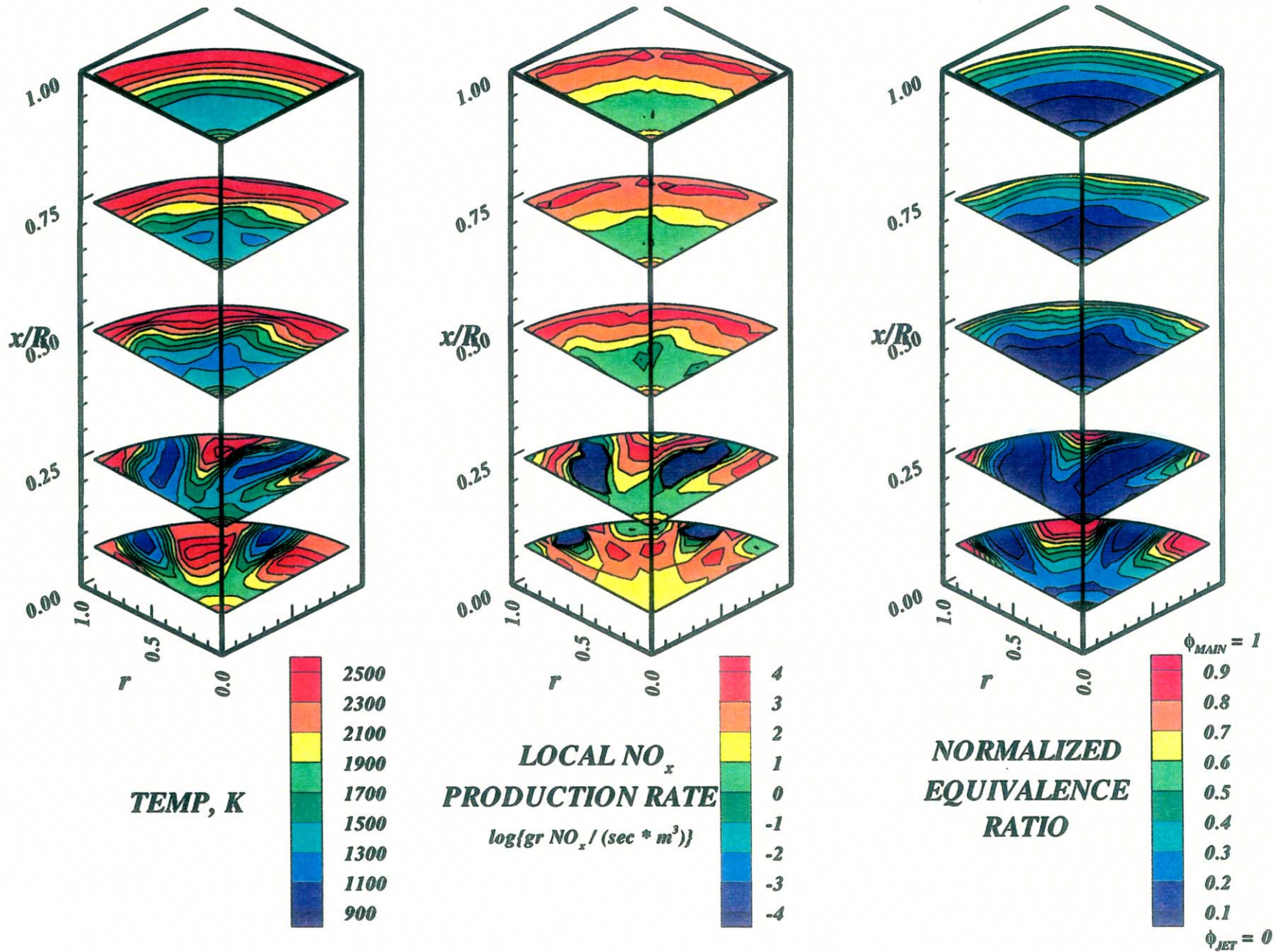
Figure-E12. Configuration #30, 8 round orifices / row
$J=92.9$, $MR=2.96$, $DR=2.28$, $\phi_{RZ}=1.80$, $\phi_{LZ}=0.416$
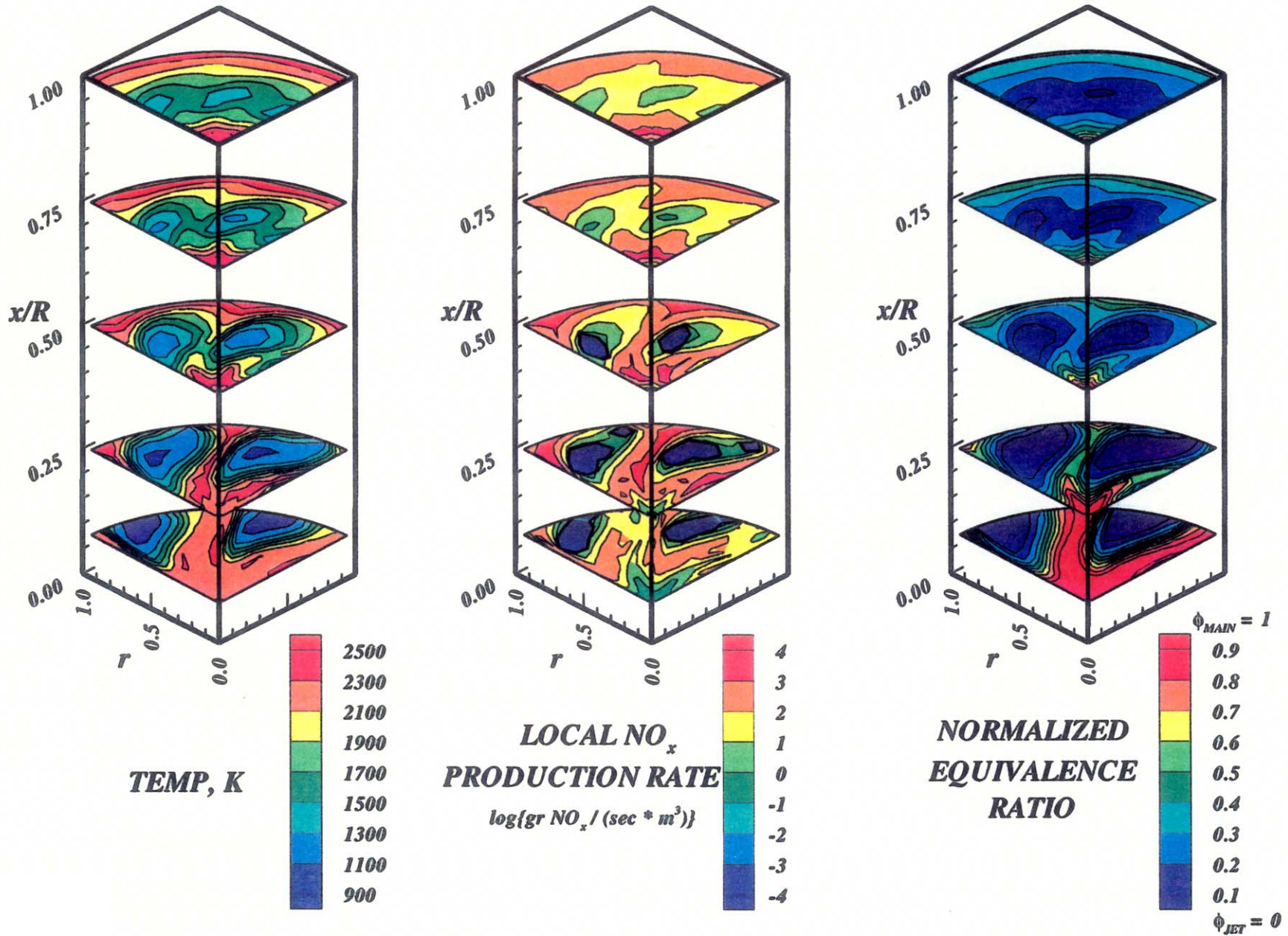
Figure-E13. Configuration #31, 8 round orifices / row
$J=59.9$, $MR=2.96$, $DR=2.28$, $\phi_{RZ}=1.80$, $\phi_{LZ}=0.416$
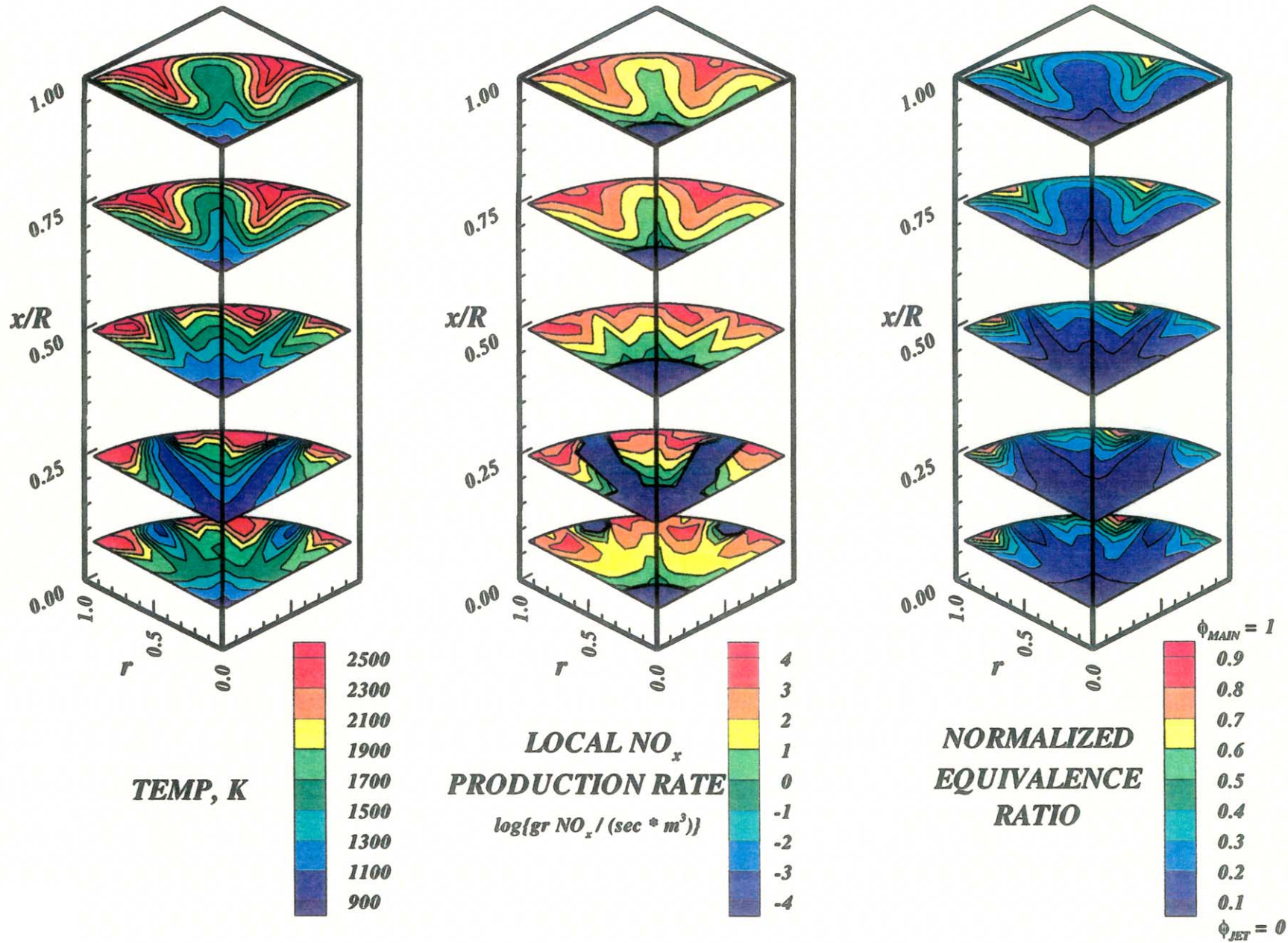
Figure-E14. Configuration #32, 8 round orifices / row
$J=93.0$, $MR=2.96$, $DR=2.28$, $\phi_{RZ}=1.80$, $\phi_{LZ}=0.416$
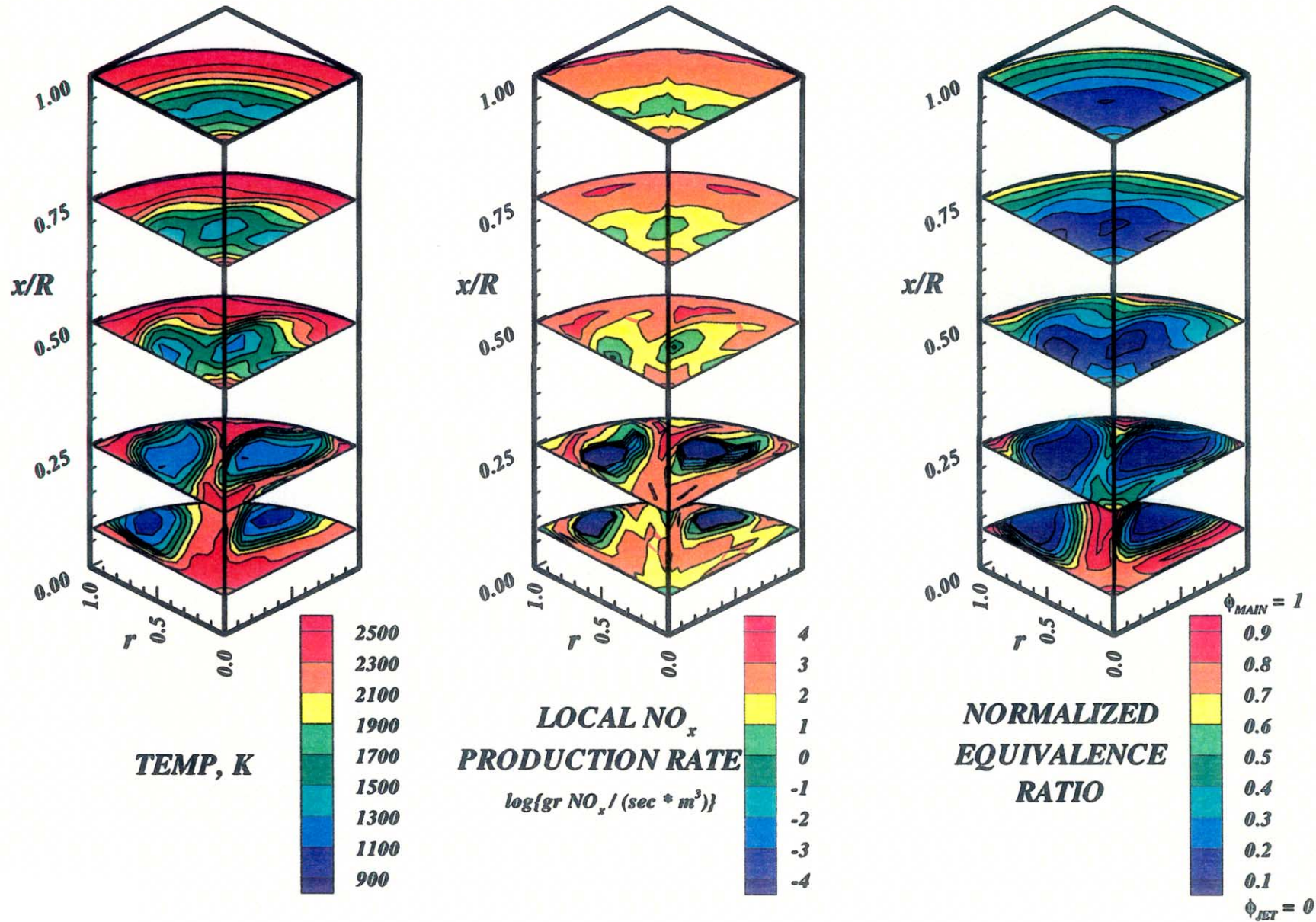
Figure-E15. Configuration #33, 8 round orifices / row
J=99.3, MR=2.96, DR=2.28, ϕ_{RZ}=1.80, ϕ_{LZ}=0.416
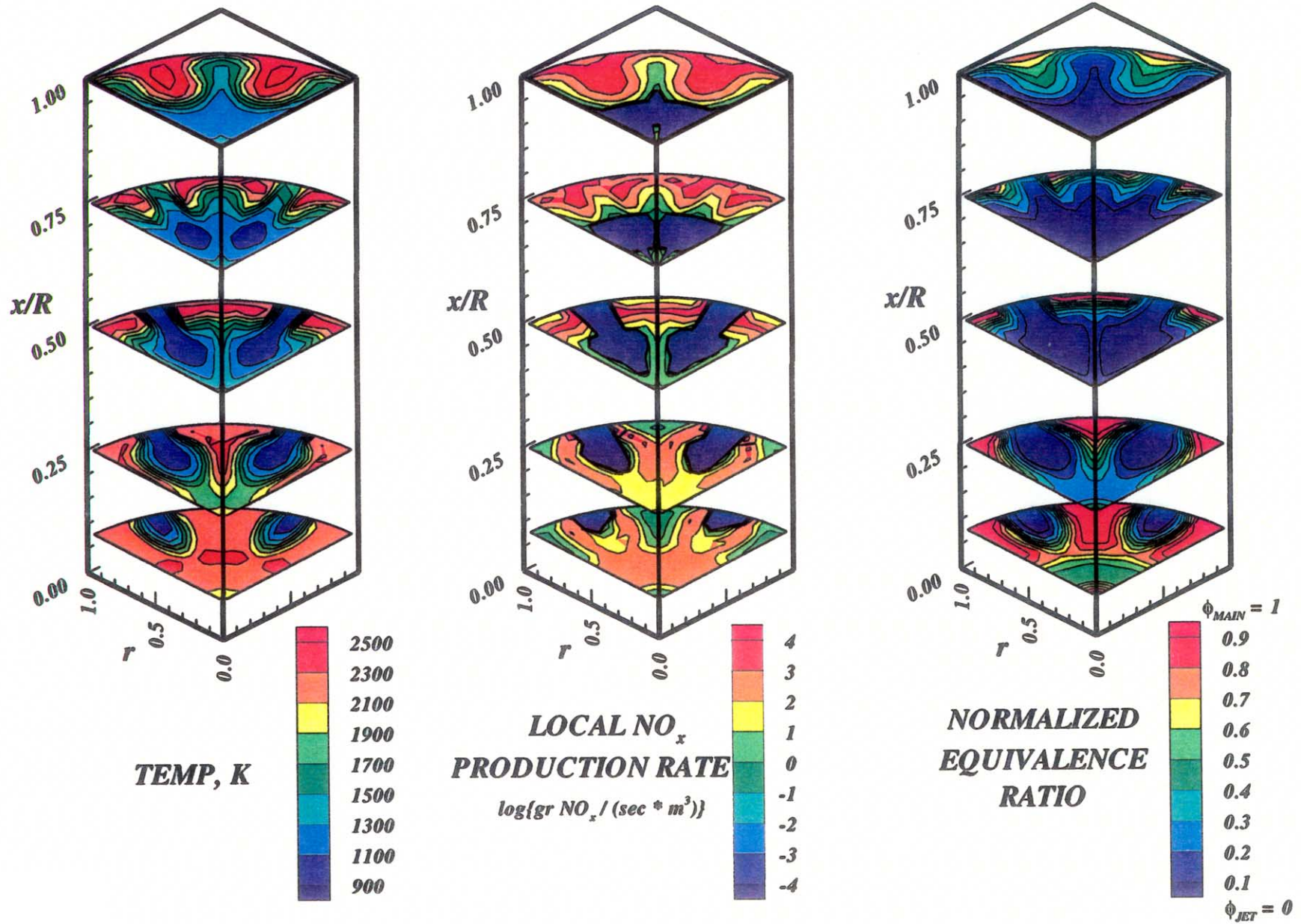
Figure-E16. Configuration #34, 8 round orifices / row
$J=26.0$, $MR=2.96$, $DR=2.28$, $\phi_{RZ}=1.80$, $\phi_{LZ}=0.416$
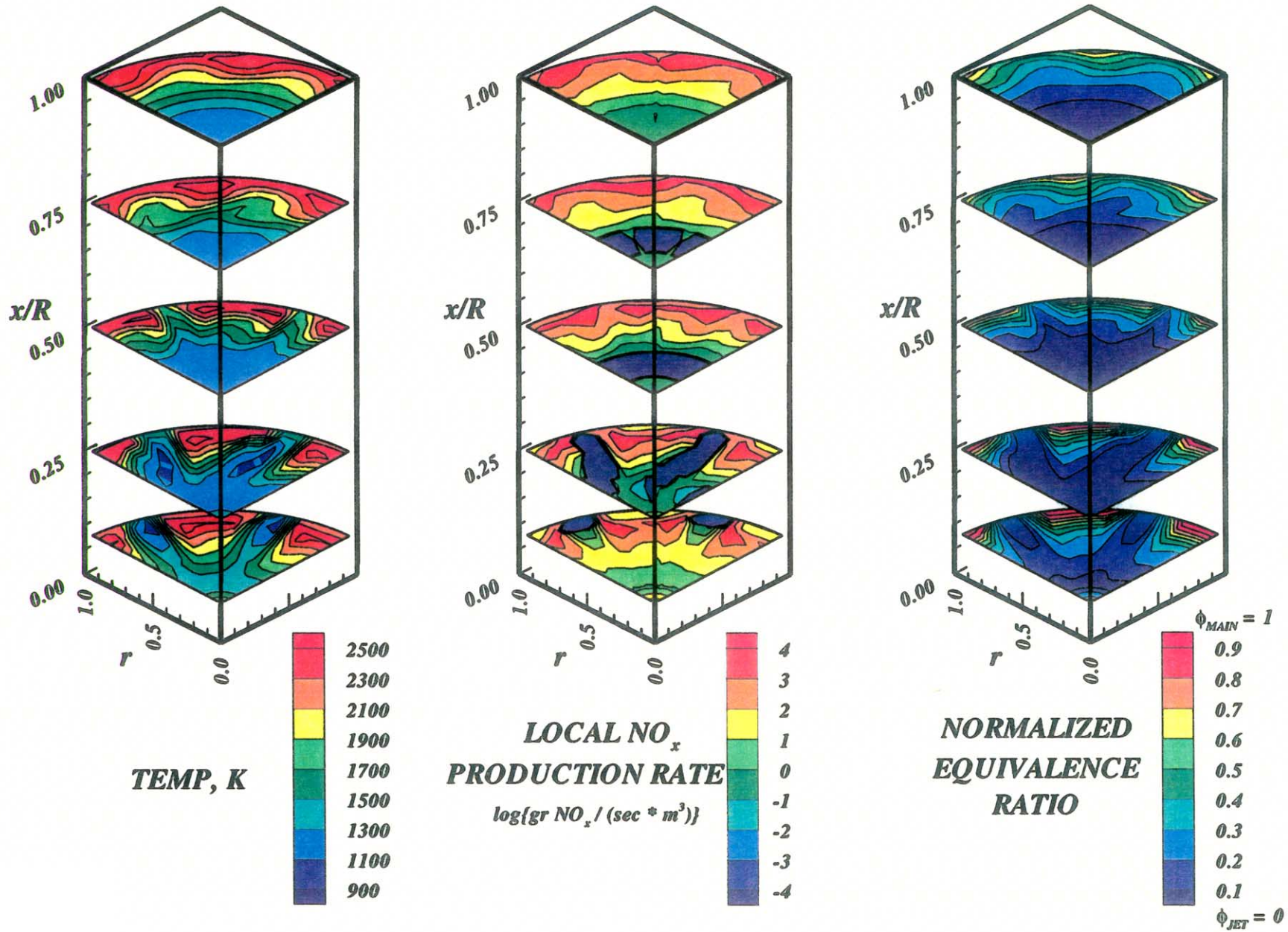
Figure-E17. Configuration #35, 8 round orifices / row
J=88.1, MR=2.96, DR=2.28, ϕ_{RZ}=1.80, ϕ_{LZ}=0.416

TEMP, K

	2500
	2300
	2100
	1900
	1700
	1500
	1300
	1100
	900

LOCAL NO$_x$
PRODUCTION RATE

log{gr NO$_x$ / (sec * m^3)}

	4
	3
	2
	1
	0
	-1
	-2
	-3
	-4

NORMALIZED
EQUIVALENCE
RATIO

|	
	$\phi_{MAIN} = 1$
	0.9
	0.8
	0.7
	0.6
	0.5
	0.4
	0.3
	0.2
	0.1
	$\phi_{JET} = 0$
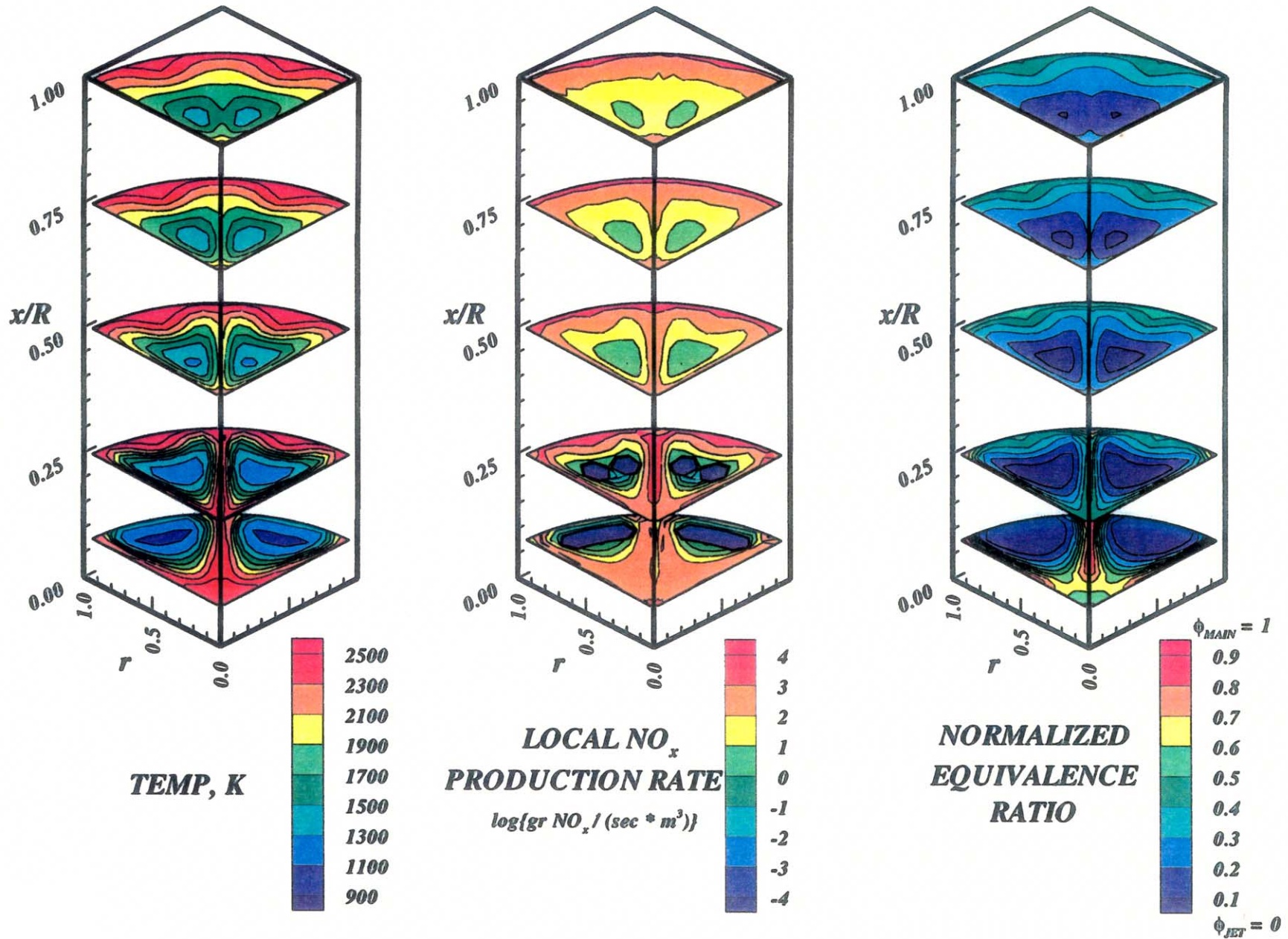
Figure-E18. Configuration #36, 8 round orifices / row
J=106.2, MR=2.96, DR=2.28, ϕ_{RZ}=1.80, ϕ_{LZ}=0.416

REPORT DOCUMENTATION PAGE

Form Approved
OMB No. 0704-0188

1. AGENCY USE ONLY (*Leave blank*)	2. REPORT DATE	3. REPORT TYPE AND DATES COVERED
	June 2003	Final Contractor Report

4. TITLE AND SUBTITLE

Mixing and NOx Emission Calculations of Confined Reacting Jet Flows in a Cylindrical Duct

5. FUNDING NUMBERS

WBS–22–714–01–38
NAS3–25950, Task Order 1

6. AUTHOR(S)

Victor L. Oechsle

7. PERFORMING ORGANIZATION NAME(S) AND ADDRESS(ES)

Allison Engine Company
P.O. Box 420, Speed code u–05
Indianapolis, Indiana 46206–0520

8. PERFORMING ORGANIZATION REPORT NUMBER

E–13908

9. SPONSORING/MONITORING AGENCY NAME(S) AND ADDRESS(ES)

National Aeronautics and Space Administration
Washington, DC 20546–0001

10. SPONSORING/MONITORING AGENCY REPORT NUMBER

NASA CR—2003-212321

11. SUPPLEMENTARY NOTES

This reseach was originally published internally as HSR005 in August 1995. Project Manager, James D. Holdeman, Turbomachinery and Propulsion Systems Division, NASA Glenn Research Center, organization code 5830, 216–433–5846.

12a. DISTRIBUTION/AVAILABILITY STATEMENT

Unclassified - Unlimited
Subject Category: 07   Distribution: Nonstandard

Available electronically at http://gltrs.grc.nasa.gov

This publication is available from the NASA Center for AeroSpace Information, 301–621–0390.

12b. DISTRIBUTION CODE

13. ABSTRACT *(Maximum 200 words)*

Rapid mixing of cold lateral jets with hot cross-stream flows in confined configurations is of practical interest in gas turbine combustors as it strongly affects combustor exit temperature quality, and gaseous emissions in for example rich-lean combustion. It is therefore important to further improve our fundamental understanding of the important processes of dilution jet mixing especially when the injected jet mass flow rate exceeds that of the cross-stream. The results reported in this report describe some of the main flow characteristics which develop in the mixing process in a cylindrical duct. A 3-dimensional tool has been used to predict the mixing flow field characteristics and NOx emission in a quench section of an RQL combustor, Eighteen configurations have been analyzed in a circular geometry in a fully reacting environment simulating the operating condition of an actual RQL gas turbine combustion liner. The evaluation matrix was constructed by varying three parameters: 1) jet-to-mainstream momentum-flux ratio (J), 2) orifice shape or orifice aspect ratio, and 3) slot slant angle. The results indicate that the mixing flow field significantly varies with the value of the jet penetration and subsequently, slanting elongated slots generally improve the mixing uniformity at high J conditions. Round orifices produce more uniform mixing and low NOx emissions at low J due to the strong and adequate jet penetration. No significant correlation was found between the NOx production rates and the mixing deviation parameters, however, strong correlation was found between NOx formation and jet penetration. In the computational results, most of the NOx formation occurred behind the orifice starting at the orifice wake region. Additional NOx is formed upstream of the orifice in certain configurations with high J conditions due to the upstream recirculation.

14. SUBJECT TERMS

Gas turbine; Combustor; Mixing; Emissions; Cylindrical

15. NUMBER OF PAGES

223

16. PRICE CODE

17. SECURITY CLASSIFICATION OF REPORT	18. SECURITY CLASSIFICATION OF THIS PAGE	19. SECURITY CLASSIFICATION OF ABSTRACT	20. LIMITATION OF ABSTRACT
Unclassified	Unclassified	Unclassified	